

DISRUPTION OF GIANT MOLECULAR CLOUDS BY MASSIVE STAR CLUSTERS

by

Elizabeth Harper-Clark

A thesis submitted in conformity with the requirements
for the degree of Doctor of Philosophy
Graduate Department of Astronomy and Astrophysics
University of Toronto

Copyright © 2011 by Elizabeth Harper-Clark

Abstract

Disruption of Giant Molecular Clouds by Massive Star Clusters

Elizabeth Harper-Clark

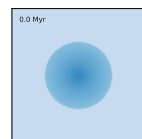
Doctor of Philosophy

Graduate Department of Astronomy and Astrophysics

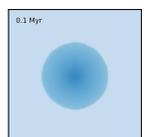
University of Toronto

2011

The lifetime of a Giant Molecular Cloud (GMC) and the total mass of stars that form within it are crucial to the understanding of star formation rates across a whole galaxy. In particular, the stars within a GMC may dictate its disruption and the quenching of further star formation. Indeed, observations show that the Milky Way contains GMCs with extensive expanding bubbles while the most massive stars are still alive. Simulating entire GMCs is challenging, due to the large variety of physics that needs to be included, and the computational power required to accurately simulate a GMC over tens of millions of years. Using the radiative-magneto-hydrodynamic code Enzo, I have run many simulations of GMCs. I obtain robust results for the fraction of gas converted into stars and the lifetimes of the GMCs: (A) In simulations with no stellar outputs (or “feedback”), clusters form at a rate of 30% of GMC mass per free fall time; the GMCs were not disrupted but contained forming stars. (B) Including ionization gas pressure or radiation pressure into the simulations, both separately and together, the star formation was quenched at between 5% and 21% of the original GMC mass. The clouds were fully disrupted within two dynamical times after the first cluster formed. The radiation pressure contributed the most to the disruption of the GMC and fully quenched star formation even without ionization. (C) Simulations that included supernovae showed that they are not dynamically important to GMC disruption and have only minor effects on subsequent star formation. (D) The inclusion of a few μG magnetic field across the cloud slightly reduced the star formation rate but accelerated GMC disruption by reducing bubble shell disruption and leaking. These simulations show that new born stars quench further star formation and completely disrupt the parent GMC. The low star formation rate and the short lifetimes of GMCs shown here can explain the low star formation rate across the whole galaxy.



For Bryant



Acknowledgements

The last few months have really emphasized the incredible generosity of my work colleagues and the unshakable support from my friends and family. I am deeply touched and honoured to know so many amazing people.

I would like to start by thanking my supervisor Norm. His extensive memory and unwavering ability to understand the vast work of the community has proved invaluable in my education. I would like to thank my thesis committee - Peter and Chris - for interesting discussion and useful suggestions to help me along the way. Special thanks also to Bob and Ernie on my qualifier committee and James and Bob on my thesis defence committee.

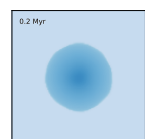
I would like to thank my collaborator Tom for introducing me to the world of Enzo and opening up their incredible code for my thesis. Special thanks to the Enzo development team - especially Matt and John - for their extensive coding, impressive documentation, and perpetual answering of questions. Thanks also to the yt team without whom my thesis would not be anywhere near as visually impressive.

Thanks go to all of my office mates over the years: Brian, Parandis, Ivana, Lawrence, Pascal, Zhiqi, Nick B, Marzieh, & Nick T. It has been wonderful learning about your research and sharing ideas, coding tips, and computer tricks. I would also like to thank everyone else in the astronomy community in Toronto, I have learned so much from so many of you I do not even know where to start. Thank you. Special thanks to the admins in both DAA and CITA - you guys are incredible.

To all of the faculty and fellow TAs in the department and the amazing CTSI people it has been wonderful working with all of you. Special thanks to Mike and Bob for showing me the kind of teacher I want to be and for Peter for taking the concerns and ideas of a grad student seriously.

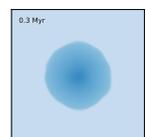
I would like to take a moment to thank Canada and Canadians. I have been stunned by the amazing acceptance, open-mindedness, and consideration of everyone here. What an amazing country to be a part of.

Last but by no means least, I would like to thank my family and friends. Bryant: for everything. My parents and parents-in-law-to-be: your love and support mean the world to me, thank you. Thanks go to the rest of our families - especially Chris, you are a star. To the Cambridge Society of Toronto - thank you for the small piece of home out here in the great North, and especially Kelly for proof reading this thesis for me. For everyone at Massey: thank you for an amazing 5 years, I have loved every minute. Special thanks to the Cherries and Cherries fans: you ladies rock!

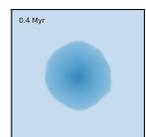


Contents

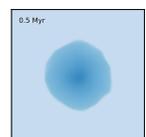
1	Introduction	1
1.1	Big Picture	1
1.2	Observations	5
1.3	Other Numerical Work	7
1.4	Key Results in This Thesis	11
1.5	Thesis Outline	12
2	1D models: Harper-Clark and Murray 2009	13
2.1	Abstract	13
2.2	INTRODUCTION	14
2.3	OBSERVATIONS OF CARINA	15
2.4	METHODS	19
2.4.1	Chevalier and Clegg bubble	19
2.4.2	Castor bubble	20
	Modifications to the Castor Bubble Model - Stellar Mass-Loss Rates	21
	Radiation Pressure	22
	Self-Gravity	23
	Leakage of Hot Gas	23
	Final bubble model	24
2.5	RESULTS	25
2.5.1	Original stellar wind models	25
2.5.2	Modified Castor et al. Model: Leakage	29



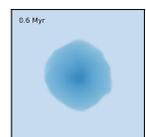
2.6	X-RAY SURFACE BRIGHTNESS PROFILES	34
2.6.1	Globule evaporation	35
2.7	DISCUSSION	40
2.7.1	Dynamics Controlled by H II Gas	43
2.7.2	Ballistic Bubbles	44
2.8	CONCLUSIONS	47
2.9	Appendix: CHEVALIER & CLEGG BUBBLES	48
2.10	Appendix: CASTOR et al. BUBBLES	49
3	Coding	52
3.1	Enzo Overview	52
3.2	Hydrodynamics	53
3.2.1	Improved PPM	53
3.2.2	Hydro_rk	54
3.2.3	Magnetohydrodynamics	55
3.3	Gravity	55
3.4	Heating and Cooling	55
3.5	Turbulence	56
3.6	Radiation	56
3.7	Particles and Star Formation	57
3.7.1	Individual Star Formation	58
3.7.2	Star Cluster Formation	58
	Star cluster outputs	59
3.8	Analysis	60
4	Three Dimensional Simulations	61
4.1	Base Simulation	62
4.1.1	Base Simulation Results	64
4.1.2	Base Simulation Summary	88
4.2	Output study	89



4.2.1	Output Study Results	89
	No outputs	91
	Supernovae	93
	Ionisation	97
	Radiation Pressure	99
4.2.2	Radiation Pressure Investigation	103
4.2.3	Radiation Pressure Investigation Results	104
4.3	Surrounding Medium Investigation	114
4.3.1	Surrounding Medium Results	115
4.3.2	Surrounding Medium Summary	115
4.4	Magnetic Fields	119
4.4.1	Magnetic Fields Results	119
4.5	Cloud Mass	127
4.5.1	More Massive Cloud Base Simulation	127
4.5.2	More Massive Cloud Base Results	131
4.5.3	More Massive Cloud Investigations	138
	Outputs	138
5	Testing Numerical Algorithms	142
5.1	Star Formation Parameter Study	142
5.1.1	Star Formation Parameter Study Results	144
	PopIIIOverDensityThreshold	144
	StarClusterMinDynamicalTime	152
	StarClusterMinimumMass	157
	StarClusterFormEfficiency	163
	Parameter Study with No Outputs	167
	Parameter Study Summary	175
5.2	Resolution Tests	176
5.2.1	Star formations parameters for changing resolution	176

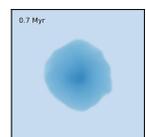


5.2.2	Unigrid Results	176
5.2.3	AMR Results	183
	Effective 256 ³	184
	128 ³ Top Grid	188
5.2.4	More Massive Cloud Resolution Tests	192
5.3	Turbulent Seeds	196
5.3.1	Turbulent Seeds Results	196
5.3.2	Turbulent Seeds Summary	197
5.4	Hydrodynamic Solver	202
5.4.1	Hydrodynamic Solver Base Results	202
5.4.2	Hydrodynamic Solver Seeds Results	212
6	Interesting Asides	221
6.1	Abstract	221
6.2	Introduction	221
6.3	Code	222
6.4	Simulation Set-up	222
6.5	Preliminary Results	224
6.5.1	Local conditions for star formation	224
6.5.2	Location of first stars within the GMC	224
7	Conclusions	227
7.1	Summary	227
7.2	Conclusions	229
7.3	Further Work	230
	Bibliography	232



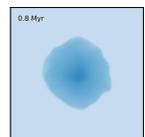
List of Tables

2.1	Properties of Trumpler 16 (Carina)	16
2.2	Dust masses in Carina	23
4.1	Base simulation details	61
4.2	Cluster details at 14 Myrs	80
4.3	Simulations in output study	89
4.4	Radiation pressure investigation	103
4.5	Surrounding medium investigation	114
4.6	Massive cloud simulation details	127
5.1	Parameter study parameters	143
5.2	Parameter study parameters - finer dynamical time	154
5.3	Parameter study parameters - no stellar outputs	168
5.4	Unigrid resolution investigation	176
5.5	AMR resolution investigation	183
5.6	Seeds in turbulence investigation	196
5.7	Seeds in hydro solver investigation	212

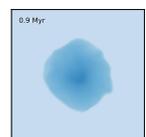


List of Figures

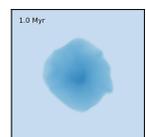
1.1	‘Madau plot’ from Karim et al. (2011)	2
1.2	Protostellar jets in Carina	4
1.3	Westerlund 2 (Povich et al. 2008)	6
1.4	Carina Nebula	7
1.5	Vela Nebula as imaged by BLAST	8
2.1	Cartoons of original and modified Castor et al. bubble	20
2.2	Plots of the basic Castor et al. (1975) model evolution for Tr 16	26
2.3	Plot of the steady state Chevalier & Clegg (1985) model for Tr 16	27
2.4	X-ray Luminosity and Pressure with radius for models of Trumpler 16	28
2.5	Graphs of Castor style bubble evolution for different shell covering fractions	30
2.6	Graphs of Castor style bubble evolution with different ISM models	32
2.7	Parameter study results for modified Castor bubbles	33
2.8	Visual image of Carina with X-ray contours	34
2.9	Graphs of X-ray luminosity from modified Castor bubbles	36
2.10	X-ray profile for a modified Castor bubble	37
2.11	X-ray image of Carina	38
2.12	X-ray surface brightness profiles for Carina	39
2.13	Image of ultra compact HII region showing shell complexity	45
3.1	Cartoon of AMR	53
3.2	hydro_rk solver cartoon	54
3.3	HEALPix explanation	57



4.1	Base simulation setup	63
4.2	Turbulent velocity structure	65
4.3	Column densities for base simulations	65
4.4	Stellar mass evolution for base simulation	66
4.5	Base simulation at 5.5 Myrs	67
4.6	Base simulation at 6.5 Myrs	68
4.7	Base simulation at 7.5 Myrs	69
4.8	Base simulation at 8.5 Myrs	70
4.9	Base simulation at 9.5 Myrs	71
4.10	Base simulation at 10.5 Myrs	72
4.11	Radiation force for base simulation at 9.5 Myrs	74
4.12	Mass structure for the base simulation	75
4.13	Radiation force absorbed by the gas with time for the base simulation	76
4.14	Radiation force absorption efficiency for the base simulation	77
4.15	Turbulent weighted mean Mach number for base simulation	78
4.16	Kinetic energy against time for base simulation	79
4.17	Star cluster distribution	81
4.18	Cluster positions at 14 Myrs	82
4.19	Base simulation shell radius	84
4.20	Base simulation shell covering fraction	84
4.21	Leaking shell for base simulation	85
4.22	Base simulation gas pressure profile at 9 Myrs	86
4.23	Base simulation density profile at 9 Myrs	86
4.24	Base simulation ionization fractions	87
4.25	Base simulation ionization position	88
4.26	Mass and number of stars for output study	90
4.27	Turbulent weighted mean Mach number for none simulation	92
4.28	Slices showing the dynamical effects of supernovae with no other outputs	94
4.29	Slices showing the dynamical effects of supernovae with ionization	95



4.30 Slices showing the dynamical effects of supernovae with ionization and radiation pressure	96
4.31 Density and HII fraction projections for only HII output	98
4.32 Density projections showing star cluster formation in bubble shell	100
4.33 Density and HII fraction projections comparing HII and HIIRP	101
4.34 Mass structure for different stellar outputs	102
4.35 Mass and number of stars for lowHII simulations	106
4.36 Mass and number of stars for RPlowHII simulations	107
4.37 Mass of stars for Q reduced by 100 simulations	108
4.38 Efficiency of radiation force absorbed by gas for varying Q	109
4.39 Mass structure for the simulations with varying Q	110
4.40 Mass structure for the simulations including radiation pressure with varying Q	111
4.41 Density projections for different Qs at 9.5 Myrs	112
4.42 Density projections for different Qs at 13 Myrs	113
4.43 Initial velocities for different external densities	114
4.44 Mass and number of stars for different external densities	116
4.45 Box1den simulation at 8.8 Myrs	117
4.46 Mass structure for different exterior densities	118
4.47 Magnetic energy against time	120
4.48 Kinetic energy against time for magnetic simulation	121
4.49 Stellar mass evolution for magnetic fields	122
4.50 Mass structure for the magnetic simulation	123
4.51 Magnetic field simulation at 9.5 Myrs	124
4.52 Density and magnetic field projections for magnetic run at different times	125
4.53 Density slice comparing with and without magnetic field at 9 Myrs	126
4.54 More massive cloud simulation setup	129
4.55 More massive cloud turbulent velocity structure	130
4.56 Column densities for more massive cloud simulation	130
4.57 Stellar mass evolution for more massive cloud base simulation	132



4.58 More massive cloud base simulation at 9.5 Myrs 133

4.59 More massive cloud base simulation at 11.5 Myrs 134

4.60 More massive cloud base simulation at 13.5 Myrs 135

4.61 More massive cloud base simulation at 15.5 Myrs 136

4.62 Mass structure for the more massive cloud base simulation 137

4.63 Stellar mass evolution for more massive cloud with different stellar outputs . . . 139

4.64 Mass structure for the more massive cloud with different outputs 140

4.65 Density projections for different outputs for more massive cloud at 11 Myrs . . . 141

5.1 Mass and number of stars for different critical densities 146

5.2 Simulation with low critical density 3.1 Myrs after first cluster formation 147

5.3 Simulation with highest critical density 5 Myrs after first cluster formation . . . 148

5.4 Simulation with highest critical density 13.2 Myrs after first cluster formation . . 149

5.5 Mass structure for the simulation with low critical density 150

5.6 Mass structure for the simulation with highest critical density 151

5.7 Mass and number of stars for different dynamical times 153

5.8 Unrealistic star formation from too large a sphere 154

5.9 Mass and number of stars for finer dynamical times 155

5.10 Density slices showing star formation sphere for different dynamical times 156

5.11 Mass and number of stars for different minimum masses 158

5.12 Density projections for different star formation routines 159

5.13 Mass structure for lowest minimum mass 160

5.14 Simulation with low minimum mass 1.1 Myrs after first cluster formation 161

5.15 Simulation with low minimum mass 8.6 Myrs after first cluster formation 162

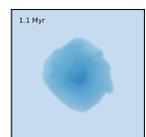
5.16 Mass and number of stars for different minimum masses 164

5.17 Mass structure for different efficiencies 165

5.18 Density projections for different efficiencies at 8.5 Myrs 166

5.19 Mass in clusters for no outputs and different critical densities 169

5.20 Mass in clusters highest critical densities in both parameter studies 170



5.21 Mass in clusters for no outputs and different dynamical times 171

5.22 Mass in clusters for no outputs and different minimum masses 172

5.23 Density projections at 12.5 Myrs for no outputs and different minimum masses . 173

5.24 Mass in clusters for no outputs and different star cluster formation efficiencies . . 174

5.25 Mass and number of stars for unigrid resolution test 178

5.26 Density projections showing turbulent structure for different resolution 179

5.27 Density projections showing star clusters and bubble for different unigrid simu-
lations 179

5.28 256r0d4 simulation at 7.3 Myrs 180

5.29 256r0d4 simulation at 9.3 Myrs 181

5.30 Mass structure for base and 256r0d4 182

5.31 Density projections for AMR resolution 185

5.32 Mass and number of stars for AMR study with 256^3 effective resolution 186

5.33 Mass structure for same effective resolution 187

5.34 Mass and number of stars for AMR study with 128^3 top grid 189

5.35 Density projections at 10.5 Myrs for different resolution with 128 top grid 190

5.36 Mass structure for base, 128r1d2, and 128r2d8 191

5.37 Star formation history for different resolutions for the more massive cloud simu-
lation. 193

5.38 Mass structure for more massive cloud with different resolutions 194

5.39 Density projections for different resolutions for more massive cloud at 14.5 Myrs 195

5.40 Mass and number of stars for different turbulent seeds 198

5.41 Mass structures for simulations with highest and lowest stellar mass 199

5.42 Density projections for Seed2 200

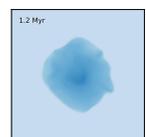
5.43 Density projections for Seed9 201

5.44 Stellar mass evolution for base simulation with PPM 203

5.45 Base simulation with PPM at 5.4 Myrs 204

5.46 Base simulation with PPM at 6.4 Myrs 205

5.47 Base simulation with PPM at 7.4 Myrs 206



5.48 Base simulation with PPM at 8.4 Myrs 207

5.49 Base simulation with PPM at 9.4 Myrs 208

5.50 Base simulation with PPM at 10.4 Myrs 209

5.51 Mass structure for the base simulations with different solvers 210

5.52 Radiation force absorbed by the gas with time for the PPM base simulation . . . 211

5.53 Mass of stars for different hydro solvers 214

5.54 Mass of clusters for different hydro solvers 215

5.55 Mass of clusters for different hydro solvers 216

5.56 Hydro solver density comparisons 217

5.57 Mass structures for PPM simulations with highest and lowest stellar mass 218

5.58 Density projections for Seed2 PPM 219

5.59 Density projections for Seed9 PPM 220

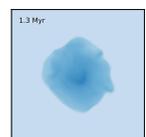
6.1 Cartoon of possible GMC star formation rate 222

6.2 Image of G298-0.34, a GMC being disrupted 223

6.3 Density projection of small cloud simulation setup 224

6.4 Density slices showing filament collisions 225

6.5 Density projections of simulation setup showing strong dependence on central concentration 226



Chapter 1

Introduction

The title of this thesis is:

Disruption of Giant Molecular Clouds by Massive Star Clusters.

By this we mean:

Disruption of - the movement of the overwhelming majority of gas out of the original location of a cloud, unbinding it.

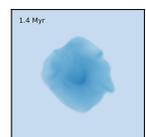
Giant Molecular Clouds - the largest clouds within our galaxy. The simulated clouds have masses of $220,237 M_{\odot}$ and $881,000 M_{\odot}$. They are initially cool (10K) and have molecular hydrogen as the principle component. Each cloud is a marginally gravitationally bound collection of gas.

by - the disruption of the cloud results from outputs from the star clusters being absorbed as feedbacks and not by any external factors.

Massive Star Clusters - observations show most stars form within groups, often with thousands of individual stars within a couple of parsecs (pc) of each other. Each cluster contains many OB stars; the simulated clusters have at least $1000 M_{\odot}$ in stars.

1.1 Big Picture

To understand why we chose to investigate GMC disruption by stars, we need to take a step back and consider how GMC star formation rates and lifetimes affect star formation on larger scales. Gas disks in spiral galaxies are marginally gravitationally stable, yet only 2% of the gas



is converted into stars each dynamical time (Kennicutt, 1998). Thus, there must be either forces counteracting gravity and reducing star formation rates or other physical effects quenching star formation.

Figure 1.1 (Fig. 11 from Karim et al. (2011)) shows a recent version of the ‘Madau plot’ - the star formation rate density history of the universe. The changes in star formation rate density are thought to be caused by changes in the accretion rate onto the halo (Karim et al., 2011). This shows the star formation rate is always a small fraction of the gas mass per dynamical time, but what sets the fraction?

Recent work shows the star formation rate within galaxies is most dependent on the surface density of molecular hydrogen (Bigiel et al. (2008) and Leroy et al. (2008)). Thus, the vast majority of stars within a galaxy form in Giant Molecular Clouds (GMCs). The largest GMCs have dynamical times approximately equal to the galactic dynamical time (Murray, 2011). For a GMC the dynamical time is the free-fall time - approximately how long it would take for the cloud to collapse if only gravity was present: $t_{dyn} = \sqrt{R^3/2GM}$, where R is the radius of the cloud, G is the gravitational constant, and M is the mass of the cloud, $t_{dyn} = 5-10$ Myrs for GMCs in the Milky Way. Throughout this thesis I will use dynamical time as the principle

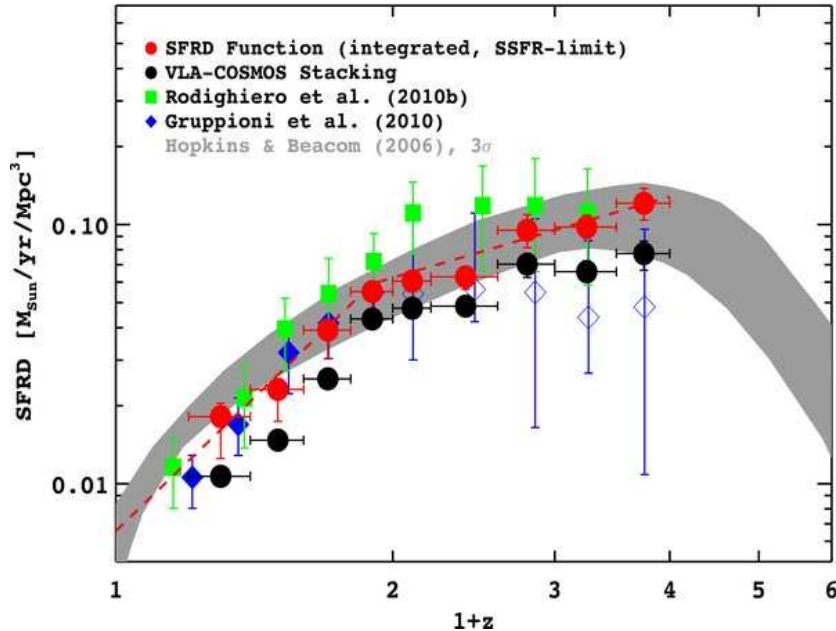
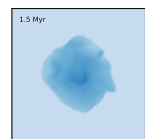


Figure 1.1: A Madau plot from Karim et al. (2011) showing the observed star formation history of the universe. The y axis is star formation rate density and the x axis redshift + 1. Different symbols are from different IR and radio surveys. The grey area is from Hopkins & Beacom (2006) who fit analytical forms to the data to derive conservative uncertainties.



time unit as it gives the minimum timescale on which significant dynamical changes can occur.

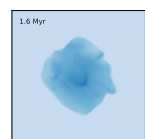
To understand how a GMC's star formation rate translates to the galactic star formation rate, we need to know how long GMCs last and what the star formation rate is throughout a GMC's lifetime. Unfortunately, the lifetimes of GMCs are difficult to observe directly. Estimates range from a single dynamical time (Elmegreen, 2000) up to 10 or more dynamical times (Scoville & Wilson, 2004). More recent work has deduced a GMC lifetime of 2 to 3 dynamical times (Elmegreen (2007), Kawamura et al. (2009), and Fukui & Kawamura (2010)). Williams & McKee (1997) applied models of blister HII regions from Whitworth (1979) to statistics of GMC size and distribution. They found with star formation totalling about 10% of the clouds mass that $10^6 M_{\odot}$ clouds lasted at most 30 Myrs and smaller clouds were disrupted faster. Schrubba et al. (2010) find significant variations in the depletion time of H_2 at small scales in M33 implying a wide range of evolutionary stages over a GMC lifetime. This supports the idea of leaking and disrupting clouds rather than a steady state GMC whose star formation rate is passively regulated by, for example, turbulence (Krumholz & McKee, 2005). If GMCs do only live 2-3 dynamical times, this is highly suggestive that it could be the stars themselves that are disrupting the clouds during their lifetimes, as deduced by observations (e.g. Leroy et al. (2008)).

It has been suggested that feedback in the highest mass GMCs in a galaxy could cause a larger scale feedback: galactic winds (Murray et al. (2010a) and Murray et al. (2010b)). How long GMCs last and how much they leak while the most massive stars are still alive will have affected the efficiency of re-ionization of the universe at early redshifts (Robertson et al., 2010).

The most massive stars, O-type, live the shortest lives, yet release the most energy and momentum. The greater and more rapid release of energy and momentum suggests that O-type stars have the greatest effect on their surroundings. The energy and momentum emitted from O-type stars is released in several different ways:

Protostellar Jets - While stars are forming and accreting material from a protostellar disk, a fraction of the disc mass is accelerated along the poles of the star at high velocity. Observations of these jets show that they carry a significant momentum with them. These jets are often attributed to localized effects during star formation (Li & Nakamura, 2006). Figure 1.2 shows protostellar jets in the Carina Nebula.

Stellar Winds - During their lifetimes, O-type stars have significant stellar winds. These high velocity atomic components leave the stellar surface at speeds of thousands of kilometres per second. The mass loss rate in stellar winds is up to a few millionths of a solar mass per year. This gives a luminosity (rate of energy) of stellar wind up to a few thousand



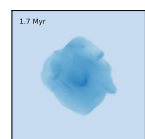
solar luminosities. Stellar winds are discussed in much greater detail in Chapter 2. We find that stellar winds do not have a significant dynamical effect on the GMC as most of the hot gas escapes through holes in the shell caused by the turbulent structure of the GMC, as can be seen in Fig. 1.3. Supernovae and stellar winds have been found to be insignificant in other work as well, such as Matzner (2002).

Ionizing radiation - O-type stars are so hot and energetic that half of the bolometric luminosity from the whole cluster is emitted at energies greater than 13.6eVs (assuming a standard IMF). These photons strip the electrons from hydrogen atoms in the surrounding gas. During ionization the gas is heated to 10^4 K, and so the gas pressure increases by a factor of 10^3 .

Radiation Pressure - All photons carry momentum. Whenever light is absorbed, that momentum is deposited into the gas or dust that absorbed it. The rate of momentum emitted by the stars is the radiation force, $F_{rad} = L_{bol}/c$. While a cluster is embedded in a GMC,



Figure 1.2: Image of protostellar jets in parsec sized pillars in the bubble wall of the Carina Nebula. Credit: NASA, ESA, and M. Livio and the Hubble 20th Anniversary Team (STScI). This colour enhanced images shows colours as: oxygen (blue), hydrogen and nitrogen (green), and sulphur (red)



most of its light will be absorbed within that GMC. The ionizing radiation is absorbed by neutral hydrogen, while visible light is predominantly absorbed by the dust. As the photons carry momentum in the direction they are travelling, which is generally away from the source, the absorbed momentum pushes the absorbing gas away from the light source. Radiation pressure has only recently been included in simulations and has been shown to be important, especially close to the star clusters (Krumholz & Matzner, 2009) and in IR optically thick regions (Fall et al., 2010).

Supernovae - Massive stars end their lives by exploding. These explosion release energy and momentum into the immediate surroundings. Many galaxy scale simulations use only supernovae as stellar feedback; see §1.3 for further discussion of supernovae in simulations. However, models of supernovae explosions off centre from a cloud show they expand and blow out of the side of the cloud and leave the majority of the cloud unaffected (Tenorio-Tagle et al., 1985).

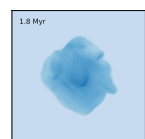
Outputs from stars can be considered feedbacks only if the energy or momentum from the outputs have any effect on the surrounding material. If the energy and momentum sources just listed are, for a reasonable star formation rate, enough to disrupt the cloud and quench further star formation, then the outputs from stars could explain the low star formation rate in spiral galaxies.

1.2 Observations

There have been many observations across many different wavelengths of GMCs both within the Milky Way and beyond. The Carina Nebula, Fig. 1.4, is one of the best studied large star clusters and observations of it are discussed at length in §2.3. In the last few years more massive clusters have been discovered in the Milky Way with the analysis of WMAP foreground data and alignment with Spitzer Glimpse images (Murray & Rahman (2010) and Murray (2011)). These studies find that the GMCs hosting the most massive star clusters are all undergoing disruption and suggest a time varying star formation rate with disruption inevitable once star formation rate reaches certain levels.

Figure 1.5 shows the Vela nebula as mapped by the BLAST. This is a region of very young star formation and a clear turbulent structure can be seen. There are significant filaments and star formation is occurring within distinct regions in the filaments.

Recent observations of 30 Doradus (in the LMC) have tested the leaking bubble predictions of Harper-Clark & Murray (2009) - Chapter 2 - (Lopez et al., 2011). They find that any hot



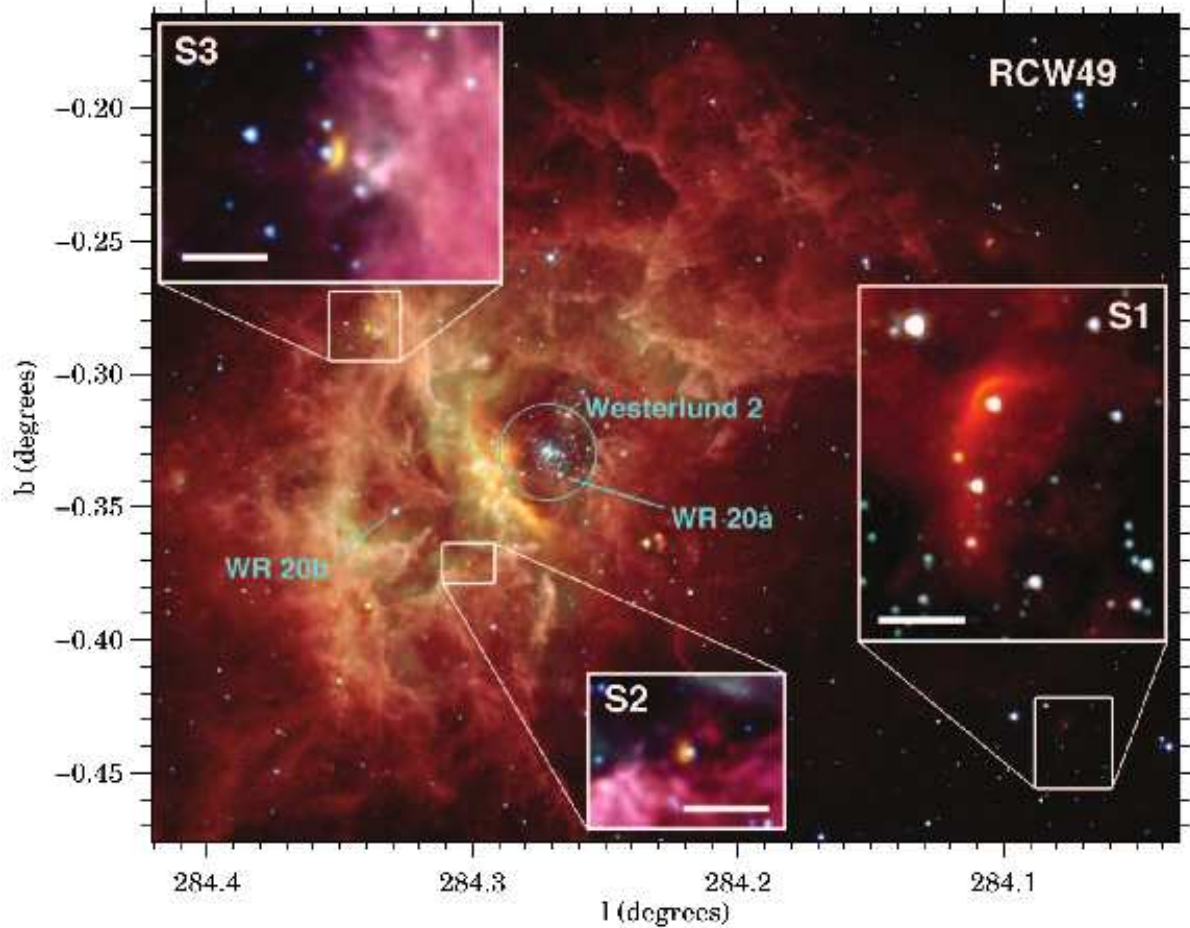
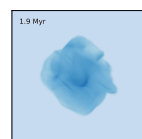


Figure 1.3: An IR image of Westerlund 2 from Povich et al. (2008). The insets show shocks from escaping gas colliding with stellar winds outside the bubble. A significant bubble shell can also be seen with a low density interior surrounding the cluster. Given that we can see inside the bubble there are clearly significant holes in the shell along our line of sight.



gas (10^7 K, e.g. shocked stellar winds) is leaking out and that only radiation pressure and ionized gas pressure are dynamically important, in agreement with Harper-Clark & Murray (2009). They are now analysing more GMCs and are finding similar results (Lopez 2011, private communication).

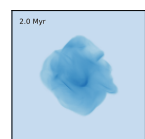
1.3 Other Numerical Work

Many other groups have been simulating star formation at a variety of scales and with varying stellar output contributions. Here follows a brief overview of this recent work.

Observations show the specific star formation rate (\dot{M}_*/M_* , where M_* is mass in stars) is nearly constant for redshifts 7 to 2 implying a constant specific star formation rate in each galaxy as it grows (Stark et al., 2009). Semi-analytic models by Weinmann et al. (2011) showed increased stellar feedback (i.e. more than just supernovae) are necessary to explain this plateau in specific star formation rate.



Figure 1.4: Image of the Carina nebula showing complex turbulent structure and a clear bubble shell with significant holes. Image is in H-alpha and BVR filters. Image is approximately 30pc across. Credit: Robert Gendler and Stephane Guisard.



While modelling galaxy clusters Battaglia et al. (2010) found that thermal feedback from massive stars in galaxies can deliver the high mass to energy efficiencies needed to sustain the hot inter cluster medium. Momentum driven feedback from stars have the advantage of not being as prone to catastrophic cooling as thermal feedback.

Petkova & Springel (2011) found that radiative feedback from stars could re-ionize the universe by redshift 6. These simulations are able to fit many observed properties of the universe by careful choice of absorption and heating efficiency. The value they found that best fit observations suggest significant ionizing radiation absorption within galaxies but with at least 10% of ionizing photons escaping the galaxy suggesting at least partially leaking bubbles.

On cosmological scales, many groups have found that without significant stellar feedback the star formation rate is an order of magnitude too high (e.g. Kereš et al. (2009) and Springel & Hernquist (2003)). Many cosmological and galaxy scale simulations use only supernovae as stellar feedback (e.g. Bournaud et al. (2011)). Many of these simulations ‘switch off’ cooling around supernovae to prevent the rapid cooling that would be expected given the density of the

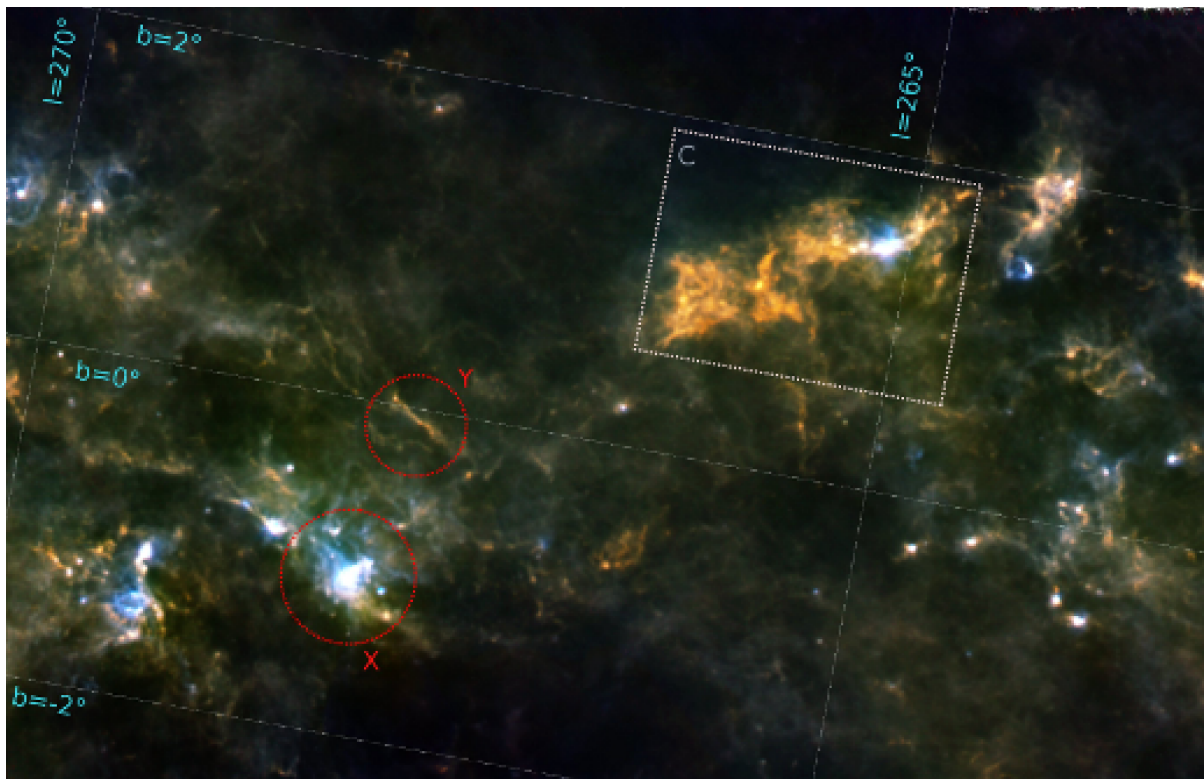
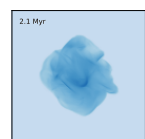


Figure 1.5: Part of the map of the Vela nebula from Netterfield et al. (2009). Imaged in the sub-mm the significantly filamentary structure of the cool dust is clearly seen, tracing the structure of the cloud. Colours are: 250, 350, and 500 μm



surroundings they are exploding into (e.g. Governato et al. (2007)). Preventing cooling allows the supernovae bubble to expand and affect its surroundings. The need to suppress cooling itself proves supernovae alone are likely to be inadequate. Bournaud et al. (2011) ran one simulation with 500% efficiency of supernovae to account for the other feedbacks and found little difference in galactic star formation rates. However, they added this feedback as supernovae rather than forming a bubble during the stars' lives then setting off supernovae. Ceverino et al. (2010) have taken a step in the correct direction using a constant combined wind modelling stellar winds and supernovae.

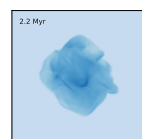
SPH simulations have used a blast wave model for supernovae feedback from Stinson et al. (2006) as the only feedback from stars (e.g. Stinson et al. (2010)). To account for earlier feedbacks from stars Stinson et al. (2010) release the accumulated energy from all feedbacks at a random time rather than as individual supernovae. The release of more energy at once creates a larger blast wave and circumvents the rapid cooling problem of supernovae exploding in a dense region rather than the low density bubble they actually explode in. Using the same techniques, simulations of satellites around Milky Way sized galaxies (Nickerson et al., 2011) find that stellar feedback is significant in mass stripping medium sized satellites where stars form.

On galactic scales Hopkins et al. (2011) found that, for physically reasonable feedback efficiencies, a steady state of star formation rate and GMC creation and disruption emerges. These forms of feedback work for a wide range of galaxy sizes and are nearly independent of the numerical conditions for star formation.

Ostriker & Shetty (2011) ran simulations showing that momentum feedback from stars can drive turbulence within galaxies. Their models assume momentum is input from supernovae, but not exclusively so, and argue that for high density regions in starburst galaxies it is the radiation pressure from the stars which will dominate the momentum feedbacks.

Work on the GMC size scale is limited but currently being explored with a variety of techniques. Matzner (2002) found that feedback from a moderate star formation rate was enough to balance the decay of turbulence for several crossing times. In addition, Goldbaum et al. (2011) performed 1D virial models including accretion onto GMCs. They showed accretion can contribute to driving turbulence within a GMC along with stellar feedback. Krumholz et al. (2006) conducted semi analytic models and saw cloud disruption within 20-30 Myrs purely with ionization from 5-10% cloud mass in stars. In these simulations they saw oscillations in the cloud shell as the 1D models cannot fully describe the expansion through a turbulent medium.

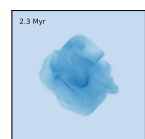
There have been many simulations of stellar feedback on sub-GMC scales. Simulations of Ultra Compact HII Regions (UCHRs) by Mac Low et al. (2007) showed that turbulence in the



surrounding material is needed to understand the lifetimes and frequency of observed UCHRs. Mellema et al. (2006) ran 4 pc sized simulations of HII regions expanding in a turbulent medium. They found that globules of neutral gas are able to survive while the HII region expands through the lower density material. Further work by this group showed that the magnetic field would get swept up the the neutral shell into parallel lines with the interior material having field lines perpendicular to the shell (Arthur et al., 2011).

Simulations have shown that protostellar jets break up their host filaments, slow accretion onto individual stars, and reduce the star formation rate compared to simulations with no feedbacks (Wang et al., 2010).

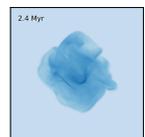
Simulations of individual stars show the importance of protostellar feedback on massive star formation (e.g. Cunningham et al. (2011)). MHD simulations of single core collapse show that magnetic fields and radiative feedback can significantly affect the efficiency of star formation in each core (Hennebelle et al., 2011).



1.4 Key Results in This Thesis

The main results from the simulations in this thesis are:

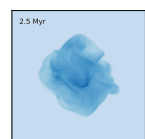
1. With no outputs these simulations form stars at a rate: $\dot{M}_\star = 0.3M_{GMC}/\tau_{dyn}$, where M_{GMC} is the original gas mass in the GMC and τ_{dyn} is the original dynamical time for the GMC (~ 6 Myrs).
 - (a) Decaying turbulence does not limit star formation rate.
2. Supernovae alone give the same result; thus supernovae are an output from the stars but not a significant feedback into the local ISM.
 - (a) Cooling makes the supernovae ineffective unless they are exploding within an already formed bubble.
3. Ionization gas pressure and radiation pressure individually disrupt the GMC and quench star formation at around $M_\star = 0.1M_{GMC}$ in approximately a dynamical time. The star formation thus occurs in a burst with the majority of stars forming within a couple of million years of each other.
 - (a) With radiative outputs supernovae again do not have any significant effects as the GMC is already significantly disrupted by the time they explode. Thus the hot gas leaks out of the bubble and away from the GMC.
4. With a few μG magnetic field the rate of star formation was lowered slightly but the rate of disruption was increased as the magnetic field held the bubble shell together reducing leaking and increasing absorption of radiation pressure in the shell.
5. Simulations of a more massive cloud ($0.8 \times 10^6 M_\odot$) agreed with the above results.
6. Numerical studies in star cluster formation parameters, resolution, turbulent seeds, and hydrodynamic solver showed the above results to be robust.



1.5 Thesis Outline

This thesis is organized as follows:

- §2: 1D models: Harper-Clark and Murray 2009** - A paper detailing the initial work for this thesis, the theory and the 1D models run. We find that to fit observed bubbles in the Milky Way they must be significantly leaky - subsequently supported by observations (Lopez et al., 2011). The hot gas from the stellar winds escape and only the ionization gas pressure and radiation pressure are significant in disrupting the cloud.
- §3: Coding** - A chapter describing the code used for the 3D simulations. I use the 3D radiative-magneto-hydro code Enzo which includes many algorithms for relevant physics.
- §4: Three Dimensional Simulations** - A description, discussion and results from the physical investigation in my 3D simulations, as described in key results, §1.4.
- §5: Testing Numerical Algorithms** - A description, discussion and results from the numerical tests in my 3D simulations.
- §6: Interesting Asides** - Interesting results that are not central to the argument of this thesis. We find that individual star formation often occurs where multiple filaments come together. We also note that the original density structure of the cloud affects the position of clusters within the cloud despite turbulence.
- §7: Conclusions** - A summary of the thesis and the main results.



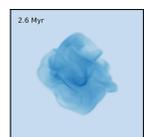
Chapter 2

1D models: Harper-Clark and Murray 2009

A version of this chapter has been published in the Astrophysical Journal, 2009, vol. 693 pp. 1696. Reproduced by permission of the AAS.

2.1 Abstract

We have tested the two main theoretical models of bubbles around massive star clusters, Castor et al. and Chevalier & Clegg, against observations of the well-studied Carina Nebula. The Castor et al. theory overpredicts the X-ray luminosity in the Carina bubble by a factor of 60 and expands too rapidly, by a factor of 4; if the correct radius and age are used, the predicted X-ray luminosity is even larger. In contrast, the Chevalier & Clegg model underpredicts the X-ray luminosity by a factor of 10. We modify the Castor et al. theory to take into account lower stellar wind mass-loss rates, radiation pressure, gravity, and escape of or energy loss from the hot shocked gas. We argue that energy is advected rather than radiated from the bubble. We undertake a parameter study for reduced stellar mass-loss rates and for various leakage rates and are able to find viable models. The X-ray surface brightness in Carina is highest close to the bubble wall, which is consistent with conductive evaporation from cold clouds. The picture that emerges is one in which the hot gas pressure is far below that found by dividing the time-integrated wind luminosity by the bubble volume; rather, the pressure in the hot gas is set by pressure equilibrium with the photoionized gas at $T = 10^4$ K. It follows that the shocked stellar winds are not dynamically important in forming the bubbles.



2.2 INTRODUCTION

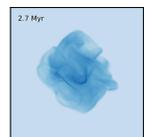
Over a dynamical time only 2% of the gas in a typical disk galaxy is turned into stars (Kennicutt, 1998), in spite of the fact that the disks are marginally gravitationally stable (Kennicutt, 1989). This puzzling result suggests that something other than gravity plays a (negative) role in star formation. Passive support against collapse and subsequent star formation can come from magnetic fields or turbulence. Examination of star forming galaxies and individual star forming regions commonly shows evidence for more active support against gravity, for example, expanding bubbles. Active mechanisms, which come under the rubric of ‘feedback’, include energy or momentum input by active galactic nuclei, or from stars. Since most disk galaxies, including our own Milky Way, show little or no nuclear activity, and since bubbles in individual star forming regions are clearly not due to active galactic nuclei, in this paper we focus on feedback from stars.

Stars of type B2 and earlier supply several types of feedback, including protostellar jets, main-sequence stellar winds, radiation pressure, gas pressure associated with ionizing radiation, and supernovae (SNe). The mechanical energy imparted via an SN is comparable to that injected by the star’s stellar wind over its lifetime (Castor et al., 1975). However, it is clear that many observed bubbles have formed before any of the stars in the central cluster have exploded in an SN. Since we are interested in bubble formation, we will ignore SNe, leaving open the question of whether SNe provide the feedback necessary to limit the rate of star formation.

There are two competing theoretical models of stellar wind bubbles in the literature: that of Castor et al. (i.e. Castor et al. (1975) and Weaver et al. (1977)) and that of Chevalier & Clegg (1985), as implemented in, e.g., Stevens & Hartwell (2003). In the theory explored by Castor, the stellar wind shocked gas is confined by a cool shell of swept-up interstellar medium (ISM). In contrast, the Chevalier & Clegg theory ignores any surrounding material and simply has a steady-state wind. The temperatures, pressures, and the predicted sizes of the X-ray emitting regions in the two theories are significantly different.

However, these differences can be masked if the stellar content of the bubble is not well constrained. Recent work by Smith (2006a) provides a detailed accounting of the number of early type stars in the well studied Carina nebula. Combined with the wealth of multiwavelength observations available for Carina, this allows for a stringent test of the models.

Observations of star forming regions in the Milky Way show that the gas density is highly variable. In particular, the projected surface density is consistent with a log-normal distribution, e.g., Goodman et al. (2009) and Wong et al. (2008). These observations are consistent with



both analytic and numerical studies of supersonic turbulent flows, which predict log-normal density and column density distributions (Passot & Vázquez-Semadeni, 1998; Ostriker et al., 2001). These results call into question one of the fundamental assumptions of the Castor et al. model - that the gas surrounding the central star or star cluster has a rather uniform density distribution. If the mass distribution is nonuniform, the shell swept-up by the shocked stellar wind is likely to have holes. If so, this will lead to incomplete confinement of the hot gas and a consequent reduction in the pressure and associated X-ray emission of the hot gas. Such a situation would be intermediate between the Castor et al. model of a completely confined wind and the Chevalier & Clegg picture of a free-flowing wind. We explore such intermediate models below.

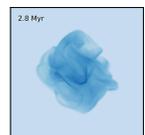
This paper is organized as follows. In the next section we summarize some relevant observations of Carina, as well as some order of magnitude estimates of the pressures and forces acting on the surrounding cold, dense gas. In §2.4 (and the appendices: §2.9 & §2.10), we describe the Chevalier & Clegg model, the Castor et al. model, and our modifications to the Castor et al. models. We also describe our numerical methods. In §2.5 we present the results of our modeling, including a parameter study of the (modified) Castor et al. bubbles. In §2.6 we discuss the X-ray emission. In §2.7 we discuss the results and compare to previous work. We give our conclusions in §2.8.

2.3 OBSERVATIONS OF CARINA

The distance to Carina is 2.3 kpc (Allen & Hillier, 1993; Smith, 2006b). The complex contains about 70 O stars (Smith, 2006a), of which 47 (including evolved massive stars) reside in Trumpler 16 (Tr 16), a star cluster with a radius $r \sim 3$ pc. This makes Carina one of the most massive (and best studied) star formation regions in the Milky Way. The bolometric luminosity emerging from the stars is 9.6×10^{40} erg s⁻¹. This is about twice the far-infrared luminosity of the complex (Smith & Brooks, 2007), indicating that half the stellar flux is intercepted by dust grains within $\sim 10 - 20$ pc of the stars.

We note that this rather low ratio of infrared to bolometric luminosity is consistent with the fact that we can see Tr 16 in the optical, and with turbulent models of the ISM, but it is inconsistent with the assumption of the Castor et al. model that the ISM and swept-up bubble shell surrounding the cluster is homogeneous. It suggests that hot gas can escape the bubble, a point we return to later.

The number of ionizing photons emitted per second is $Q = 9 \times 10^{50}$ s⁻¹. The kinetic energy of the stellar winds is $L_w \sim 3.5 \times 10^{38}$ erg s⁻¹, assuming standard estimates of the mass-loss



Number of stars \geq B2	72
Total bolometric luminosity	$1.7 \times 10^7 L_{\odot}$
Total ionizing flux (Q)	$5.9 \times 10^{50} \text{ s}^{-1}$
Total mass-loss rate \dot{M}_w	$1.1 \times 10^{-3} M_{\odot} / \text{year}$
Total stellar wind luminosity	$6.7 \times 10^4 L_{\odot}$

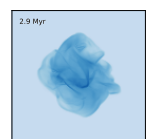
Table 2.1: Properties of Tr 16 in the Carina Nebula using all stars of spectral type B2 or earlier assuming standard mass-loss rates (Repolust et al., 2004). From Smith (2006a).

rates; we argue below that this is likely to be an overestimate by a factor of 3–10. The massive stars of Tr 16 are responsible for about 70% of the bolometric and stellar wind luminosity and of the ionizing flux of the entire nebula; see Table 2.1.

A reasonably reliable estimate for the age of Tr 16 is given by the age of η Carina, currently the most massive star in the region. η Carina is ~ 3.6 million years old, since it has clearly evolved off the main-sequence, while estimates of its initial mass based on its current luminosity and stellar models (Bressan et al., 1993) are in the range of $120M_{\odot}$. We thus assume that the cluster is approximately 3.6 million years old. It is believed that no SNe have occurred in Tr 16 (Retallack, 1983; Lopez & Meaburn, 1984; Whiteoak, 1994), but in any case the integrated energy deposited by the winds, 4×10^{52} erg, substantially exceeds the energy input of an SN, of order 10^{51} erg.

For the 17th anniversary of the Hubble Space Telescope, Smith & Brooks (2008) took a 50 light-year-wide mosaic of the centre of the Carina nebula. This image has unprecedented detail of globules within the bubble and star birth at the edge of the bubble. Triggered star formation around the edge of the bubble in Carina is also observed in X-ray and near-IR studies of Carina (Sanchawala et al., 2007). There are many directional markers, such as pillars, showing that the bubble edge is dominated by the effects of Tr 16. The images show that the main bubble shell is markedly non-spherical. Smaller bubble structures within the main bubble can be seen. Smith & Brooks (2007) compiled a multiwavelength analysis of the Carina nebula enabling approximate edges of the bubble to be located. We estimate radii in the range 10 – 20 pc.

There have been many observations of Carina in X-rays, which establish the existence of diffuse emission from the nebula itself (Seward et al., 1979; Flaccomio, 2005; Hamaguchi et al., 2007a,b). The largest area coverage of the Carina region is provided by Seward et al. (1979), who used the Einstein Observatory to find a diffuse X-ray emission of $4.8 \times 10^{34} \text{ erg s}^{-1}$ for the 0.5 – 3.0 keV band (scaled from their distance estimate of 2.6 to 2.3 kpc).



The pressure inside the bubble surrounding Tr 16 contributes directly to the outward force on the surrounding material. We estimate the pressure in several ways.

First, the pressure can be calculated from the free-free radio emission, e.g., as reported in Huchtmeier & Day (1975), who measured a flux of $S_\nu = 1.43 \times 10^3$ Jy. From calculations of the expected bremsstrahlung radio flux at the observer

$$n_{HII} = 3.6 \left(\frac{R}{pc} \right)^{-3/2} \left(\frac{D}{kpc} \right) \left(\frac{T}{K} \right)^{1/4} \left(\frac{S_\nu}{Jy} \right)^{1/2} \epsilon_{HII}^{-1/2} \text{ cm}^{-3}, \quad (2.1)$$

where ϵ_{HII} is the volume filling factor of the H II gas inside the bubble. For the radius of the bubble, $R = 10$ pc and distance, $D = 2.3$ kpc, we find $n_{HII} = 100 \text{ cm}^{-3}$ for $T_{HII} = 10^4$ K. Thus, $P = 1.4 \times 10^{-10} \epsilon_{HII}^{-1/2} \text{ dynes cm}^{-2}$.

As a consistency check, we note that the pressure of an H II region powered by a cluster emitting Q ionizing photons per second is given by

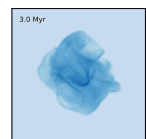
$$P_{HII} = \sqrt{\frac{3Q}{4\pi r^3 \alpha_r \epsilon_{HII}}} k_b T_{HII} \quad (2.2)$$

where $\alpha_r \approx 4 \times 10^{-13} \text{ cm}^3 \text{ s}^{-1}$ is the recombination coefficient, and $T_{HII} \approx 10^4$ K. Using $Q = 9 \times 10^{50} \text{ s}^{-1}$ and $r \approx 10$ pc, we find $P_{HII} \approx 2 \times 10^{-10} \epsilon_{HII}^{-1/2} \text{ dynes cm}^{-2}$.

Second, we can use the observed X-ray flux to estimate the pressure in the hot ($T_x \sim 10^7$ K) gas. From Figure 1 in Seward et al. (1979), we estimate the radius of the diffuse X-ray emission region to be ~ 12 pc, similar to the size of the free-free emission region. Combined with the diffuse X-ray luminosity and $T_x = 6 \times 10^6$ K, this yields $n_x \approx 9 \times 10^{-2}$ and $P_x \approx 7 \times 10^{-11} \text{ dynes cm}^{-2}$, which we take to be equal to the pressure of the radio emitting gas.

The surface brightness of both the radio and X-ray emission is not uniform, indicating that the pressure is not constant inside the bubble. For example, for the two classical and smaller-scale embedded H II regions Carina I and Carina II, using the fluxes and sizes from Huchtmeier & Day (1975), we find a pressure of $9 \times 10^{-10} \text{ dynes cm}^{-2}$. Similarly, Seward et al. (1979) estimate the density of the hot X-ray emitting gas in the prominent $r \sim 1.25$ pc diffuse patches to be $n \sim 0.4$, giving $P \approx 3 \times 10^{-10} \text{ dynes cm}^{-2}$.

Finally, we can estimate the pressure from the outflow seen to be emerging from the globule known as ‘the finger’, which has a dense ionization front and photoevaporative flow, with a terminal shock resolved close to the edge. Estimates of the ionization front density can be obtained from the S II emission line and from the H α emission measure. These give electron densities of 2000-6000 cm^{-3} at various positions. The dense ionization front drives a photoevaporative flow out into the H II region until it reaches a terminal shock where the pressure is balanced with the ambient medium. To calculate P_{IF} assume that the temperature is 10^4 K



due to hydrogen ionization and the flow is spherical. N. Smith (private communication, 2008) made two estimates, one using the tip of the finger with a very small ionization front radius but a relatively high number density of 6000 cm^{-3} and a second using the main part of the fist with a larger ionization front radius and a lower density of 3300 cm^{-3} . These yield $5.4 \times 10^{-10} \text{ dynes cm}^{-2}$ and $7.3 \times 10^{-10} \text{ dynes cm}^{-2}$, respectively.

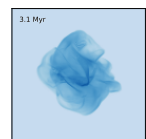
These rather direct measurements of the pressure in several gas phases can be compared to two other pressures, the pressure exerted by the self-gravity of the surrounding molecular gas (as estimated from CO measurements) and the pressure of radiation from the stars in Tr 16 on dust grains in the ISM. Yonekura et al. (2005) find a mass of molecular gas $M_g \approx 3.5 \times 10^5 M_\odot$ in a region of radius $r \approx 20 \text{ pc}$, yielding a surface density $\Sigma \approx 6 \times 10^{-2} \text{ g cm}^{-2}$. Assuming that this gas is in hydrostatic equilibrium (there is evidence that it is expanding outward, but we ignore this for the moment), the dynamical pressure is $P \approx \pi G \Sigma^2 \approx 8 \times 10^{-10} \text{ dynes cm}^{-2}$.

The near equality between the pressure in the X-ray gas and that of the H II gas likely reflects the fact that the sound crossing time (of the cooler gas) is similar to the dynamical time or the age of the system. Like the hot gas, the H II gas will ‘head for the exits’; pressure gradients will drive the warm gas toward any holes in the bubble shell, reducing the pressure on a (H II gas) sound crossing time.

Unlike the hot gas, the velocity of the warm gas is comparable to the velocity of the bubble wall, so a pressure-driven flow will not reduce the H II pressure in the bubble by a large (factor of 10 or more) amount. Thus it appears natural that the H II gas will have a pressure similar to that estimated from the ionizing photon luminosity. Conversely, the hot gas pressure will, if it ever reaches values similar to $L_w \tau / V$, drive outflows through holes in the bubble that have velocities of the order of the sound speed of the hot gas, which is two orders of magnitude larger than the velocity of the bubble wall. This will lower the pressure of the hot gas until it approaches that of the H II gas, at which point the pressure gradients in the two components are similar.

Using the dynamical argument that the H II pressure and the X-ray gas pressure should be roughly equal, we can draw one more conclusion: that ϵ_{HII} is of order unity. To do so, set the right hand side of eqn. 2.2 equal to the (observed) pressure of the X-ray gas and solve for ϵ_{HII} , then use the known values of Q , r , and T_{HII} .

The pressure exerted by radiation is $P_{rad} = L_{bol} / (4\pi r^2 c) \approx 4 \times 10^{-10} (10 \text{ pc} / r)^2 \text{ dynes cm}^{-2}$. This near equality, unlike that between the H II and X-ray gas pressure, is a bit of a coincidence. The radiation pressure scales as R^{-2} while the H II gas pressure scales as $R^{-3/2}$; the radiation pressure was more important in the past, while the gas pressure will become more important as the bubble expands in the future.



All of these observationally driven estimates are well below the pressure estimated by dividing the total stellar wind kinetic energy by the volume of the bubble; the latter is $P_{wind} = 3.6 \times 10^{-7} (10 \text{ pc}/r)^3 (L_w/4 \times 10^{38} \text{ erg s}^{-1}) \text{ dynes cm}^{-2}$. Either the wind has expanded over a volume larger by a factor of ~ 1000 , the wind luminosity is overestimated by a similar factor, the shocked gas loses most of its internal energy (but not by radiation in the X-ray band), or some combination of all three. We note that if the hot gas expanded at its sound speed, it would reach radii of 1 kpc, so the notion that the hot gas has expanded through holes in the ISM to occupy region with a typical size of 100 pc is not implausible.

Assuming an age of 3.6 Myr, we find an average expansion velocity for the bubble wall of $\sim \pm 3 (R/10 \text{ pc}) \text{ km s}^{-1}$, similar to the 5 km s^{-1} splitting seen in CO (Grabelsky et al., 1988). Observations of ionized gas typically find larger velocity splittings, of order $\pm 20 \text{ km s}^{-1}$, ranging up to several hundred kilometres per second, e.g., Walborn & Hesser (1975); Walborn & Hesser (1982), but we regard this as a measure of the velocity of gas in the interior of the bubble, not a measurement of the velocity of the bubble wall.

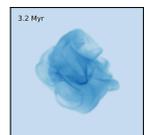
To sum up, the warm and hot gas appear to be in pressure equilibrium, with a pressure of $P_g \approx 2 \times 10^{-10} \text{ dynes cm}^{-2}$. This is similar to the radiation pressure, and to the pressure exerted by the surrounding, self-gravitating molecular cloud. The kinetic energy input from stellar winds greatly exceeds the integral of this pressure over the apparent size of the H II region, $R \approx 10 \text{ pc}$, suggesting that the winds have escaped to occupy a much larger volume, or have been otherwise dissipated.

2.4 METHODS

2.4.1 Chevalier and Clegg bubble

Stevens & Hartwell (2003) applied the Chevalier & Clegg (1985) steady-state wind to super star clusters. The flow is assumed to pass through the sonic point at the cluster edge where the source terms become zero. The equations describing the flow are given in Appendix I, §2.9.

Numerical integration of the flow (equations (2.22) to (2.24)) using iterative calculations of the mach number (equation (2.27) or (2.28)) at every step enables the flow to be accurately calculated. The X-ray luminosity from bremsstrahlung is numerically integrated from the resulting temperature and density profiles. The actual X-ray luminosity will be somewhat larger than this estimate by about a factor of 3 at $T_x = 10^7 \text{ K}$, see, e.g., Sutherland & Dopita (1993).



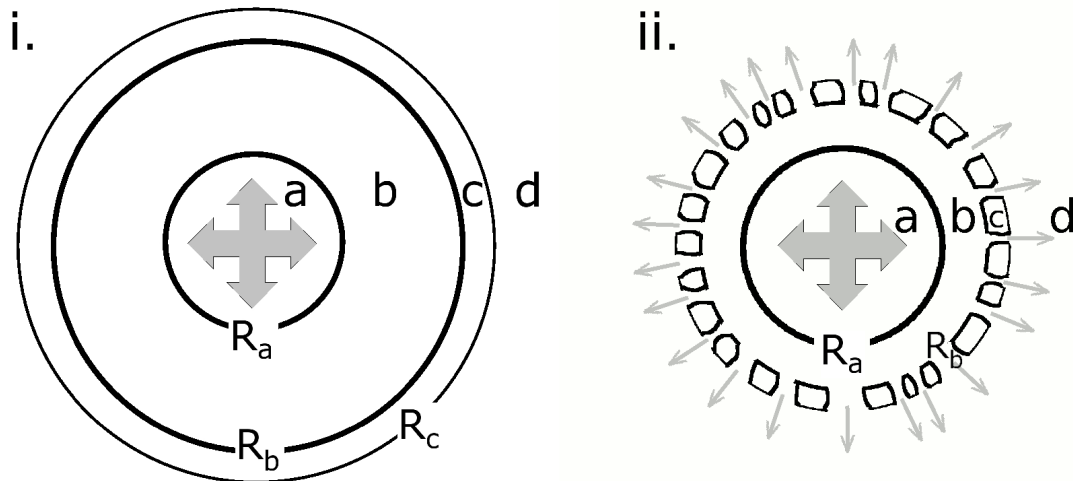
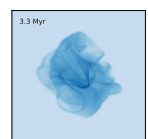


Figure 2.1: Cartoons of the Castor et al. bubble (i.) and the modified Castor et al. bubble (ii.). The Castor et al. bubbles have a four zone structure. Zone a is hypersonic stellar wind; zone b is shocked stellar wind and evaporated material from the shell; zone c is the bubble shell; and zone d is the ambient ISM. ii. - The structure of the modified Castor et al. bubble, showing leaking from the shell. Note the larger size of region a, smaller size of region b and material escaping into region d.

2.4.2 Castor bubble

In the Castor et al. theory the stars are assumed to blow a constant, spherically symmetric stellar wind that interacts with the ambient ISM and produces a bubble. For the first few hundred years the stellar wind freely expands at the wind velocity. Once the wind shocks, there is a period of adiabatic expansion for a few thousand years. The bubble then enters the “snow plough” stage when swept-up mass densities reach the critical point for radiative cooling and a thin shell forms. In the Castor scenario, the snow plough stage is the most readily observed phase as it is by far the longest lived. During this time the bubble has a four-zone structure, (Fig. 2.1(i)): **a**) A hypersonic stellar wind. **b**) A hot ($T \sim 10^6$ K), almost isobaric region consisting of shocked stellar wind mixed with a small fraction of the swept-up interstellar gas. **c**) A thin, dense, cold ($T \ll 10^6$ K) shell containing most of the swept-up material at R_b . **d**) Ambient interstellar gas.

One of the most important features of the snow plough structure is the cooling between zones b and c. The shell, c, is dense and cold due to efficient radiative cooling. However, zone b is hot as its density is too low to radiatively cool. Thermal conduction between b and c causes gas from the inner edge of c to evaporate into b. Although the mass-loss from c is negligible



compared to the accretion of mass from swept-up ISM, it dominates over stellar wind as a source of matter in b. The bubble shell is pushed outward by the pressure from the confined hot gas. The equations describing the evolution are given in Appendix II, §2.10.

Unlike the Chevalier & Clegg theory, the Castor theory takes into consideration the mass swept-up from the surrounding nebula, requiring an ISM or GMC model. The original papers (Castor et al., 1975; Weaver et al., 1977; Chevalier & Clegg, 1985) assumed a homogeneous ISM. However, in our models for Carina we sometimes employ an isothermal sphere as an approximation for the GMC surrounding the cluster. The values for the cluster gas mass and radius, and the surrounding GMC mass and radius were taken from Murray et al. (2010c) assuming a density profile in the cluster of r^{-1} and in the GMC of r^{-2} . The ‘standard’ ISM model used for our bubble models was $R_{cl} = 1 \text{ pc}$, $M_{cl} = 2.6 \times 10^4 M_{\odot}$, $R_G = 24.62 \text{ pc}$, and $M_G = 3.2 \times 10^5 M_{\odot}$, where M_{cl} is the mass in gas and dust remaining in the cluster after star formation assuming a star formation efficiency of $\sim 35\%$. The R_G was chosen so that the density at the boundary between the cluster and GMC was continuous.

In other cases we assumed that the density fell off as $\rho(r) \sim 1/r$, or even that the density was (on average) uniform.

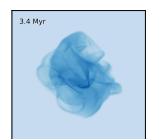
In the Castor models, we assume that the cluster produces a point source wind from the centre of the cluster. Although this does not accurately represent the stellar wind within the cluster radius, simulations by Cantó et al. (2000) show that the approximation is valid once outside the cluster radius.

To model the Castor bubble, we used the `integrate_ode` program from Numerical Recipes (Press et al., 1996) to simultaneously integrate the momentum, radius, mass and energy evolution equations (equations (2.39) to (2.42)) from the initial conditions in Weaver et al. (1977) (equations (2.43) to (2.51)).

The X-ray luminosity was calculated taking into account the radial profile of density and temperature through the bubble (Weaver et al., 1977). When the X-ray luminosity is calculated the bubble is split into 5000 shells of equal width between R_a and R_b and the X-ray luminosity in the Einstein band from bremsstrahlung radiation is calculated for each shell. A resolution check was conducted at many different bubble radii to ensure accuracy.

Modifications to the Castor Bubble Model - Stellar Mass-Loss Rates

The generally accepted mass-loss rate of O stars assumes a smooth (not clumpy) outflow throughout the main-sequence lifetime. However, recent observations show that stellar winds are clumpy and hence the mass-loss rates are likely lower than previously accepted (Fullerton



et al., 2006; Bouret et al., 2005; Evans et al., 2004; Puls et al., 2006). These observations suggest that the mass-loss rate is at least three times and possibly more than 30 times lower than previously expected. We introduce α to parameterize the reduction in the the mass-loss rate: $\dot{M}_w = \alpha \dot{M}_{w,original}$ and $L_w = \alpha L_{w,original}$.

Radiation Pressure

The far-infrared luminosity in the direction of Carina is roughly half the total stellar luminosity. It follows that half or more of the momentum carried by light emitted by the stars is deposited into the gas near the stars. Thus, the radiation pressure contributes to the outward force on the bubble shell (where the UV optical depth is large),

$$F_{rad} = \eta \frac{L_{bol}}{c}, \quad (2.3)$$

where η is of order 1/2, c is the speed of light, and L_{bol} is the total bolometric luminosity from the cluster.

Using a multiwavelength analysis of the Carina nebula, Smith & Brooks (2007) estimate dust temperatures and calculate the total mass in dust. Smith & Brooks (2007) calculate the masses using the models of Gilman (1974). We employed more recent dust models (Laor & Draine, 1993); the mass in dust can be calculated using the mass per grain, $4\pi a^3 \rho / 3$ and luminosity per grain $= Q_e \sigma T_d^4 4\pi a^2$,

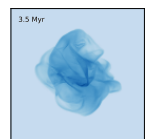
$$M_d = \frac{a\rho}{3\sigma Q_e T_d^4} L_d, \quad (2.4)$$

where a is the effective grain radius, σ is the Stefan-Boltzmann constant, Q_e is the mean thermal emissivity, T_d is the dust temperature, and L_d is the dust luminosity. No silicate features are seen so we can assume that the grains are carbon. We also assume that grains are small ($a < 0.2\mu\text{m}$). The Q_e values for each temperature can be read from the graph in Laor & Draine (1993). In particular, $Q_e \approx 3 \times 10^{-3}$ for $T_d = 35$ K. This is a factor of 9 larger than the value employed by Smith & Brooks (2007); consequently, we find a total dust mass $M_d \approx 1000(\rho/3 \text{ g cm}^{-3})M_\odot$, Table 2.2, a factor of 9 smaller than Smith & Brooks (2007).

Assuming a dust-to-gas ratio of 1:100, the total mass for the surrounding nebula is $\sim 10^5 M_\odot$, corresponding to an $A_V \approx 1$ ($20 \text{ pc}/R_b$)². In contrast, Smith & Brooks (2007) find $9.6 \times 10^5 M_\odot$, corresponding to an $A_V \approx 10$ ($20 \text{ pc}/R_b$)².

Smith & Brooks (2007) find $T_D \approx 35$ K, which we argue supports the lower-mass estimate, as follows. Using the expression for dust temperature

$$T_d = 49 f^{-1/(4+\beta)} \left(\frac{2 \times 10^{17} \text{ cm}}{r} \right)^{2/(4+\beta)} \left(\frac{L_{bol}}{10^5 L_\odot} \right)^{1/(4+\beta)} \quad (2.5)$$



T/K	$L_d / \text{erg s}^{-1}$	Q_e	M_d/M_\odot
35	2.93×10^{40}	8.72×10^{-5}	6 610
80	1.19×10^{40}	4.71×10^{-4}	18.2
35	4.24×10^{39}	3.72×10^{-3}	0.014

Table 2.2: Dust masses of the three components seen in Smith & Brooks (2007) with better dust modelling, compared to Smith & Brooks (2007) total dust mass of $9.6 \times 10^3 M_\odot$

from Scoville & Kwan (1976) with $f = Q_{abs}(\lambda = 50\mu) \approx 0.01$ we find that the typical distance between a dust grain and Tr 16 is $\sim 24 \text{ pc}$ (taking $\beta = 1$). We note that this is similar to the estimated bubble size. Since the bulk of the stellar radiation is initially emitted in the UV, it will be absorbed at $A_v \lesssim 1$, consistent with the lower-mass estimate given above.

Self-Gravity

As the shell sweeps up a substantial amount of mass, the self-gravity of the shell and gravity between the shell and the stars and interior gas should be considered in the momentum equation

$$F_{grav} = -\frac{GM_c^2}{2R_b^2} - \frac{GM_c(M_b + M_{stars})}{R_b^2}. \quad (2.6)$$

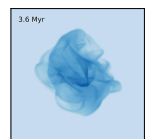
Leakage of Hot Gas

The Castor theory assumes expansion through an homogeneous ISM. However, as noted in the introduction, turbulence is expected to produce density fluctuations in the ISM, while observations show that the column density is log-normally distributed. Thus, sections of the bubble shell with low column will expand faster and high column sections will expand more slowly. This uneven expansion will result in gaps in the shell, allowing the hot gas to escape from the bubble.

We investigated the effects of holes in the expanding shell using a toy model. Our model consisted of a Castor-style bubble with a shell cover fraction C_f : when $C_f = 1$ the shell has no holes and when $C_f = 0$ the shell is covered with holes, i.e. no shell exists. These holes allow the interior gas to escape at the speed of sound, $c_s = (5k_bT/(3m_p))^{1/2}$, with a mass flux and energy flux given by

$$\dot{M}_b = -(1 - C_f)4\pi R_b^2 \rho_b c_s, \quad (2.7)$$

$$\dot{E}_b = -(1 - C_f)4\pi R_b^2 \frac{5}{2} \rho_b c_s^3, \quad (2.8)$$



where R_b is the radius of the bubble interior, ρ_b is the density inside the shell, which is assumed to be homogeneous and $\gamma = 5/3$ throughout this chapter.

We are not concerned with the bubble evolution within the cluster radius (of order 3 pc for Tr 16). Thus, we neglect gravity and radiation pressure for $r < R_{cl}$; once the bubble expands, under the influence of the other forces, beyond this radius, we smoothly turn on gravity and radiation pressure.

With hot gas from the interior able to leak away, it is important to consider the location of the stellar wind shock, R_a (see Fig. 2.1): if R_a approaches the shell radius at any time our model breaks down. We use the assumed ambient ISM density profile for the regions where the shell is still intact and negligible density where there are holes. Although this is not an accurate description of a clumpy ISM, it does allow the shell to leak while still gaining mass as it expands through a variable density ISM. The gas and radiation pressure only acts on the remaining shell (i.e. area = $C_f 4\pi R_b^2$).

Without leaking the radiative losses in region b were negligible. However, with leaking this may not always be the case. To ensure these losses are taken into account when significant we calculate the radiative luminosity of region b, L_b , and include it in the energy equation.

The sizes of the holes in the shell may vary as the bubble expands, so that $C_f = C_f(t)$ or $C_f(r)$. To investigate the effects of different hole expansion models, we conducted runs with many different power-law relationships with time (including $C_f(t) = \text{const.}$), which we discuss below.

Final bubble model

Considering radiation pressure, gas pressure, stellar winds, gravity, and leaking, the evolution equations for momentum, radius, mass, and energy become

$$\frac{d\mathcal{P}_c}{dt} = 4\pi R_b^2 P_b + \frac{L_{bol}}{c} - \frac{GM_c^2}{2R_b^2} - \frac{GM_c(M_b + M_*)}{R_b^2}, \quad (2.9)$$

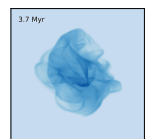
$$\frac{dR_b}{dt} = \frac{\mathcal{P}_c}{M_c}, \quad (2.10)$$

$$\frac{dM_b}{dt} = C_1 T_b^{5/2} R_b^2 (R_b - R_a)^{-1} - 10^{-5} \frac{\mu}{k_b} L_b - (1 - C_f) 4\pi R_b^2 \rho_b c_s, \quad (2.11)$$

$$\frac{dE_b}{dt} = L_w - 4\pi R_b^2 P_b \frac{dR_b}{dt} - L_b - \frac{5}{2} (1 - C_f) 4\pi R_b^2 \rho_b c_s^3. \quad (2.12)$$

respectively, see Fig. 2.1(ii).

\mathcal{P} is the momentum of the shell, t is time, R_b is the radius of the bubble, P_b is the gas pressure in the bubble interior, L_{bol} is the total bolometric luminosity of the stars, c is the



speed of light, G is the gravitational constant, M_c is the mass of gas in the bubble shell, M_b is the mass of gas in the bubble interior, $M_* = 10^4 M_{sun}$ is the mass of stars in the cluster, C_1 is a combination of constants associated with conduction, T_b is the temperature of the gas in the bubble interior, R_a is the radius of the stellar wind shock, k_b is the Boltzmann constant, L_b is the luminosity emitted from the bubble interior, C_f is the covering fraction of the shell, ρ_b is the mass density of the bubble interior, c_s is the speed of sound of the bubble interior, E_b is the energy in the gas in the bubble interior, and L_w is the stellar wind luminosity.

The terms on the right-hand side of the momentum equation (2.9), represent, in order, the outward force from the gas pressure, the outward force from radiation, the inward force from the self-gravity of the bubble shell, and the inward force from gravity between the star cluster (with a minor contribution from the gas in the bubble interior) and the bubble shell. The terms on the right-hand side of the mass equation, (2.11), are the mass input associated with conduction evaporating the bubble wall, a (downward) correction in the conductive mass-loss rate associated with radiative cooling, and mass-loss from hot gas escaping the bubble. The terms on the right-hand side of the energy equation (2.12) are stellar wind luminosity, adiabatic expansion, radiative cooling, and energy advection associated with the loss of hot gas through the bubble wall.

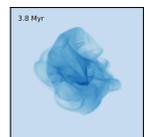
2.5 RESULTS

2.5.1 Original stellar wind models

The Chevalier & Clegg model predicts a free-free X-ray luminosity in the Einstein band (0.5 – 3 keV) of $L_x = 3.75 \times 10^{33} \text{ erg s}^{-1}$ for Carina. The Castor model predicts an X-ray luminosity of $L_x = 5.4 \times 10^{36} \text{ erg s}^{-1}$ for $R_b = 13 \text{ pc}$ and $L_x = 3.8 \times 10^{36} \text{ erg s}^{-1}$ for $R_b = 20 \text{ pc}$. Plots of the models can be seen in Fig. 2.2 and Fig. 2.3. Both of these models considered X-ray emission from $r > R_{cl}$ to match the observations, in which the cluster region is ignored due to contaminating stellar and wind-wind collisional X-ray emission.

In the Chevalier & Clegg model, the inner region of the wind dominates the X-ray luminosity, so a strong radial gradient in the X-ray surface brightness is predicted; beyond a few parsecs the X-ray luminosity is negligible. In contrast, in the Castor et al. model the density is almost homogeneous within the bubble, so very little radial surface brightness gradient is expected, aside from a sharp edge at R_b .

Observations of diffuse X-ray emission in Carina give $L_x = 6.1 \times 10^{34} \text{ erg s}^{-1}$ (Seward et al., 1979); these authors assumed the distance to the cluster was 2.6 kpc. If we assume that the



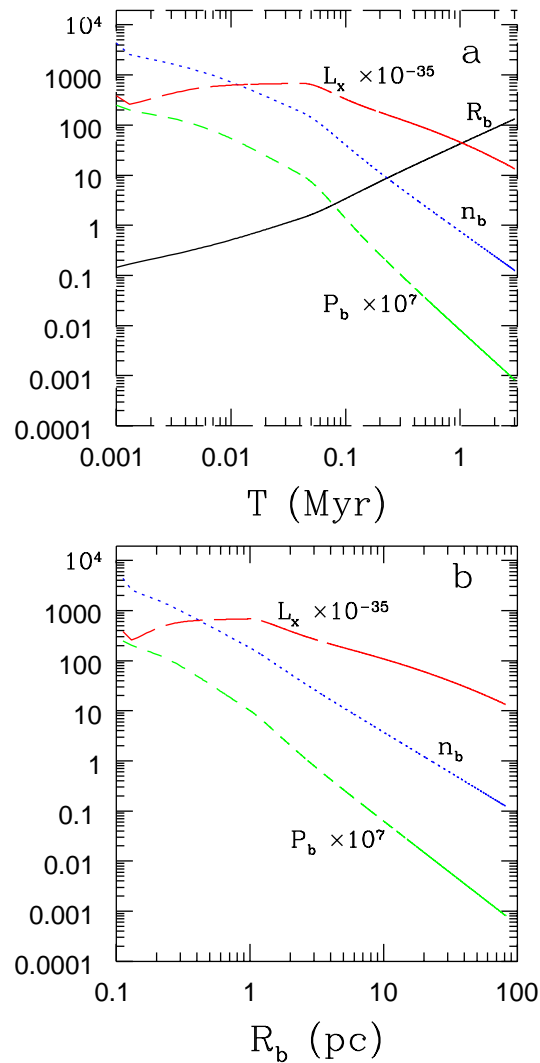
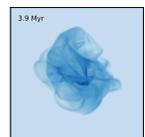


Figure 2.2: Plots of the basic Castor et al. (1975) model evolution against time (a) and R_b (b) for Tr 16. These plots show how pressure, number density and total X-ray luminosity change through the evolution of the bubble. Pressure and X-ray luminosity have been scaled to fit on the graphs.



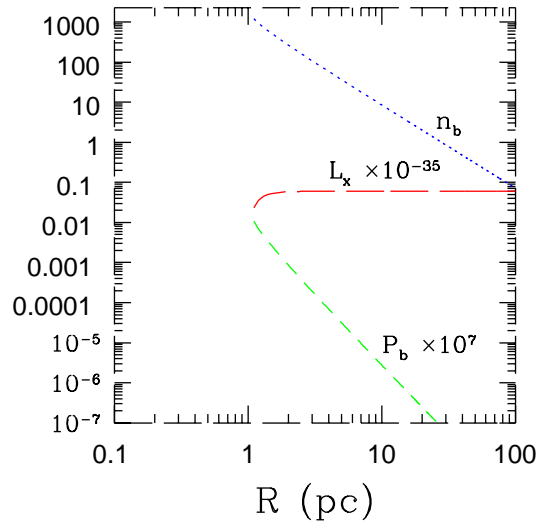


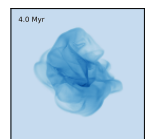
Figure 2.3: Plot of the steady state Chevalier & Clegg (1985) model for Tr 16. The number density, pressure and X-ray luminosity against radius are plotted. Pressure and X-ray luminosity have been scaled to fit on the graphs. Note that we plot the *cumulative* X-ray luminosity as a function of radius.

distance is 2.3 kpc, the luminosity becomes $4.8 \times 10^{34} \text{ erg s}^{-1}$. The observed X-ray emission is 10 times higher than predicted by Chevalier & Clegg model but 100 times lower than predicted by the Castor model, Fig. 2.4. The observed pressure, as estimated by ‘the finger’ and radio emission, is closer to the calculated Castor pressure when the bubble has the currently observed radius $R_b \approx 20 \text{ pc}$.

As noted elsewhere, the Chevalier & Clegg model predicts a pressure that has a strong radial gradient, so the pressure is dependent upon the location within the bubble rather than the bubble size. However, the Chevalier & Clegg pressure is far below the observed pressure at most points in the bubble.

It is unclear how long it takes the bubble to reach the cluster radius, as the expansion time will depend upon the rather complicated wind-wind interactions within the cluster. To properly understand the early evolution of bubbles, full hydrodynamical models are needed. However, for now we will assume it is much less than a million years, as material will be displaced during star formation due to pre-main-sequence jets and outflows. We assume that the majority of the time taken to expand to the observed size is accumulated when $R_{cl} < r < R_{obs}$. Using this assumption we found that to expand to 20 pc the Castor model took only 0.90 million years, far shorter than the estimated age of Carina (around 3.6 Myr).

It follows that the situation for the Castor et al. model is actually worse than the impression



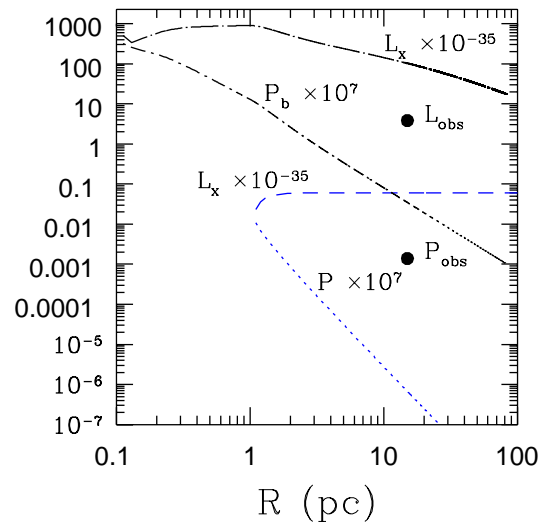
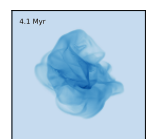


Figure 2.4: Plot of the scaled X-ray luminosity and pressure calculated as a function of radius for the two classes of (unmodified) models for Tr 16, as discussed in §2.5.1. The Castor model is plotted as a function of bubble size whereas the Chevalier model is plotted as a cumulative function of radius (due to its steady state nature). The upper L_x and P lines are for the Castor model and the lower lines for the Chevalier model. The two dots show the observed pressure (lower) and X-ray luminosity (upper). In the Castor et al. model the pressure is roughly constant for $r < R_b$, but this constant pressure is a function of the bubble radius, as shown. In the Chevalier & Clegg model there is no bubble, but pressure decreases with increasing radius.



conveyed by the figure, for the following reason. The actual age of the bubble is a factor of 4 higher than in the model, so the energy content of the bubble is underestimated in the model by the same factor, as is the pressure. Given the weak dependence of the temperature on time, the X-ray luminosity scales as the square of the pressure; if the radius, wind luminosity, and age of the bubble are set by observations, then the X-ray luminosity would be a factor of 16 larger than in the model.

2.5.2 Modified Castor et al. Model: Leakage

Taken together, the overestimate of the pressure and X-ray flux, and the underestimate of the bubble age (or overestimate of the bubble size at a fixed age) suggest that the outward force in the Castor et al. model is overestimated.

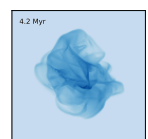
The inclusion of radiation pressure and gravity for the Tr 16 model makes only a small difference to the evolution of the bubble. For Tr 16 $|F_{HII}| \approx |F_{RP}| \approx |F_{grav}|$; in the model, unlike the case in Carina, all are much smaller than the gas-pressure force exerted by the shocked stellar wind, assuming no leakage and a standard O star mass-loss rate.

In an attempt to produce models in closer agreement with observations, it is clear that the internal pressure of the bubble must be reduced. One way to do this is to allow hot gas to leak out of the bubble ($C_f < 1$), or equivalently to allow energy to leak out of the hot gas, via radiation or conduction; another is to reduce the mass-loss rate and hence the kinetic luminosity of the stellar winds ($\alpha < 1$).

Observation of massive clusters support the possibility of leaking. Firstly, for Carina and many other clusters you can see the stars, showing that there must be a gap in the shell along our line of sight (Smith & Brooks, 2008). Secondly, recent observations of M17 and RCW49 by Povich et al. (2008) show stellar wind bow shocks around O stars at the edge and outside of the bubbles suggestive of large-scale gas outflow from the H II region (see their Figure 2, especially RCW49-S1).

Our initial simulations of a leaking bubble looked at three examples in detail: $C_f = 1.0$, $C_f = 0.65$, and $C_f = 0.3$. The results are given in Fig. 2.5. Not surprisingly, these simulations reveal that as C_f decreases, the shell expands more slowly, the bubble interior pressure is lower, as is the predicted X-ray luminosity.

The effects of varying C_f with time were then investigated. These simulations started with $C_f = 0.6$ at $t = 10^3$ yr and evolved $C_f(t)$ with different power laws until $t = 3\text{Myr}$, when $C_f = 0.2$. The simulations show that expansion rate, pressure, temperature, and density differ very little with different power-law exponents; however, the X-ray luminosity does depend on



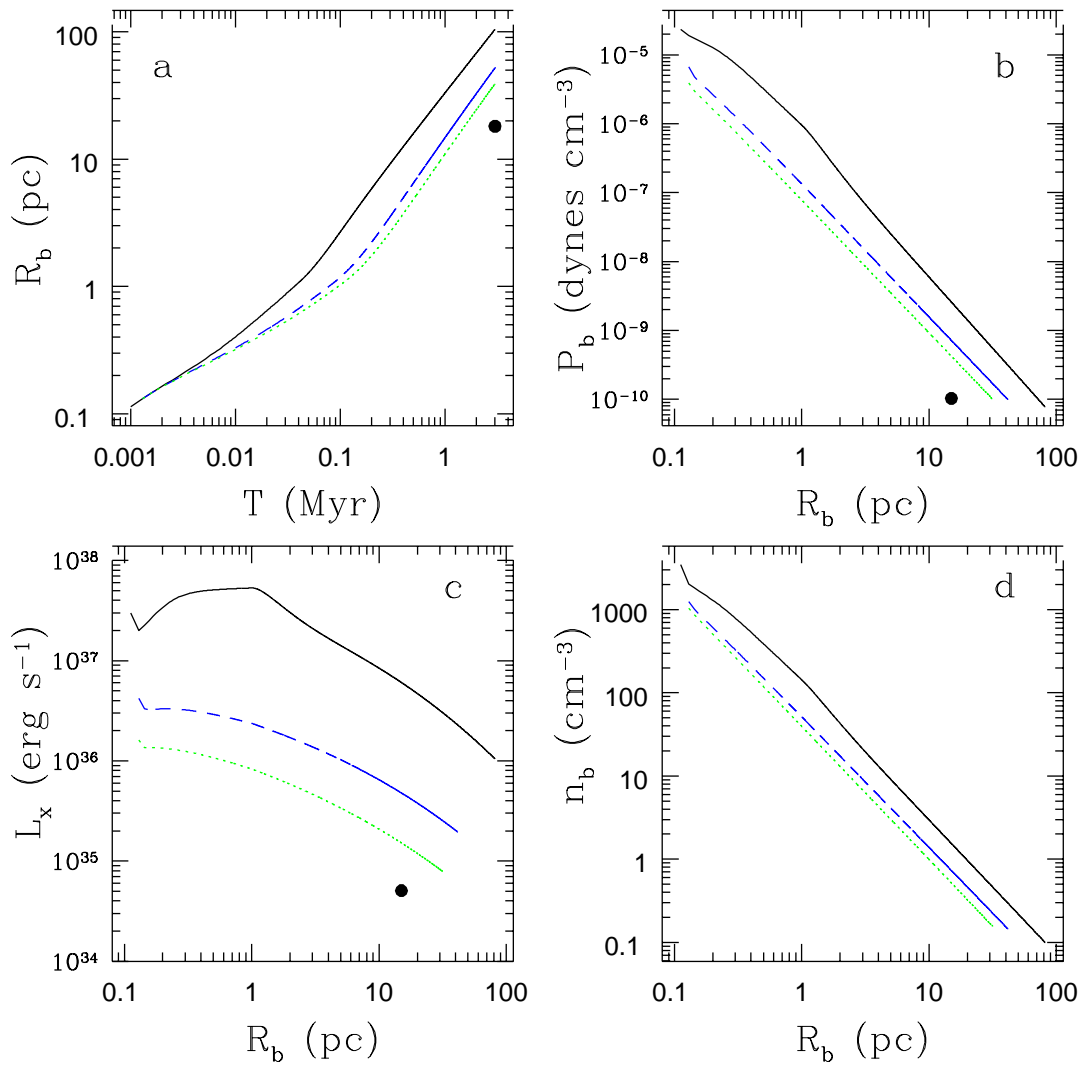


Figure 2.5: Graphs for three modified Castor simulations with $C_f = 1$ (solid), $C_f = 0.65$ (dashed), and $C_f = 0.3$ (dotted). (a) radius versus time, (b) pressure versus radius, (c) X-ray luminosity versus radius, and (d) number density inside the bubble versus radius. Observed results are shown as a black dot. See the discussion in §2.5.2.



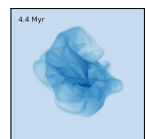
the exponent. The difference in X-ray luminosity is due to the combination of the small changes in the parameters giving larger X-ray luminosities for larger exponents; larger exponents imply C_f being large for longer times. Thus, less material escapes over the lifetime of the bubble: $\dot{M}_{escape} \propto (1 - C_f)$ and the X-ray luminosity is higher during the expansion when the power-law exponent is larger.

To see the way C_f and the run of density in the ISM affected the evolution of the bubble we ran four different models. We considered $C_f = 1.0$ or 0.5 and either isothermal or constant density models (with the same total mass), Fig. 2.6. From this study, we find that a homogeneous medium leads to a faster expansion; the mass swept-up in the bubble shell is less at a given radius in the constant density model. However, the isothermal sphere model does approach the homogeneous model near the end of the simulations when both reach R_G and hence the same shell mass. The models with $C_f = 0.5$ expanded more slowly and had significantly lower X-ray luminosities than models with $C_f = 1.0$, as expected.

We conducted a parameter study in α and C_f to see if any combination would result in acceptable fits to the observed bubble in Carina. Models were calculated for $0.15 \leq C_f \leq 0.99$ and $0.01 \leq \alpha \leq 1.00$, stepping both parameters at intervals of 0.01. The results are shown in Fig. 2.7; contours are only plotted for $R_b < 50$ pc at a bubble age of 3 Myr. This parameter space study was run for four different ISM models. Runs shown in part (a) of the figure are for an isothermal sphere model with $R_G = 24$ pc; run (b) shows an constant density model with $R_G = 24$ pc; run (c) is for an isothermal sphere model with $R_G = 60$ pc; and run (d) is for a constant density model with $R_G = 60$ pc.

The results show that isothermal sphere models gives smaller radii and slightly higher X-ray luminosity for any given (α, C_f) pair. The final radius at 3 million years increases with increasing α and with increasing C_f , as expected. For the isothermal ISM model the shell actually collapses inward for low values of α and low values of C_f , a result of the self-gravity of the shell exerting an inward force larger than the sum of the gas-pressure force and radiation pressure force on the shell.

The X-ray luminosity increases with increasing α and increasing C_f ; again, as expected. The region of parameter space that best fits the observations is for an isothermal sphere model with $R_G = 60$ pc. For this class of model there is a large parameter space with R_b between 10 and 20 pc and X-ray luminosities less than 4.8×10^{34} erg s⁻¹. For example, for $\alpha = 0.2$ and $C_f = 0.5$, $R_b = 16.5$ pc, $L_x = 1.2 \times 10^{34}$ erg s⁻¹, and $P_b = 1.1 \times 10^{-10}$ dynes cm⁻².



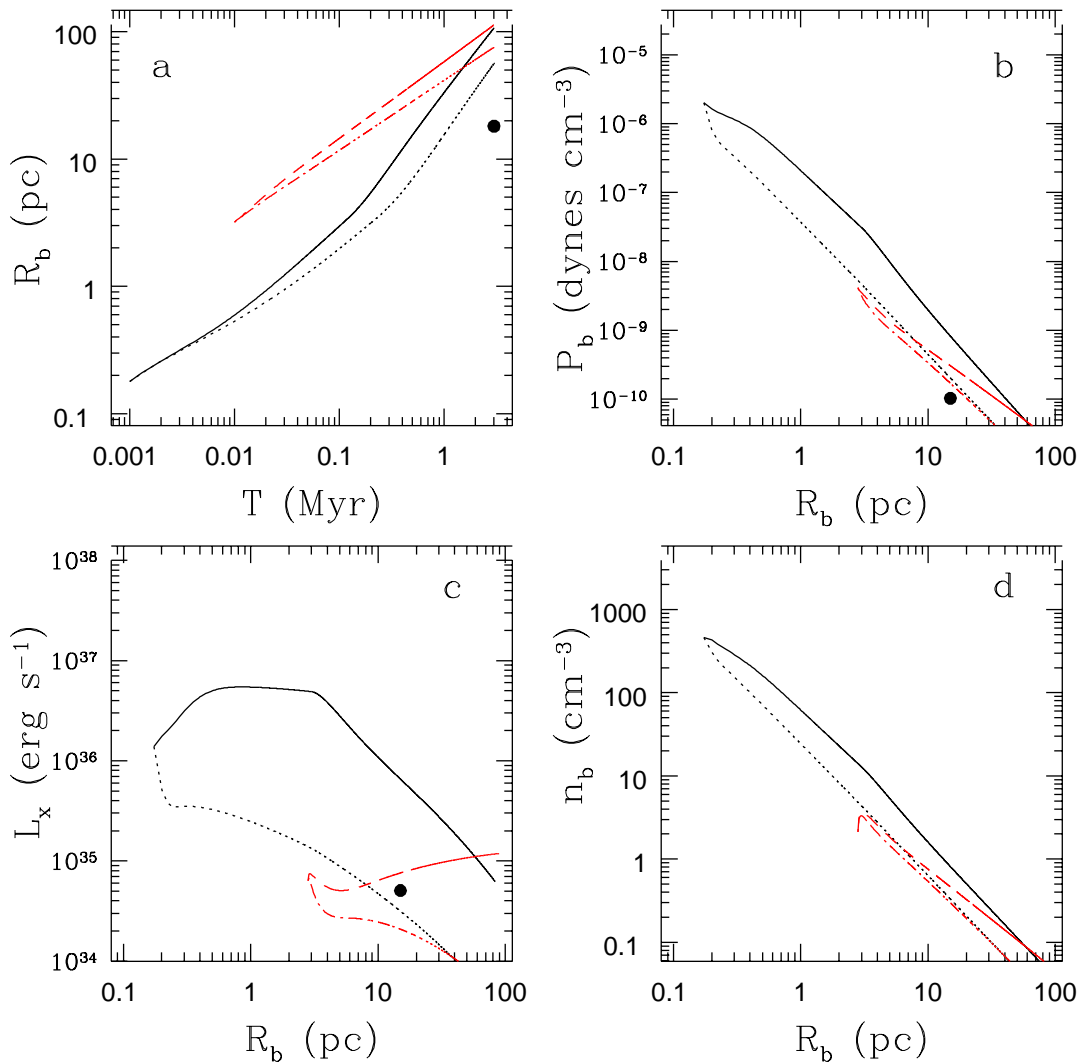
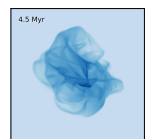


Figure 2.6: Graphs showing the details of modified Castor simulations with different ISM models and different shell cover factors C_f . All runs have $R_{cl} = 3$ pc, $R_G = 73.86$ pc and $\alpha = 1/3$. (a) is R_b versus time, (b) pressure versus R_b , (c) X-ray luminosity versus R_b , and (d) n_b versus R_b . The solid line is for an isothermal GMC, with $C_f = 1$, the dotted line is an isothermal GMC with $C_f = 0.5$, the dashed line has constant ISM density with $C_f = 1$, and the dash-dotted line has constant ISM density with $C_f = 0.5$. Note that (b) and (c) are plotted against radius so although some models do fit the observed quantities at that radius, they do so after too short a time.



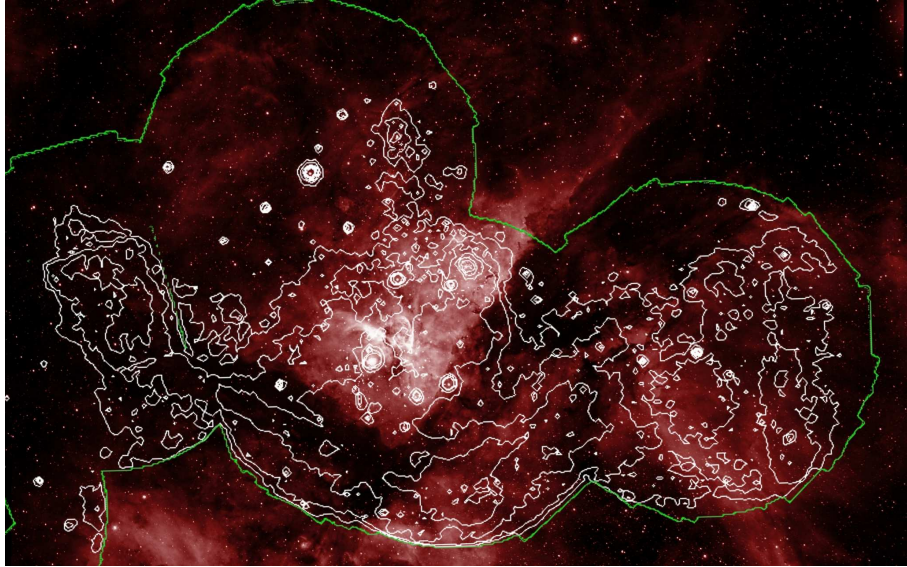
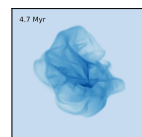


Figure 2.8: Image of the Carina nebula in visual (Smith & Brooks, 2007) and X-ray contours (Hamaguchi et al., 2007a). The visual image is a combination of H II, O IV and S II and the X-ray image is between 0.7 keV and 1.3 keV. The green outline shows the edge of the X-ray image. See the electronic edition of the Journal for a colour version of this Figure.

2.6 X-RAY SURFACE BRIGHTNESS PROFILES

The morphology of the X-ray emission provides a diagnostic to test our models. Matching up the X-ray emission (Hamaguchi et al., 2007a) and the visual images of the Carina nebula (Smith & Brooks, 2008), Fig. 2.8, it can be seen that the X-ray surface brightness increases near the edge of the bubble, the latter seen as a silhouette in the visible image. This strongly suggests that a significant fraction of the diffuse X-ray emission seen by Seward et al. (1979) was produced by gas evaporating from the bubble wall.

This surface brightness profile is not predicted by either the Chevalier & Clegg (1985) or the Castor et al. (1975) models; the former predicts that surface brightness falls monotonically with increasing r , while the latter predicts a nearly flat surface brightness profile out to $r = R_b$. For an example of the latter, consider one run with $\alpha = 1/3$, $C_f = 0.5$, an isothermal sphere ISM with $R_G = 60$ pc, and stellar wind, radiation pressure, and gravity all included. At an age of 3 Myr we find a bubble radius of 34 pc and a total X-ray luminosity of 1.3×10^{34} erg s⁻¹, roughly consistent with the observed bubble. The cumulative X-ray emission as a function of the three-dimensional (not projected) radius is shown in Fig. 2.9(a); the X-ray profile with two-dimensional (projected) radius is shown in Fig. 2.9(b). The calculated profiles show an almost flat X-ray profile with a sharp edge at the bubble boundary. This contrasts with the



Seward et al. (1979) and more recent *XMM* images (Hamaguchi et al., 2007a), which are much more complex, with an elevated surface brightness near the bubble walls as noted above.

2.6.1 Globule evaporation

To estimate the emission from the interface between the hot stellar wind material and the molecular gas around the bubble, we first look at a simplified case of a spherical globule of cold gas embedded within the hot gas of the bubble interior, the latter having temperature T_f and number density n_f at large distances from the cold globule. The cold gas will be heated by conduction and evaporate, as discussed in, e.g., Cowie & McKee (1977). The theory makes three assumptions; first, the globule is large enough to give a roughly time-independent solution for the mass-loss rate, second, that the thermal conduction is unsaturated, and third that the flow has a moderate Mach number ($\mathcal{M}^2 \ll 5$). The conduction is unsaturated if the thermal mean free path for electrons is much shorter than the temperature scale height. For the Carina nebula, with $n_x \approx 0.1 \text{ cm}^{-3}$ and $T_x = 6 \times 10^6 \text{ K}$, the conductivity is approaching the saturated limit for globule radius $R_1 \approx 1 \text{ pc}$. Assuming we are in the unsaturated case, the mass-loss rate is given by the classical equation (same as equation 2)

$$\dot{m} = \frac{16\pi\mu K(T)R_1}{25k_b} \quad (2.13)$$

where μ is the mean mass per particle, $K(T)$ is the conductivity at T_f , and R_1 is the radius of the globule. The dimensionless form of the equation of motion is

$$(1 - \mathcal{M}^2) \frac{d \ln \mathcal{M}^2}{dy} = \frac{2(6 - 5y) + \mathcal{M}^2 - 1}{2.5y(y - 1)}, \quad (2.14)$$

where \mathcal{M} is the mach number of the flow and $y = r/R_1$. We assume that the flow will shock somewhere close to the sonic point and thus still satisfy $\mathcal{M}^2 \ll 5$ at all radii.

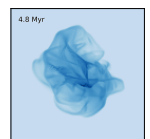
The solution of the energy equation gives the temperature profile

$$T(y) = T_f \left(1 - y^{-1}\right)^{2/5}, \quad (2.15)$$

assuming that the globule temperature $T \ll T_f$. The local sound speed can be calculated from the temperature profile and thus the velocity deduced from the local Mach number. The local density is then

$$n(y) = \frac{\dot{m}}{4\pi y^2 R_1^2 c_s \mathcal{M}}. \quad (2.16)$$

The run of temperature and density can be combined with the expression for bremsstrahlung X-ray emission to give the expected X-ray luminosity and surface brightness for an evaporating globule. The intensity along a line of sight with an impact parameter b to a globule is



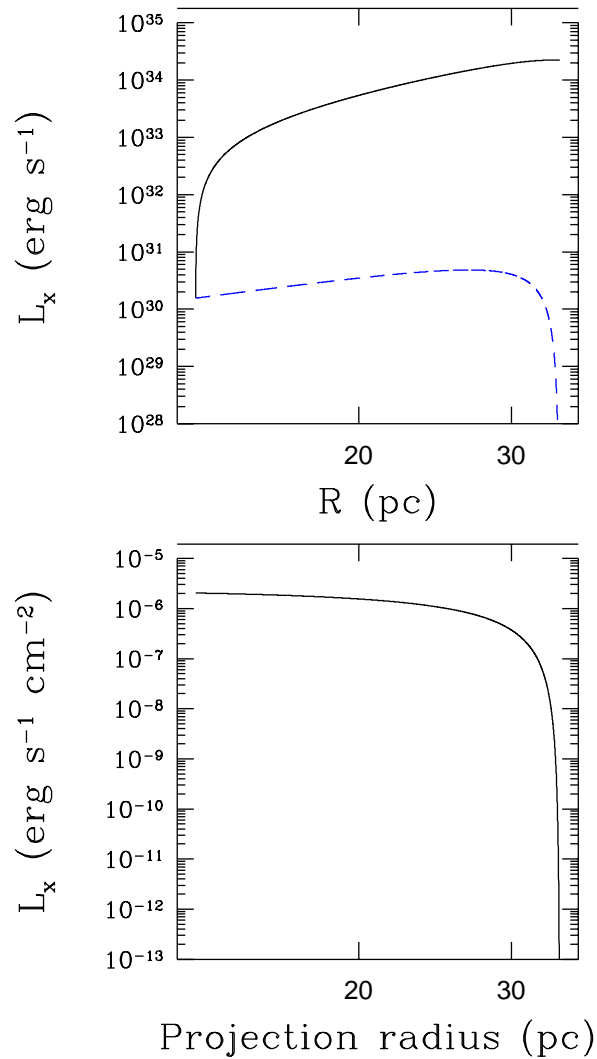
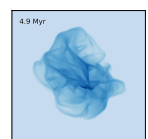


Figure 2.9: Graphs of a modified Castor model showing (a) the cumulative X-ray luminosity (solid) and X-ray profile (dashed) with three-dimensional radius and (b) shows the X-ray profile with projected radius (z); we expect an almost flat X-ray profile with a sharp cutoff at the bubble edge. This model is for $\alpha = 1/3$, $C_f = 0.5$, isothermal sphere ISM model with $R_G = 60$ pc.



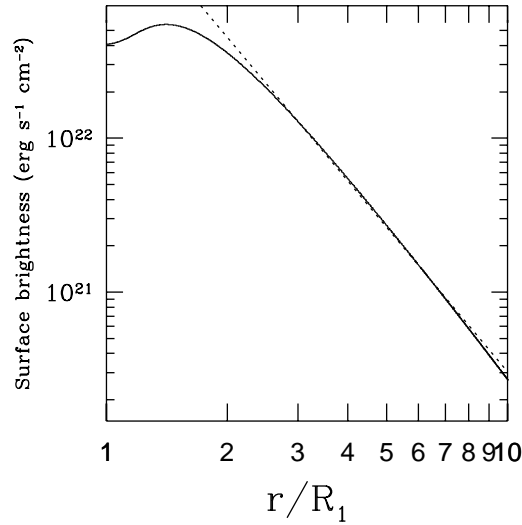


Figure 2.10: The X-ray emission profile against r/R_1 for $T_f = 10^6$ and $R_1 = 1$ pc for an evaporating globule (solid line) showing a fairly sharply defined X-ray halo. The dotted line shows a gradient of -3.

proportional to

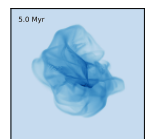
$$\int dz n^2(z) T^{1/2}(z) e^{-kT/h\nu} \approx \int dz \frac{T^{1/2}(r(z))}{(b^2 + z^2)^2} e^{-kT/h\nu} \sim \left(\frac{R_1}{b}\right)^3 \quad (2.17)$$

where z is measured along the line of sight, $z = 0$ in the plane of the sky at the location of the globule, and $r = \sqrt{b^2 + z^2}$. Once $T(r)$ approaches $h\nu/k$, the surface brightness depends primarily on b , falling rapidly with increasing b as long as $R_1 < b$. Doing the integral numerically, setting $T_f = 6 \times 10^6$ and $R_1 = 1$ pc, we get $\dot{m} = 6 \times 10^{21} \text{ g s}^{-1}$ and the X-ray emission profile shown in Fig. 2.10; the dotted line shows the b^{-3} scaling. In other words, a spherical globule should be surrounded by a fairly sharply defined X-ray halo.

As a check, the dependence of the total X-ray luminosity and mass-loss rate on T_f and R_1 were investigated. We varied the external temperature for a globule of $R_1 = 1$ pc; in a separate set of integrations at fixed $T_f = 10^6 \text{ K}$ we varied the radius of the globule R_1 . These simulations show that $\dot{M} \propto T^{2.5}$, $L_x \propto T$, and $\dot{M} \propto T$ as expected analytically for an unsaturated conductivity.

A very crude calculation of the X-ray emission produced by the conductive evaporation of a collection of globules forming the bubble wall suggests that most or all of the X-ray emission could arise in this manner:

$$L_x = \int 4\pi r^2 \Lambda_x n^2(r) dr. \quad (2.18)$$



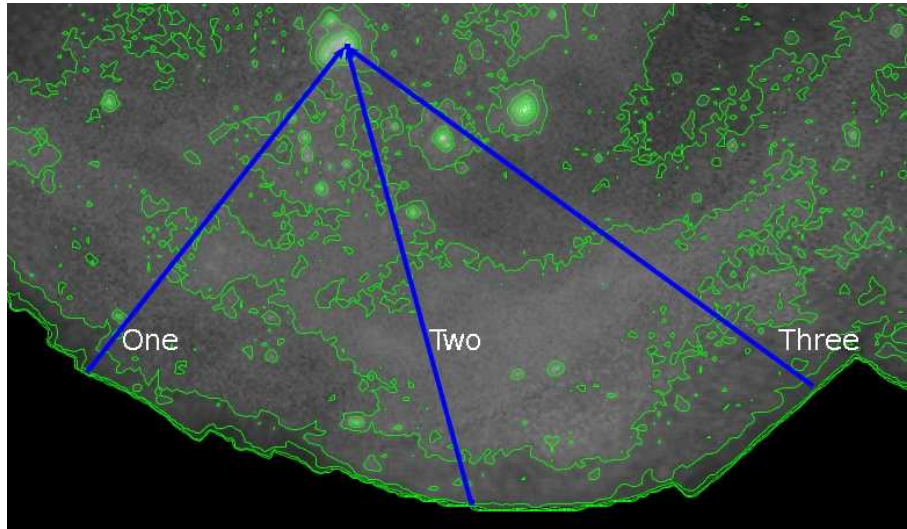


Figure 2.11: XMM image of the southern part of the Carina Nebula between 700 eV and 1300 eV with contours. η Carina can be seen along the top (with all three profile lines pointing at it). Thick lines are the profile lines used in Fig. 2.12.

Using eqn. (2.16),

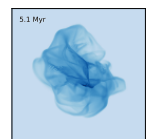
$$L_x \approx 4\pi\Lambda_x \left(\frac{\dot{m}}{4\pi c_s m_p} \right)^2 \frac{1}{R_1} \approx 2.6 \times 10^{33} \left(\frac{R_1}{1 \text{ pc}} \right) \left(\frac{\Lambda_x}{3 \times 10^{-23} \text{ erg s}^{-1} \text{ cm}^3} \right) \text{ erg s}^{-1}. \quad (2.19)$$

If the bubble wall (or about half of it) were tiled with $R_1 \sim 3$ pc globules, evaporation from the wall could explain the observed X-ray emission.

In Carina the situation is much more complicated than this toy model. The density of the hot gas is manifestly not uniform, and in addition we have seen that hot gas apparently escapes rapidly from the bubble interior. We are assuming that this implies that the gas density decreases rapidly away from the bubble wall, on a scale comparable to the size of the wall fragments, which are typically much smaller than the radius of the bubble. Further work along these lines is clearly needed.

We have extracted surface brightness profiles along rays emanating from η Carina using the XMM observations of (Hamaguchi et al., 2007a). The southern part of the XMM image is shown in Fig. 2.11, which also shows the three rays along which the surface brightness was calculated for Fig. 2.12. These profiles were produced by interpolating through the pixels using IDL and then smoothing. All three lines were interpolated through 2554 points and then smoothed by a box car average with a width of 60 points.

Emission was converted from counts to flux using the PIMMS package. We assumed a spectrum of two black bodies as found by Hamaguchi et al. (2007a).



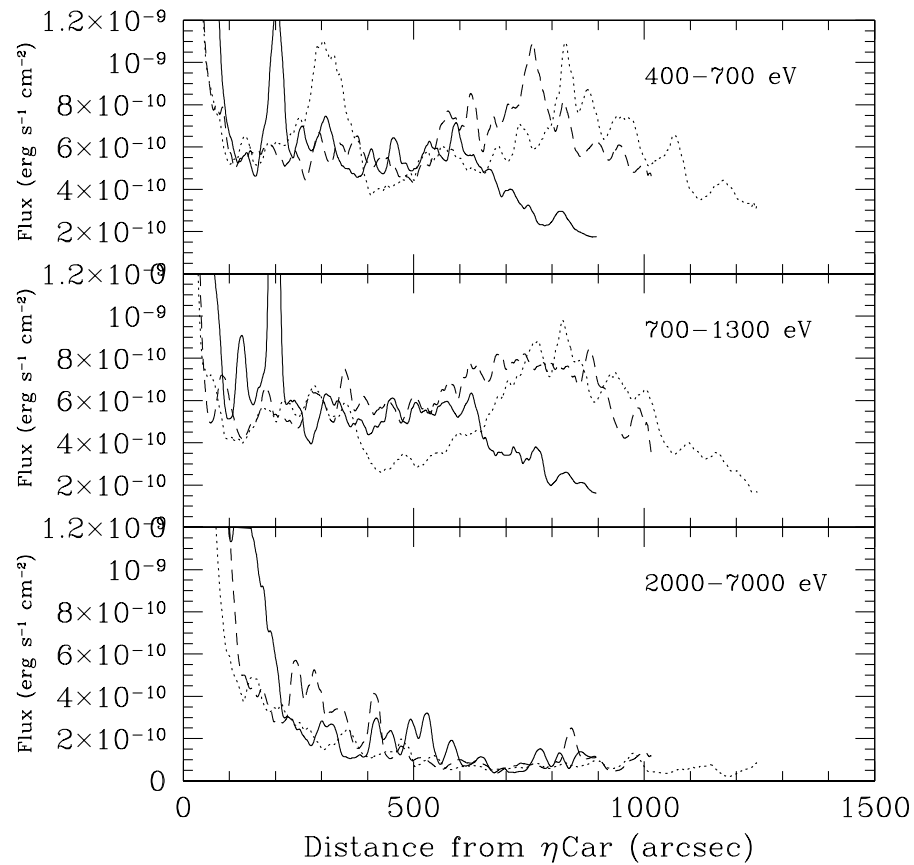
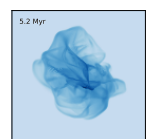


Figure 2.12: Surface brightness along the lines in Fig. 2.11 for the three different XMM bands. The solid line is for profile one, the dashed line for profile two and dotted line for profile three. Surface brightness is given in $\text{erg cm}^{-2} \text{s}^{-1}$, with an assumed $N_H = 1.8 \times 10^{21} \text{ cm}^{-2}$ (Hamaguchi et al., 2007a); projected distances from η Carina are given in arcseconds. Recall that at a distance of 2.3 kpc, 1000 arcseconds is about 11 pc.



The 700-1300eV band shows the greatest contrast, from little emission in the bubble interior (but away from η Carina) to substantial emission near the optically dark lanes. The 400-700eV band also shows some edge effects, especially along lines two and three. The high-energy band, 2000 – 7000 eV, shows essentially no enhanced emission near the bubble walls.

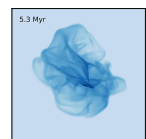
In the 700-1300eV band, line one shows a decrease in the surface brightness from η Carina out to 200 arcsec, a fairly flat profile between 200 and 650 arcsec, followed by a decrease out to the edge of the image. Line two shows a similar flat profile between 150 and 400 arcsec, decreases to a minimum surface brightness at 500 arcsec, then increases to a peak at about 900 arcsec. The profile along line three is similar to line two but with a less pronounced minimum, and a peak closer to η Carina (at 750 arcsec). The peak along ray three is wider than that along ray two as it makes a larger angle with the bubble edge normal. These profiles quantify the visual impression that the bulk of the bubble interior has a fairly flat X-ray surface brightness but that there is strong emission from the edges. The edge profiles are of significantly different shape to that expected from a Castor bubble, Fig. 2.9(a) and are more curved than would be expected from globule evaporation, Fig. 2.10.

2.7 DISCUSSION

We have noted three discrepancies between the Castor et al. scenario and observed bubbles: the predicted bubble radii are too large at a given cluster or stellar age: the predicted X-ray luminosities are too high by a factor of 100 or more; and concomitantly, the predicted pressure of the hot gas is too large by a factor of 10 or more. Finally, we have noted that the radio free-free emission is consistent with a filling factor of H II gas that is of order unity, suggesting that the pressure in the bubbles is controlled by the H II gas rather than that of the shocked stellar wind gas.

A number of authors have noted the small observed R_b , roughly by a factor of 5, compared to predictions (Dorland et al., 1986; Dorland & Montmerle, 1987; Oey, 1996; Rauw et al., 2002; Dunne et al., 2003; Smith et al., 2005). These authors have also noted the deficit of X-ray luminosity or hot gas pressure compared to predictions. Suggested resolutions involve one or more of the following: lower stellar wind luminosities, mass-loss from the bubble, or energy loss from the bubble, e.g., from super-Spitzer effective conductivities, or highly efficient mass loading so that the shocked stellar wind cools by conduction below X-ray temperatures.

Castor et al. (1975) and Weaver et al. (1977) make three assumptions; first, that the energy deposited by the stellar winds (or 5/11 of it) is stored in the hot gas inside the bubble; second, that the hot gas mass is controlled by conduction (at the Spitzer rate); and third, that the



surrounding ISM is uniform (represented by their constant density n_0). Applying the model requires knowledge of L_w , n_0 , and the age of the system. The predicted bubble radii depend only weakly on L_w and n_0 , while the ages of star clusters are reasonably well constrained (to within a factor of 2 – 4). Since the bubble radii are universally overestimated, at least one assumption must be incorrect.

We can acknowledge the fact that the dynamics of the model are wrong, but still test the first assumption that the energy deposited by the stellar winds is stored inside the bubble. We will also assume that conduction drives gas from the bubble wall into the interior until $T_b \sim 10^6 - 10^7$ K; this assumption is bolstered by the observed gas temperatures, which cluster around 6×10^6 K.

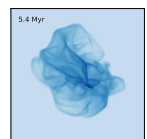
The argument is that the time-integrated wind luminosity deposits an energy $E = (5/11)L_w\tau$ in the bubble interior, and that the corresponding pressure is $2E/3V$, where the volume is assumed to be a sphere with the observed bubble radius. Together with the assumption that the temperature is $T \approx 5 \times 10^6$ K, we can calculate the mean density and hence the X-ray luminosity.

Both X-ray and other observations give estimates of the bubble radius. Star counts (to a given limiting magnitude) and radio observations give estimates of L , the bolometric stellar luminosity, or Q . The stellar wind luminosity can then be estimated from either L or Q , with the caveats mentioned above. Finally, from the presence of Wolf-Rayet stars and/or SN remnants, we have estimates of the cluster age. In terms of these quantities, the X-ray luminosity is

$$L_x \approx 3 \times 10^{38} \xi \left(\frac{L_w}{4 \times 10^{38} \text{ erg s}^{-1}} \right)^2 \left(\frac{20 \text{ pc}}{r} \right)^3 \left(\frac{6 \times 10^6 \text{ K}}{T} \right)^2 \left(\frac{3.6 \times 10^6 \text{ yr}}{\tau} \right)^2, \quad (2.20)$$

where we have assumed an X-ray cooling rate $\Lambda_x \approx 3 \times 10^{-23} \xi \text{ erg s}^{-1} \text{ cm}^3$, e.g., Chu et al. (1995), ξ is the metallicity relative to solar, and τ is the age of the cluster. We have scaled to values appropriate to Carina. As previously noted, this is 10,000 times too high.

In addition to Carina, we have calculated this predicted X-ray luminosity for the LMC H II regions detected in X-rays by the *Einstein* satellite, and discussed in Chu & Low (1990). We estimate the bolometric luminosity of the H II region in two ways; first, we use the star counts from Lucke & Hodge (1970); these authors report star counts for stars with $m_V < 14.7$, about $M_V = -3.85$ at the distance of the LMC; second, we use the observed radio free-free flux from McGee et al. (1972) to estimate Q and thence L ; the results from the two methods are consistent, within a factor of 3 or so. As in the case of Milky Way bubbles, this indicates that the filling factor of the H II gas is of order unity, and hence that the pressure in these bubbles is not set by the X-ray emitting gas. From the bolometric luminosity we then estimate L_w .



Using these values, eqn. (2.20) overpredicts the X-ray luminosity by factors ranging from a few to five hundred.

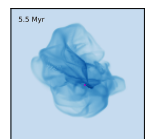
Thus, the picture for the LMC is consistent with our finding for Carina. Confusingly, other authors have found an *excess* of observed X-ray emission compared to predictions of the Castor et al. model (Chu & Low, 1990; Chu et al., 1995; Wang & Helfand, 1991). Why should this be?

Chu & Low (1990), Chu et al. (1995), and Wang & Helfand (1991) all use the scaling laws of Castor et al. to predict the X-ray luminosity of bubbles in the LMC. The latter two give expression for L_x that appear to contain only directly observed quantities, such as the bubble radius and the bubble expansion velocity. However, the coefficient relating L_x to the observed quantities depends on the theoretical estimate for the bubble radius and central bubble density. This dependence results in an estimate for the stellar wind luminosity that is more than a factor of 10 smaller than the wind luminosity as estimated from either simple star counts, or from the free-free radio emission.

In the case of Chu & Low (1990), this can be seen explicitly in their discussion of N51D, where they infer $L_w = 1.08 \times 10^{37} \text{ erg s}^{-1}$ in their appendix B Section IV. From the star counts of Lucke & Hodge (1970) we estimate $L_w = 2 \times 10^{38} \text{ erg s}^{-1}$; from the radio flux from McGee et al. (1972) we find $L_w = 6 \times 10^{37} \text{ erg s}^{-1}$. Using the lower value, and the observed $R_b = 48 \text{ pc}$, eqn. (2.20) yields $L_x = 1.6 \times 10^{36} \text{ erg s}^{-1}$, about a factor of 5 larger than the observed $L_x = 3.3 \times 10^{35} \text{ erg s}^{-1}$.

Since their estimates of L_x are smaller than the observed X-ray luminosities, Chu & Low (1990) suggest that the X-ray emission of the LMC objects is provided by SNe that have gone off near the bubble wall. We argue that, using the estimate given here, recourse to SNe is unnecessary. In addition, the morphology of the X-ray emission in Carina does not support this picture, nor does that of the objects studied by Chu & Low (1990) in the LMC. In Carina, as stated above, the emission is slightly enhanced near the bubble walls, but not at a particular point, as would be expected following an SN.

Similarly, the X-ray images presented by Townsley et al. (2006) of N 157 (30 Doradus), especially their Figures 14 and 15, generally show rather diffuse emission in the cavities surrounded by cold dusty gas, reminiscent of what is seen in Carina. However, as Townsley et al. (2006) also remark, in some cases the emission comes from the interior of the cavity, while in others it comes from edge brightened regions with distinct central voids, similar to Carina. Two exceptions may be the regions referred to as numbers 5 and 9, which Townsley et al. (2006) suggest may be the result of SNe interacting with the bubble wall, a la Chu & Low (1990).



2.7.1 Dynamics Controlled by H II Gas

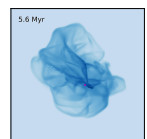
As we noted in section §2.3, the H II gas pressure in Carina, as estimated from the radio free-free emission, is similar to the pressure in the X-ray emitting gas; both are similar to the pressure where the outflows from photo-dissociation regions shock. This was pointed out earlier by Dorland & Montmerle (1987). Since the sound speed of the cooler gas is comparable to the bubble expansion velocities observed, this is not surprising.

What is more surprising is that the free-free luminosity is consistent with a filling factor for the H II gas that is of order unity (see eqn. 2.2) a fact apparently not noted before. This implies that the gas pressure is set by the H II gas rather than the hot gas. It suggests that the shocked stellar winds escape from the partially confining bubble at the sound speed of the hot gas, as long as the pressure in the hot gas exceeds the H II gas pressure in the region. When enough hot gas has escaped that $P_x \approx P_{HII}$, the escape will slow, as the hot gas is impeded by the cooler gas. This sets up a rough pressure balance between the hot and H II gas.

Dorland et al. (1986) and Dorland & Montmerle (1987) consider the loss of wind energy (by an enhanced conduction by a non-Maxwellian tail of high-energy electrons, according to the latter). Dorland & Montmerle (1987) note that the thermal energy in hot gas in the Rosette as well as the Carina nebula cavities is well below that input by stellar winds over the age of the respective star clusters. These authors suggest that the excess energy is conducted away from the hot gas to surrounding cold gas, rather than by simply flowing out through holes in the bubble wall as suggested here and elsewhere. This would alleviate the dynamical problem (the predicted bubble radius would be smaller than in the Castor et al. theory) and the X-ray luminosity problem.

In a similar vein, McKee et al. (1984) consider the evolution of wind blown bubbles in conjunction with H II regions. Like us, they conclude that the pressure and hence the dynamics of the bubble are controlled not by the 10^7 K gas, but by the H II gas. They suggest that the energy density of the shocked wind is dissipated in situ, rather than leaving the bubble. In the case of a high wind luminosity (as in Carina), they suggest that the hot gas will engulf a large number of globules, producing a large mass loading and resultant catastrophic radiative cooling.

Examination of the Hubble Carina mosaic (Smith & Brooks, 2008), which has a spatial resolution of $\sim 10^{-3}$ pc, does not reveal a large population of evaporating globules in the interior of the bubble. If the bubble wall consists of a large number of subresolution globules it might be possible to dissipate the wind luminosity; the bulk of the wind luminosity would be radiated near or just beyond the Lyman edge, or possibly as optical light. Radiation beyond the



Lyman edge would be hard to detect due to absorption along the line of sight to Earth, while optical emission would be hard to distinguish from emission associated with ionizing radiation from the star clusters. However, preliminary calculations of the emission region associated with an evaporating globule suggest that a few percent of the luminosity would emerge in the X-ray band; only if the globules are $\sim 100\text{AU}$ in radius is the fraction of emission emerging in the X-ray band small enough to escape detection. The conduction around such globules is highly saturated; in fact, the mean free path for electrons to thermalize is $\lambda \sim 0.1\text{ pc}$. Hence, the globules would have to be separated by many times their own radii to avoid an X-ray emission fraction larger than observed. These small globules are surrounded by a saturated conduction region roughly 10 times their own radius; if these saturated conduction regions overlap they will radiate X-rays like a single, much larger globule. We defer further discussion of this possibility to a later publication.

Neither Dorland et al. (1986) nor McKee et al. (1984) explain why $P_{HII} \approx \sqrt{3Q/4\pi R_b^2 \alpha_r}$ (where the latter assumes a filling factor near unity). It is not clear why the energy-loss rate of the hot gas would tune itself so that the filling factor of both warm and hot gas is near unity. A large cooling luminosity would lead to an essentially complete absence of hot gas, while a low cooling luminosity would result in too high a hot gas pressure. Unlike a simple mass-loss scenario, an energy-loss scenario requires some fine tuning to match the observations.

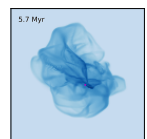
Finally, we note that our leaky bubble models, which predict smaller bubble radii and gas pressures, have implications for the prediction of spectral energy distributions of starburst galaxies. As pointed out by Dopita et al. (2005), using a standard Castor et al. bubble model results in ionization parameters too small (by a factor of 10 or more) than that inferred from spectral energy distributions of such galaxies. Both the smaller radii and the lower gas pressure (hence gas density) will increase the ionization parameter associated with bubbles surrounding massive star clusters.

2.7.2 Ballistic Bubbles

In the Castor et al. scenario, if the shocked stellar wind gas from a star or star cluster was confined to a bubble of volume V , the pressure of the hot gas would be

$$P_x = \frac{2}{3} \frac{5}{11} \frac{L_w \tau}{V}, \quad (2.21)$$

where the energy in the bubble $E_b = (5/11)L_w \tau$ and τ is the age of the star cluster. As already mentioned, this pressure is orders of magnitude larger than the observed pressure in Carina, so the hot gas is not currently exerting the predicted pressure on the surrounding dense gas.



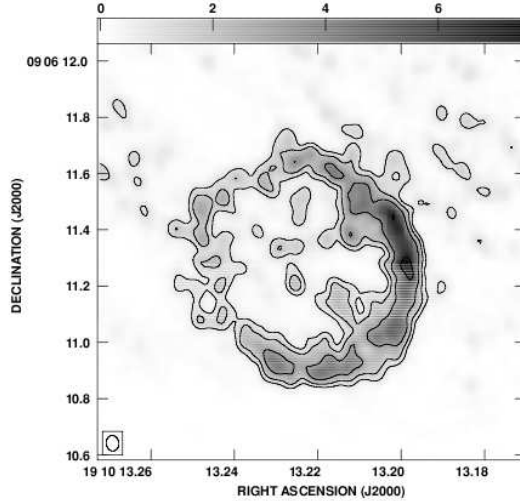


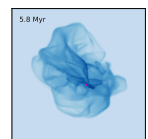
Figure 2.13: VLA 7mm observation of W49A/D from De Pree et al. (2005). Beam size shown lower left is about 500 AU. The shell has a radius of ~ 0.03 pc and the column density through the shell is significantly variable.

However, it is possible that in the past the hot gas was confined. The force exerted by the gas on the bubble would have been much larger than that exerted by the H II gas or by radiation, resulting in a nearly impulsive expansion of the bubble. After this early impulsive phase, the hot gas could then leak out of the bubble, leaving the bubble to expand in a nearly ballistic manner. This could happen, for example, if the density of the trapped hot gas grew large enough that the radiative cooling time scale became shorter than the expansion time scale (Shull, 1980). We argue that this is not the case.

First, high-resolution radio images of ultracompact H II (UCHII) regions ($R \sim 0.1$ pc) by De Pree et al. (2005) show that most are either shell-like (see Fig. 2.13) or cometary (a significant fraction are bipolar). The former two would allow hot gas to leak out of the UCHII region. Observations show that the expansion velocities are typically ~ 10 km s^{-1} , e.g. Chakraborty & Anandarao (1997, 1999). The expanding shell will sweep up mass; if the motion is ballistic the velocity will decrease and the bubble will never reach sizes of order 10pc.

Second, there are UCHII regions that emit diffuse X-rays, e.g., in the Welch ring of W49 (Tsujiimoto et al., 2006) and in the Hourglass region of the Lagoon nebula, M8 (Rauw et al., 2002). In both cases, the X-ray luminosity is well below that expected under the assumption that the shocked wind gas is confined in a bubble; it is also well below L_w . We discuss each source in turn.

The W49 ultracompact ($r \sim 0.15$ pc, $D = 11.4$ kpc) source G_X has $L_x \approx 3 \times 10^{33}$ erg s^{-1} and $T \approx 7$ keV (Tsujiimoto et al., 2006), much hotter than the plasma in Carina. The high

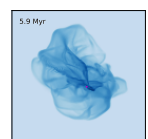


temperature of the X-ray gas is difficult to reconcile with the Castor et al. model; such hot gas is more likely to occur in a wind-wind collision. If this is the case, then the luminosity of any truly diffuse, shocked, partially confined gas is even smaller than the value given here. The column toward the source is $\Sigma \approx 0.8 \text{ g cm}^{-2}$, suggesting a dynamical pressure $P = \pi G \Sigma^2 \approx 10^{-7} \text{ dynes cm}^{-2}$, and a mean cold gas density $\rho \approx 2 \times 10^{-18} \text{ g cm}^{-3}$. This is consistent with their estimated hot gas pressure based on the emission measure ($n_x \approx 10 \text{ cm}^{-3}$, $P_x \approx 10^{-7} \text{ dynes cm}^{-2}$). They suggest that the driving source is one or two O5 or O6 stars, with a luminosity in the range $2 - 6 \times 10^5 L_\odot$, consistent with the ionizing photon luminosity $Q \approx 10^{49} \text{ s}^{-1}$ for each of the five G sources listed by de Pree et al. (1997). The corresponding wind luminosity is $L_w \approx 500 L_\odot$.

The age of the source can be estimated in two ways. First, using the mean density, the dynamical time is $\tau_{dyn} = 1/\sqrt{G\rho} \approx 3 \times 10^{12} \text{ s} = 0.1 \text{ Myrs}$. Second, using the force exerted by the hot, X-ray emitting gas; as just noted, the latter has a much lower density than the absorbing gas, but a similar pressure. The outward acceleration is $P_x/\Sigma \approx 10^{-7} \text{ cm s}^{-2}$. The dynamical time is then $\tau_{dyn} \approx 2 \times 10^{12} \text{ s}$, roughly the same as the estimate based on the self-gravity of the cold gas.

Assuming that the stellar wind is trapped in a Castor-style bubble, the energy in the shocked gas is $E = \frac{5}{11} L_w \tau \approx 4 \times 10^{48} \text{ erg s}^{-1}$, and the pressure $P = 2 \times 10^{-5} \text{ dynes cm}^{-2}$, two orders of magnitude higher than observed (and with an associated X-ray luminosity four orders of magnitude too high). Since this pressure is so much higher than the dynamical pressure, and the sound crossing time of the hot gas so much smaller (by a factor of about 1000), the simplest interpretation is simply that the shocked stellar wind gas escapes, as in Carina. The radio images of the G sources in Figure 2 of Pree et al. (2005) show a very incomplete ring, strengthening the argument for rapid escape.

The second case is the ultracompact H II region G 5.97 -1.17 associated with the Hourglass nebulae in M8. It is believed to be powered by the O7 V star Herschel 36; using values for \dot{M}_w from Repolust et al. (2004) (not allowing for a clumped wind), we estimate $L_w = 2 \times 10^{36} \text{ erg s}^{-1}$, while Rauw et al. (2002) use a wind luminosity of a factor of 3 smaller. They estimate a dynamical age of $2 \times 10^4 \text{ yr}$ based on the size of the Hourglass (they use $R = 0.2 \text{ pc}$) and the observed expansion velocity of 10 km s^{-1} (Chakraborty & Anandarao, 1997, 1999). Using their values for L_2 , τ_{dyn} , and R_b , we find a predicted hot gas pressure of $P = 4 \times 10^{-7}$ and $n_x \approx 200 \text{ cm}^{-3}$. The predicted $L_x = 7 \times 10^{35} \text{ erg s}^{-1}$, larger than that observed by a factor of 1000. Using the full Castor et al. model, Rauw et al. (2002) note that the predicted bubble radius is larger than that observed (but only by a factor of 2) and that the predicted X-ray flux is $L_x \approx 10^{35} \text{ erg s}^{-1}$. This is smaller than our prediction by a factor of 7, consistent with their



use of the (two times too large) Castor et al. radius. Their predicted X-ray flux is still larger than observed by a factor of 175.

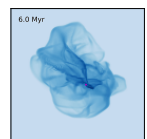
Radio observations by Turner et al. (1974) find a radius $r \sim 0.1$ pc (half that suggested by Rauw et al.) and a flux at 11 cm of 0.54 Jansky. The H II gas pressure is 1.5×10^{-9} dynes cm^{-2} from the observed radio flux, and 1.5×10^{-8} dynes cm^{-2} using Q for an O 7 V star. This should be compared to the pressure of the X-ray emitting gas $P_x = 8 \times 10^{-9}$ dynes cm^{-2} , and to the radiation pressure $L/4\pi r^2 c = 1.6 \times 10^{-8}$ dynes cm^{-2} . All these pressures are at least a factor 10 below the pressure found under the assumption that the wind luminosity is trapped in the bubble. We conclude that, as for G_x , the most likely explanation of the low observed X-ray flux and the small bubble radius is that the shocked stellar gas simply escapes from the bubble interior.

2.8 CONCLUSIONS

We use both the Castor et al. theory and the Chevalier and Clegg theory for bubble evolution around massive star clusters to try to understand observations of Milky Way and LMC bubbles. The Castor theory overpredicts X-ray luminosity in the Carina bubble by a factor of 60 and expands too fast by a factor of 4. In contrast, the Chevalier and Clegg model underpredicts the X-ray luminosity by a factor of 20; since it is a steady state it has no expansion time.

These results suggest there is a partially confined hot, homogeneous interior but there are also holes in the shell through which the hot gas escapes like a free-flowing wind. We constructed a model in which the confining shell covered only a fraction C_f of the sky as seen from the cluster, and allowed hot wind gas to escape at its sound speed from the uncovered portion of the shell. As an example one model consistent with observations of Carina is an isothermal sphere GMC model with $R_G = 60$ pc, $\alpha = 0.2$, and $C_f = 0.5$, $R_b = 16.5$ pc, $L_x = 1.2 \times 10^{34}$ erg s^{-1} , and $P_b = 1.1 \times 10^{-10}$ dynes cm^{-2} . This compromise is the best way to fit the many observations of the Carina nebula and is likely the best solution for all bubbles. Our models suggest that the exact size, distribution and evolution of holes does not matter much, it is the weighted average of the fraction of total area that matters.

The bottom line is that the dynamics of X-ray bubbles are not strongly affected by the presence of luminous stellar winds; rather, they are controlled by a combination of the self-gravity of the surrounding GMC gas, radiation pressure, and H II gas pressure. This conclusion is in contrast to that of Castor et al. (1975) and Shull (1980), but in agreement with McKee et al. (1984). We argue that the X-ray fluxes of the bubbles are *always* below those predicted by the Castor et al. picture, properly interpreted, i.e. using the observed rather than predicted



bubble radii. As noted by Dorland et al. (1986) and Dorland & Montmerle (1987), the X-ray observations show that the pressure in the hot gas is well below that predicted by Castor et al. (1975); unlike Dorland et al. (1986), Dorland & Montmerle (1987), and McKee et al. (1984), we argue that this is a result of leakage of hot gas from the bubble, rather than leakage of energy in the form of radiation.

The results of the models in this chapter are dependent upon the ISM model used, both the run of mean density and the fluctuations in the surface density in different directions from the bubble centre. According to both simulations and observations, the latter is distributed log-normally, meaning that in many directions the surface density will be far below the mean surface density. We suggest that hot gas escapes along these directions, which in our simplified models we treat as holes in the bubble wall.

Full hydrodynamical models are needed to check that the semianalytical solutions shown in this chapter are correct and to understand both the early evolution of bubbles and the development of holes in the shell.

2.9 Appendix: CHEVALIER & CLEGG BUBBLES

Chevalier & Clegg assume a spherically symmetric wind with mass input \dot{M}_w and energy input $\dot{E} = L_w$. For a smooth transition from subsonic flow at the centre to supersonic flow at large distances the Mach number must equal one at some radius, which Chevalier & Clegg take to be $r = R_{cl}$.

The flow is described by

$$\frac{1}{r^2} \frac{d}{dr} (\rho u r^2) = \phi, \quad (2.22)$$

$$\rho u \frac{du}{dr} = -\frac{dP}{dr} - \phi u, \quad (2.23)$$

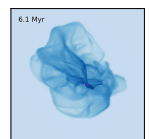
$$\frac{1}{r^2} \frac{d}{dr} \left[\rho u r^2 \left(\frac{1}{2} u^2 + \frac{5P}{2\rho} \right) \right] = \Phi, \quad (2.24)$$

where u is the wind velocity, r is the radial co-ordinate, ρ is the density, P is the pressure, and γ , the adiabatic index, = 5/3 throughout this chapter. For $r < R_{cl}$, $\phi = \dot{M}_w/V$, $\Phi = \dot{E}/V$, $V = 4\pi R_{cl}^3/3$; for $r > R_{cl}$, $\phi = \Phi = 0$. Equations (2.22)-(2.24) have the solution

$$\left(\frac{5 + 1/\mathcal{M}^2}{6} \right)^{\left(-\frac{9}{14}\right)} \left(\frac{1 + 3/\mathcal{M}^2}{4} \right)^{\left(\frac{1}{7}\right)} = \frac{r}{R_{cl}}, \quad (2.25)$$

for $r < R_{cl}$, and

$$\mathcal{M}^3 \left(\frac{1 + 3/\mathcal{M}^2}{4} \right)^2 = \left(\frac{r}{R_{cl}} \right)^2, \quad (2.26)$$



for $r > R_{cl}$, where \mathcal{M} is the Mach number.

The flow can be integrated in two sections, $r < R_{cl}$ and $r > R_{cl}$ using the outer boundary conditions of the first as the inner boundary of the second. Thus, it is possible to follow the evolution of the wind and numerically integrate the expected X-ray luminosity from the cluster edge out to arbitrarily large distances.

Initially a small radius ($r \ll R_{cl}$) and small initial mach number, \mathcal{M}_0 are assumed. The true Mach number is then found iteratively to 10 decimal places for that radius

$$\mathcal{M}_{i+1} = \left[6 \left(\frac{1 + 3/\mathcal{M}^2}{4} \right)^{\frac{2}{9}} \left(\frac{r}{R_{cl}} \right)^{-\frac{11}{9}} - 5 \right]^{-0.5}. \quad (2.27)$$

The calculated Mach number was then combined with the observed mass loss rate and stellar wind luminosity for Tr 16 (Table 1) to find the initial conditions (from Chevalier & Clegg (1985))

$$\begin{aligned} \rho &= 0.296 \dot{M}_w^{1.5} L_w^{-0.5} R_{cl}^{-2}, \\ n &= \frac{\rho}{\mu}, \\ P &= 0.118 \dot{M}_w^{0.5} L_w^{0.5} R_{cl}^{-2}, \\ T &= \frac{P}{nk_b}, \\ c_s &= \sqrt{\frac{5P}{3\rho}}, \\ u &= \mathcal{M}c_s. \end{aligned}$$

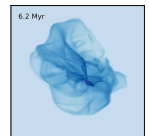
From these initial conditions equations (2.22)-(2.24) can be integrated to the cluster radius. The integration continues with the evolution equations (without the source terms outside the cluster) and the appropriate Mach number iteration,

$$\mathcal{M}_{i+1} = \left(\frac{r}{R_{cl}} \right)^{\frac{2}{3}} \left(\frac{4}{1 + 3/\mathcal{M}_i} \right)^{\frac{1}{6}}. \quad (2.28)$$

2.10 Appendix: CASTOR et al. BUBBLES

For a bubble in the snow plough stage, R_b is large enough that the flow from c to b can be considered stationary and plane parallel. Weaver et al. (1977) considered the effects of relaxing this assumption and found the results are only changed by $\leq 10\%$, much less than the observational errors for, e.g., the bubble radius in Carina. For a stationary plane parallel flow at constant pressure (Penston & Brown, 1970)

$$\rho v \frac{dH}{dz} = \frac{d}{dz} \left[K(T) \frac{dT}{dz} \right] - \rho \Lambda(T), \quad (2.29)$$



where T is temperature, $z = R_b - r$, $\rho v = \dot{M}_b/4\pi R_b^2$, M_b is the mass in region b, $H = 5k_b T/2\mu$ the specific enthalpy, $K(T) = CT^{5/2}$ is the thermal conductivity, and $C = 1.2 \times 10^{-6} \text{ erg cm}^{-1} \text{ s}^{-1} \text{ K}^{7/2}$ (Spitzer, 1962). Integrating equation(2.29) from the b-c boundary: $z = 0$, $T \sim 0$ to the centre: $z = R_b$, $T = T_b$ gives the mass evaporating from c to b as

$$\dot{M}_b = \frac{16\pi}{25} \frac{\mu}{k_b} K(T) R_b. \quad (2.30)$$

To get this solution we have assumed the cooling term, $\rho\Lambda(T)$ is negligible in the transition zone between b and c.

Energy is constantly added into region b by the stellar winds with the total luminosity L_w and the dominant energy loss is through the expansion of the bubble. The energy in region b obeys

$$\dot{E}_b = L_w - 4\pi R_b^2 P_b \dot{R}_b, \quad (2.31)$$

where P_b is the pressure in region b and

$$\frac{4}{3}\pi R_b^3 P_b = \frac{2}{3}E_b. \quad (2.32)$$

When considering radiative losses from region b it is necessary to follow the evolution of region a (the hypersonic stellar wind region) as eventually region b will cool enough to collapse. Therefore, the equations need to be altered to account for the fact that the size of region a is not negligible. In that case, the energy in region b is given by

$$E_b = 2\pi P_b (R_b^3 - R_a^3), \quad (2.33)$$

where R_a is the radius of region a. R_a can be calculated from pressure balance at R_a . The pressure from region b on a shell at R_a is

$$P_b = \frac{1}{2\pi} \frac{E_b}{R_b^3 - R_a^3}. \quad (2.34)$$

The stellar wind luminosity is $L_w = \dot{M}_w v_w^2/2$ so the rate of momentum deposition by the stellar wind is

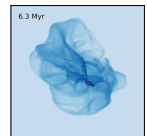
$$\dot{M}_w v_w = \frac{2L_w}{v_w}. \quad (2.35)$$

This then gives a pressure at radius R_a of

$$P_w = \frac{2L_w}{v_w} \frac{1}{4\pi R_a^2}. \quad (2.36)$$

Setting these pressures equal gives

$$R_a = \left[\frac{L_w}{v_w E_b} (R_b^3 - R_a^3) \right]^{1/2}. \quad (2.37)$$



Radiative losses within region b can be calculated by reference to the cooling functions in Sutherland & Dopita (1993)

$$L_b \approx n_b^2 \frac{4}{3} \pi (R_b^3 - R_a^3) \Lambda(T). \quad (2.38)$$

Including radiative losses into the Castor et al. evolution equations results in the following closed set of evolution equations

$$\frac{d\mathcal{P}_c}{dt} = 4\pi R_b^2 P_b, \quad (2.39)$$

$$\frac{dR_b}{dt} = \frac{\mathcal{P}_c}{M_c}, \quad (2.40)$$

$$\frac{dM_b}{dt} = C_1 T_b^{5/2} R_b^2 (R_b - R_a)^{-1} - 10^{-5} \frac{\mu}{k_b} L_b, \quad (2.41)$$

$$\frac{dE_b}{dt} = L_w - 4\pi R_b^2 P_b \frac{dR_b}{dt} - L_b, \quad (2.42)$$

where \mathcal{P}_c is the momentum of the shell and $C_1 = 4.13 \times 10^{-14}$ cgs.

The initial conditions of the bubble are taken from Weaver et al. (1977) at time $t_0 = 10^3$ years:

$$E_b = \frac{5}{11} L_w t_0, \quad (2.43)$$

$$R_b = \left(\frac{125}{154\pi} \frac{L_w}{\rho_0} \right)^{1/5} t_0^{3/5}, \quad (2.44)$$

$$v_c = \frac{3}{5} \frac{R_b}{t_0}, \quad (2.45)$$

$$V_b = \frac{4}{3} \pi R_b^3, \quad (2.46)$$

$$P_b = \frac{E_b}{V_b}, \quad (2.47)$$

$$M_b = \frac{28}{205} \times 1.646^{5/2} \times V_b \frac{\mu}{k_b} \left(\frac{t_0 C}{R_b^2} \right)^{2/7} P_b^{5/7}, \quad (2.48)$$

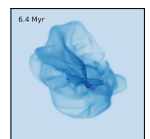
$$\rho_b = \frac{M_b}{V_b}, \quad (2.49)$$

$$n_b = \frac{\rho_b}{\mu}, \quad (2.50)$$

$$T_b = \frac{P_b}{n_b k_b}. \quad (2.51)$$

These give initial conditions close enough to the true values that the numerical solution settles down by the cluster boundary and is a valid solution for $R_b > R_{c1}$.

Initially the parameters were set up to match those used in Weaver et al. (1977) and results compared to Figure 6 of that paper as a check of our code. Once the code was tested parameters for Tr 16 could be used (from Table 1).



Chapter 3

Coding

To further investigate the effects of stars on their parent Giant Molecular Clouds (GMCs) I ran three dimensional simulations. We collaborated with Tom Abel to use the development version of Enzo, given the extensive physics already coded within it. In §3.1 will give a brief overview of Enzo, in §3.2-3.7 go into details of the specific physics I used, and in §3.8 discuss the analysis package I used to create all of the figures in Chapters 4 and 5.

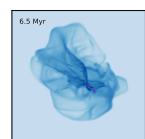
3.1 Enzo Overview

Most of the algorithms in the development version of Enzo are now available in the publicly released stable Enzo2.0. Both the stable and development versions of Enzo can be found at: <http://enzo.googlecode.com/>.

The primary references for Enzo are: O’Shea et al. (2004) and Norman et al. (2007). These papers outline the basic structure and algorithms of Enzo. References for specific parts of code are referenced within the relevant section in the remainder of this chapter.

Enzo is a parallel grid-based code developed for astrophysics and cosmology. Enzo’s higher level functions and data structures are written in C++ and the computationally intensive lower level functions in Fortran. The code is parallelised using the MPI message passing library and uses HDF5 for data output.

Enzo uses the Structured Adaptive Mesh Refinement (SAMR) as developed by Berger & Colella (1989). The code identifies regions of the grid in breach of the refinement criterion (e.g. Jeans length too short) and creates a child grid with an integer higher resolution in that region. This continues until the maximum depth of refinement is reached. For example, with a 256^3 parent grid and 5 levels of refine by 2 the highest level of refinement has an effective



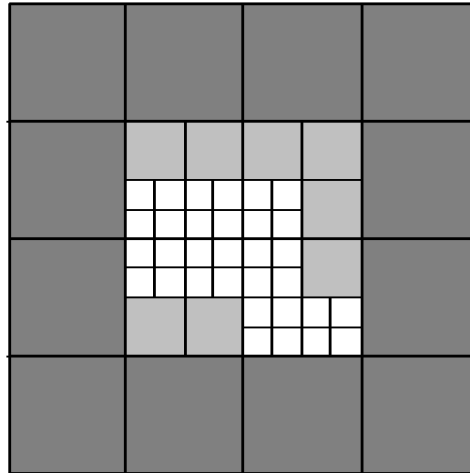


Figure 3.1: A 2D diagram showing adaptive mesh refinement. This diagram shows two levels of refinement around the region on interest.

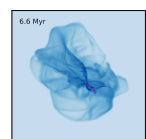
resolution of $256 \times 2^5 = 8192$. Fig. 3.1 shows a cartoon of an AMR grid in 2D refining to two levels. AMR was only used in 5.2 where I ran resolution tests and compared unigrid and AMR simulations; all other simulations were unigrid (usually 128^3).

3.2 Hydrodynamics

Enzo included several hydro solvers including PPM (Colella & Woodward, 1984), ZEUS (Stone & Norman, 1992), and a Runge-Kutta time integrating hydro solver, `hydro_rk`, with the capacity for ideal MHD (Wang & Abel, 2009).

3.2.1 Improved PPM

At the end of February 2011 John Wise added several improvements to the PPM solver in `enzo_unstable`. Previously, when running high Mach number turbulence, the PPM solver would break. The main change implemented by John was improving the PPM reconstruction. He added an additional “van Leer” slope limiter and enforced the monotonized states to be bounded by the neighbouring cell centred values.



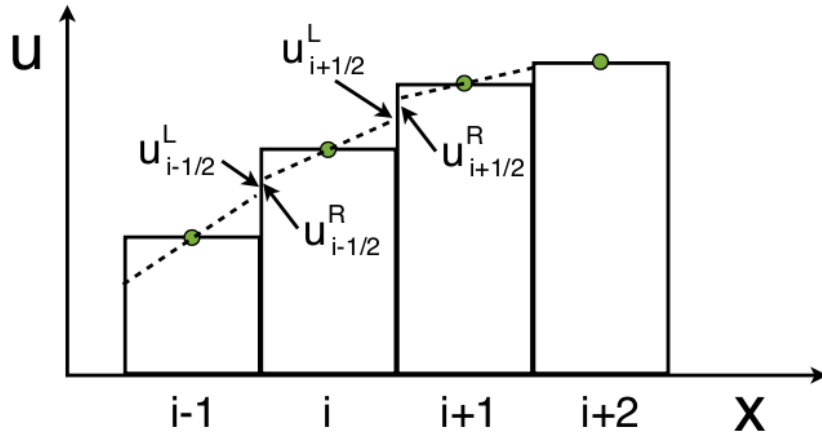


Figure 3.2: A diagram showing how PLM and LLM solve fluxes across cell boundaries.

3.2.2 Hydro_rk

In my simulations the high Mach number and significant velocity of clumps across the simulation grid requires the more robust hydro_rk solver.

In hydro_rk reconstruction is done using the Piecewise Linear Method - PLM (van Leer, 1979). PLM takes the distribution of physical quantities of the gas inside a cell to be linear. The slope across the cell is fit with least squares and limited by monotonicity conditions (e.g. edge values do not go beyond the average values in neighbouring cells). Fluxes at cell interfaces are calculated using the local Lax-Friedrichs Riemann solver - LLM (Kurganov & Tadmor, 2000). LLM is based on central differences. For example consider a simple 1D wave equation:

$$u_t + F_x(u) = 0 \quad (3.1)$$

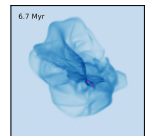
where u represents a state variable and F a flux variable. LLM calculates fluxes at the cell interfaces using the method of lines (semi-discrete) as follows:

$$F_{i-\frac{1}{2}}^* = \frac{1}{2} \left\{ \left[F \left(u_{i-\frac{1}{2}}^R \right) + F \left(u_{i-\frac{1}{2}}^L \right) \right] - a_{i-\frac{1}{2}} \left[u_{i-\frac{1}{2}}^R - u_{i-\frac{1}{2}}^L \right] \right\}, \quad (3.2)$$

$$F_{i+\frac{1}{2}}^* = \frac{1}{2} \left\{ \left[F \left(u_{i+\frac{1}{2}}^R \right) + F \left(u_{i+\frac{1}{2}}^L \right) \right] - a_{i+\frac{1}{2}} \left[u_{i+\frac{1}{2}}^R - u_{i+\frac{1}{2}}^L \right] \right\}. \quad (3.3)$$

‘where a is the local propagation speed. Fig 3.2 shows the locations for the different values of u used in equations 3.2 and 3.3.

Time integration is performed using the total variation diminishing (TVD) second-order Runge-Kutta (RK) scheme (Shu & Osher, 1988). In this scheme two separate Euler steps each of timestep Δt are taken to advance the solution to time $t^n + 2\Delta t$. The solutions at $t^n + \Delta t$ and $t^n + 2\Delta t$ are then averaged to get a second order accurate approximation at $t^n + \Delta t$.



3.2.3 Magnetohydrodynamics

One of the most important parts of an MHD solver is the enforcement of the divergence-free condition $\nabla \cdot B = 0$. `Hydro_rk` used the Dedner formulation of MHD equations (Dedner et al., 2002) as it is capable of coping with extreme variation in physical quantities expected from gravitational collapse, turbulence, and the effects of stellar outputs. The Dedner formulation works by simultaneously damping and transporting the divergence errors to the domain boundary at the maximal admissible speed.

3.3 Gravity

The self-gravity equation, $\nabla^2 \phi = 4\pi G \rho$, is solved in `Enzo` using FFTs. FFTs work by breaking down the discrete Fourier transform into smaller discrete Fourier transforms multiplied by complex roots of unity. The FFTs in `Enzo` divides the transform into two equal sized pieces at each step and is thus best used on power of two sized grids (e.g. 128 and 256).

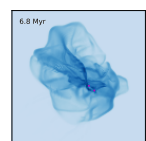
`Enzo` also has the capacity for a static external gravity field which can be used in combination with self gravity or by itself. I do not use an external gravity field in my simulations.

`Enzo` calculates collisionless particle dynamics with the Particle Mesh N-body method (Bertschinger & Gelb, 1991). Particle Mesh N-body method works by approximating the force onto a mesh. Each particle mass becomes a grid density on the mesh and Poisson's equation is solved on the mesh. The force field is then calculated from the potential and interpolated to find the force on each particle.

3.4 Heating and Cooling

There are several techniques for heating and cooling coded into `Enzo` to address many different astrophysical situations. For gas without metals the cooling can be calculated by solving a reaction network of collisional and radiative processes for several species (e.g. H, H+, He, He+, He++, H-, H2+, H2 and e-). Alternatively, if metals are significant the cooling can be done from cooling tables. For cosmological simulations cooling curves for e.g. metallicity 0.3 of Solar can be used. More complex cooling models can be used by creating cooling tables from `Cloudy` (Ferland et al., 1998). `Cloudy` cooling has been implemented into `Enzo` by Britton Smith. `Cloudy` cooling works by creating a cooling table giving cooling rates depending on physical condition, e.g. metallicity, density, and temperature.

In my simulations I used a cloudy cooling table for solar metallicity so the rate of cooling



is only dependent upon density and temperature. This table assumes no incident radiation. Although in my simulations there is incident radiation, the variety of luminosities cannot be covered by a single cooling table so we use the no radiation cooling table for everywhere as a satisfactory approximation (without stimulated emission).

3.5 Turbulence

Supersonic turbulence is generated during simulation initialization following the standard treatment (e.g. Mac Low et al. (1998)). The velocity profile is created by a randomly seeded velocity perturbation field confined to produce a Larson’s law spectrum, $v_k^2 \propto k^{-4}$ (Larson, 1981), where v_k is the velocity perturbations and k is the wavenumber. To ensure the turbulence created is properly resolved I usually constrain k and its x, y, and z components to range between two and one tenth of the number of cells in a box width (e.g. for a simulation box 128^3 , $2 \leq k \leq 13$).

Driven turbulence is possible within Enzo with a fixed force field. However, I allow the turbulence to decay as the filaments form and the GMC evolves into a realistic marginally virial cloud. Once star clusters form I do not want driven turbulence to confuse the subsequent dynamical evolution of the GMCs.

3.6 Radiation

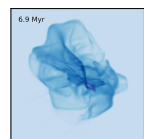
Enzo has both ray tracing (Wise & Abel, 2010) and flux limited diffusion (Reynolds et al., 2009). For our simulations we used ray tracing.

Each light source emits rays across a full range of solid angles and uses ray splitting to ensure a minimum of 5.1 rays per cell. Ray splitting is based on Hierarchical Equal Area iosLatitude Pixelisation - HEALPix (Górski et al., 2005). Figure 3.3 shows the splitting of a sphere with HEALPix for different levels. In Enzo rays are emitted at Healpix level 1 and then split to maintain a minimum of 5.1 rays per cell.

As each ray passes through a cell, the optical depth for that ray is calculated. The radiation is then absorbed according to its optical depth, ionizing and heating the gas in the cell and depositing momentum for radiation pressure accordingly.

Enzo uses adaptive time stepping and a fast approximation of the optically thin radiation field to ensure accurate and efficient calculations of radiative processes.

Recombination is calculated every time step when chemistry and energies are updated.



3.7 Particles and Star Formation

Enzo has many different algorithms for star formation, each with different options and properties. There are two main types I used during investigation of massive star formation within GMCs: individual star formation (§3.7.1) and star cluster formation (§3.7.2).

Particles were originally implemented in Enzo to model dark matter but with an increase in “test problem” usage (non-cosmological simulations), a new class of particles have been created called star particles. There are at present 11 different types of star particles ranging from individual stars to whole clusters to supermassive black holes. Enzo includes several options for feedbacks including protostellar jets and supernovae energy and momentum input.

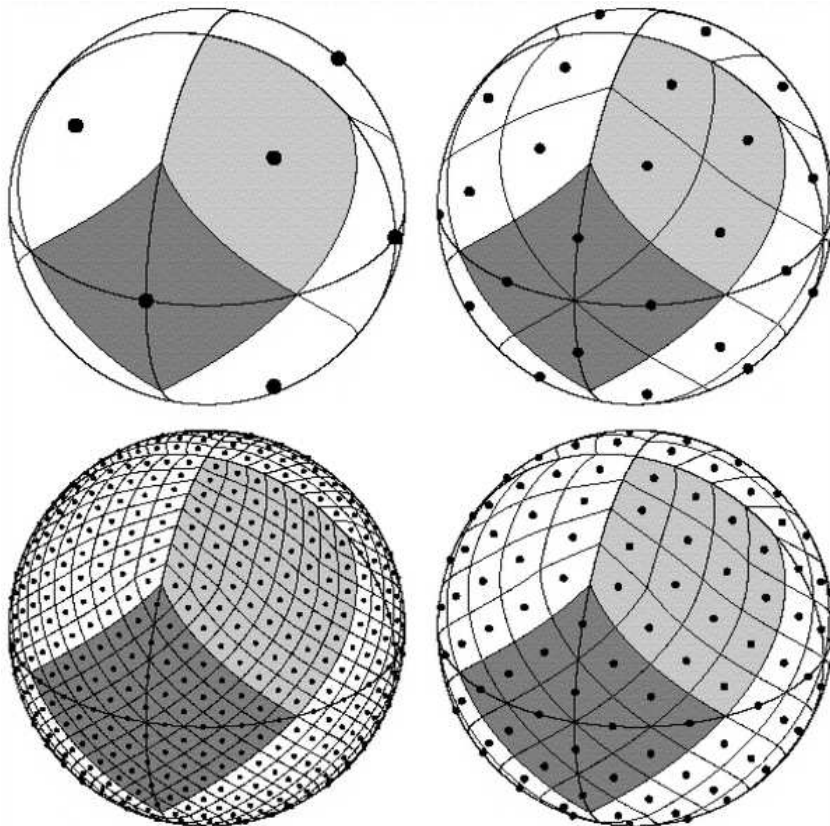
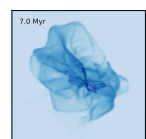


Figure 3.3: Figure 3 from Górski et al. (2005) showing the splitting up of a sphere using HEALPix. Clockwise from top left for HEALPix levels, $l = 1, 2, 4,$ and 8 . Number of pixels for each level is given by $N_{\text{pix}} = 12 \times 4^l$.



3.7.1 Individual Star Formation

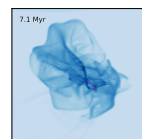
If individual star particle creation is switched on and a cell at the highest refinement breaks the Truelove criterion (Truelove et al., 1997), i.e. the Jeans length is shorter than 4 cell widths, then a star particle is formed. The mass of formation, accretion, merging, and feedback from the star particle are defined within the particle type specific algorithms.

The star particles used for Wang et al. (2010), known as MustRefine particles, are used to model realistic individual star formation. The mass of formation of a MustRefine particle is set so that the remaining gas within the cell has a Jeans length equal to four cell width. The particle then accretes material from its surroundings using the modified Bondi Hoyle algorithm to account for the motion of surrounding gas (Bondi, 1952). MustRefine particles are so named as they force the host cell and surrounding cell to be at the maximum refinement.

3.7.2 Star Cluster Formation

Forming every star individually in a GMC is computationally limiting. Thus, it is advantageous to form whole clusters as single particles instead. Cluster particles are formed when a cell has density above a critical value (`PopIIIOverDensityThreshold`), and a sphere of gas around that cell has a dynamical time above a minimum value (`StarClusterMinDynamicalTime`) and a mass above a given value (`StarClusterMinimumMass / StarClusterFormEfficiency`). `StarClusterMinDynamicalTime` sets a maximum average density for the sphere to enforce the whole core is included when the cluster forms. In my base simulation I used a minimum density of 10^4 times the average density of the simulation, a minimum dynamical time of 2 Myrs (maximum average density of 10^{-21} g cm $^{-3}$, 250 times the box average), and a minimum cluster mass of 1000 M_{\odot} . A cluster particle then forms in the host cell with a mass equal to a given fraction of the sphere's mass; for my simulation 0.5. The remaining gas is evenly distributed throughout the sphere but the velocity structure remains. The cluster particles do not accrete material after formation, remaining at formation mass until the stars die and the cluster starts losing mass in supernovae ejecta.

The star cluster forms from gas that has a dynamical time of the order of a million years yet forms and starts shining within one time step. This single star cluster particle is representing thousands of stars that all form from fragments of that sphere of gas in their own dynamical time. The computational time step when the first star cluster forms is approximately 0.01 Myrs (10,000 years). The star clusters luminosities ramp up over the first two million years after formation. The smoothing of the remaining mass throughout the sphere accounts for any feedbacks that would occur while the cluster is young. Thus, there is a loss in detailed structure



around and within the cluster that may affect the initial evolution of the region. However, this is not expected to alter the evolution of the large scale structure in the GMC substantially. Given our resolution constraints we are not able to quantify the effect this has, though, as with in Chapter 2, we expect this to be a negligible length of time compared to the timescale for GMC disruption.

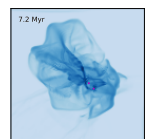
Using this star cluster formation routine means small clusters (without O-type stars) are not created in our simulations. However, the clusters that do form are assumed to have a normal IMF which should account for any small clusters formed. The star formation rate is an upper limit given the rapid formation of the star clusters.

Star cluster outputs

The star cluster particles shine with monochromatic light at 21.62eV at a rate of 10^{47} photons per second per solar mass. The photons are absorbed by the surrounding gas, ionizing and heating it. When radiation pressure is switched on, the momentum from the photons is also deposited into the gas.

For a massive star cluster half of the bolometric luminosity is emitted below 13.6 eV so does not contribute to ionization but will to radiation pressure. Enzo does not yet have opacity algorithms for sub-ionizing radiation. Thus, I created a scale factor that could be set in the parameter file to scale the momentum deposited. For the base simulations this factor is set to 2.0 to approximate the sub-ionizing photons that would be absorbed and deposit momentum but are not simulated in these runs. Dust is expected to be destroyed within the HII region rapidly, which would cause the longer wavelength radiation to be absorbed in a different location than the ionizing radiation. Most of the ionizing photons are absorbed in the bubble shell. Evaporation of globules within the HII region will maintain a small dust fraction within the bubble interior (Everett & Churchwell, 2010). Therefore the doubled momentum from ionizing radiation reionizing combined hydrogen within the bubble interior is accurate. Ionizing radiation from the star clusters ceases at 4 Myrs giving a lower limit on ionizing radiation and especially on radiation pressure from the star clusters.

The cluster particles can also release energy and momentum with supernovae. Supernovae are modelled as a steady mass and energy output from the clusters when they are 4 - 20 Myrs old. The energy per solar mass is set by the parameter StarClusterSNEnergy which is set to zero when SNe are not wanted and 6.8×10^{48} erg M_{\odot}^{-1} when they are (Woosley & Weaver, 1986). The energy and mass are deposited in a sphere around the star cluster set to two cell widths in radius (2.8pc). Over the 16 Myrs of supernovae the mass deposited from the stars is equal to a given fraction of the cluster particle mass, StarMassEjectionFraction = 0.25. Thus



every time step a mass:

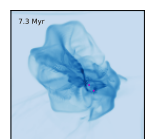
$$\Delta M = \text{StarMassEjectionFraction} \times \text{Cluster Mass} \times \text{time step}/(16 \text{ Myrs}) \quad (3.4)$$

is removed from the cluster and deposited into the sphere around the cluster with thermal energy equal to `StarClusterSNEnergy`. The gas is not given an explicit outward velocity but the thermal energy causes the sphere to expand. As the ejecta has zero net momentum the clusters velocity is increased to conserve momentum.

3.8 Analysis

I used the analysis package `yt` to analyse my simulations and to create the figures included in Chapters 4 and 5. `yt` is a Python analysis and visualization package created by Matthew Turk (Turk, 2008). It was designed specifically to handle AMR data, reading in the entire hierarchy and providing easy access to physically relevant quantities for analysis. There is now quite a large development team working on `yt` making it usable on many codes and analysing simulations in many different ways.

More information and downloading instructions can be found on the `yt` website:
<http://yt.spacepope.org/>.



Chapter 4

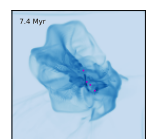
Three Dimensional Simulations

This chapter describes and gives results for the physical investigations with 3D simulations in this thesis. All of the simulations are adaptations of a base simulation. Throughout the next two chapters, simulations are named to identify the difference between them. In all sections the base simulation is included and also named in the same format for ease of comparison.

The structure of this chapter is as follows; the base simulation is described in §4.1 and an investigation of the outputs from the stars in §4.2; an investigation into the surrounding medium of the cloud is detailed in §4.3 and the simulation with a magnetic field in §4.4; finally, simulations of a more massive cloud are in §4.5.

Physical Quantity	Value
Simulation Box Length	179.2 pc
Grid Structure	128^3 (no AMR)
Cloud Radius	44.8 pc
Cloud Mass	$220,237 M_{\odot}$
Total Mass	$360,422 M_{\odot}$
Cloud Dynamical Time	6.7 Myrs
Cloud Half Mass Dynamical Time	4.8 Myrs
Turbulence Mach Number	$13 = 3.4 \text{ km/s}$

Table 4.1: Physical Details for the initial setup of the base simulation.



4.1 Base Simulation

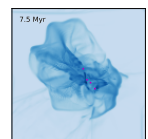
Table 4.1 lists the physical quantities of the base simulation initial setup. The simulation box is a cube, 179.2pc on each side, with 128^3 unigrid resolution. It has periodic boundary conditions in hydrodynamics and gravity. At the centre of the simulation cube is a spherical cloud of radius 44.8 pc. This cloud has a mass of $220,237 M_{\odot}$ and a cored isothermal sphere density profile:

$$\rho(r) = \frac{\rho_{cl}}{1 + (4r/r_{cl})^2}, \quad (4.1)$$

where r is the radius from the centre of the box and cloud, $\rho_{cl} = 3.16 \times 10^{-22} \text{ g/cm}^3$ is the central cloud density, and r_{cl} is the cloud radius. The cloud has a dynamical time, $t_{dyn} = \sqrt{R^3/2GM} = 6.7 \text{ Myrs}$, where R is the cloud radius and M is the cloud mass. The half mass radius of the cloud is $0.633r_{cl}$ and has $t_{dyn} = 4.8 \text{ Myrs}$. Exterior to the cloud the material is homogeneous with a density of $\rho = 1.76 \times 10^{-24} \text{ g cm}^{-3}$ ($n = 1.05 \text{ cm}^{-3}$). This gives a total mass in the simulation box of $360,422 M_{\odot}$. The cloud is approximately virial in turbulence and gravity, initializing with Mach 13 Larson’s Law turbulence giving $v_T = 3.4 \text{ km/s}$ (see §3.5). The surrounding material is stationary. The gas in the cloud has a uniform temperature of 10 K and the external gas has an initial temperature of 1000 K, to approximately pressure balance at the cloud edge. The exterior gas cools with a cooling time longer than the dynamical time of the cloud so pressure balance is only temporary. However, the initial pressure balance is enough to constrain the initially unbound outer regions of the cloud.

Figure 4.1 (left) shows the projected density and temperature at the start of the simulation. The spherical symmetry is easily seen in the projected images with density increasing towards the centre of the cloud. The temperature for the cloud is 10K throughout, though looks like it is slightly higher at the edges since there is more 1000K external gas included in the projection. Figure 4.2 (left) shows projected velocity arrows on the projected density for the initial Mach 13 turbulence. The length of the arrow shows magnitude and the direction direction. The turbulent velocity is constant throughout the cloud leading to a slight bulk motion as the density is higher in the centre. There are regions of the cloud that will initially collapse and others that will initially expand given their velocity structure. The regions where velocity is converging will form the first filaments. The dots in the external material show its zero velocity.

When the simulation begins the turbulence rapidly breaks the spherical symmetry of the cloud, creating filaments and the complex structure observed in GMCs (Figs. 1.4 and 1.5). The gas shocks, heats, and cools as described in §3.4. Figure 4.1 (right) shows the projected density and temperature approximately one dynamical time after the simulation started just before star formation begins. Note the larger overall size of the cloud as the outer cloud regions



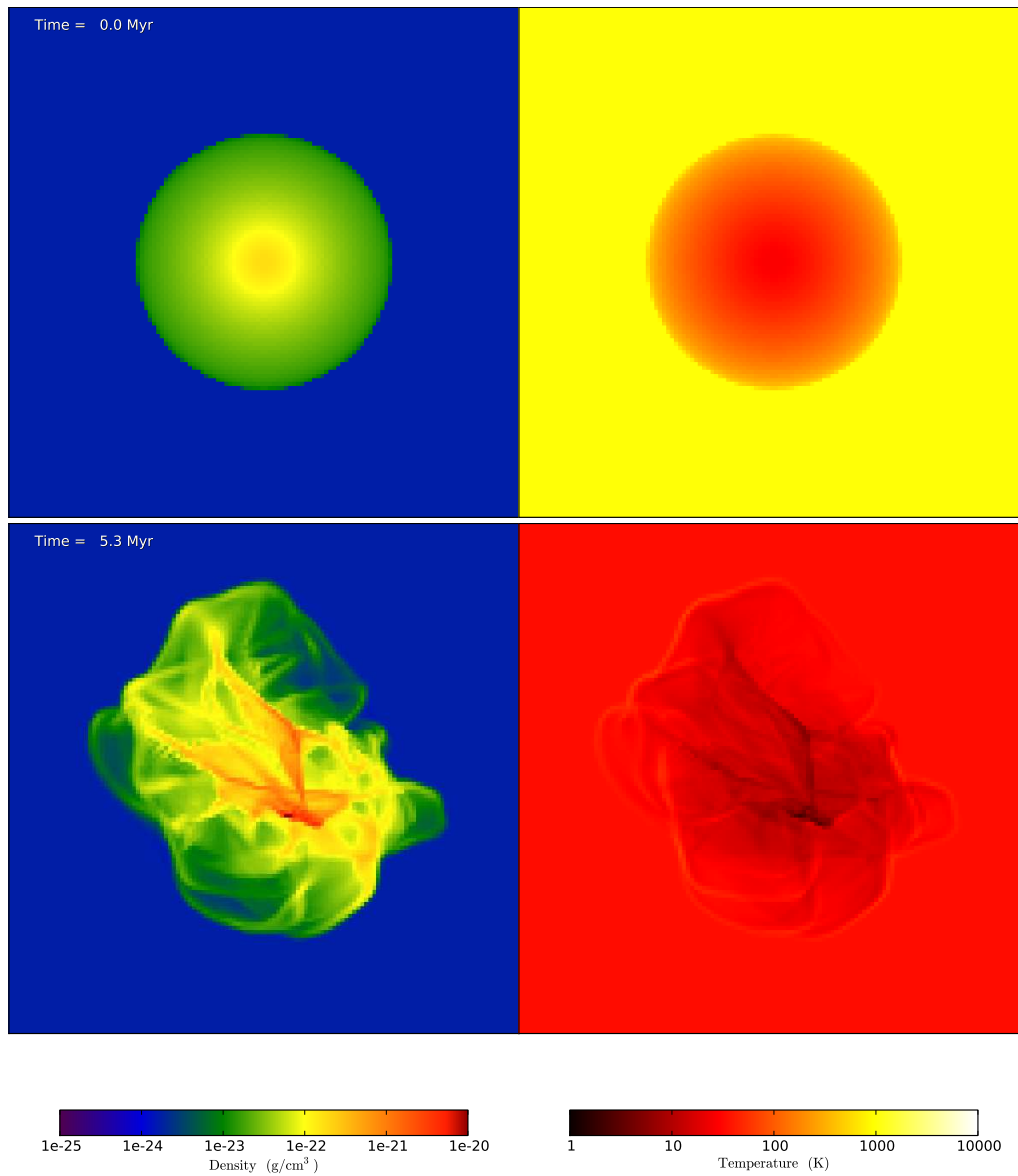
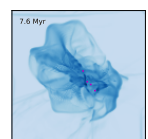


Figure 4.1: *Top:* the cored isothermal sphere embedded in a homogeneous medium at the simulation start. *Bottom:* Within one dynamical time after the simulation start a complex turbulent structure can be seen with many filaments and non-spherical features. *Left:* The projected density (density weighted mean density) along the x axis. *Right:* The temperature projected along the x axis. Note the external gas has cooled significantly over the 5 Myrs between images as there is no source of heating yet.



were unbound and the higher densities near the centre where the turbulence and self gravity have pulled the material in. Figure 4.2 (right) shows velocity arrows on the projected density just before star formation. There are some regions of convergence, especially towards the main filament. Also note how the gravity has started to pull the close external material in towards the cloud and by nature of periodic boundary conditions the material at the box edges feels no gravitational pull.

Figure 4.3 shows the column density through the cloud at the simulation set up and just before star formation.

4.1.1 Base Simulation Results

This thesis contain frames showing density projections with a constant colour bar for the base simulation in steps of 0.1 Myrs per page starting from initialization. For the printed version: frames are on the bottom right of odd pages in this thesis starting on page iii (Abstract). Holding the thesis in your left hand use your right hand to flip the pages rapidly from the front to back to see the animation. For the online version: frames are on the bottom right of every page starting on page ii (Abstract). Click down through pages to see the animation.

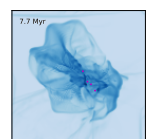
The first star cluster forms at 5.38 Myrs from 5.6 pc sphere of mass $8176 M_{\odot}$. Immediately before the cluster forms the sphere has gravitational potential energy of 1.9×10^{14} ergs and turbulent kinetic energy 1.1×10^{14} ergs. Therefore, the sphere is bound. The sphere has a mass weighted mean inward radial velocity of 1.37 km/s.

Once a star cluster forms, radiation is emitted from the particle. The radiation ionizes and heats the surrounding medium and deposits momentum from radiation pressure; see §3.7.2 for more details. In the base simulation ionization and radiation pressure are included but supernovae are not.

Figure 4.4 shows the total mass in stars over the course of the simulation. Each step up in mass is a new star cluster forming and the decrease in mass after 9.4 Myrs is due to the evolution of the star clusters as the more massive stars die. At 12 Myrs the simulation has the maximum mass in star clusters, equal to 12.8% of the original cloud gas mass (8% of the original total gas mass).

Figures 4.5 - 4.10 show the projected density, temperature, HII ionization fraction, and radiation force absorbed by the gas at different times throughout the base simulation.

During the first two million years after the first star cluster is made (Figs 4.5 and 4.6) a leaky bubble forms with the HII region easily blowing out through the lower density regions. The gas and radiation pressure blow the denser material steadily outward, also shown in Fig. 4.12.



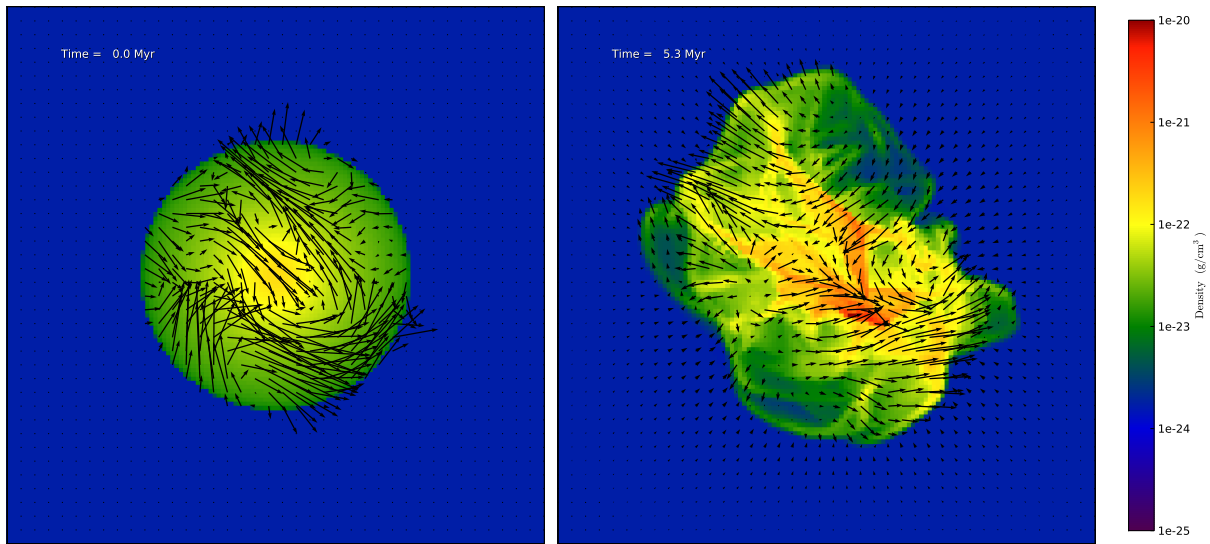


Figure 4.2: *Left*: Projected velocity vectors on a density projection to show the initial turbulence at the simulation start. *Right*: Velocity vectors on a density projection one dynamical time into simulation showing the continued turbulence prior to star formation. Gravity is pulling in the surrounding material. Turbulence creates the filaments that can then collapse under their own self gravity. Arrow length is proportional to velocity magnitude.

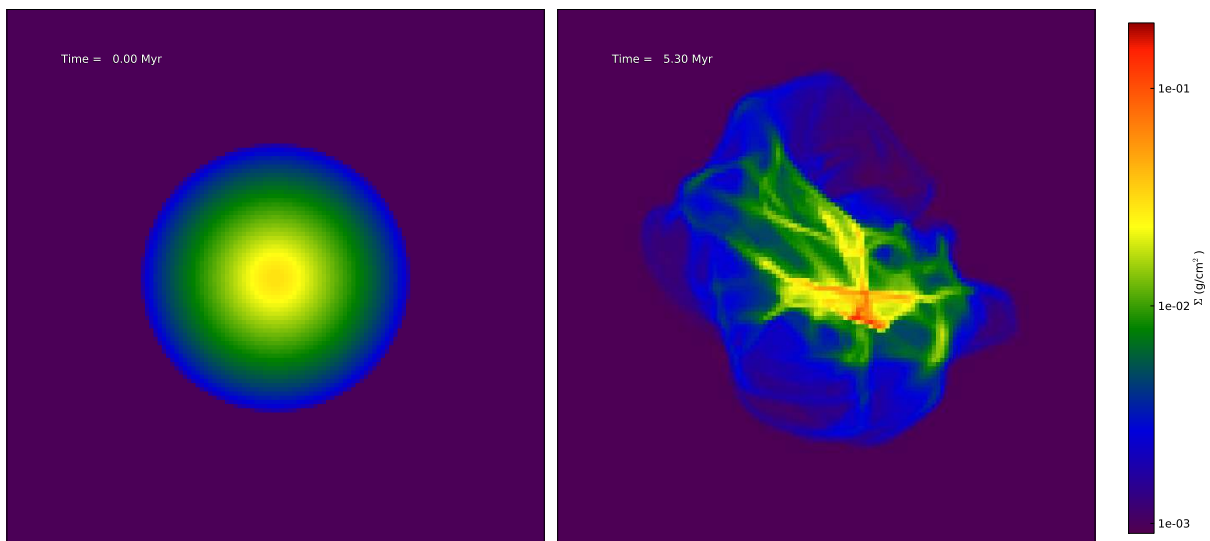
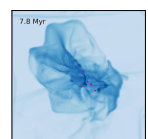


Figure 4.3: The column density through the x axis of the simulation *left*: at simulation set up and *right*: just before star formation begins.



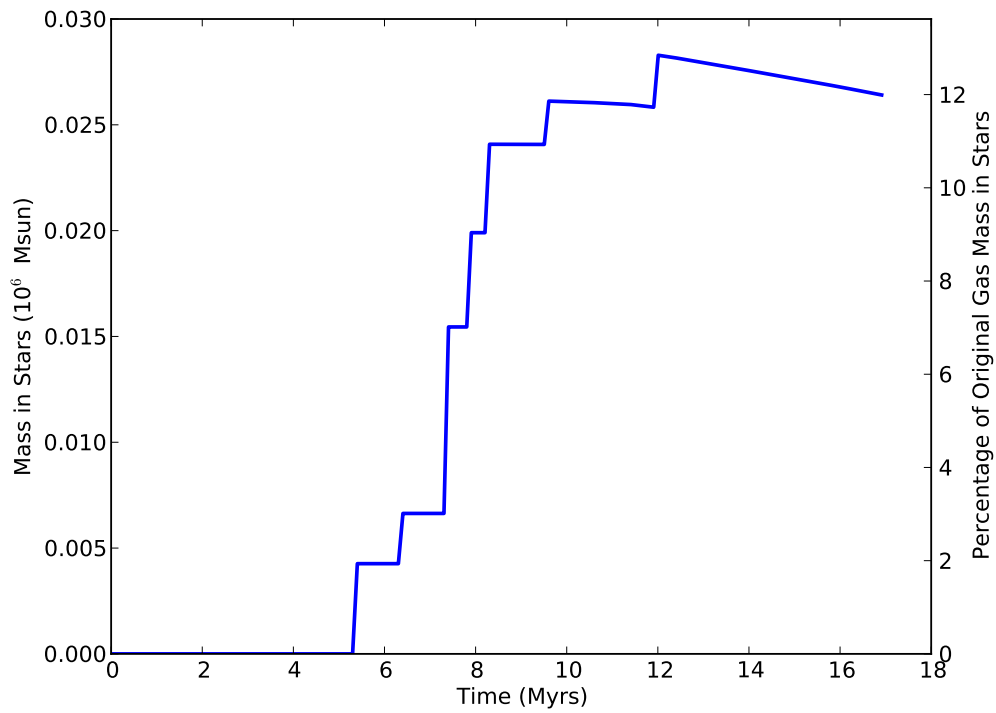
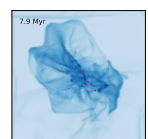


Figure 4.4: The total mass in star cluster particles for the base simulation. The original gas mass in the simulation was $360,422 M_{\odot}$. The star formation occurs in a rapid burst and is then quenched. The maximum mass, at 12 Myrs, corresponds to 12.8% of the original cloud gas mass. The decline in mass after 9.4 Myrs is due to the evolution of the star clusters.



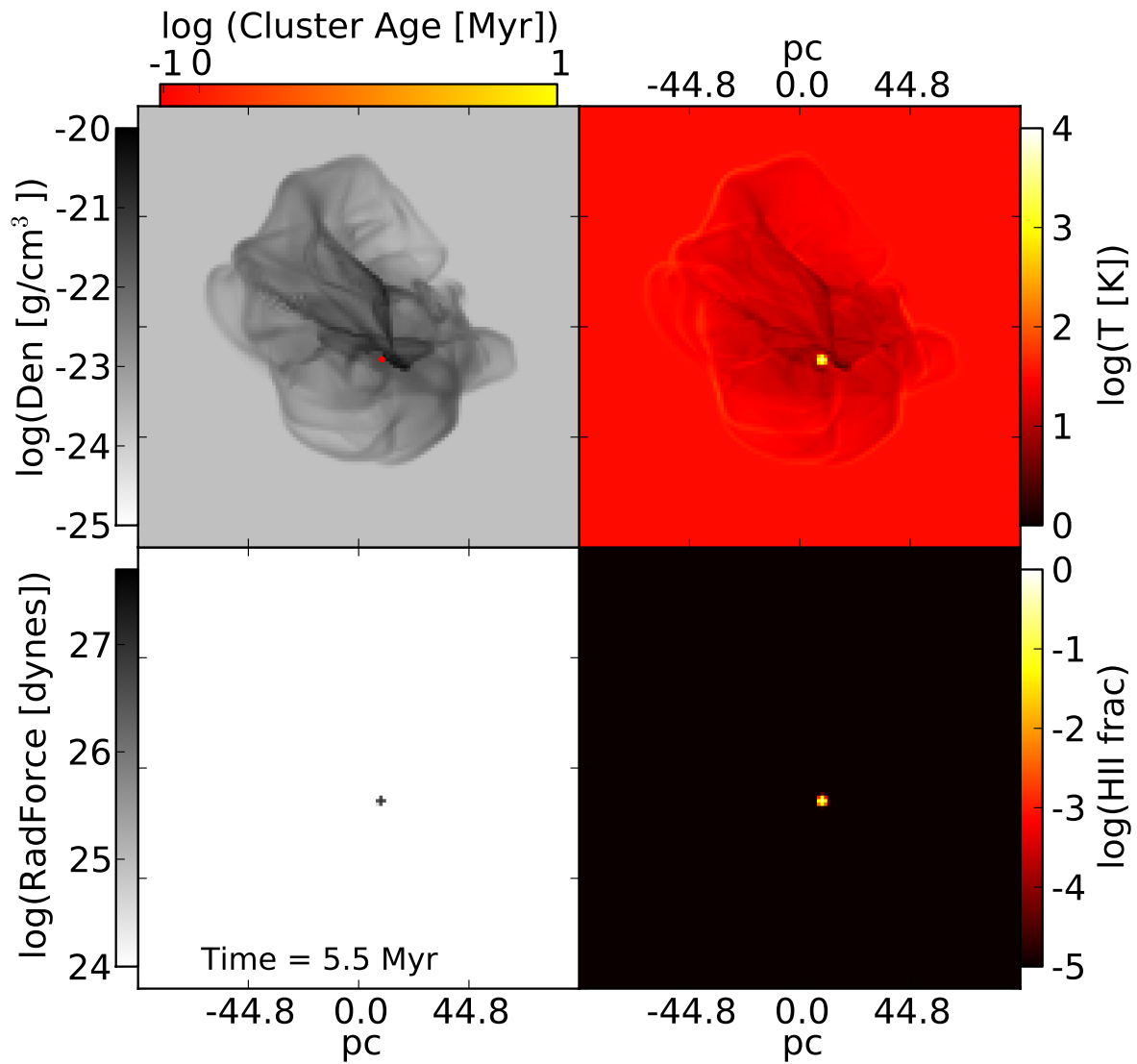
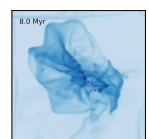


Figure 4.5: Density, temperature, radiation force (momentum deposited), and HII fraction for the base simulation at 5.5 Myrs (0.1 Myrs after first cluster formed). Star cluster particles are shown as filled circles on the density projection. Star cluster circle size is relative to mass and colour indicates the age of the cluster at this time. Only the material immediately around the star cluster is ionized, heated, and has radiation momentum absorbed. The sum of radiation force absorbed by the gas in this frame is 1.83×10^{28} dynes.



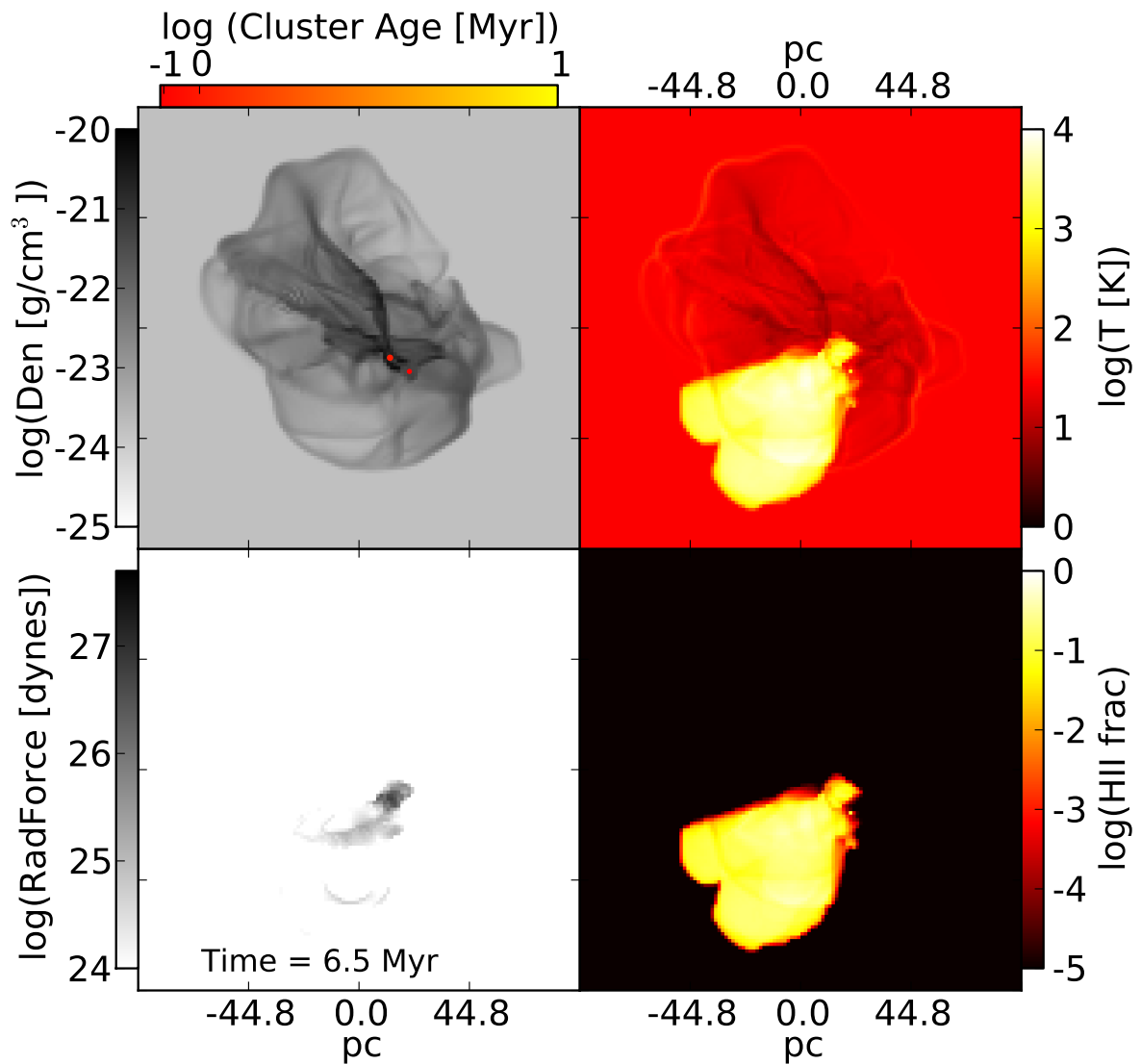
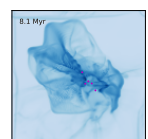


Figure 4.6: Density, temperature, radiation force (momentum deposited), and HII fraction for the base simulation at 6.5 Myrs (1.1 Myrs after first cluster formed). Star cluster particles are shown as filled circles on the density projection. Star cluster circle size is relative to mass and colour indicates the age of the cluster at this time. After 1 Myrs of shining, the radiation pressure and ionized gas pressure have expanded the HII region and it is starting to leak out of the side with the least resistance. The sum of radiation force absorbed by the gas in this frame is 4.05×10^{29} dynes.



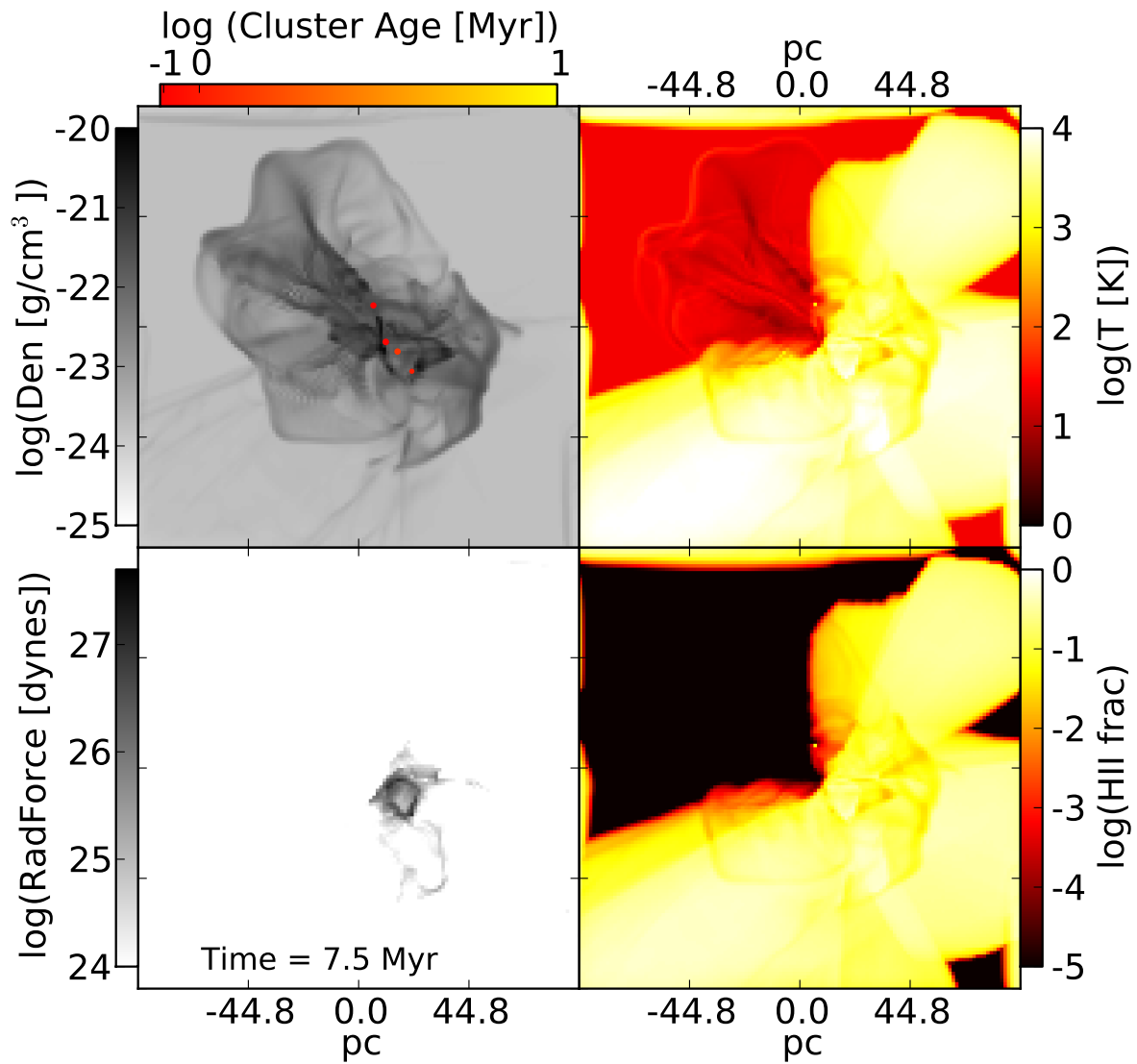
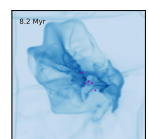


Figure 4.7: Density, temperature, radiation force (momentum deposited), and HII fraction for the base simulation at 7.5 Myrs (2.1 Myrs after first cluster formed). Star cluster particles are shown as filled circles on the density projection. Star cluster circle size is relative to mass and colour indicates the age of the cluster at this time. Note the bubble shell seen in density and radiation force projections. The HII region has now blown out on many sides. The sum of radiation force absorbed by the gas in this frame is 7.97×10^{29} dynes.



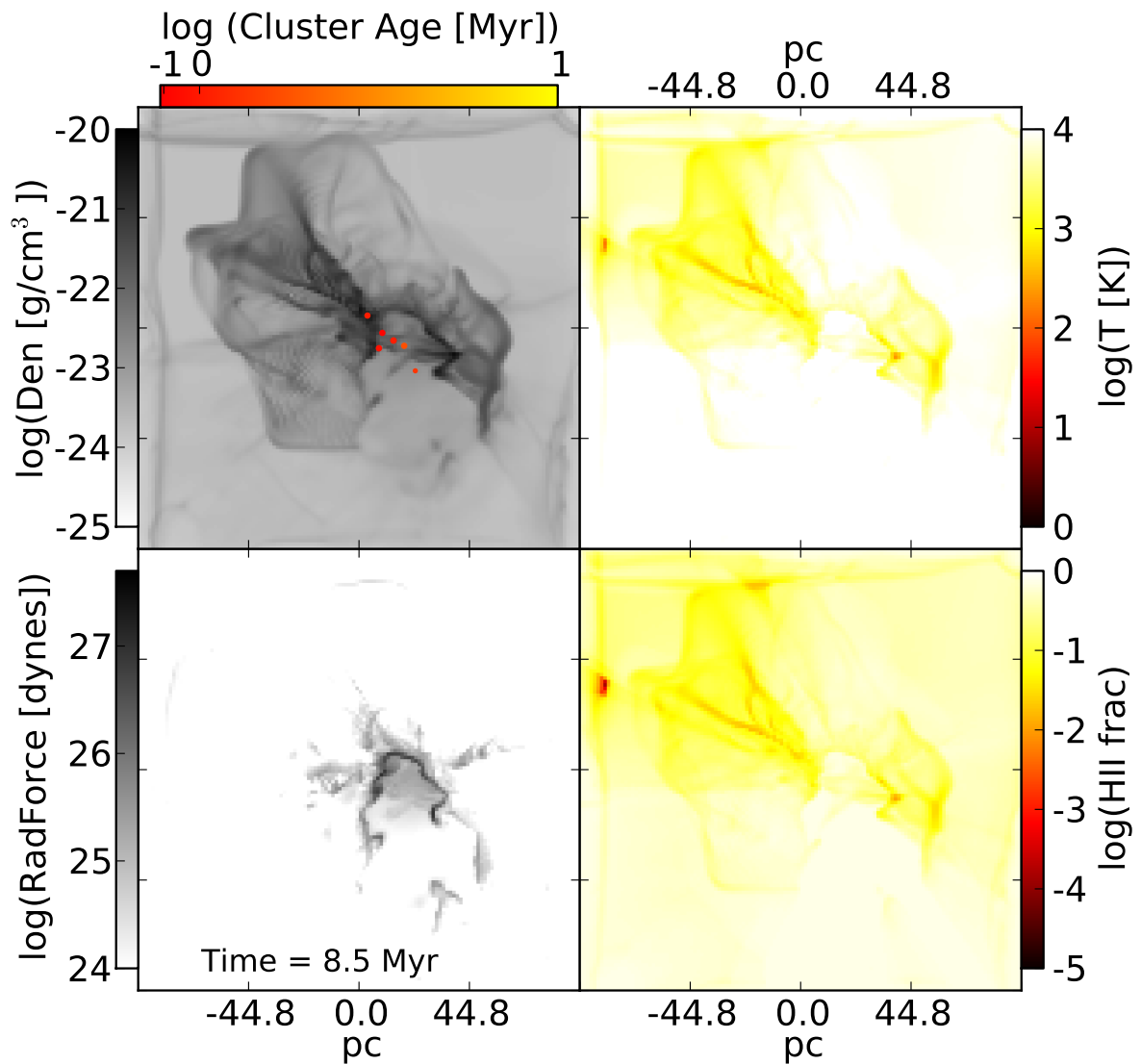
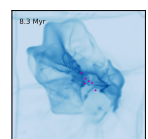


Figure 4.8: Density, temperature, radiation force (momentum deposited), and HII fraction for the base simulation at 8.5 Myrs (3.1 Myrs after first cluster formed). Star cluster particles are shown as filled circles on the density projection. Star cluster circle size is relative to mass and colour indicates the age of the cluster at this time. The remaining bubble shell is clearly seen in radiation force and density. Almost the entire simulation box is ionized and heated by the radiation from the stars. The sum of radiation force absorbed by the gas in this frame is 1.04×10^{30} dynes.



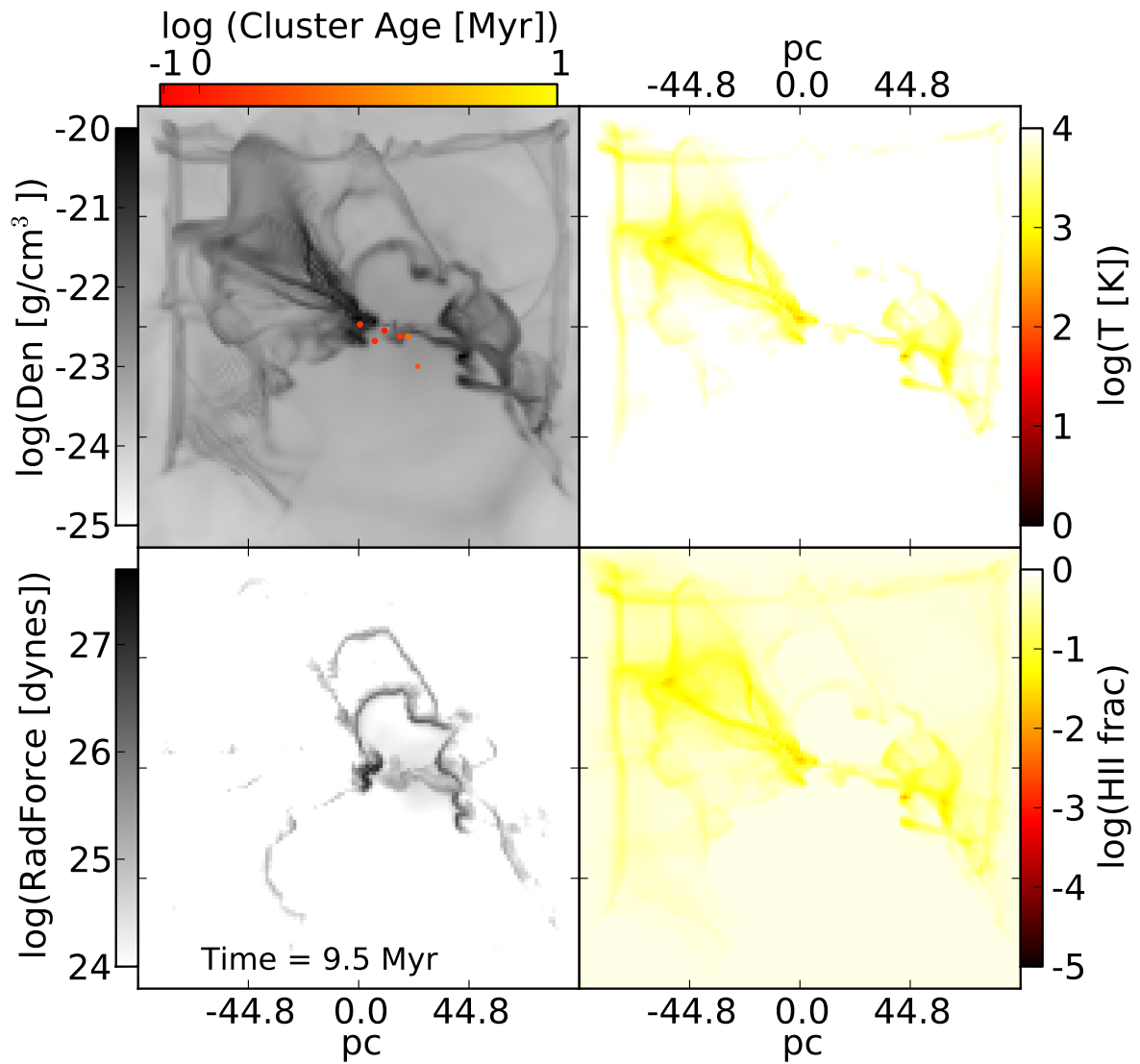
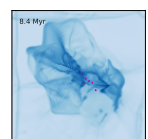


Figure 4.9: Density, temperature, radiation force (momentum deposited), and HII fraction for the base simulation at 9.5 Myrs (4.1 Myrs after first cluster formed). Star cluster particles are shown as filled circles on the density projection. Star cluster circle size is relative to mass and colour indicates the age of the cluster at this time. The remaining shell is still absorbing significant radiation force and is being pushed away from the stars. The sum of radiation force absorbed by the gas in this frame is 9.42×10^{29} dynes.



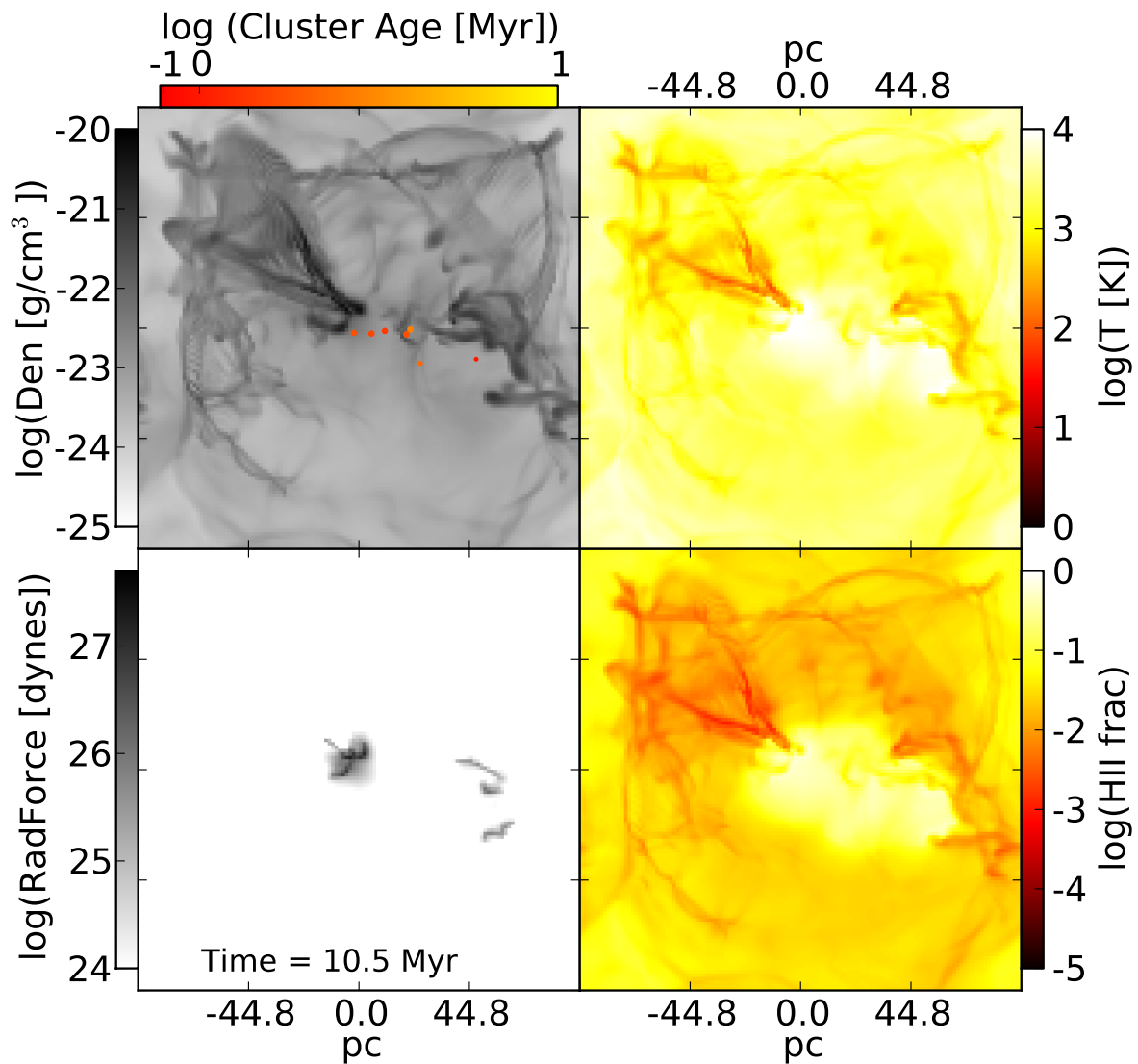
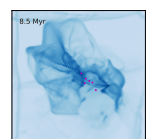


Figure 4.10: Density, temperature, radiation force (momentum deposited), and HII fraction for the base simulation at 10.5 Myrs (5.1 Myrs after first cluster formed). Star cluster particles are shown as filled circles on the density projection. Star cluster circle size is relative to mass and colour indicates the age of the cluster at this time. Only a few dense regions of gas remain to absorb any substantial radiation force. Note the significant drop in HII fraction as massive stars die and the ionized gas recombines. The sum of radiation force absorbed by the gas in this frame is 2.38×10^{29} dynes.



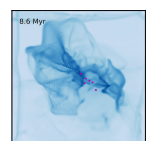
As an example of the directionality of the radiation force, Fig. 4.11 shows the projected radiation force and arrows showing the direction and magnitude of the force. The gas is all being pushed away from the central star clusters.

By two million years after the first star cluster forms (Fig. 4.7) there is a noticeable bubble shell forming and expanding outwards from the first star cluster. Within a few hundred thousand years the shell is significantly non-spherical and then completely blows out on one side (Fig. 4.8). The remaining shell continues to expand, sweeping out quickly where the density is lower and more slowly where denser gas remains.

The radiation force magnitude projections show the radiation momentum being deposited mostly in what remains of a bubble shell over the bubble evolution. By 10.5 Myrs (5.1 Myrs after the first cluster particle formed, Fig. 4.10) most of the ionizing radiation from the first star clusters has disappeared as the most massive stars die. By 12.5 Myrs the region is completely blown apart by the feedback from the star clusters and there is no further star cluster formation in the GMC.

The structure of the mass in the simulation box over time is shown in Fig. 4.12. This plots the mass enclosed at different radii with time. The drops in total mass (blue line) show conversion of gas into star cluster particles each time one is made. Prior to the first star cluster forming the mass within $2 R_{cl}$ slightly increases, within $1.5 R_{cl}$ remains constant, within $1 R_{cl}$ decreases, and within $0.5 R_{cl}$ increases. This shows the turbulence stirring up the gas and self gravity pulling mass together. As the turbulent velocity is constant throughout the cloud the outer regions of the cloud are unbound but the inner regions collapse. After star cluster formation the bubble can be seen to be forming with the decrease in mass within $0.5 R_{cl}$, then within $1 R_{cl}$, then within $1.5 R_{cl}$, and ultimately within $2 R_{cl}$ as well. By 12 Myrs there is almost no mass left within $0.5 R_{cl}$ and by 15 Myrs almost no mass left within the original cloud location.

Figure 4.13 shows the emission and absorption of momentum from the stellar radiation in the base simulation against time. When the radiation is absorbed close to the source, the spherical nature of the momentum deposition is poorly resolved within the grid. As the bubble expands and the radiation spreads further out it is better resolved and the absorption rate increases. When there is more than once source, a fraction of the emitted momentum will cancel out in the gas in between the sources. After 7 Myrs the bubble shell is significantly leaky and an increasing fraction of the radiation escapes the simulation box unabsorbed. At 12 Myrs the last star cluster forms in the remaining dense region, temporarily boosting the absorption rate while it blows its own bubble. The ratio of absorbed to emitted radiation is shown in Fig. 4.14. The efficiency rapidly increases to close to one as the radiation force is resolved and



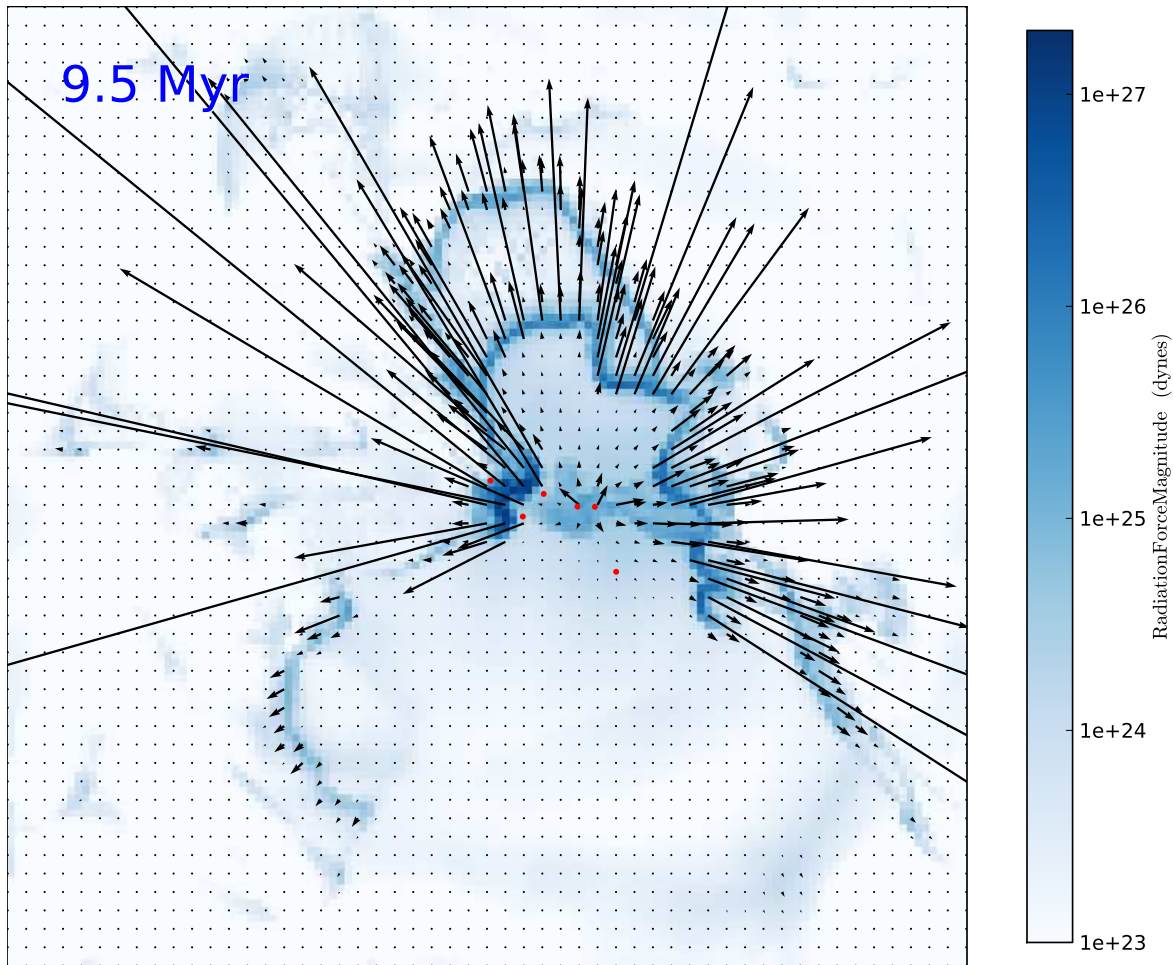
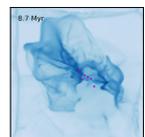


Figure 4.11: Projected radiation force (mass in cell multiplied by acceleration due to absorbed momentum from radiation) with arrows showing direction at 9.5 Myrs for the base simulation.



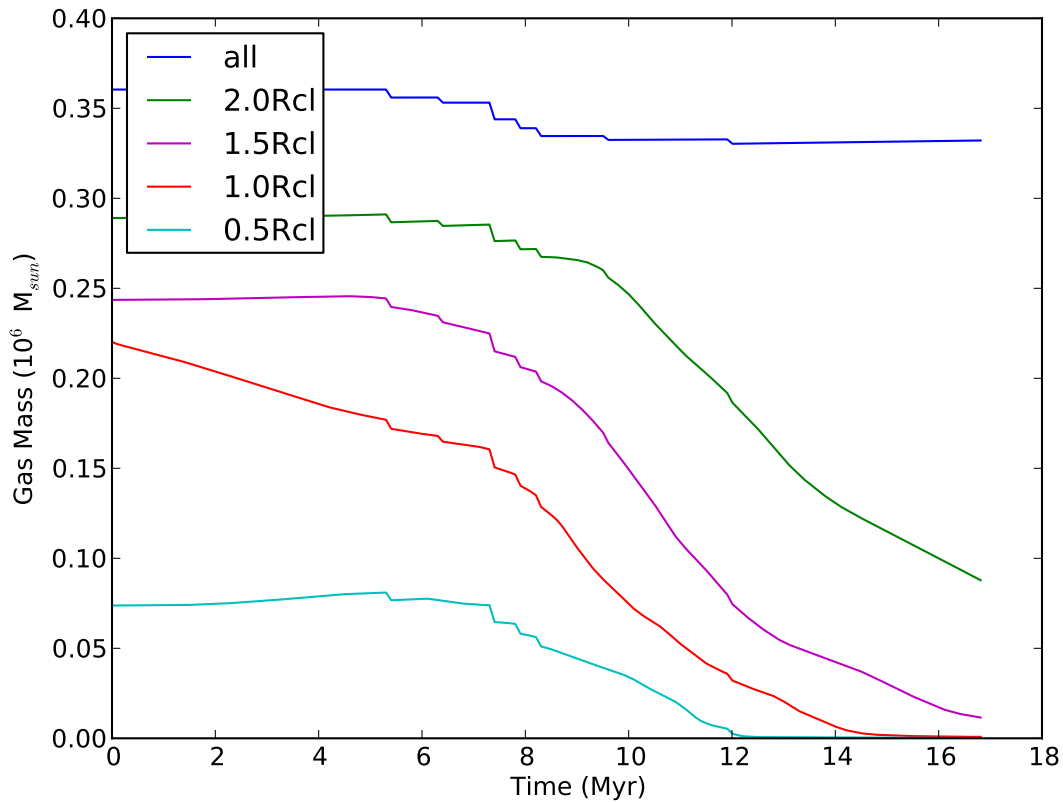
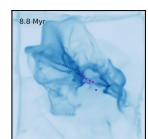


Figure 4.12: The mass structure for the base simulation. The lines show the cumulative mass for 0.5, 1.0, 1.5, and 2.0 times the original cloud radius (44.8pc) and for the whole simulation box. The drops in total mass (blue line) show conversion of gas mass into star cluster particles. Prior to the first star cluster forming the mass within $2 R_{cl}$ slightly increases, within $1 R_{cl}$ decreases, and within $0.5 R_{cl}$ increases. This shows the turbulence stirring up the gas and self gravity pulling mass together. After star cluster formation the bubble can be seen to be forming with the decrease in mass within $0.5 R_{cl}$, then within $1 R_{cl}$ and ultimately within $2 R_{cl}$ as well.



then drops as sources cancel out and radiation leaks out of the simulation box.

The average turbulent Mach number within the cloud and whole simulation box is plotted in Fig. 4.15. Both the mass weighted mean and a non-weighted mean Mach number are plotted. The average Mach number initially increases by all measures as would be expected by the cloud starting to collapse and the gas cooling. The mass weighted Mach number then starts to decrease as the shocks are dissipating the turbulent energy in the high density regions. However, the low density regions are still being driven by the gravitational collapse and dominate the volume so the non weighted mean continues to increase. After 5.3 Myrs star clusters start to

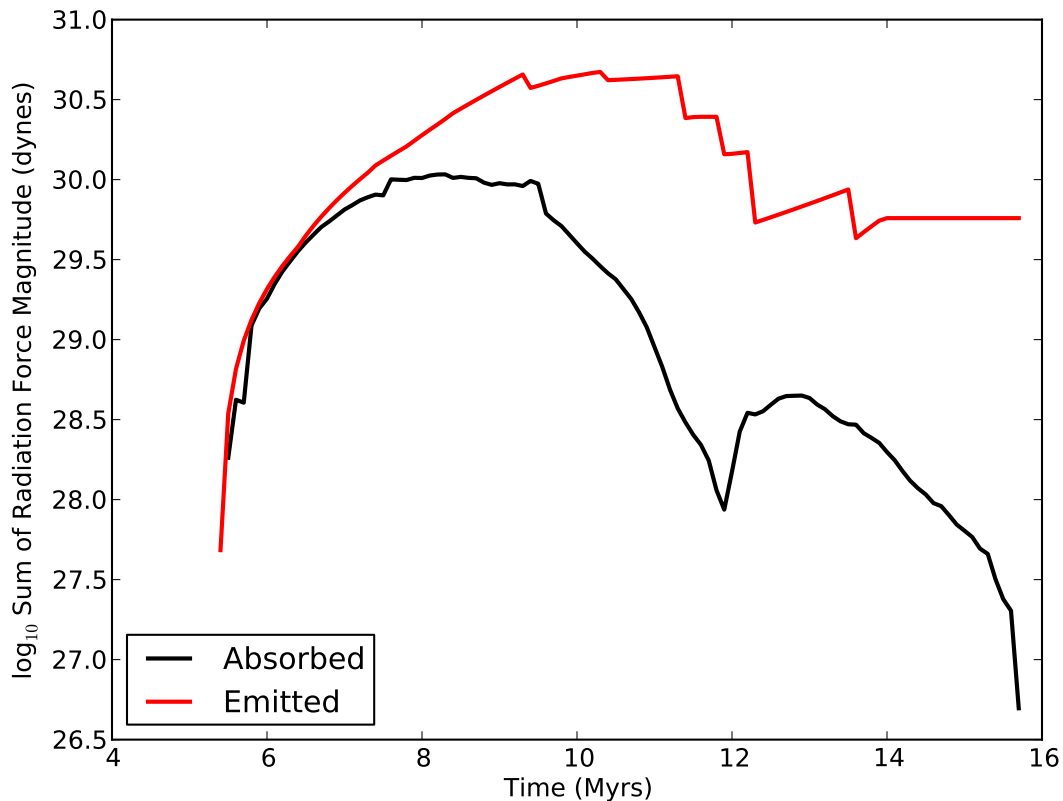
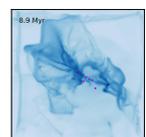


Figure 4.13: Graph showing the rate of momentum emitted by the stars in radiation and the rate of momentum absorbed by the gas in the simulation cube from the stellar radiation. The emitted radiation ramps up for the first two million years of each cluster's life. The decrease in absorption after 9 Myrs is due to the bubble breaking through the shell over a substantial fraction and thus, a significant fraction of radiation escaping unabsorbed. At 12 Myrs the last star cluster forms in the remaining dense region, temporarily boosting the absorption rate while it blows its own bubble.



be made from the high density material. The cluster formation routine removes material from the highest density regions and conserves momentum but averages over several cells in doing so, effectively dissipating the turbulence. After 8 Myrs a significant bubble is forming and the shell is pushed away from the stars. The energy and momentum from the stars is absorbed by the gas and increases the Mach number again. The kinetic energy against time is plotted in Fig. 4.16. Kinetic energy more clearly shows the dissipation of energy in the turbulence initially and then the driving by the star clusters. The transfer of kinetic energy from cloud to exterior material is seen early on by the faster decline of kinetic energy within the cloud location than the whole box.

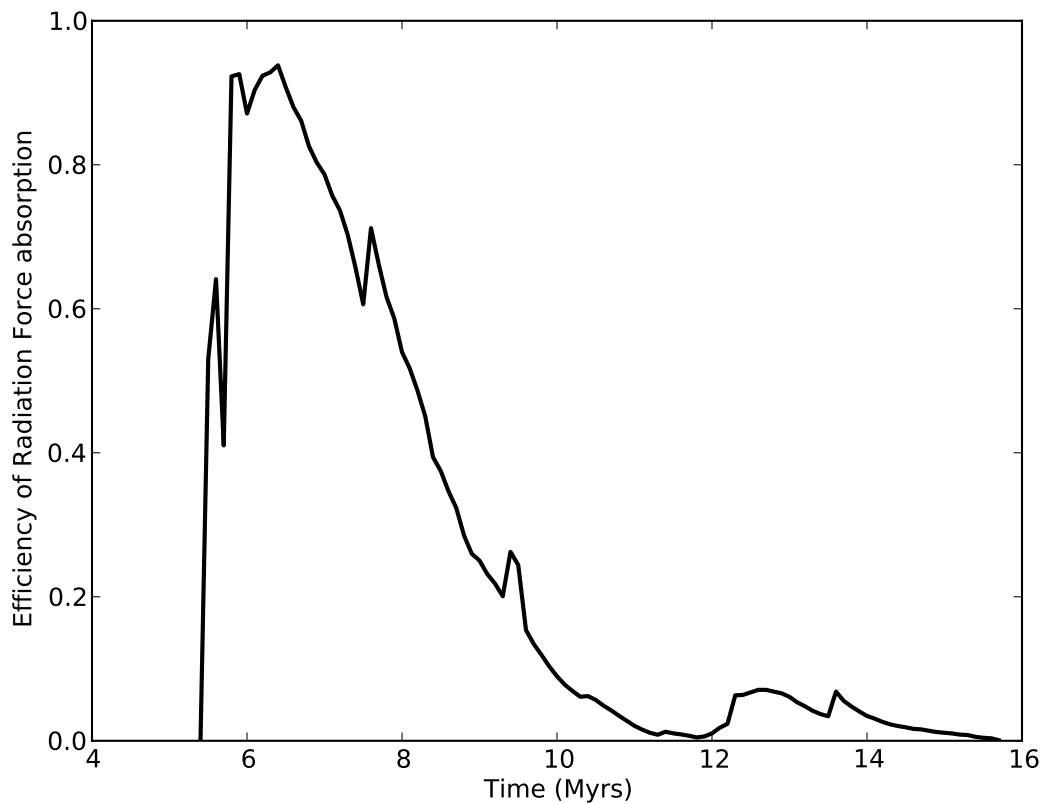
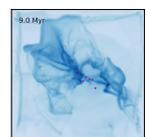


Figure 4.14: A graph showing the ratio of absorbed to emitted radiation force for the base simulation. The initial increase is largely due to numerical effects as discussed in Fig. 4.13. The decrease after 7 MYrs is due to escaping radiation leaking out of the bubble. Note the linear rather than logarithmic y axis in this graph.



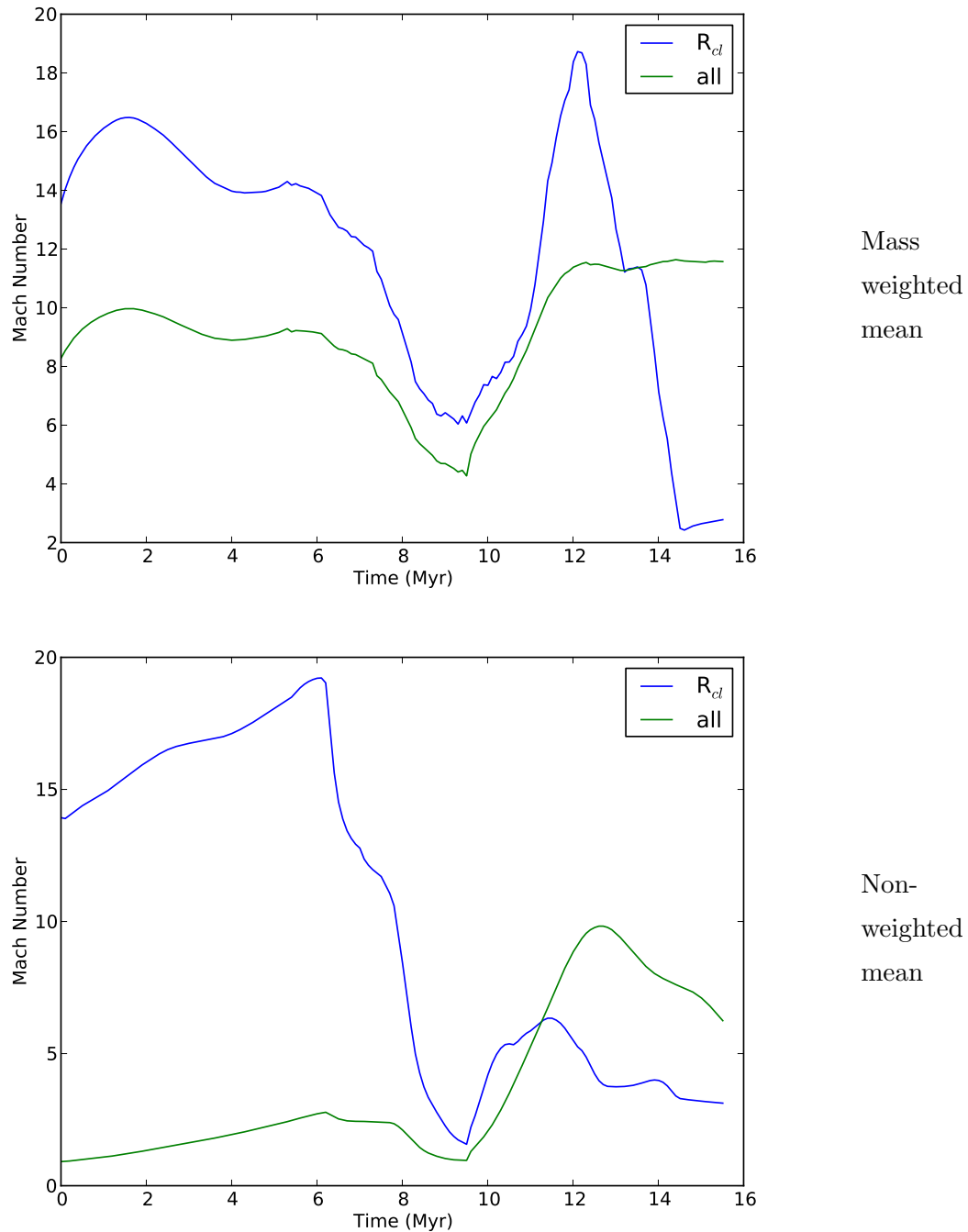
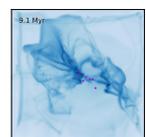


Figure 4.15: The mean Mach number (velocity magnitude / sound speed) for the gas in the base simulation. The blue lines are for the gas within the original cloud location and the green lines are for the whole simulation box. *Top*: the mass weighted means and *bottom* the non-weighted means. Throughout the simulation the gas remains supersonically turbulent with the original turbulence decaying and the gravitational collapse and outputs from stars pumping energy into the motion of the gas.



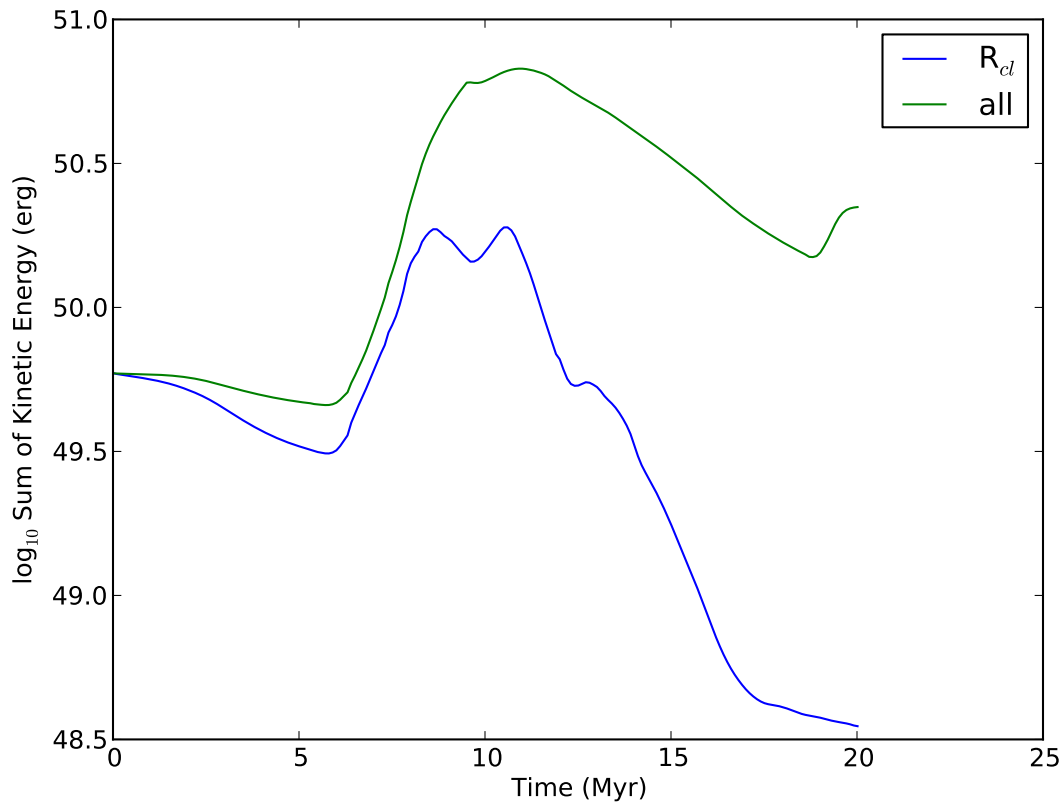
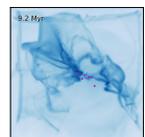


Figure 4.16: The sum of kinetic energy within original cloud location and entire simulation box for the base simulation. As the turbulence decays the kinetic energy reduces until star cluster formation begins and the outputs start driving the kinetic energy back up again.



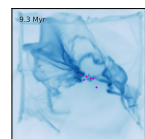
By 14 Myrs there has been no further star cluster formation and the cloud is completely disrupted. To examine the distribution of the star clusters I calculated the centre of mass for the clusters and each cluster's distance from that centre of mass at 14 Myrs. The centre of mass is at (0.50,0.57,0.52) in code units, 13 pc from the centre of the simulation box. This displacement is due to the initial velocity field giving a small bulk motion. The distance from centre of mass, creation time, and colour used in the figures for the clusters at 14 Myrs are given in Table 4.2. Figure 4.17 shows a log-log plot of the distance from centre of mass and mass for each of the star clusters (coloured stars). Also plotted is the cumulative mass in clusters moving in to the centre of mass and the half mass, quarter mass, and three quarter mass lines. The half mass radius of the clusters from the centre of mass is 15.6 pc, quarter mass radius is 29.9 pc, and three-quarter mass radius is 12.9 pc. For distances of greater than 10 pc the cumulate mass line shows an approximate -1 gradient and for less than 10 pc a flatter gradient. This implies a cluster density that follows a very similar cored isothermal structure as used for the gas in the cloud initialization.

The positions of the clusters projected along all three axes are shown in Fig. 4.18 with the same colours for each cluster as Fig. 4.17. The three dimensional location of the clusters suggests the clusters form in a few distinct groups with the widest spread in the y axis position. The two clusters furthest out from the centre of mass, at radii 0.21 (black star) and 0.33 (pink star), are the two oldest stars, forming at 11.9 Myrs and 9.5 Myrs respectively.

Fig. 4.19 shows the approximate shell position against time for the base simulation. The shell radius was estimated as the maximum in the non-weighted radially averaged density around

Distance from CoM (code units, pc)	Creation time (Myrs)	Cluster mass (Msun)	Symbol colour in figures
0.0361, 6.47	8.264	4067	blue
0.0616, 11.0	5.383	3966	green
0.0764, 13.7	7.331	4611	cyan
0.0836, 15.0	7.812	4303	red
0.0965, 17.3	6.395	2243	yellow
0.1397, 25.0	7.364	3843	white
0.2142, 38.4	11.946	2486	black
0.3318, 59.5	9.527	2038	pink

Table 4.2: The distance from centre of mass, creation time and colour used in the figures for all of the star clusters at 14 Myrs for the base simulation.



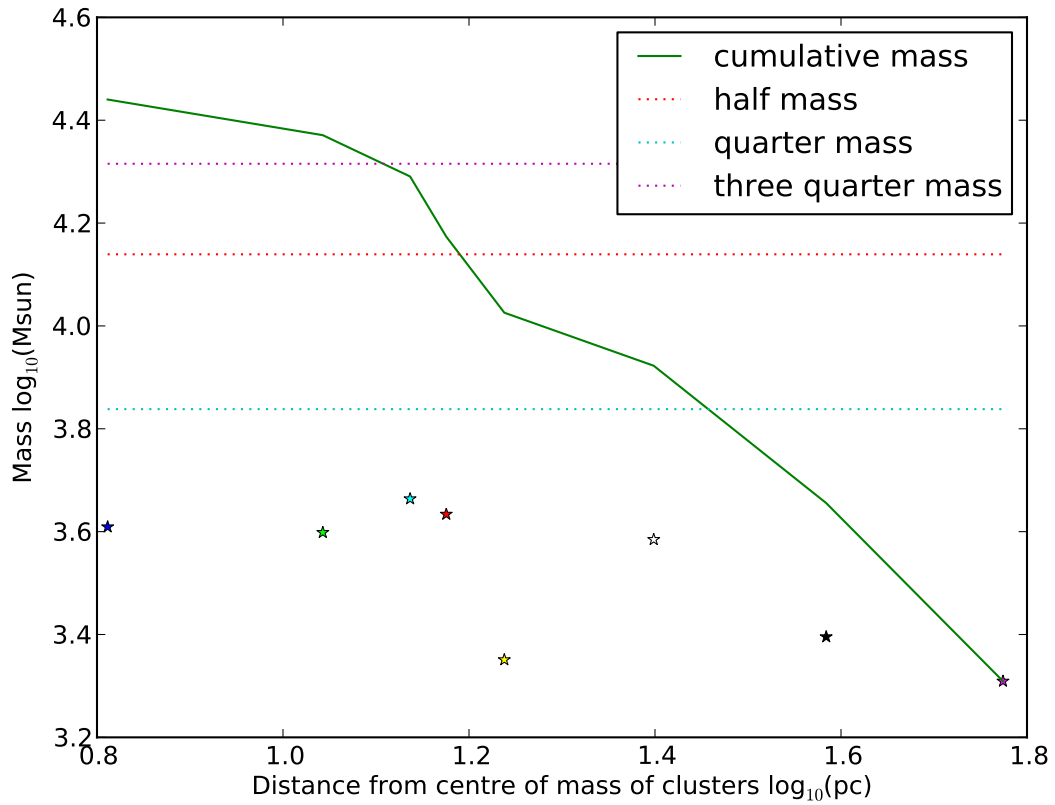
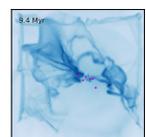


Figure 4.17: The coloured stars are the star clusters at 14 Myrs for the base simulation plotted as their mass against distance from the centre of mass of the star clusters (see Table 4.2 for more details). The green line shows the cumulative mass in stars moving in towards the centre of mass suggesting a cored isothermal sphere density distribution. The dotted lines show the half, quarter, and three quarter lines of total star cluster mass.



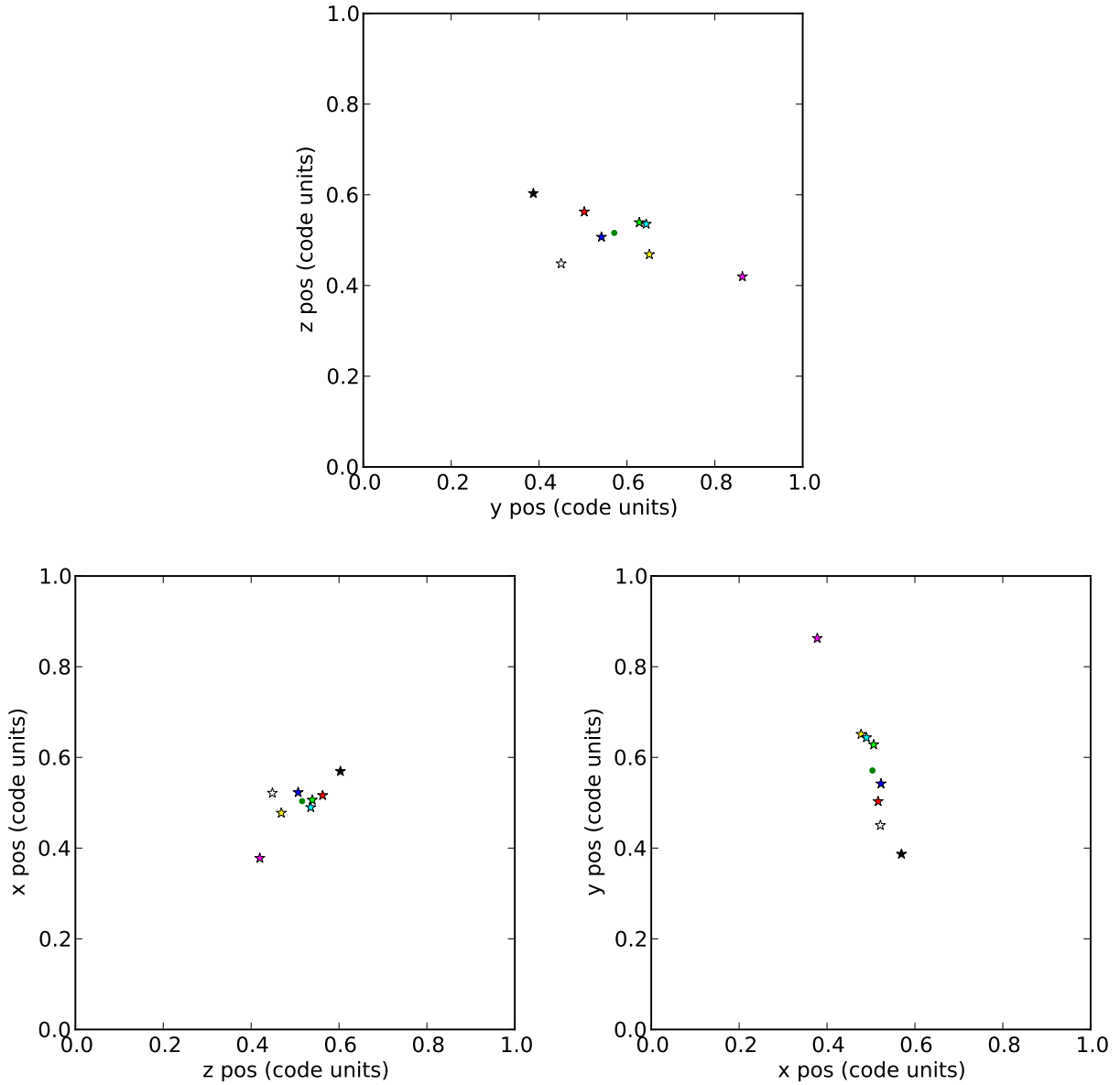
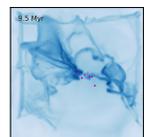


Figure 4.18: Cluster positions in y-z, z-x, and x-y space at 14 Myrs for the base simulation. Clusters are shown as stars. The colour identifying the individual cluster and is the same as in Fig. 4.17. The green dot shows the centre of mass of the star clusters. The centre of mass of the clusters is 15.6 pc from the centre of the simulation box.

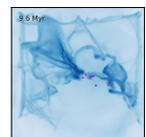


the first star cluster. The radius was estimated between 7 and 10 Myrs, when there is a bubble visible. The green line shows a least squares fit to the points giving a shell velocity of 6.31 pc/Myrs or 6.18 km/s, similar to the estimated velocity of the shell around Carina at 5 km/s (Grabelsky et al., 1988).

To calculate the covering fraction of the shell I took a shell centred around the first star cluster of cells between 0.30 and 0.35 code units in radius (54 and 63 pc). The width of the shell was chosen so that it included enough cells that a fraction of shells would be a good estimate of the fraction of solid angle. This shell is outside the original cloud location but still fully contained within the simulation box. For all cells in that shell I counted up those that contained radiation and those that did not. I assume that the fraction of cells not containing radiation are shielded by a bubble wall around the first cluster and those that do have radiation are outside a leaking hole in the bubble wall. Fig. 4.20 shows how the covering fraction varies with time. Fig. 4.21 shows three slices of the cells in the leaking calculation. This calculation is only accurate until 9.4 Myrs as then ionizing radiation from the original star cluster stops being emitted.

The base simulation has a cloud mass approximately twice our calculated mass for the gas in Carina inside a radius 2/3 the radius used in the best fit model in Chapter 2. Tr16 in Carina is an estimated 3.6 Myrs old, corresponding to my base simulations at 9 Myrs. At 9 Myrs the base simulation has $2.4 \times 10^4 M_{\odot}$ of stars and an ionizing photon rate of 2.4×10^{51} , four times that of Carina at the equivalent time. The bubble is approximately 20 pc in size, Carina was estimated 10-20 pc. The internal gas pressure is approximately 3×10^{-11} dynes/cm² (Fig. 4.22), seven times small than the HII gas pressure in Carina (assuming a radius of 10pc, i.e. eight times a smaller volume). The average internal density is $n \sim 10$ cm⁻³ (Fig. 4.23), ten times less than Carina (assuming a radius of 10pc). The covering fraction for the base simulation at 9 Myrs is 0.13 but has been declining with time giving an average covering fraction of approximately 0.5, in agreement with the semi-analytic models in Chapter 2. Within acceptable accuracies the base simulation agrees with the Carina observations.

Although the star clusters are bright in teh UV, the entire simulation box is never fully ionized. Two different ways of showing the ionization history are shown in Fig. 4.24. At its peak 89% of cells have ionization fractions above 0.5 but there is still a significant 11% of cells that are shielded and remain neutral. Centering around the oldest star cluster at 9.5 Myrs, the peak ionization fraction, I have plotted the angular coordinate of all of the cells and all of the non-ionized cells from the oldest star cluster, Fig. 4.25. The neutral gas is constricted to remaining dense regions of shell and the gas behind it.



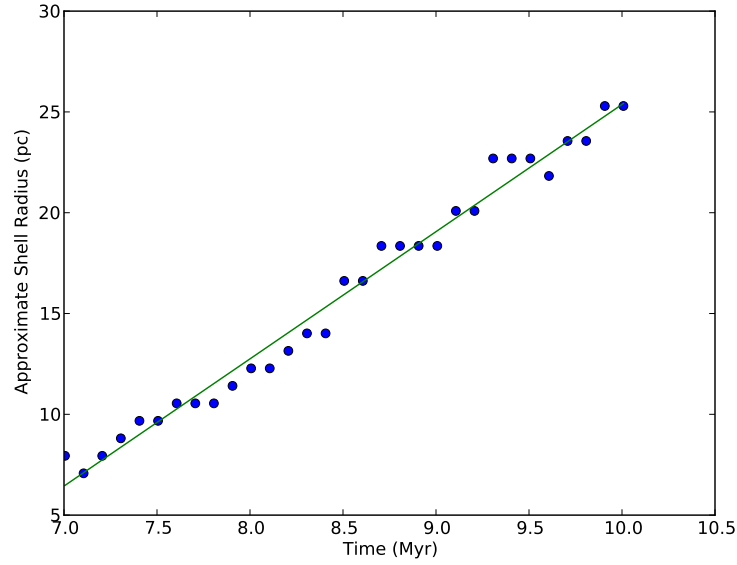


Figure 4.19: Graph showing the approximate radius of the bubble against time for the base simulation. The green line is a least squares linear best fit giving a shell velocity of 6.31 pc/Myrs or 6.18 km/s.

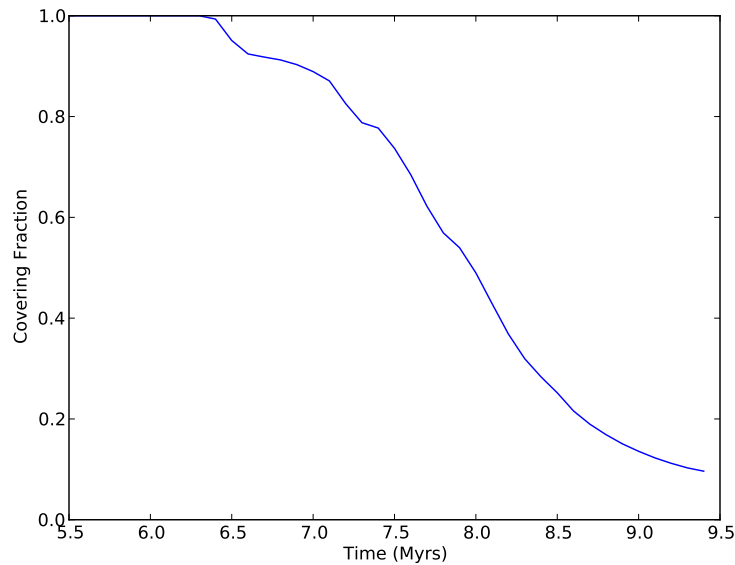
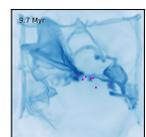


Figure 4.20: Graph showing the covering fraction against time for the base simulation. The first star cluster formed at 5.4 Myrs. The covering fraction reduces with time as the bubble expands and blows out across a greater area.



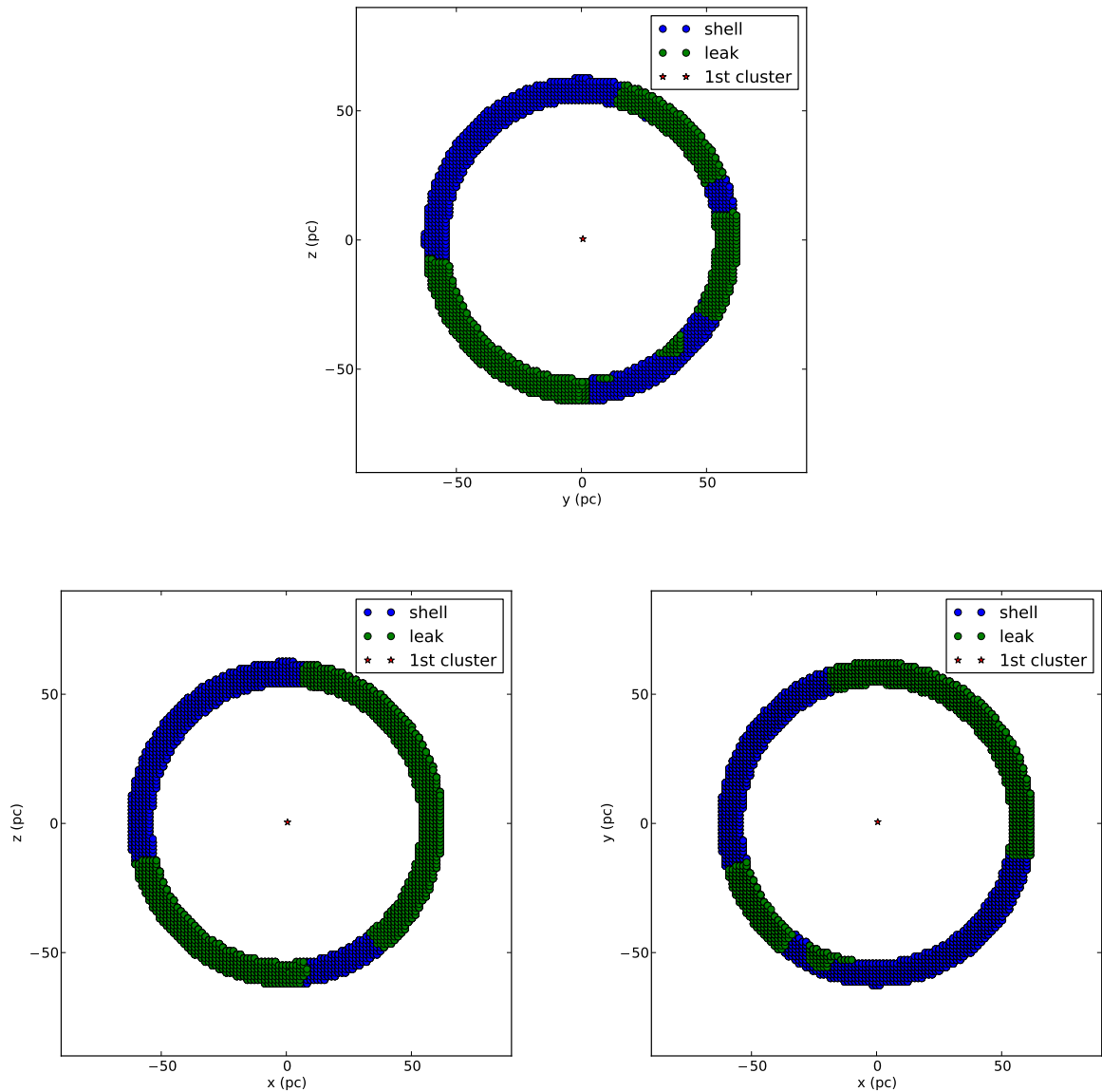
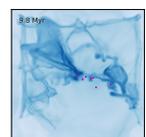


Figure 4.21: Three images showing the cells included in the covering fraction calculation at 8 Myrs. Each slice is through the location of the first star cluster and shows the shell of cells used in the calculation. Green circles show cells with radiation present (not shielded by bubble shell) and blue show cells without radiation (shielded by bubble shell). These figures show that taking the fraction of cells with radiation is a good approximation for the solid angle of leaking. Although there are some radial features they are small.



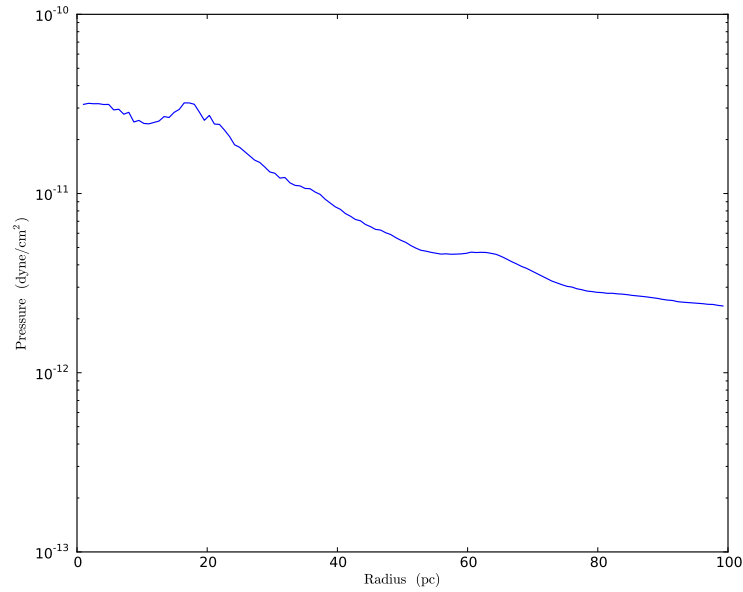


Figure 4.22: Spherically averaged gas pressure profile centred around first star cluster for the base simulation at 9 Myrs (3.6 Myrs after first cluster formed).

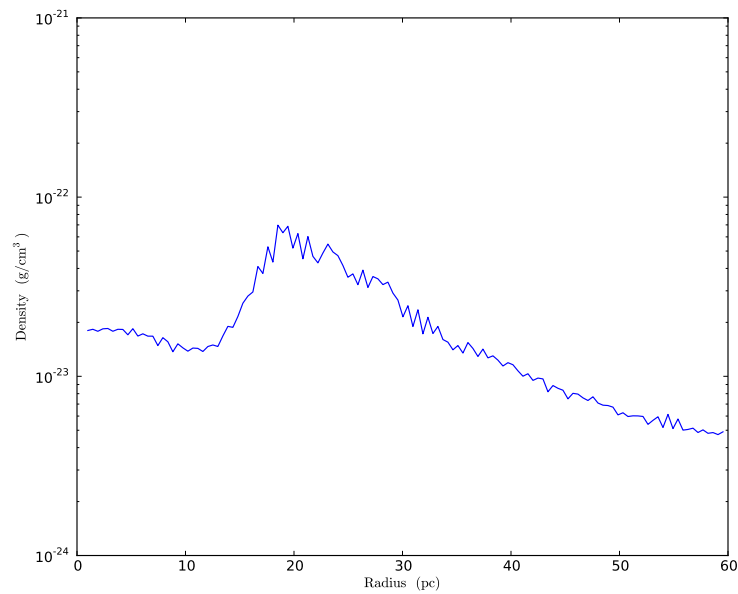
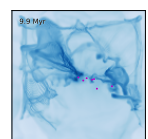


Figure 4.23: Spherically averaged density profile centred around first star cluster at 9 Myrs (3.6 Myrs after first cluster formed). The wide peak in density is caused by the shells radius varying in different directions.



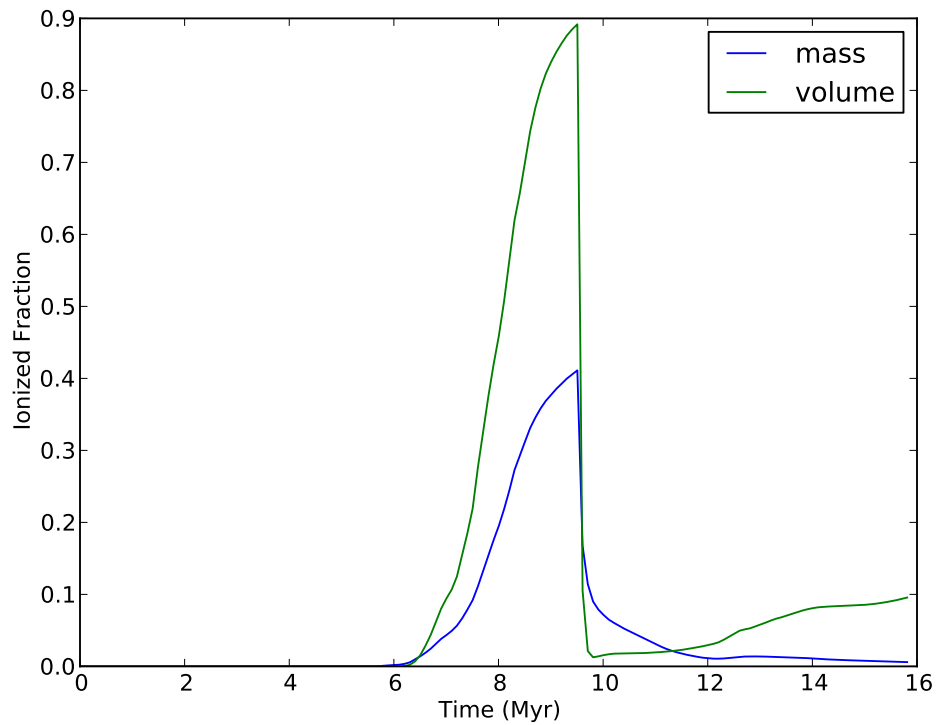
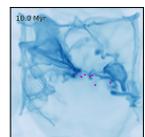


Figure 4.24: A graph showing the ionization fraction of the base simulation against time. *Mass* shows $\sum_i(I_i M_i) / \sum_i(M_i)$ where I_i is the ionization fraction of the cell and M_i is the mass in the cell. *Volume* shows the fraction of volume with ionization fraction over 0.5. The rapid drop after 9.4 Myrs is due to the first star clusters switching off and material quickly recombining.



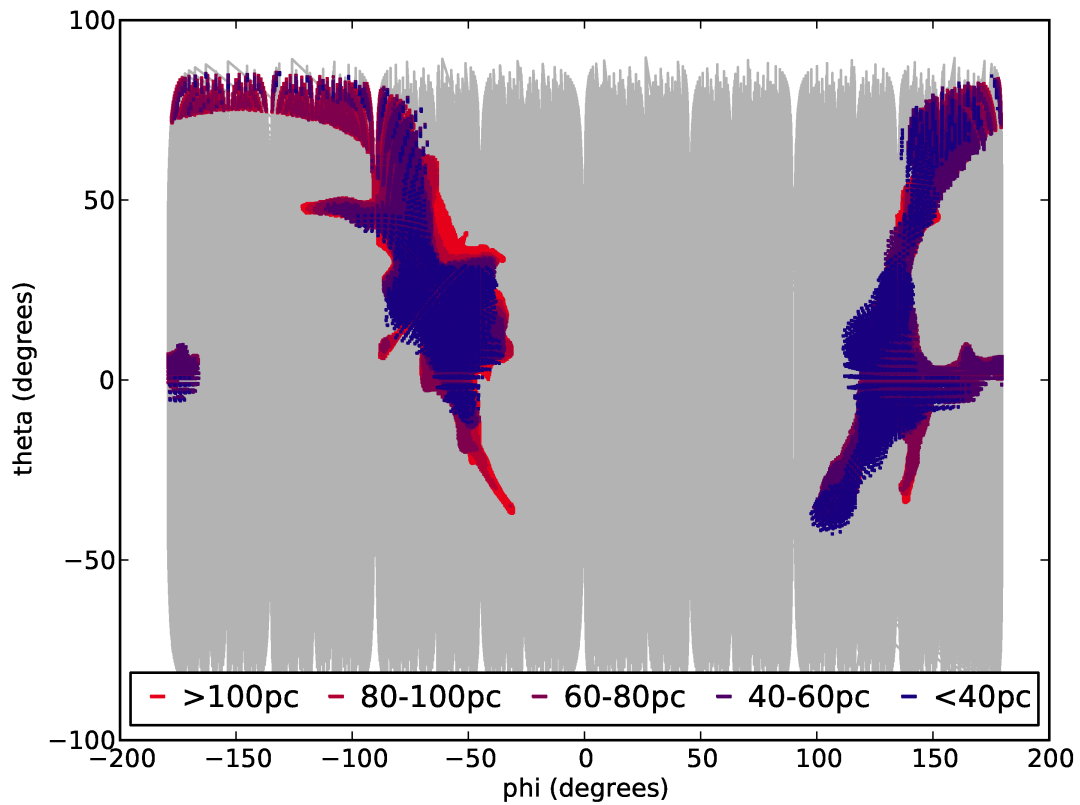
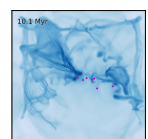


Figure 4.25: A plot of the angular position of all cells centred on the first star cluster. Grey points show the centre of cells that are fully ionized. Coloured cells show the cell centres of the neutral gas (ionization fraction < 0.5) with colour showing distance from first star cluster. This plot shows that the neutral regions are restricted to specific regions.

4.1.2 Base Simulation Summary

With 12.8% of the original cloud gas mass converted into stars it took less than one dynamical time to completely disrupt the GMC with only ionization and radiation pressure.



4.2 Output study

I ran a parameter study with various combinations of the outputs as shown in Table 4.3. I considered only ionization, radiation pressure, and supernovae as energy and momentum outputs.

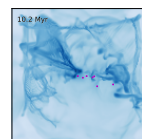
Name	HII	RP	SNe
none	-	-	-
SNe	-	-	yes
HII	yes	-	-
HIISNe	yes	-	yes
HIIRP, base	yes	yes	-
all	yes	yes	yes

Table 4.3: Star cluster outputs in the six simulations in this outputs study. Note the base simulation had ionization and radiation pressure but no supernovae outputs.

Radiation pressure cannot be simulated without ionization and the radiation must be absorbed across several cells for the radiation pressure to be resolved. I ran a study reducing the number of photons but increasing the momentum per photon to keep the total momentum emitted constant, in §4.2.2.

4.2.1 Output Study Results

All simulations in the output study are identical until the first star cluster forms. Then, the output from stars affects the surrounding region and changes the subsequent evolution. The total mass in star cluster particles against time for the different outputs are plotted in Fig. 4.26.



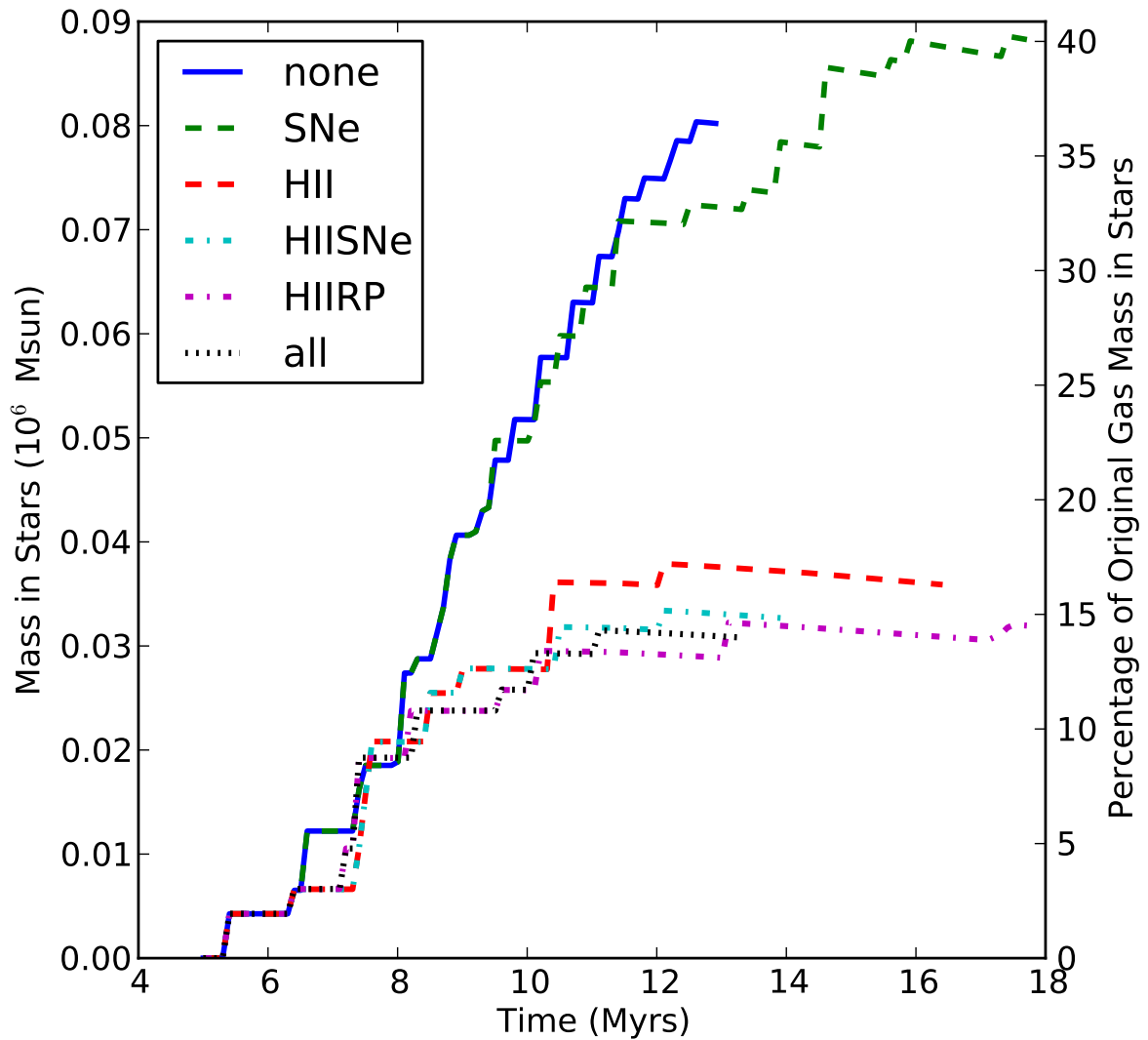
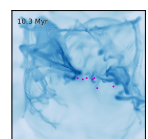
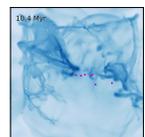


Figure 4.26: Time evolution of total mass in star cluster particles for output study simulations. HIIRP is the base run, shown in magenta. Note the significant difference when stellar output during the stars lives is included (HII and RP). The addition of supernovae to any of the runs makes very little difference to the subsequent cluster formation.



No outputs

With no outputs the rate of star formation is constant as regions collapse under self gravity. Figure 4.27 shows the mass weighted and non weighted mean Mach number for the original cloud location and the whole simulation box. Compared to Fig. 4.15, the same graphs for the base simulation, there are not as significant changes in Mach number without outputs. The lack of outputs means the gas in the cloud is not being pushed out but the densest regions are still having mass removed for star cluster formation changing the mass weighted mean. The initial increase the decrease in mass weighted values are the same as the base simulations as the simulations are identical until star cluster formation. Note the steady increase in the non-weighted Mach number as gravitational collapse continues to move gas in the simulation. Sharp changes in mass weighted Mach number are caused by cluster formation.



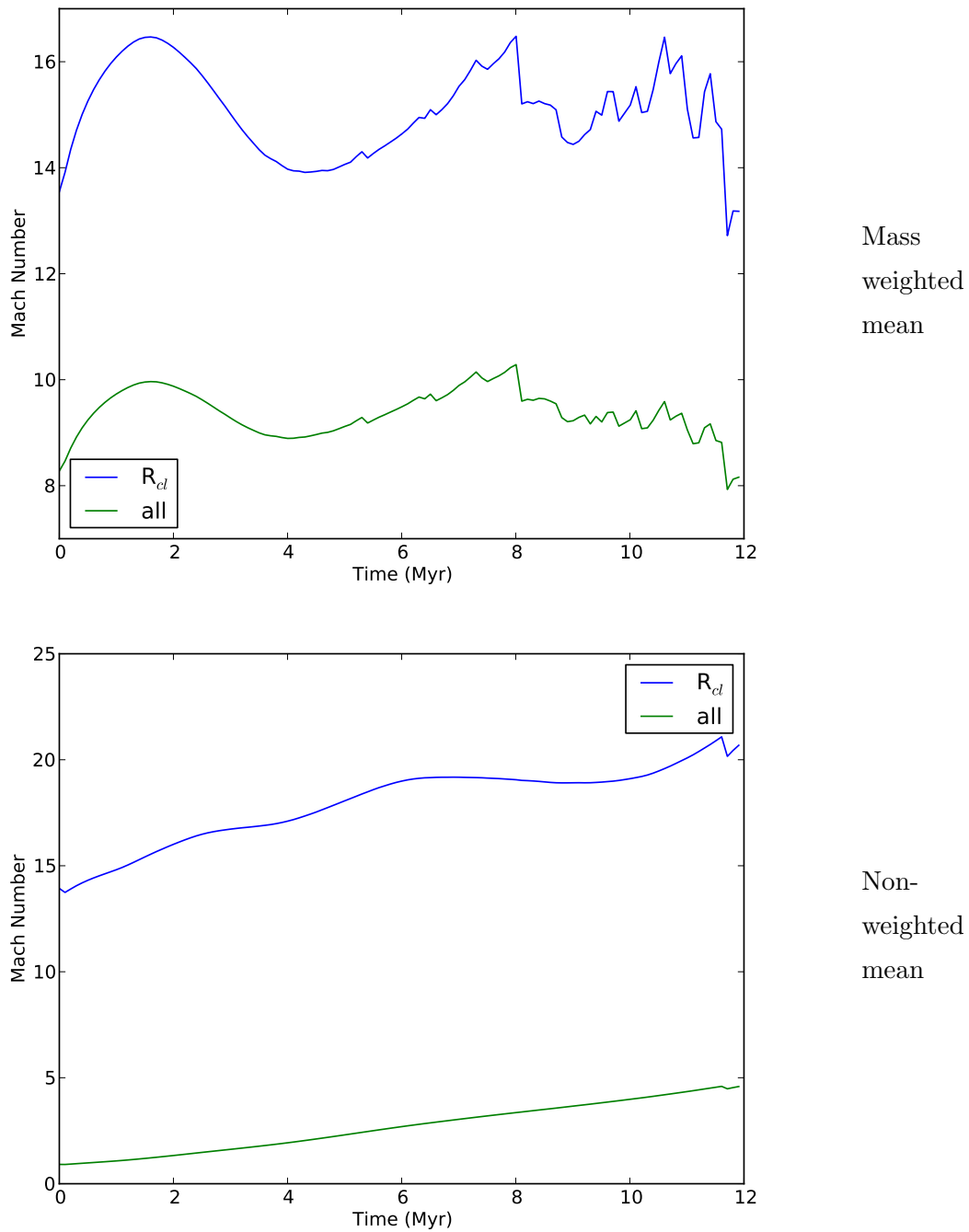
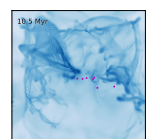
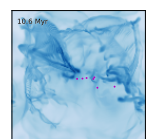


Figure 4.27: The mean Mach number for the gas in the none simulation with time. The blue lines are for the gas within the original cloud location and the green lines are for the whole simulation box. *Top*: the mass weighted means and *bottom* the non-weighted means. Without outputs from the stars mass is only removed when converted into cluster particles so there is less dramatic changes in Mach number than for the base simulation. Gravitational collapse keep the Mach number roughly constant despite the turbulent decay.



Supernovae

The run with supernovae only diverges from the run without supernovae after 9.4 Myrs when the first supernovae explode. The supernovae heat and ionize the gas immediately around the star cluster but only start 4 Myrs after the star cluster forms; see §3.7.2 for more details. Supernovae slightly alter the subsequent star cluster formation after 11 Myrs (5.6 Myrs after the first star cluster formed). Density and temperature slices of the 100 pc around the oldest star cluster for simulations with and without supernovae are shown in Figs. 4.28-4.30. Please note that the temperature scale is different from the four panelled images elsewhere in this thesis. Figure 4.28 shows that with no other outputs, the supernovae occur in a dense region and the energy and momentum deposited by the supernovae pushes some of that material out. 11.6 Myrs is 2.2 Myrs after the first supernovae occurred and still there is only a small dynamical difference in the material as the higher density causes rapid cooling of the supernovae ejecta. Figure 4.29 shows supernovae going off in an HII region (without radiation pressure). Without supernovae the material inside the HII region is quite smooth but the addition of supernovae has created structure within the bubble. Figure 4.30 shows the supernovae when the region is not only ionized but has also been evacuated by the radiation pressure. The evacuation by radiation pressure has removed so much of the material that there is very little for the supernovae blasts to shock with; thus, the additional structure seen is at very low densities. Indeed, looking at Fig. 4.26, the addition of supernovae on top of ionization and radiation pressure (all : HIIRP) actually slightly increases the mass in star clusters at 11.6 Myrs though this change is very small and reversed within another two million years.



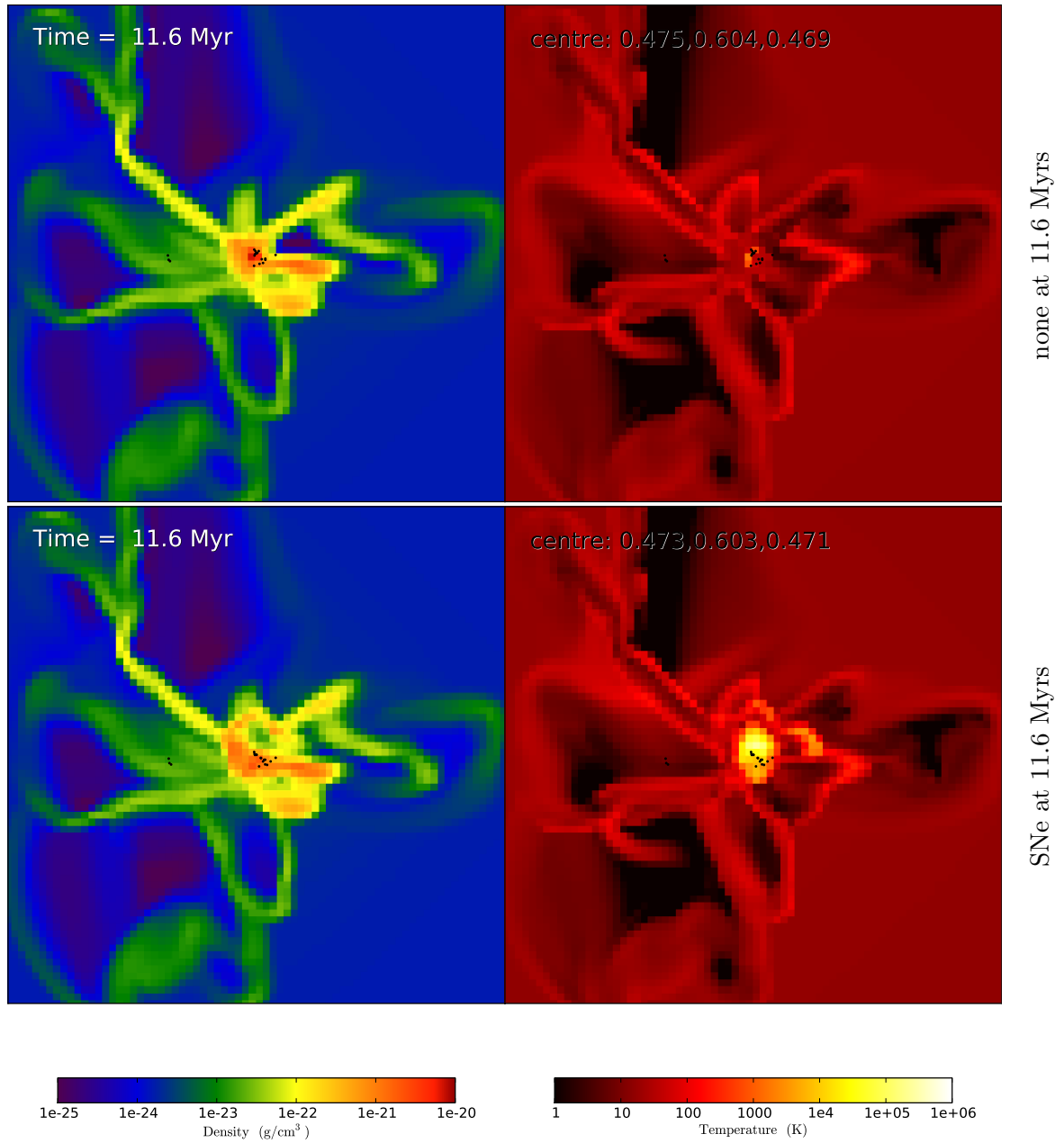
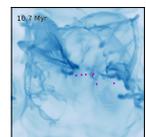


Figure 4.28: Slices of density of the central 100 pc at 11.6 Myrs for the simulations with no outputs and with only supernovae. These slices show the volume density reaching 10^{-20} g/cm³. With no other outputs the supernovae are exploding in very dense surroundings, causing the gas to cool rapidly and limiting the dynamical effect the explosion can have.



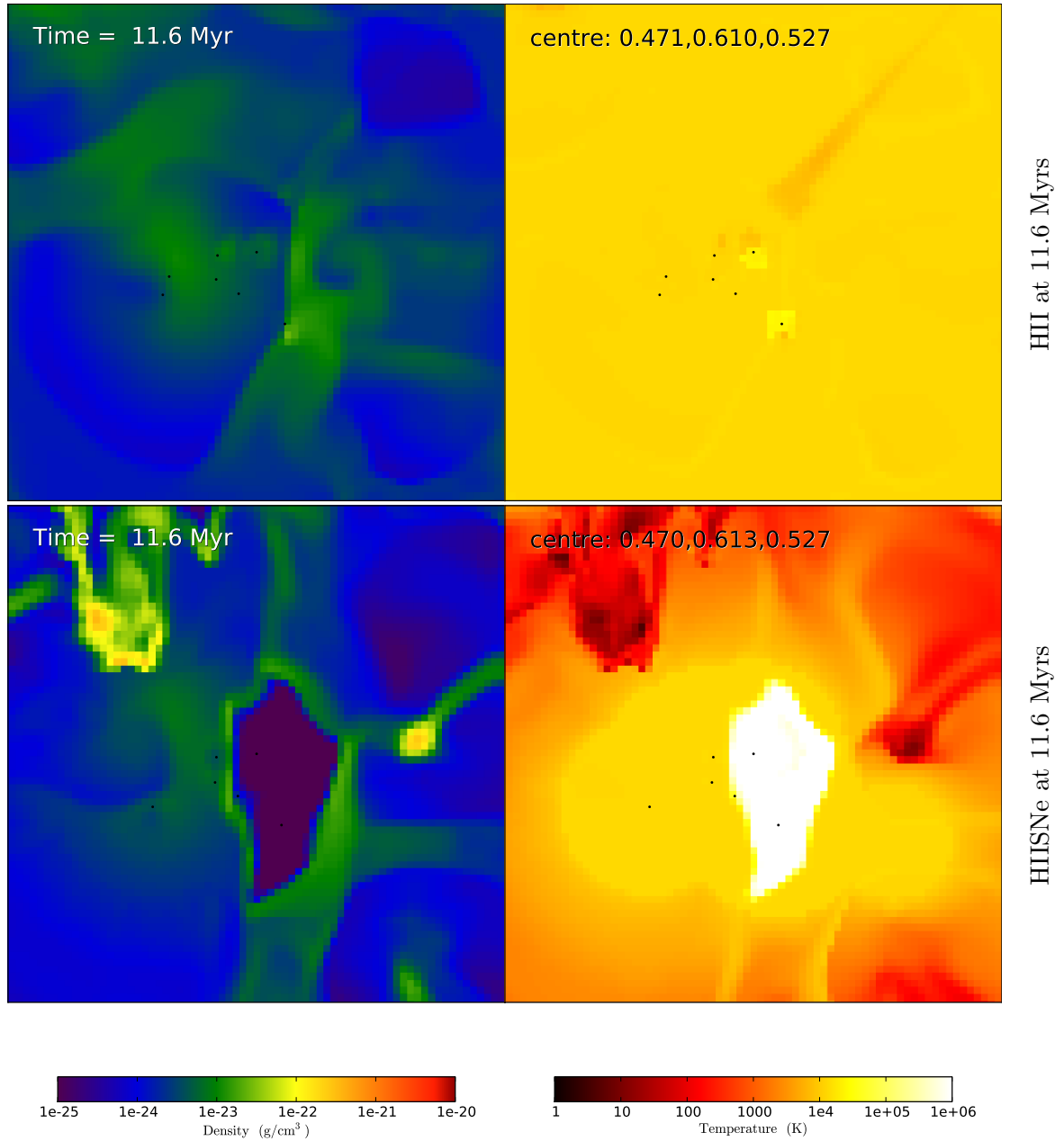
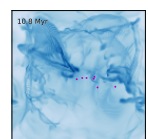


Figure 4.29: Slices of density of the central 100 pc at 11.6 Myrs for the simulations with ionization and with supernovae as well. The ionized gas pressure has cleared out the gas from the original cloud location so the supernovae bubble expand rapidly and remain hot. The addition of supernovae adds more structure inside the bubble but occur too late to affect star formation.



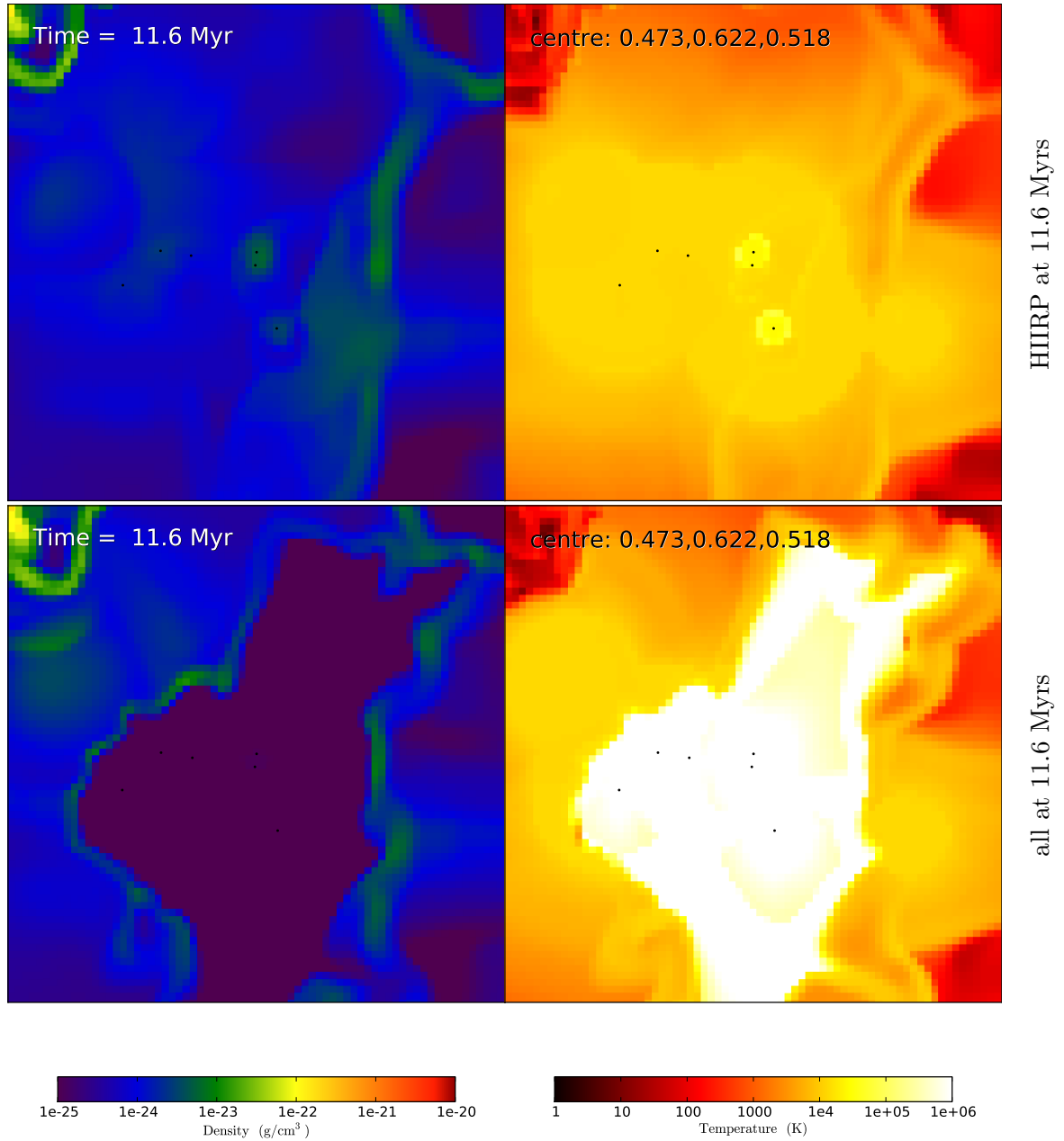
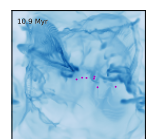


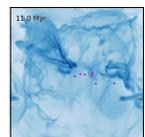
Figure 4.30: Slices of density of the central 100 pc at 11.6 Myrs for the simulations with ionization and radiation pressure and with supernovae as well. The radiation pressure has caused the density inside the bubble to be very low. The supernovae explosions expand rapidly and do not cool as quickly, but do not sweep up much mass as there is so little mass remaining inside the bubble.



Ionisation

The addition of ionization output from the stars during their lifetime has a significant affect on the subsequent star cluster formation. One million years after the first star cluster forms, the second star cluster forms in both ‘none’ and ‘HII’ runs. However, the cluster formed in HII has a 4.5% higher mass than in the none run ($2,360.6M_{\odot}$ and $2,258.8 M_{\odot}$ respectively). Although not a substantial change, this does suggest the ionized region expansion has swept up additional mass into the area where the second star cluster forms. The second star cluster forms 0.004 Myrs earlier for the HII run than the none run. Figure 4.31 shows before and after second cluster formation for the run with ionization only.

With no ionization, the third star cluster forms at 6.6 Myrs, very close to the first star cluster. With ionization this region is ionized, hot, and significantly evacuated and therefore does not form another star cluster. However the fourth star cluster in none and the third star cluster in HII form in the same region of the simulation box (position $\approx 0.51, 0.50, 0.49$). This star cluster forms 0.034 Myrs earlier and with 0.09% more mass in the HII simulation compared to the none simulation despite it being significantly further away from the ionized region than when the second star cluster formed.



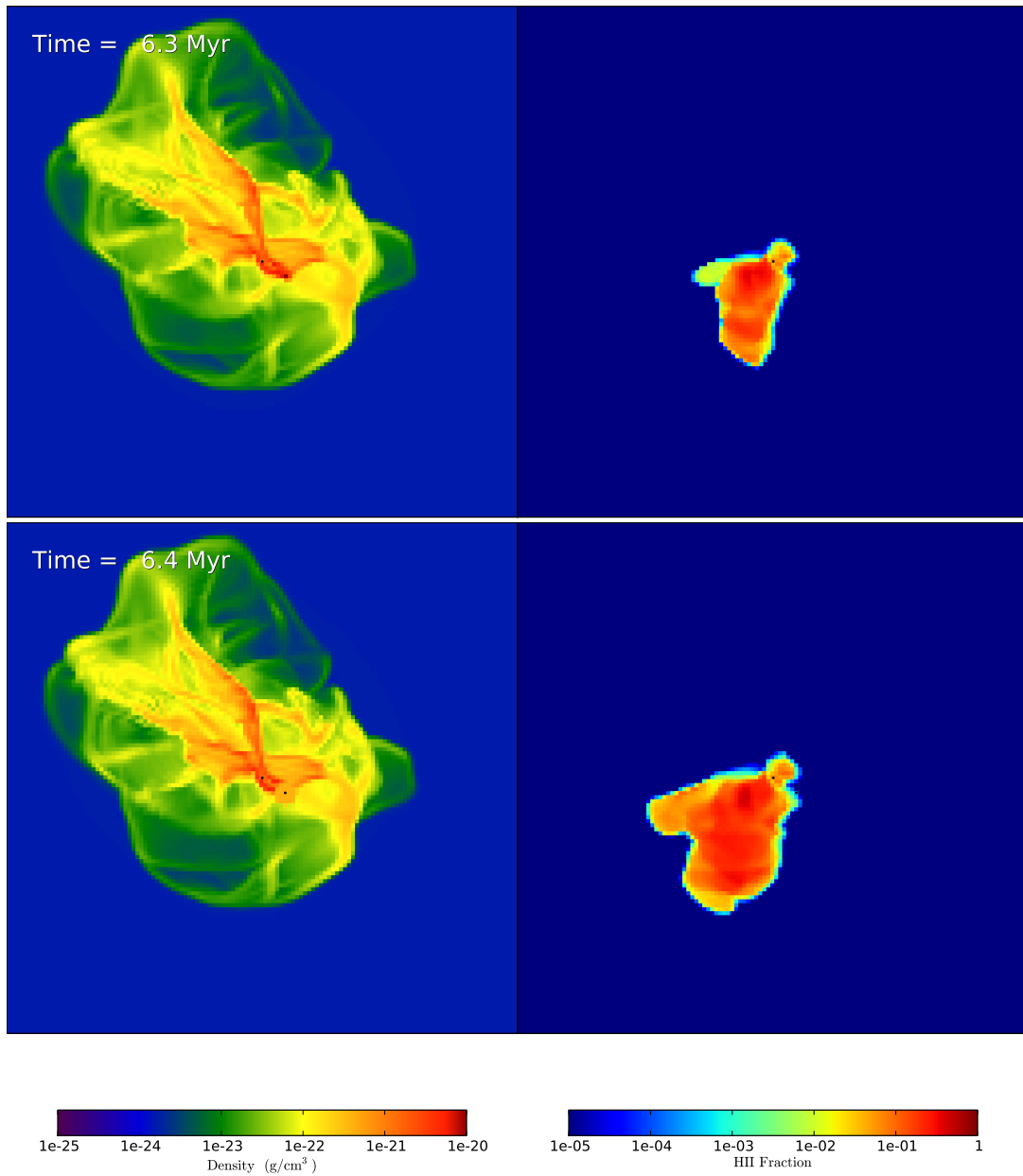
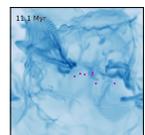


Figure 4.31: *Left:* projected density and *right:* HII fraction for the simulation with only HII output for 6.3 Myrs - just before the second star cluster forms (top) and 6.4 Myrs - just after the second star cluster forms (bottom). The second star cluster forms just outside the ionization region from the first star cluster.

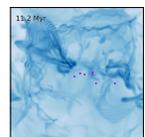


Radiation Pressure

After 7 Myrs a bubble shell is visible around the first star cluster for the simulations with ionization, and is more distinct with radiation pressure as well. Star clusters form within this shell as shown in zoomed in density projections in Fig. 4.32. At 7.1 Myrs there is a clear bubble forming around the first star cluster and then at 7.2 and 7.4 Myrs two new star clusters are formed within that shell. The cluster formation in the shell is what causes the rapid increase in total mass in clusters at ~ 7 Myrs. It is not possible to conclusively say that this is a sign of triggered star formation. The same mass still forms into star clusters as for the runs without radiation outputs at the same time. The clusters are forming on the shell around the first cluster rather than in a clump of material containing the first cluster. Clusters appear to form where the bubble shell meets existing filaments.

After 8 Myrs the star formation rates for the simulations with ionization and ionization and radiation pressure diverge significantly from the simulations with no outputs or only supernovae. By 8.5 Myrs the radiation has ionized and heated most of the gas in the simulation box and the resulting bubble is disrupting the gas significantly, especially with radiation pressure. Figure 4.33 shows the density and ionized fraction for the simulation with only ionization and with ionization and radiation pressure at 8.5 Myrs. The difference in the bubble shape and size is clear in the density projection. Radiation pressure has a significant dynamical effect on the remaining gas. The larger bubble with radiation pressure leads to a higher rate of leaking and less shielding of the surrounding gas. This can be seen by the greater volume ionized.

After 10 Myrs there is very little star cluster formation for simulations with ionization and especially for those including radiation pressure. The gas in the entire simulation box is heated and ionized by the radiation either directly or through leaking (Fig. 4.10) and the gas has been evacuated from the centre of the simulation box and distributed in the outer regions (Fig. 4.10 and Fig. 4.12). The gas is evacuated from the centre significantly faster when radiation pressure is included, as seen in Fig. 4.34. In Fig. 4.34 it can be seen that for the none simulations substantially more mass is converted into stars indicated by the decreasing lines for all and within $2 R_{cl}$ of the centre. The mass within both R_{cl} and $0.5 R_{cl}$ decrease less than the total mass in stars, suggesting that gravity is pulling material in, rather than the centre being evacuated. For the HII and HIIRP runs, less mass is converted into stars. However, the central regions are evacuated more than the mass converted into stars suggesting outputs winning over gravity and evacuating the central region. With radiation pressure the HIIRP evacuates significantly faster than the HII run. At 12 Myrs there is less mass within R_{cl} of the centre for the HIIRP simulation than within $0.5 R_{cl}$ of the centre for the none simulation.



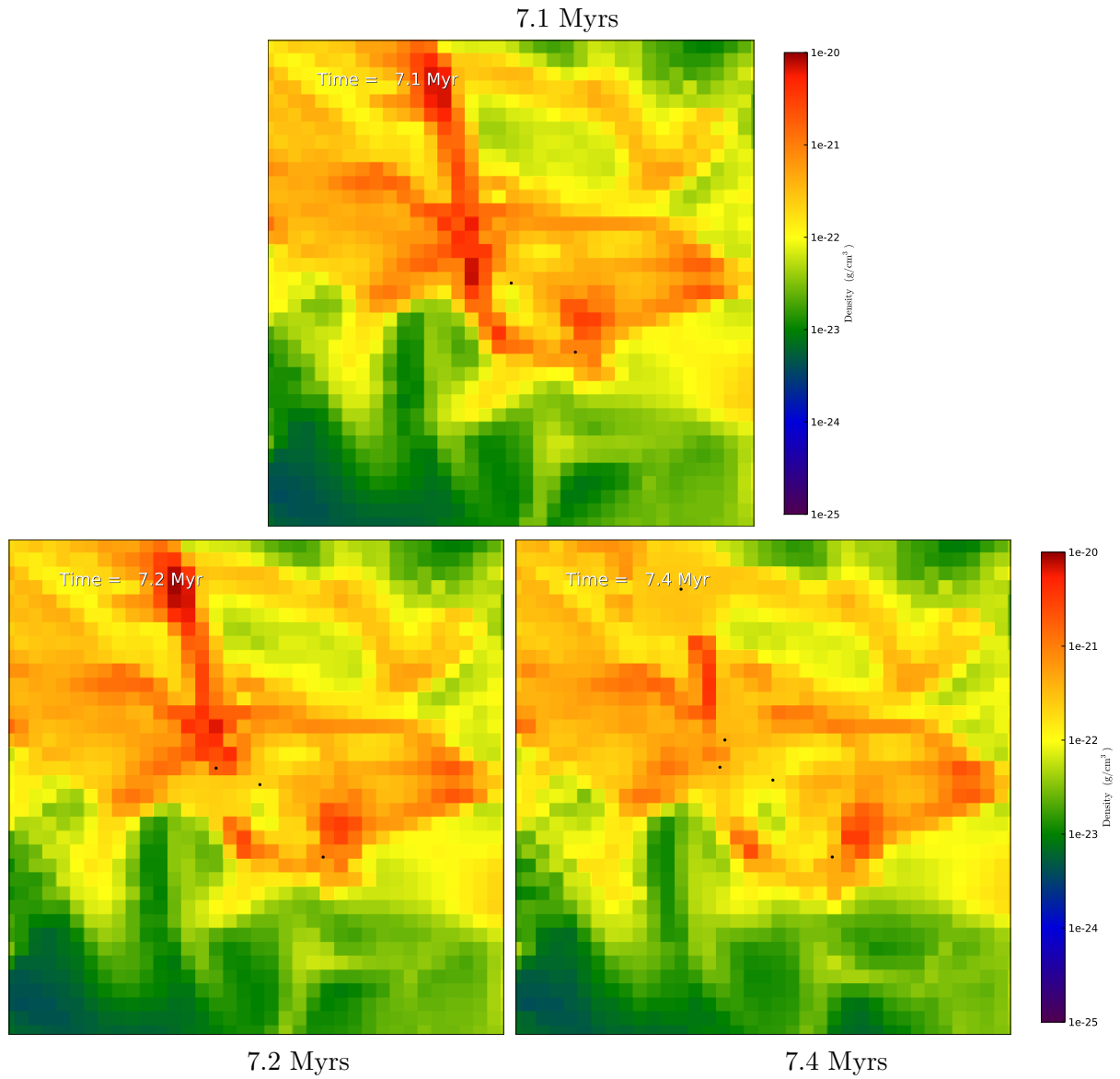
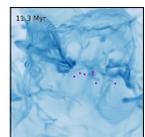


Figure 4.32: Projections of density for the 50 pc centred around the first star cluster of the all simulation. The projections at 7.1, 7.2, and 7.4 Myrs show star cluster particles forming within the shell of the bubble blown out from the first star cluster two million years after the first cluster formed.



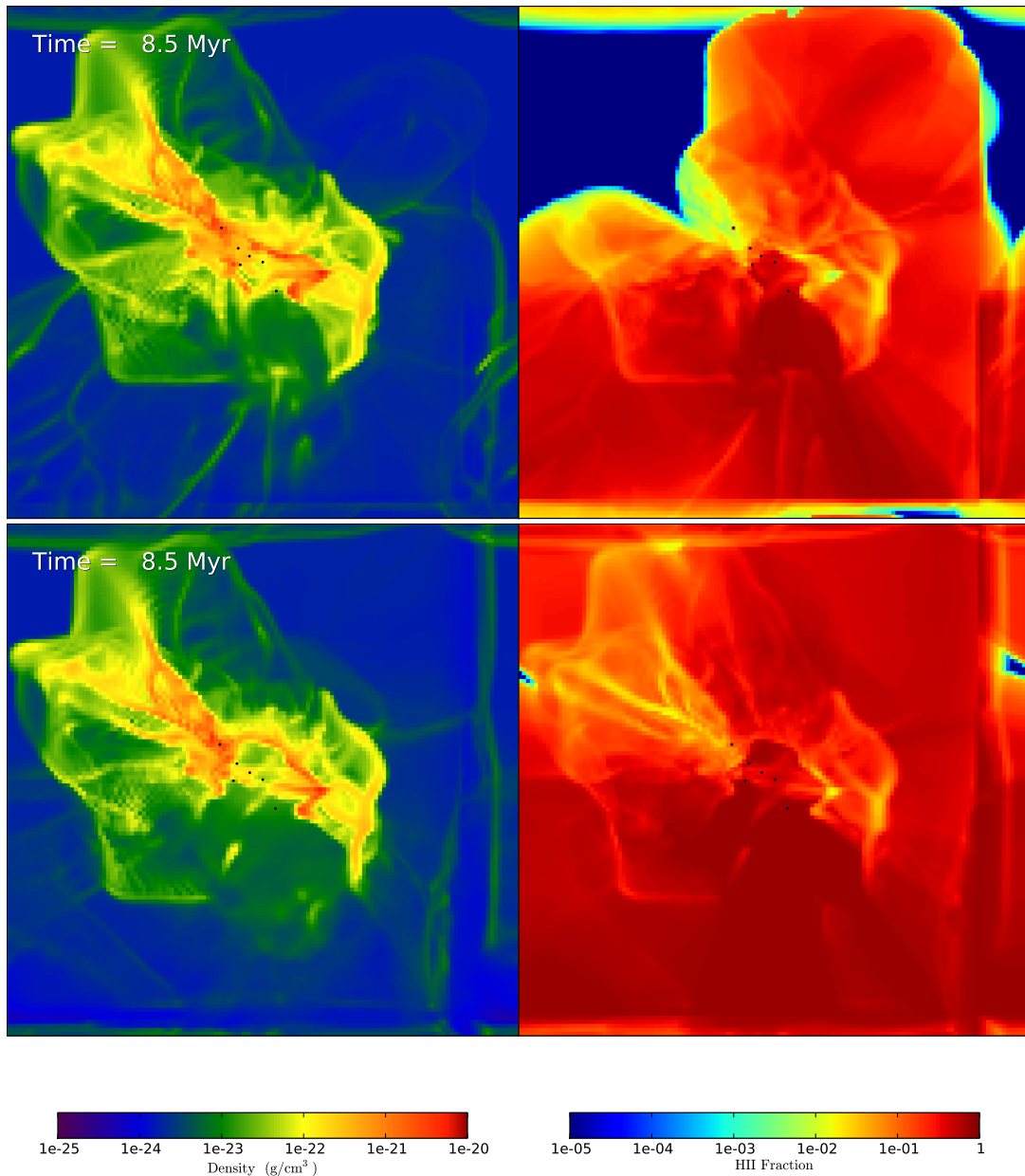
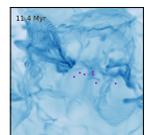


Figure 4.33: *Left*: Projected density and *right*: HII fraction for the simulation with only HII output (top) and HII and radiation pressure (bottom), both at 8.5 Myrs (3.1 Myrs after first star cluster formed). The bubble is much more pronounced for the simulation with radiation pressure, as seen by the significant bubble shell in density. Also, for the simulation with radiation pressure a much greater volume is ionized, showing that more gas and radiation is leaking from the larger bubble.



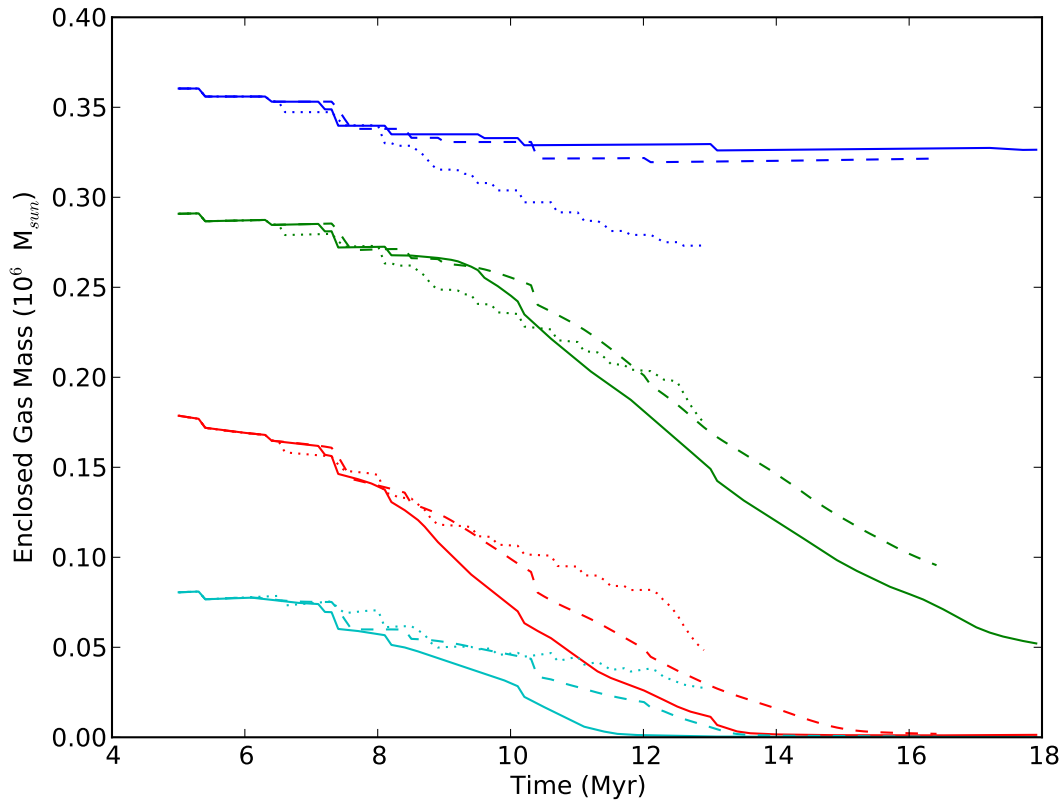
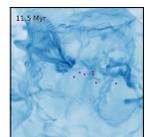


Figure 4.34: The mass structure for three of the simulations in the output study. The different line styles denote different simulations: Solid = HIIRP, dashed = HII, and dotted = none. The colour shows which region of the box is being considered: Blue = all, Green = within $2 R_{cl}$ of the centre, Red = within R_{cl} of the centre, and Cyan = within $0.5 R_{cl}$ of the centre. The decrease in mass for the whole box (blue) shows the conversion of gas into star cluster particles. The none simulation has the most mass converted into star clusters and HIIRP the least. However, the mass in the innermost region (cyan) decreases the least for none and the most for HIIRP.



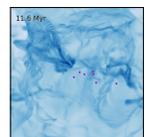
4.2.2 Radiation Pressure Investigation

Currently the code can only calculate radiation pressure when ionization is simulated. To evaluate the relative significance of radiation pressure and ionization, I ran simulations with constant momentum available from radiation, while decreasing the number of photons and therefore the energy available in ionization. Table 4.4 lists the photon rate, Q , and radiation pressure scale factor, $RPScaleFactor$, for the simulations in this investigation. The $RPScaleFactor$ boosts the amount of momentum deposited when the photons are absorbed. The base simulation has $RPScaleFactor = 2$ to account for the momentum in unsimulated sub 13.6eV photons.

The code underestimates radiation pressure at the start of the stellar feedback as it cannot resolve radiation pressure when the radiation is absorbed within the host cell of the particle. Thus, radiation pressure only starts being accurate and significant once the HII gas pressure has blown out a region and the HII region becomes several cells wide. In reality, the radiation pressure is most significant close to the star clusters (Lopez et al., 2011). The code also underestimates the radiation pressure after the clusters are 4 Myrs old as the ionizing radiation rapidly reduces - but in reality the sub-ionizing photons would still be depositing momentum.

Name	Q (s^{-1})	$RPScaleFactor$
lowHII02	5×10^{46}	0
lowHII05	2×10^{46}	0
lowHII10	1×10^{46}	0
lowHII20	5×10^{45}	0
lowHII100	1×10^{45}	0
RPlowHII01, base	1×10^{47}	2
RPlowHII02	5×10^{46}	4
RPlowHII05	2×10^{46}	10
RPlowHII10	1×10^{46}	20
RPlowHII20	5×10^{45}	40
RPlowHII100	1×10^{45}	200

Table 4.4: Simulations run investigating radiation pressure with reducing number of ionizing photons. Thus, energy in ionization is reduced but momentum available remains constant.

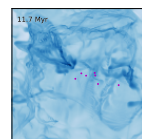


4.2.3 Radiation Pressure Investigation Results

Figure 4.35 shows the mass in star clusters for the simulations with varying photon rates (Q) but no radiation pressure. For reductions of Q by a factor of 2, 5, and 10 the masses after two dynamical times and overall rate are very similar, especially for 2 and 5. However, significant star cluster formation is still occurring after one dynamical time, unlike the base run (HIIRP). For the reductions of 20 and 100 times, significantly more stars form due to less quenching of star formation from ionization. For such low energies in ionization, the HII regions are very small and struggle to expand against the self gravity of the surrounding gas. LowHII20 only diverges from the none run at 9 Myrs and lowHII100 diverges from none at 11 Myrs. Thus the low ionization rates are affecting subsequent star cluster formation but not by much.

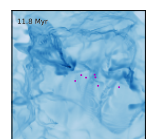
Figure 4.36 shows the mass in star clusters for the simulations *with* varying photon rates (Q) with radiation pressure. Note the significant change in y axis scale from Figs. 4.35 to 4.36. Both graphs have the none run (yellow dashed line) and the base run (black dot-dashed line) for reference. For all runs the inclusion of radiation pressure has significantly reduced the mass in clusters by 14 Myrs, as can be seen in the direct comparison between the two runs with Q reduced by 100 in Fig. 4.37. For the lower values of Q it takes longer for the radiation pressure to be resolved and therefore for the radiation pressure to be significant, as seen in Fig. 4.38. For Q reduced by 100 radiation pressure does not become significantly resolved until close to 10 Myrs, around the same time as the RPlowHII100 stellar masses start to diverge from the none run and from the lowHII100 run. The later start times for the lines in Fig. 4.38 show when ionization gas pressure manages to expand the HII region to more than a couple of grid cells. However, it still takes a little time for the region to expand enough that the radiation pressure is well resolved, as seen by the increasing efficiency for all lines. For all simulations, the decline in radiation pressure efficiency after a few million years is due to the bubbles growing large enough that a significant fraction of the radiation leaks out of the bubble and leaves the simulation box mostly unabsorbed or cancels out between sources.

Figures 4.39 and 4.40 show the structure of mass within the simulation box for three of the simulations without and with radiation pressure respectively. Q reduced by 2, 10, and 100 were chosen to best show the differences in reducing Q . Both figures have the same axis limits so direct comparisons can easily be made. The difference in star formation rate is clearly seen in the blue lines showing total mass in gas in the simulations. For the run with Q reduced by 100 and no radiation pressure significantly more mass is converted to clusters. For the inner regions (red and cyan lines) the increased energy in ionization from higher photon rates is evident in the significant increase in mass clearing, especially when radiation pressure is included. The rate of mass clearing is much greater when radiation pressure is included as shown by the steeper



negative gradients. For no radiation pressure and Q reduced by 100 the mass decrease in the very centre is less than the mass converted into stars suggesting gravity is beating disruption and more mass is collapsing into the centre. For no radiation and Q reduced by 10 the outputs seem to be just balancing the gravity as the mass reduction in the central region is the same as the mass converted into stars. With radiation pressure the outputs in both Q reduced by 10 and Q reduced by 100 are beating the gravity in the central region. However, by 15 Myrs none of the simulations with radiation pressure have completely cleared out the original cloud radius as the base simulation did but they are all headed for full disruption. However, the numerical effect of not calculating radiation pressure after 4 Myrs of a clusters life will affect the simulation results.

Figure 4.41 shows density projections for the six simulations plotted in Figs. 4.39 and 4.40 at 9.5 Myrs. The significant dynamical effect of radiation pressure on the gas is visible by the significant additional disruption for the radiation pressure included simulations in Fig. 4.41. Figure 4.42 is the same as Fig. 4.41 but 3.5 Myrs later. The dynamical difference of including radiation pressure is significant for all runs by 13 Myrs.



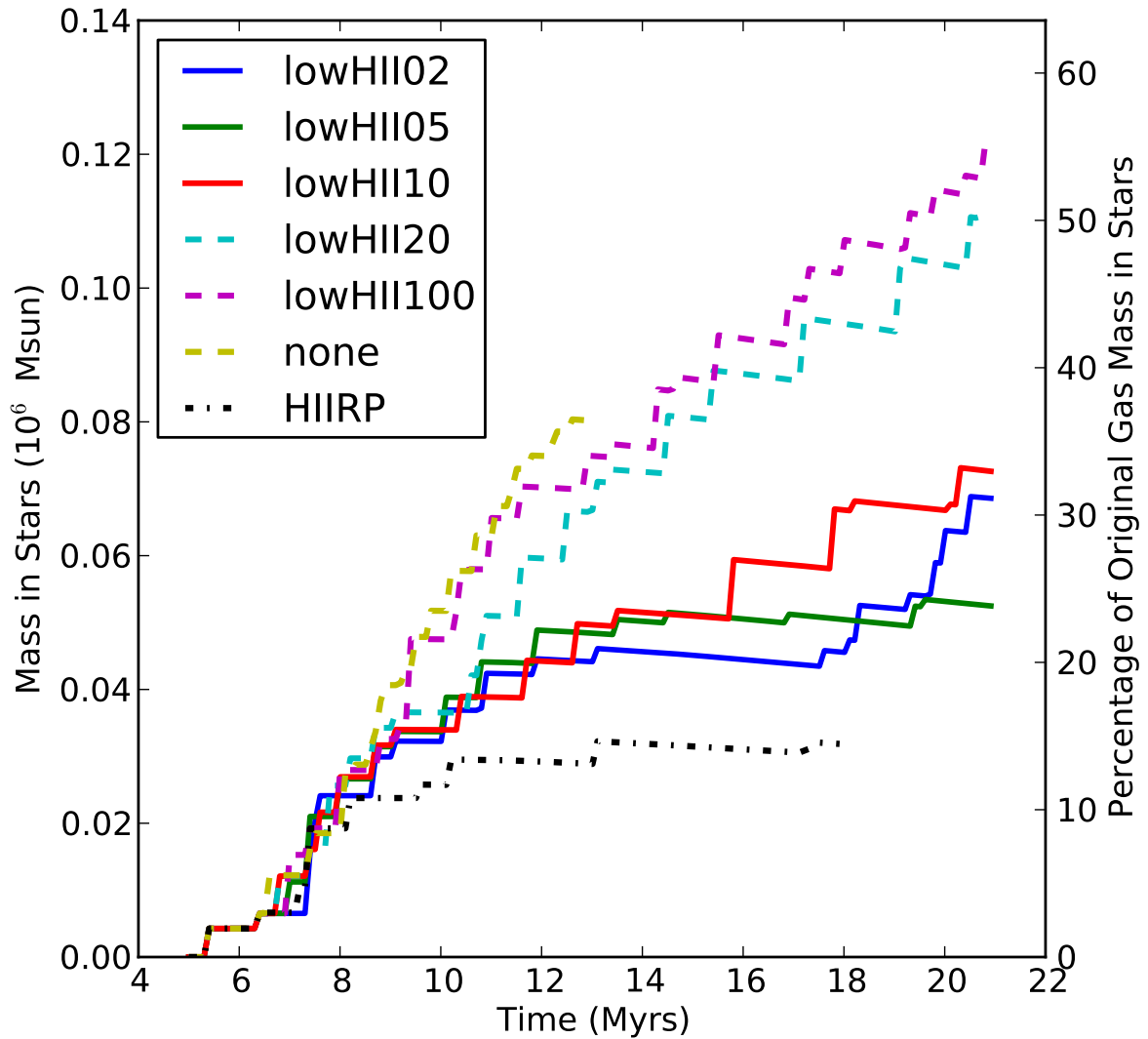
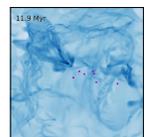


Figure 4.35: Time evolution of total mass in star cluster particles for simulations with only ionization and a reduced photon rate. The simulation with no outputs (none) and the base simulation (HIIRP) are shown for reference. The higher values of Q have lower star formation rates after 10 Myrs but all runs are still actively making stars. The rapid increase in star formation rate after 16 Myrs for the less reduced photon numbers is caused by the older star clusters switching off and the remaining gas cooling. Even for lowHIII02 five of the eight star clusters formed after 16 Myrs are within the original cloud location suggesting the cloud is not completely disrupted.



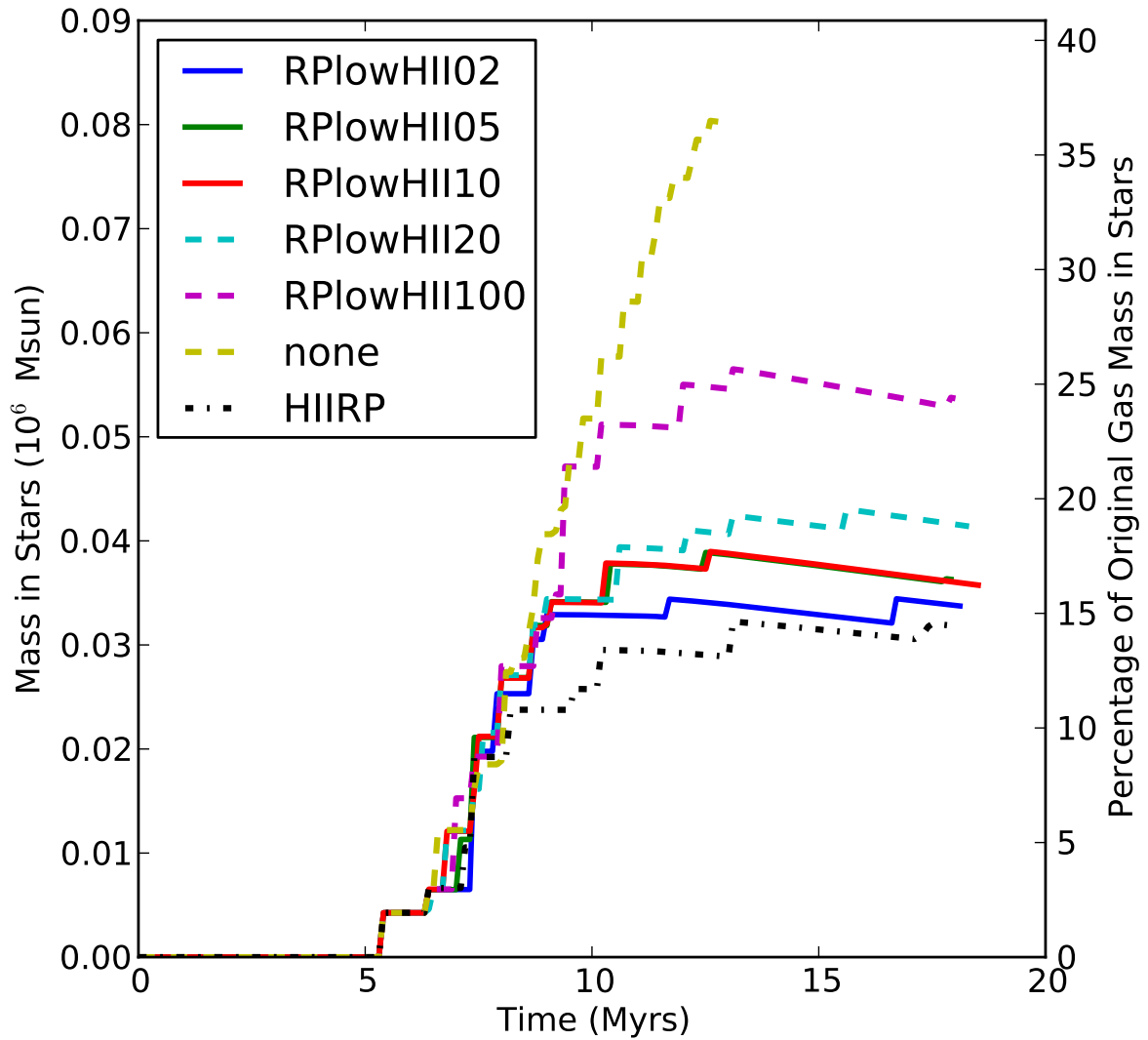
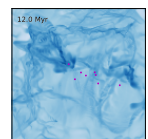


Figure 4.36: Time evolution of total mass in star cluster particles for simulations with reduced photon rate and constant radiation pressure. The simulation with no outputs (none) and the base simulation (HIIRP) are shown for reference. All runs quench star cluster formation eventually with lower values of Q taking longer for radiation pressure to be resolved and thus quenching later.



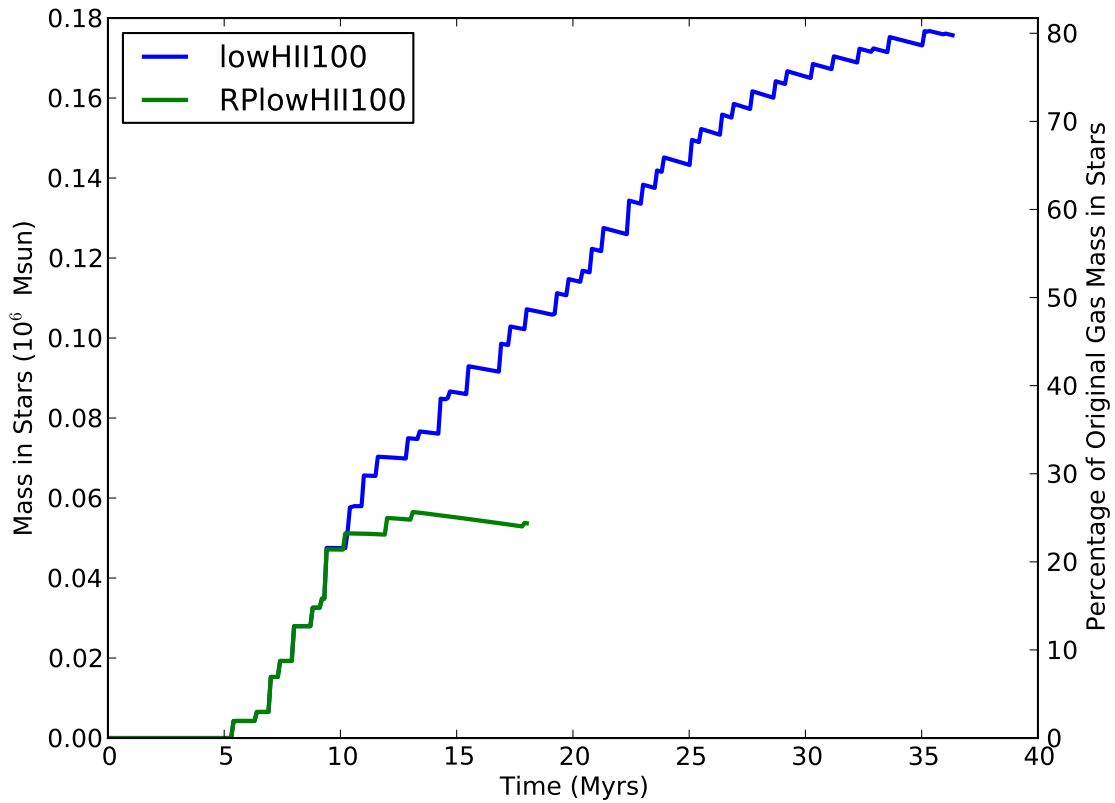
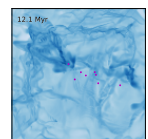


Figure 4.37: Time evolution of total mass in star cluster particles for the two simulations with number of photons (Q) reduced by a factor 100. One simulation only has ionization (blue) and the other has radiation pressure as well (green). Radiation pressure only starts to be resolved shortly before 10 Myrs so it does not take very long to start quenching star formation as the lines diverge shortly after 10 Myrs.



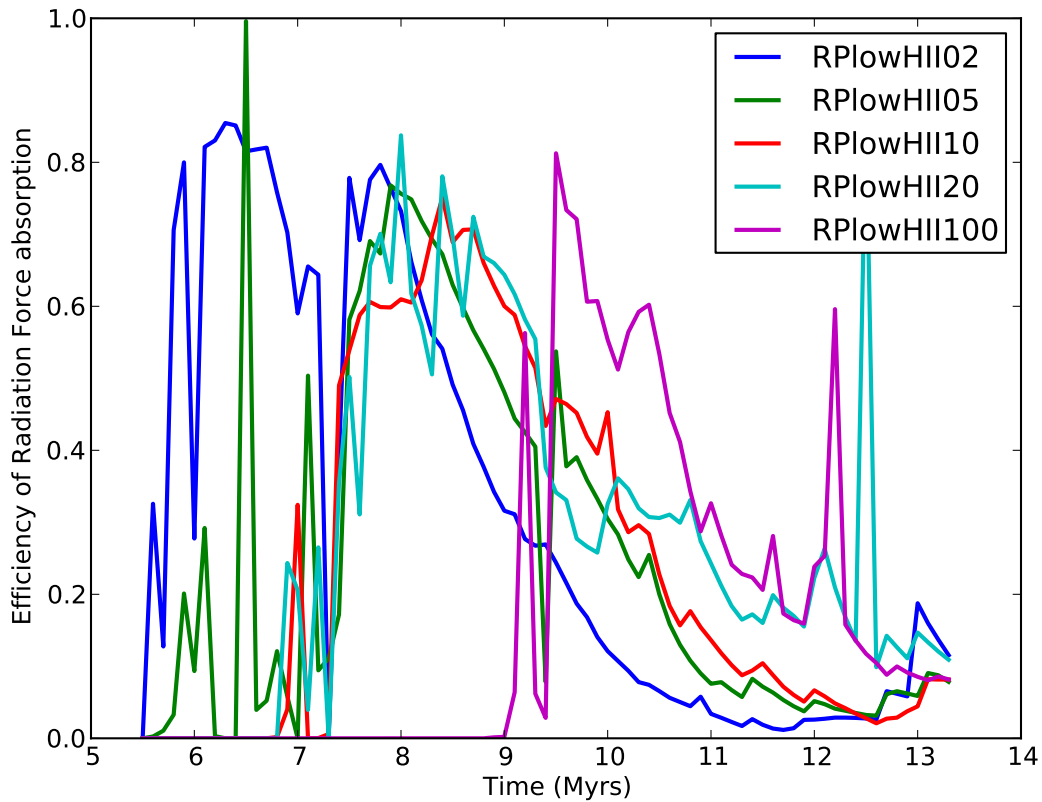
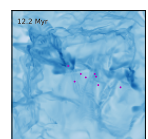


Figure 4.38: The efficiency of radiation pressure absorption for the 5 different values of Q , colours match Fig. 4.36. Efficiency is the ratio of emitted to absorbed momentum. For lower values of Q the simulation takes longer before the radiation pressure is absorbed as it cannot be resolved close to the star clusters. All simulations reach a maximum efficiency of around 0.4 due to unresolved absorption, cancelling of momentum in between sources, and eventually the loss of radiation out of the box. Spikes in the efficiency at late times are a numerical artifact caused by a cluster reaching 4 Myrs and its luminosity dropping.



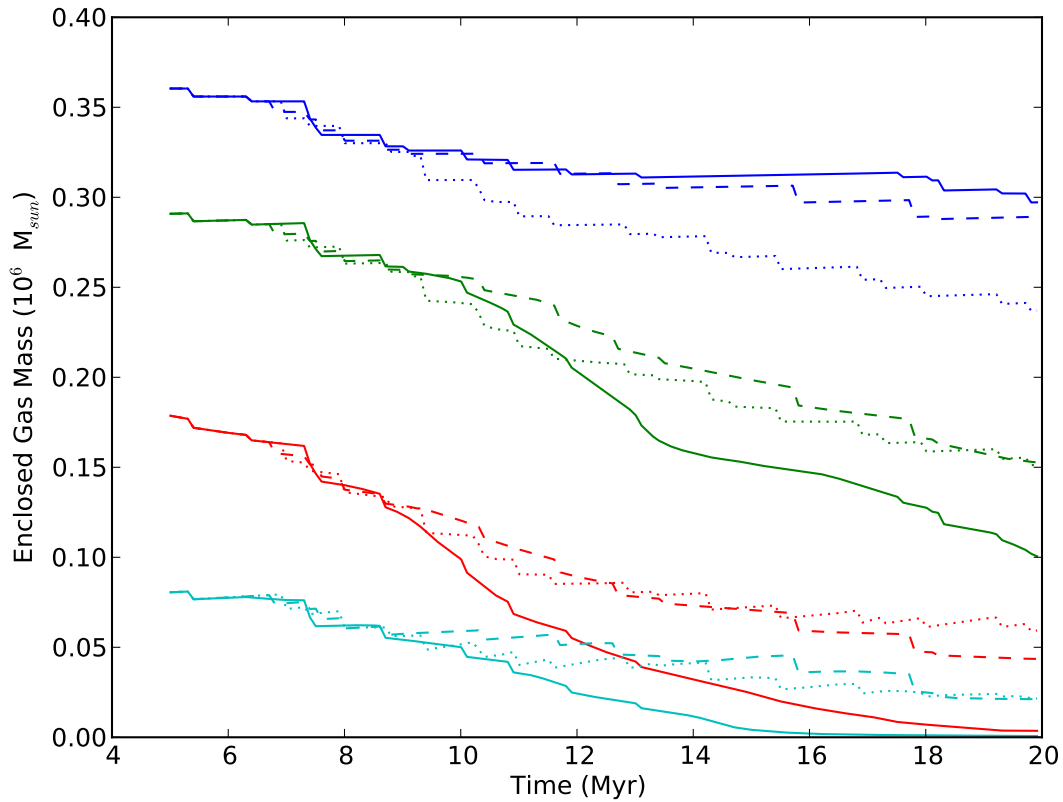
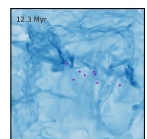


Figure 4.39: The mass structure for three simulations with Varying Q and no radiation pressure. Solid = lowHIII02 (Q reduced by 2), dashed = lowHIII10 (Q reduced by 10), dotted = lowHIII100 (Q reduced by 100). The colour shows which region of the box is being considered: Blue = all, Green = within $2 R_{cl}$ of the centre, Red = within R_{cl} of the centre, and Cyan = within $0.5 R_{cl}$ of the centre. The highest star formation rate is for the lowHIII100 and is comparable for lowHIII02 and lowHIII10. The drop in central mass (cyan) is less than the drop in total mass (blue) for lowHIII02 and lowHIII10. The drop in central mass (cyan) is less than the drop in total mass (blue) for lowHIII100 so gravity is beating the ionizing gas pressure in the centre. In contrast, for lowHIII02 the centre is being evacuated.



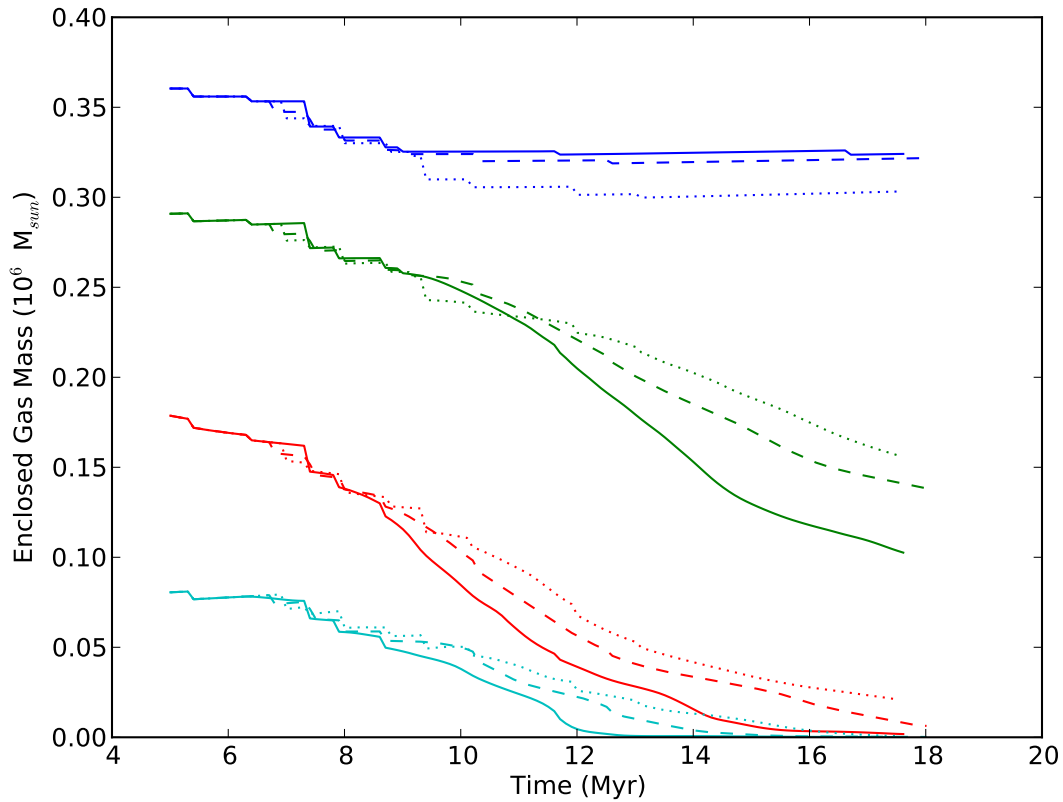
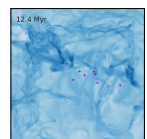


Figure 4.40: The mass structure for three simulations with Varying Q but same emitted momentum in radiation pressure. Solid = RPlowHIII02 (Q reduced by 2), dashed = RPlowHIII10 (Q reduced by 10), dotted = RPlowHIII100 (Q reduced by 100). The colour shows which region of the box is being considered: Blue = all, Green = within $2 R_{cl}$ of the centre, Red = within R_{cl} of the centre, and Cyan = within $0.5 R_{cl}$ of the centre. Comparing to Fig. 4.39 the inclusion of radiation pressure significantly reduces the star formation rate for all values of Q . Despite the lower mass in stars and thus less radiation emitted, the inclusion of radiation pressure still clears out the central region of the cloud significantly faster.



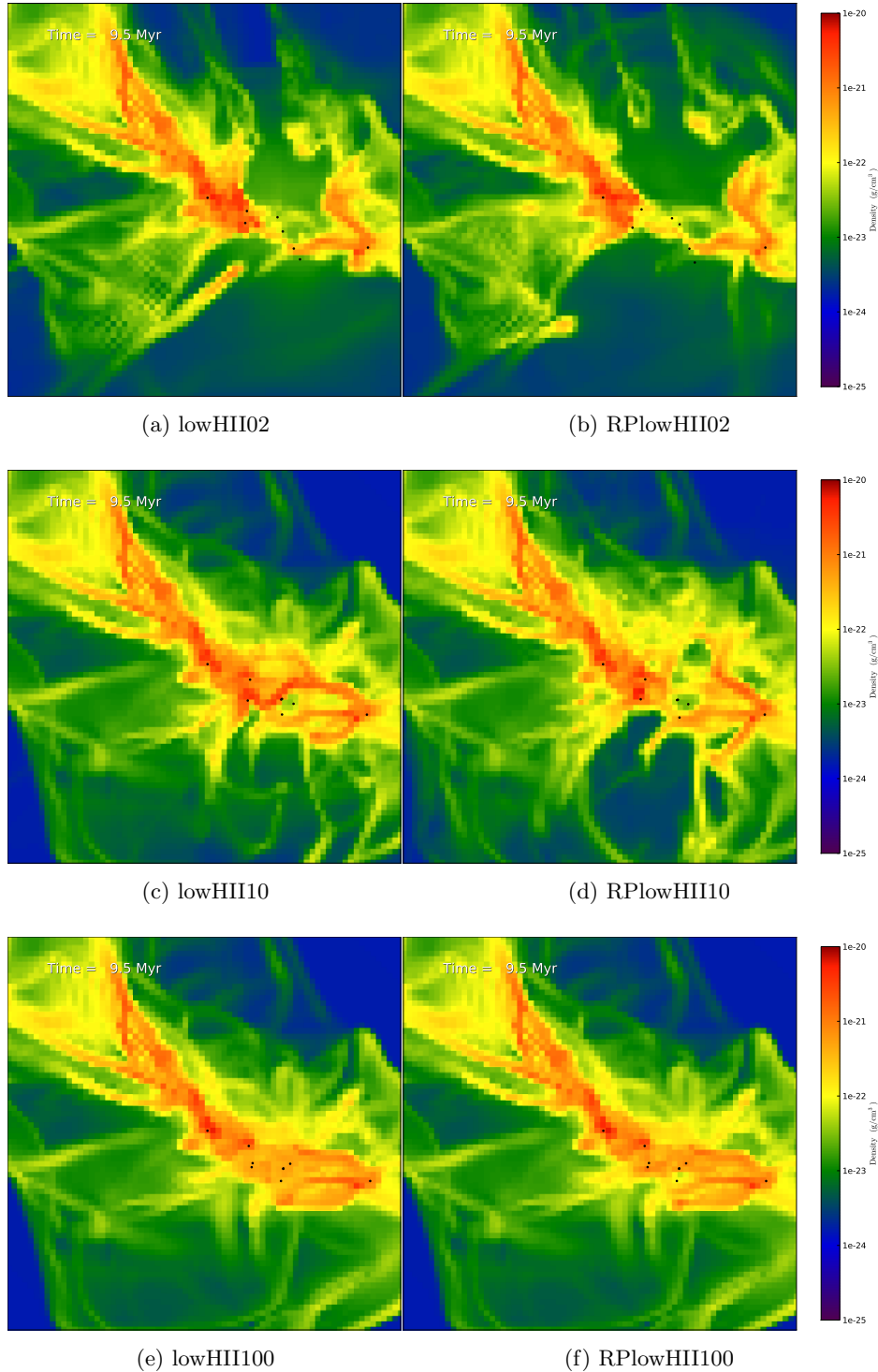
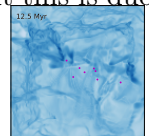


Figure 4.41: Central 100pc projections of density for six simulations with different photon rates and without or with radiation pressure at 9.5 Myrs (4.1 Myrs after the first star cluster formed). For all three reductions in photon rate (Q) the inclusion of radiation pressure has a significant dynamical effect on the gas. For the simulations with Q 100 times lower than the base simulation (lowHIII100, RPlowHIII100) the dynamical difference is the least but this is due to the later start of resolved radiation pressure, Fig. 4.38.



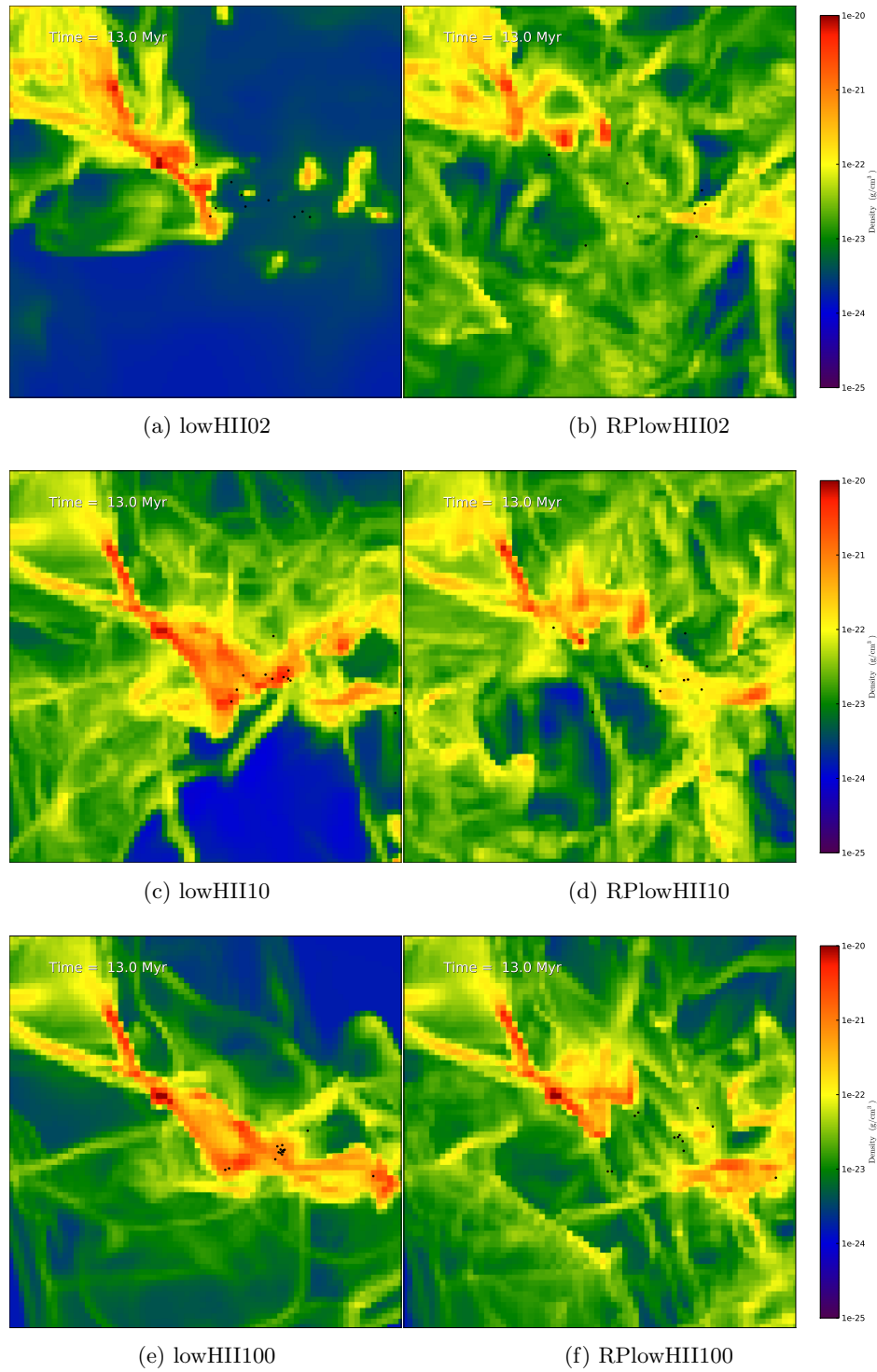
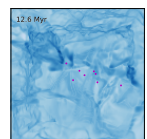


Figure 4.42: Central 100pc projections of density for six simulations with different photon rates and without or with radiation pressure at 13 Myrs (7.6 Myrs after the first star cluster formed). For all three reductions in photon rate (Q) the inclusion of radiation pressure has a significant dynamical effect on the gas for all runs at this later time.



4.3 Surrounding Medium Investigation

For most of the simulations discussed so far the HII region blows out of the cloud and rapidly expands through the surrounding material to the box edge. This could lead to edge effects. To see what effect the surrounding material had upon the simulation I ran an additional simulation with denser surrounding material to slow the expansion of the HII region. The exterior temperature is reduced as shown in Table 4.5. Figure 4.43 shows the density and velocity projections for the base simulation and the simulation with higher external density. The clouds are identical, only the external material is changed.

Name	Density /g cm ⁻³	Temperature /K
box 1, base	1.76×10^{-24}	1000
box1den	1.86×10^{-23}	10

Table 4.5: Conditions of the material exterior to the cloud.

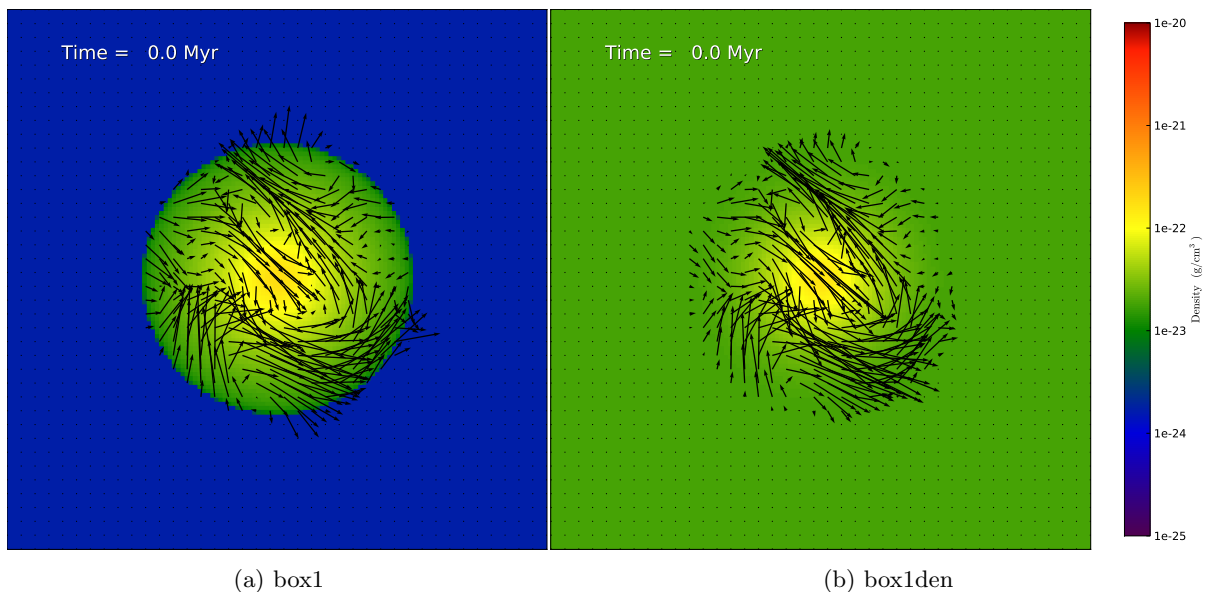
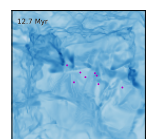


Figure 4.43: Projected Velocity vectors and densities for the simulations in the surrounding medium investigation. The velocity vectors are mostly similar though there are small differences due to projection effects as the projection is density weighted so the exterior has more weight in box1den than the base simulation.



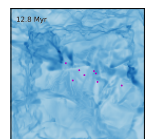
4.3.1 Surrounding Medium Results

The star formation history of the base simulation (box1) and the simulation with higher external density (box1den) is shown in Fig. 4.44. For the higher external density the first star cluster forms in the same location and approximately the same mass and only 0.4 Myrs later. The evolution of the cloud after the star cluster forms is slightly different for the two runs. The higher density outside the cloud means when the radiation starts leaking it does not reach the box edge but gets absorbed by the higher density surrounding medium instead. Figure 4.45 shows the higher external density simulation at 8.8 Myrs, 3.1 Myrs after the first star cluster formation. Comparing to Fig. 4.8, the base simulation at the same time after the first star cluster forms, the confinement of the ionized region can clearly be seen. The star clusters are still in the same location, the same age and approximately the same mass, though there is one more cluster just formed for the base simulation at this time.

The Mass structure of the simulation box for box1 and box1den is shown in Fig. 4.46. Box1den starts with a higher external density so the total mass and mass within $2 R_{cl}$ is higher. Despite the differences in external densities and the small differences in star formation history the inner most region, within $0.5 R_{cl}$ evolves almost identically, especially after 10 Myrs when it is not possible to distinguish the lines anymore. The mass inside the cloud radius is cleared out more slowly with the higher external density as there is a greater density outside the cloud resisting the bubble expansion. Interestingly, it is at approximately the same time that the mass within $2 R_{cl}$ starts declining for both simulations. The higher density means more of the radiation momentum is absorbed within the external gas rather than escaping so has a significant dynamical effect even with the greater inertia in the gas, as can be seen in the radiation force panel of Fig. 4.45.

4.3.2 Surrounding Medium Summary

There is negligible change in the final cluster mass for a simulation with ten times higher density external to the cloud than the base. This suggests there are negligible effects from the box edge during two dynamical times of the simulations.



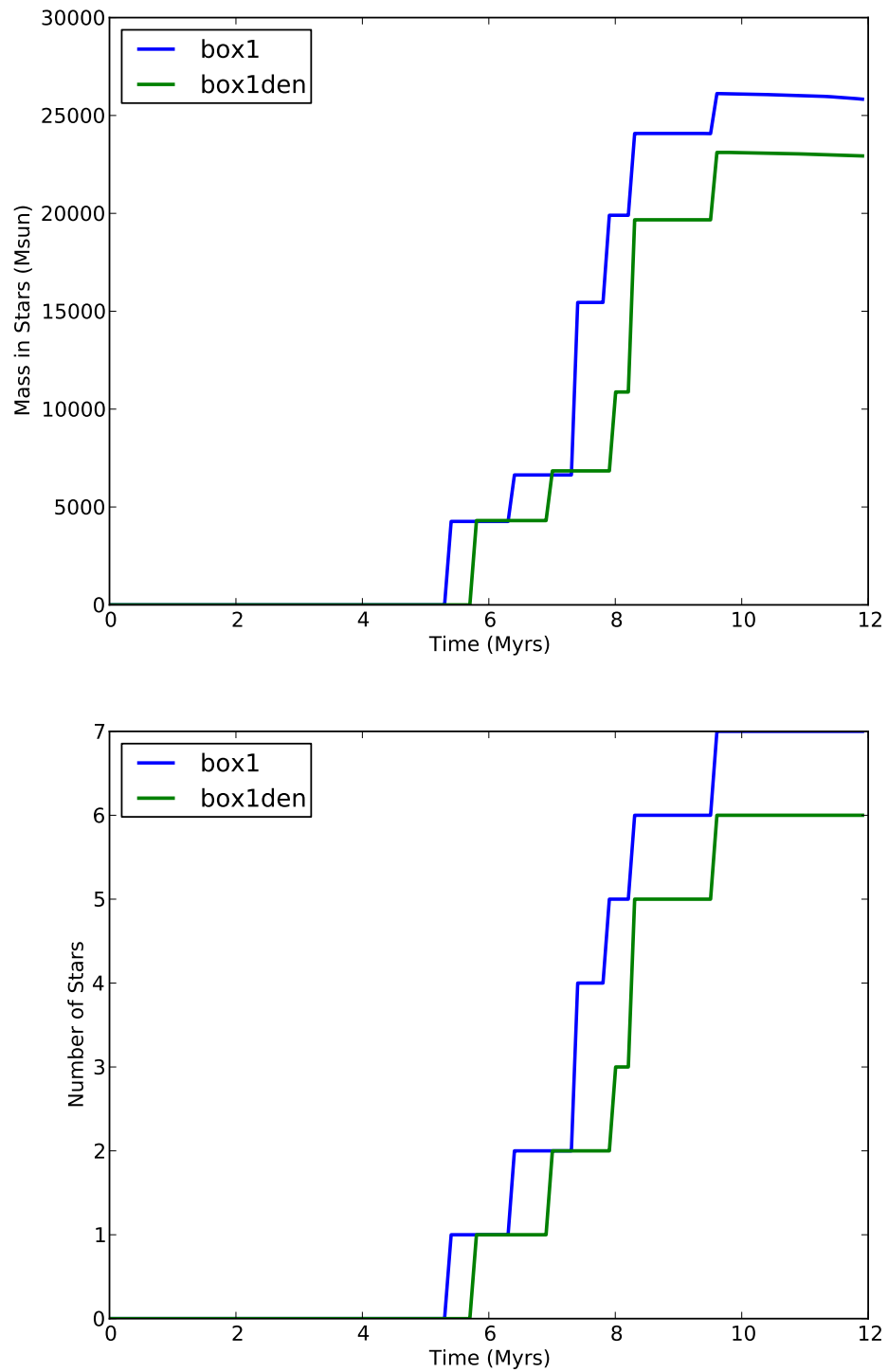
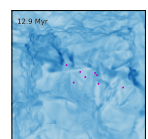


Figure 4.44: The star formation histories for the base simulation (box1) and the same simulation but with higher density external to the cloud (box1den). For the higher external densities star formation begins slightly later but is then very similar.



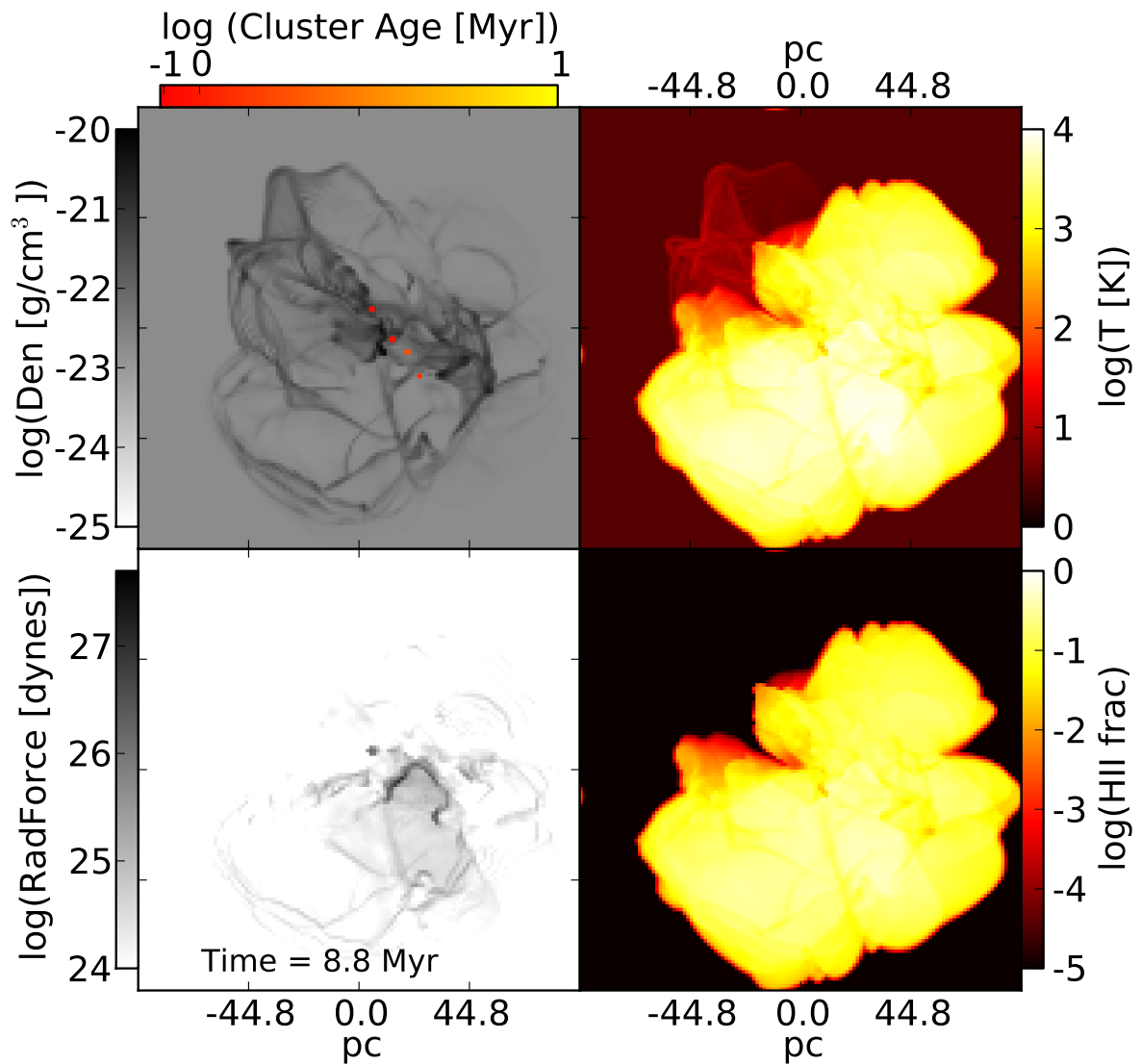
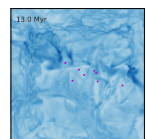


Figure 4.45: Density, temperature, radiation force (momentum deposited), and HII fraction for the simulation identical to base except for surrounding medium density and temperature, at 8.8 Myrs (3.1 Myrs after first cluster formed). Star cluster particles are shown as filled circles on the density projection. Star cluster circle size is relative to mass and colour indicates the age of the cluster at this time. The sum of the radiation force absorbed by the gas in this frame is 1.66×10^{30} dynes. Compare to Fig. 4.8, the base simulations at the same time after first star cluster formation.



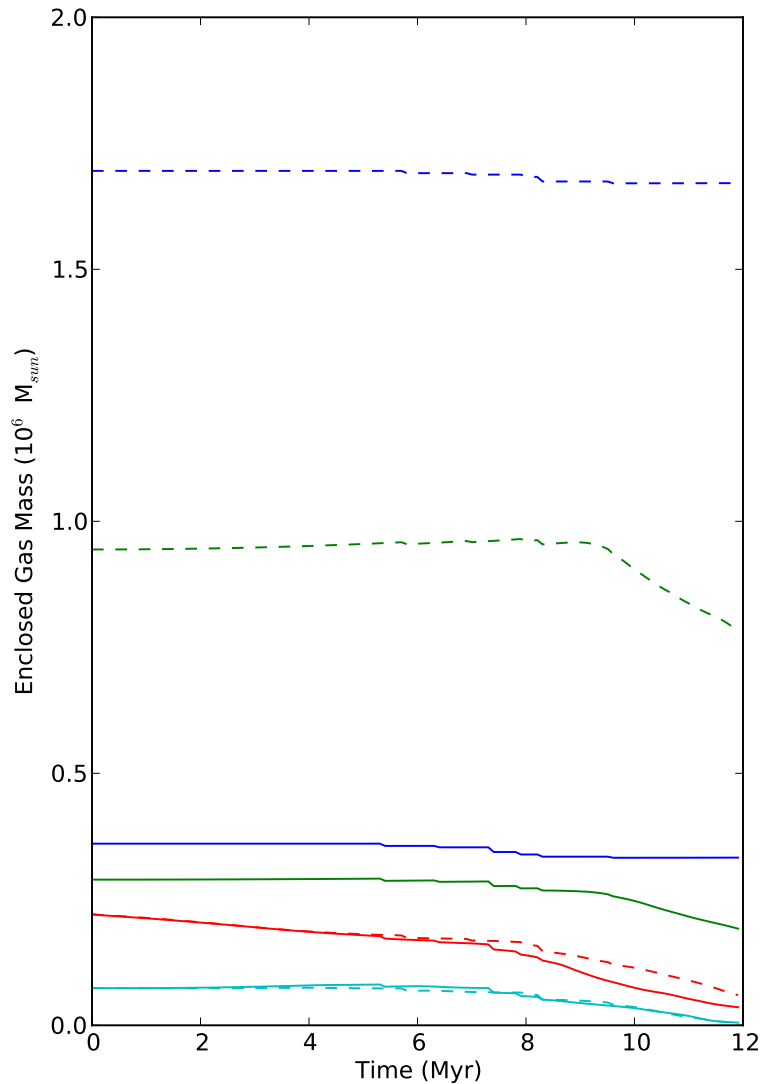
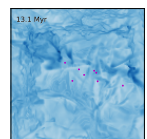


Figure 4.46: The Mass structure for the base simulation (solid lines) and the higher density exterior (dashed lines). The colour shows which region of the box is being considered: Blue = all, Green = within $2 R_{cl}$ of the centre, Red = within R_{cl} of the centre, and Cyan = within $0.5 R_{cl}$ of the centre. For the higher external densities there is more mass outside of the cloud so the all and $2 R_{cl}$ lines are much higher. The structure inside R_{cl} starts identical for both simulations. The inner most region, $0.5 R_{cl}$ (cyan), clears in the same way independent of external density. The total mass within R_{cl} (red) clears more slowly for higher external density as the disruption of the cloud is slowed by the higher external density.



4.4 Magnetic Fields

Enzo has the capacity to simulate magnetic fields as described in §3.2.3. To see how magnetic fields affect the cluster formation and feedback I ran a simulation identical to the base simulation with an initially uniform 10^{-6} Gauss field in the z direction.

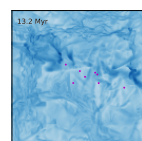
4.4.1 Magnetic Fields Results

Observations of GMC suggest a magnetic field of a few microGauss across the clouds and higher in the denser regions (Crutcher et al., 2010). The turbulence stirs up the gas and increases the magnetic field strength. Figure 4.47 plots the total magnetic energy in the original cloud location and the entire simulation box with time and Fig. 4.48 the kinetic energy. As can be seen, the turbulence rapidly increases the magnetic energy by close to an order of magnitude for inside the cloud setting the average magnetic field strength to a few microGauss as observed. The kinetic energy is much higher than the magnetic energy.

Figure 4.49 shows the mass in star clusters against time for the base simulation (blue) and the simulation with magnetic fields (green). The first star cluster is almost identical in both simulations suggesting the magnetic field has had little hinderance on the turbulence and gravitational collapse thus far. However, star cluster formation diverges after that with the second cluster taking longer to form but being more massive. By 10 Myrs the cluster formation appears to be quenched for the magnetic field case, finishing with 19,103 M_{\odot} or 8.7 % of the original cloud mass in clusters. The earlier quenching can be explained by examination of Fig. 4.50. Figure 4.50 shows the mass structure against time for the base simulation (solid) and the magnetic simulation (dashed). Despite the lower mass in stars, the inner most region (cyan) of the cloud is cleared out faster for the simulation with a magnetic field. The mass within the original cloud location (red) also appears to be cleared faster but not as significantly.

Images of the simulation with magnetic fields at 9.5 Myrs are shown in Fig. 4.51. Compared to Fig. 4.9 the HII region is more confined around the star clusters and the density structure is less well defined. Hot gas is still leaking out but not blowing out the way it did in the base simulation. This suggests that the magnetic field is resisting the leaking of the bubble by holding the material together. A less leaking bubble means the pressures are higher within the bubble and there is more material absorbing radiation pressure. Hence the more rapid mass reduction in the inner region seen in Fig. 4.50.

Density projections with arrows indicating projected magnetic field for four different times are shown in Fig. 4.52. The arrow size indicates relative strength of magnetic field within each image but with a different scale for each image. The compressing of magnetic field lines



and subsequent strengthening of the magnetic field can be clearly seen along the turbulent filaments. At 8.4 Myrs a bubble shell is visible and the swept up magnetic fields are significant. The magnetic field in the shell lines up parallel to the shell. Inside the bubble the magnetic field lines seems to be perpendicular to the shell, in agreement with Arthur et al. (2011). This explains the lower leakage rates of the bubble and, thus, the faster reduction in mass of the interior of the cloud. By 10.4 Myrs the periodic boundary conditions can be clearly seen with the increasing magnetic field strength at the box edges where material is wrapping around. The increased mass in a bubble shell is clearly shown in Fig. 4.53 - full width density slices through the centre of the simulation box for the base and magnetic simulations at 9.0 Myrs.

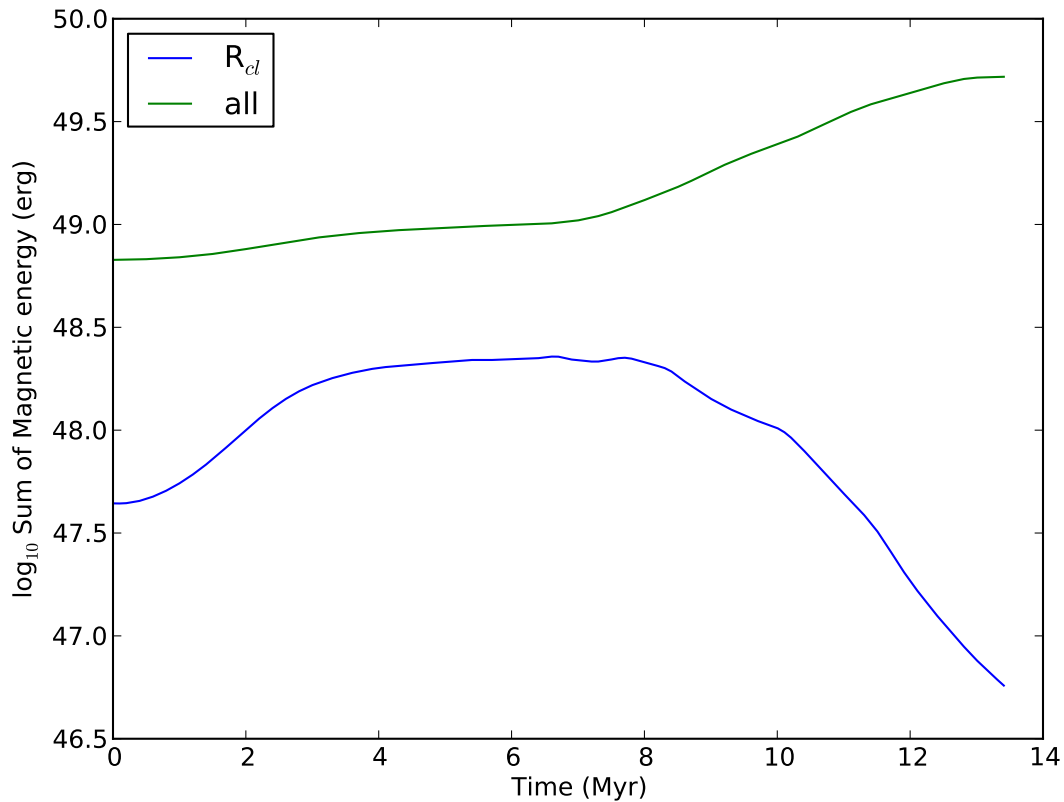
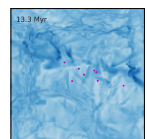


Figure 4.47: The magnetic energy within the original cloud location and the whole simulation box against time. The turbulence inside the cloud rapidly drives up the magnetic energy by close to an order of magnitude. After 8 Myrs the cloud is being disrupted and this reduced the magnetic energy in the cloud but drove up the energy in the whole box as edge effects become significant.



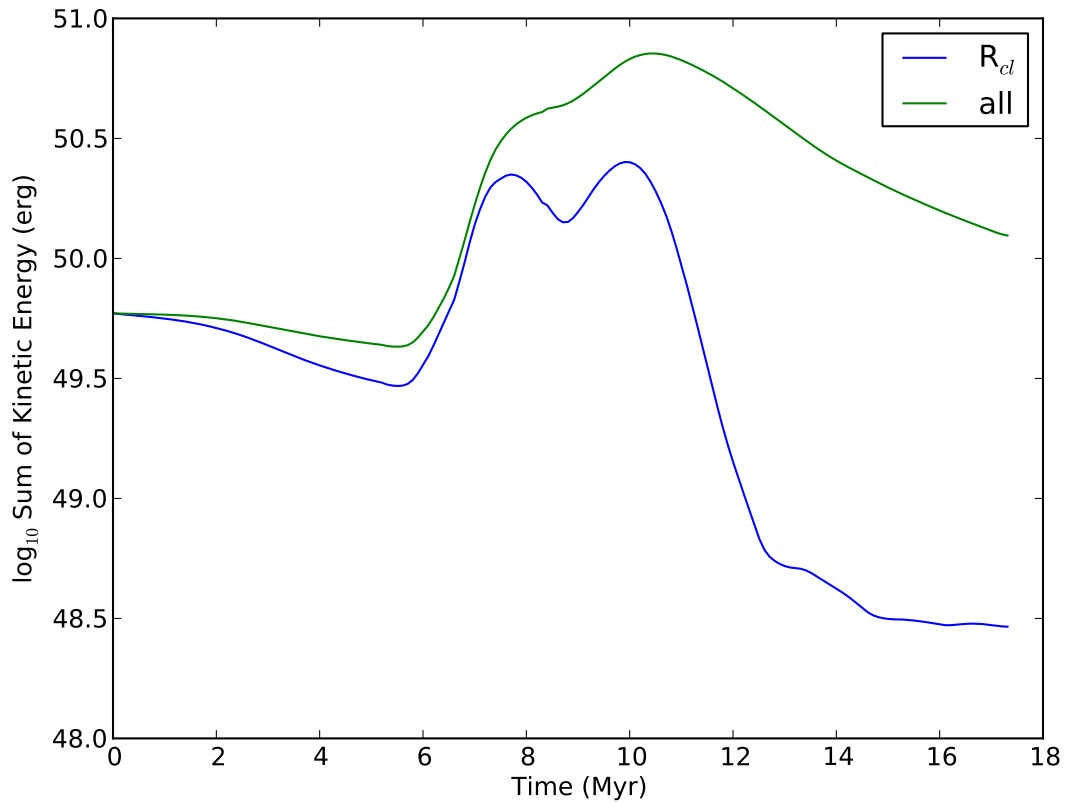
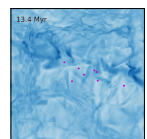


Figure 4.48: The sum of kinetic energy within original cloud location and entire simulation box for the magnetic simulation. As the turbulence decays the kinetic energy reduces until star cluster formation begins and the outputs start driving the kinetic energy back up again. The kinetic energy is substantially greater than the magnetic energy.



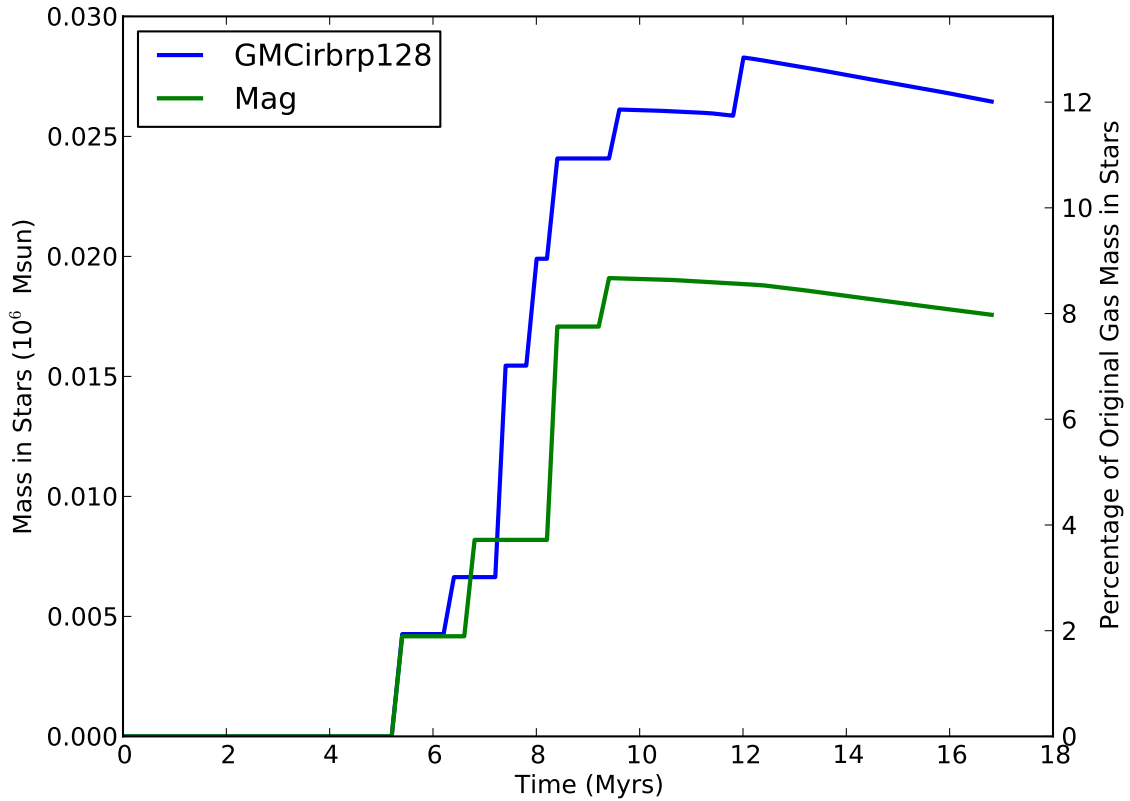
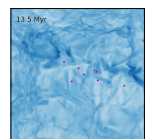


Figure 4.49: The total mass in star cluster particles for *blue* the base simulation and for *green* the simulation with magnetic fields. The first cluster is almost identical but the cluster formation diverges after that with a lower mass in clusters for the simulation with magnetic fields by the time cluster formation is quenched.



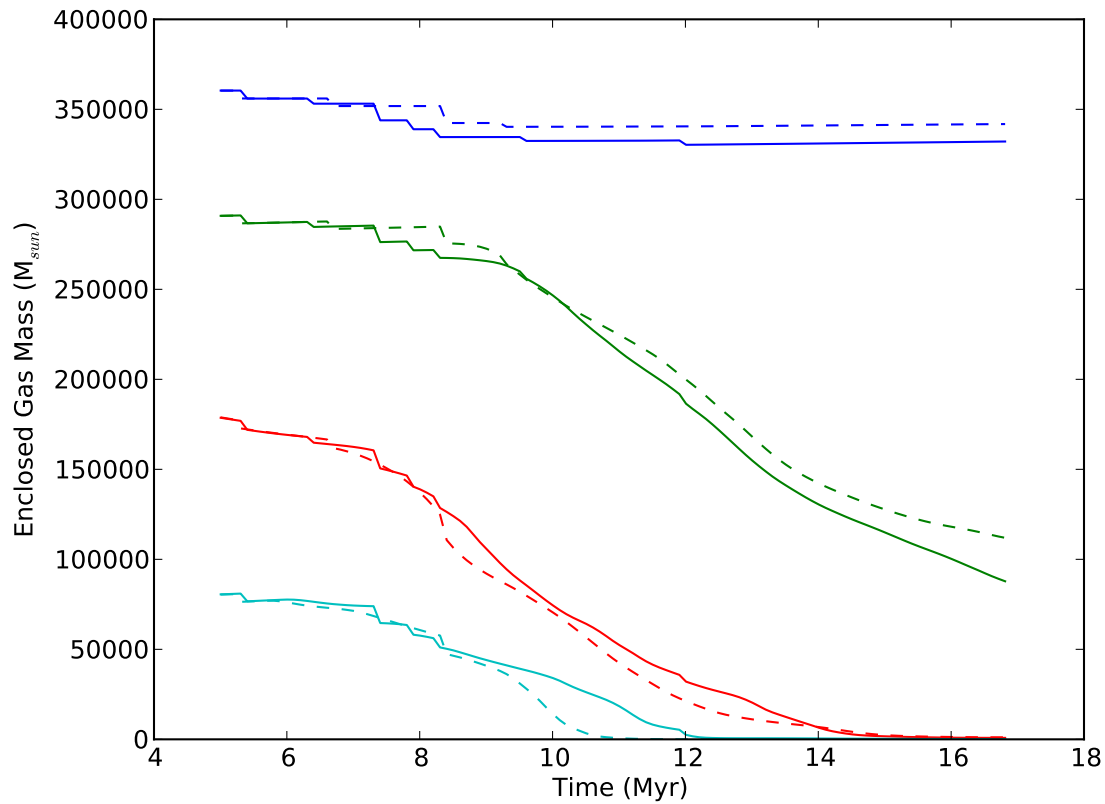
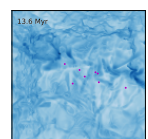


Figure 4.50: The mass structure for the base simulation (solid) and base simulation with a magnetic field (dashed). The lines show the cumulative mass for 0.5, 1 and 2 times the original cloud radius and for the whole simulation box. The drops in total mass (blue line) show conversion of gas mass into star cluster particles. The inclusion of magnetic fields causes the inner most region ($0.5 R_{cl}$, cyan) to be evacuated faster despite a lower mass in clusters and thus less energy and momentum output from the star clusters.



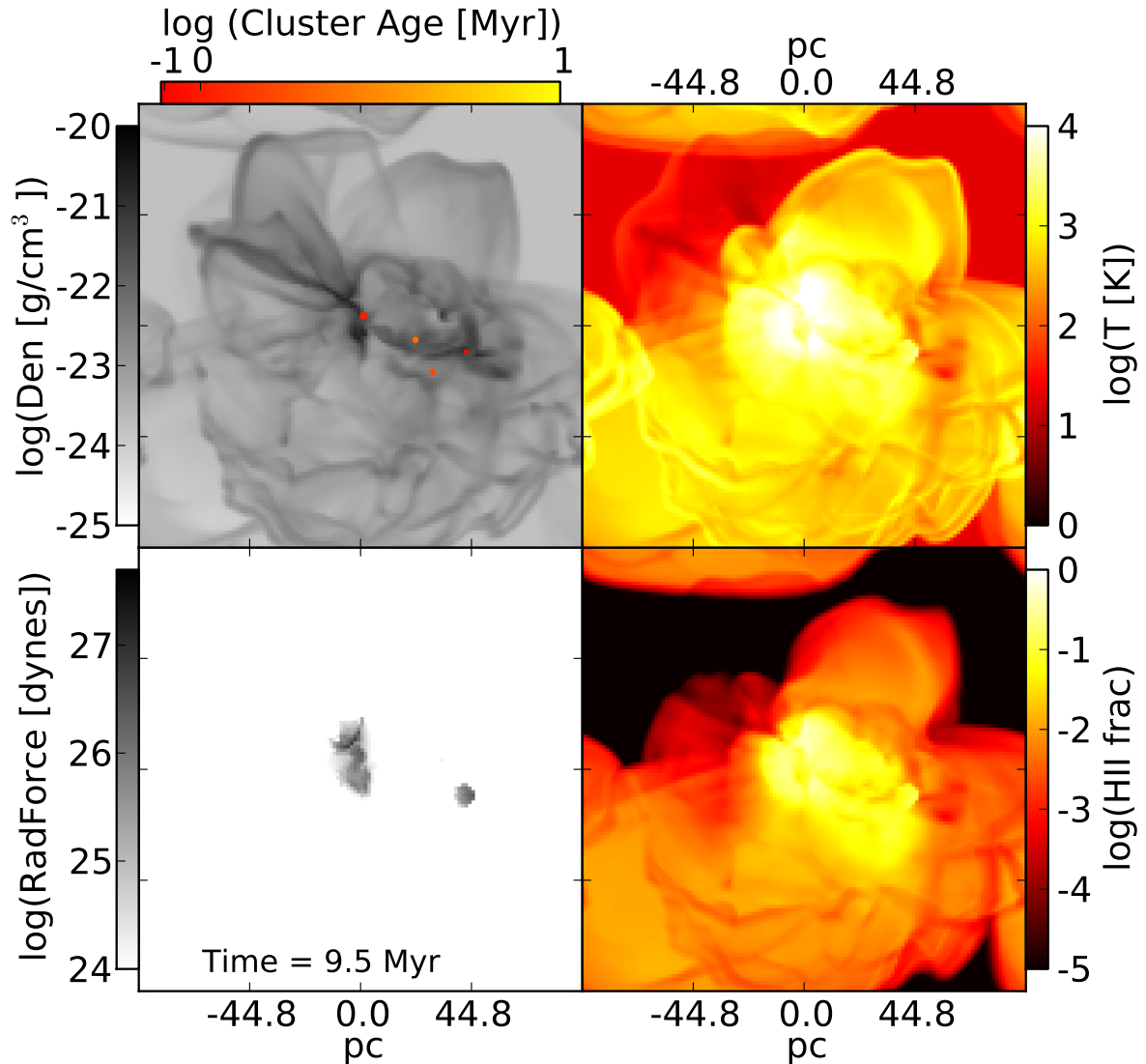
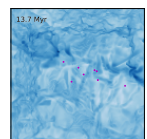


Figure 4.51: Density, temperature, radiation force (momentum deposited), and HII fraction for the simulation with a magnetic field at 9.5 Myrs (4.2 Myrs after first cluster formed). Star cluster particles are shown as filled circles on the density projection. Star cluster circle size is relative to mass and colour indicates the age of the cluster at this time. Compared to Fig. 4.9, the HII region is more confined with less gas and radiation leaking out.



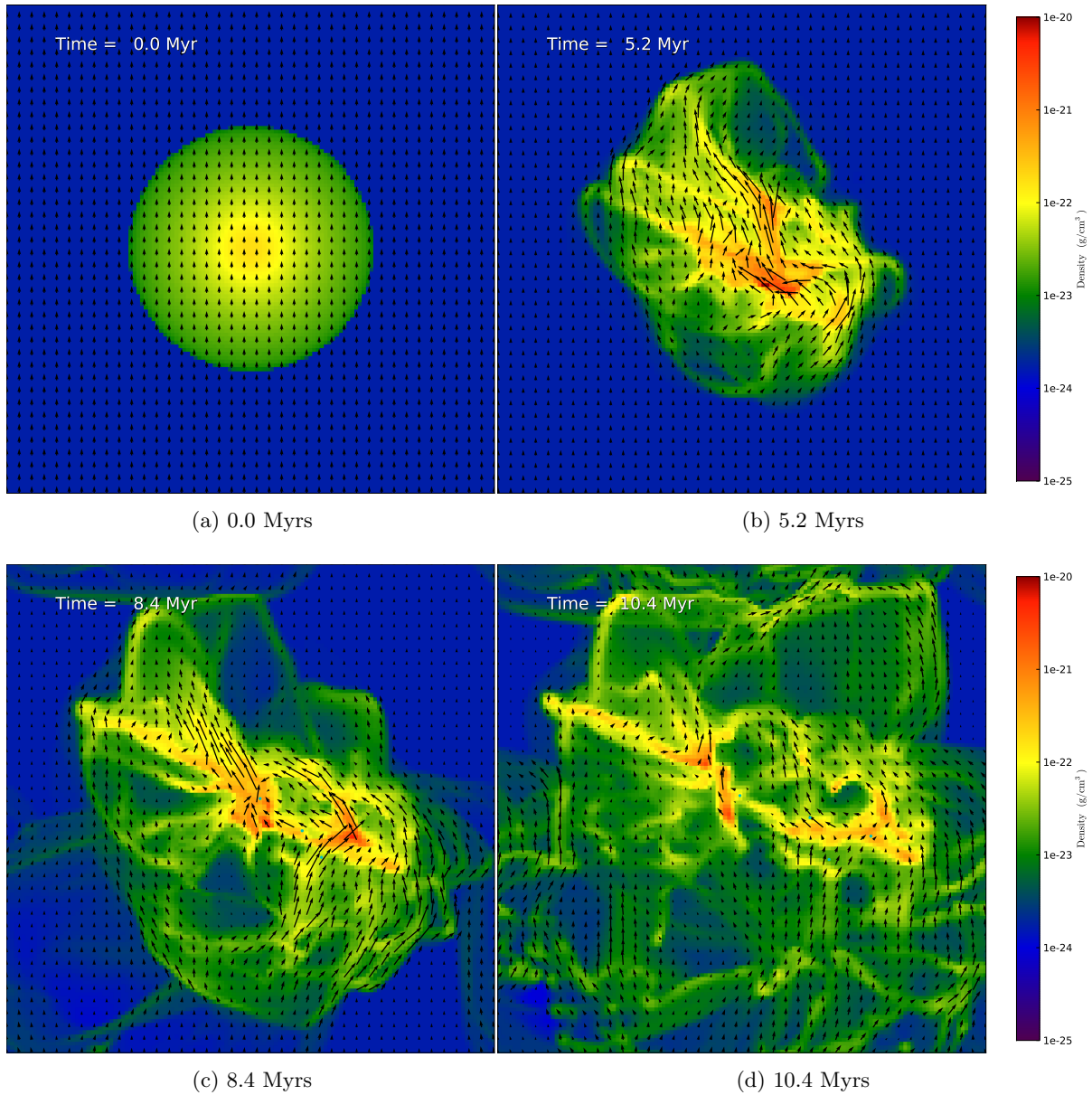
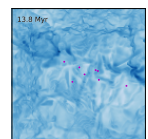


Figure 4.52: Projections of density and magnetic field for the simulation with an initial 10^{-6} Gauss uniform z direction field at different times throughout the simulation. Star clusters are shown as cyan points. Magnetic fields are stronger in filaments and are swept up in the bubble shell.



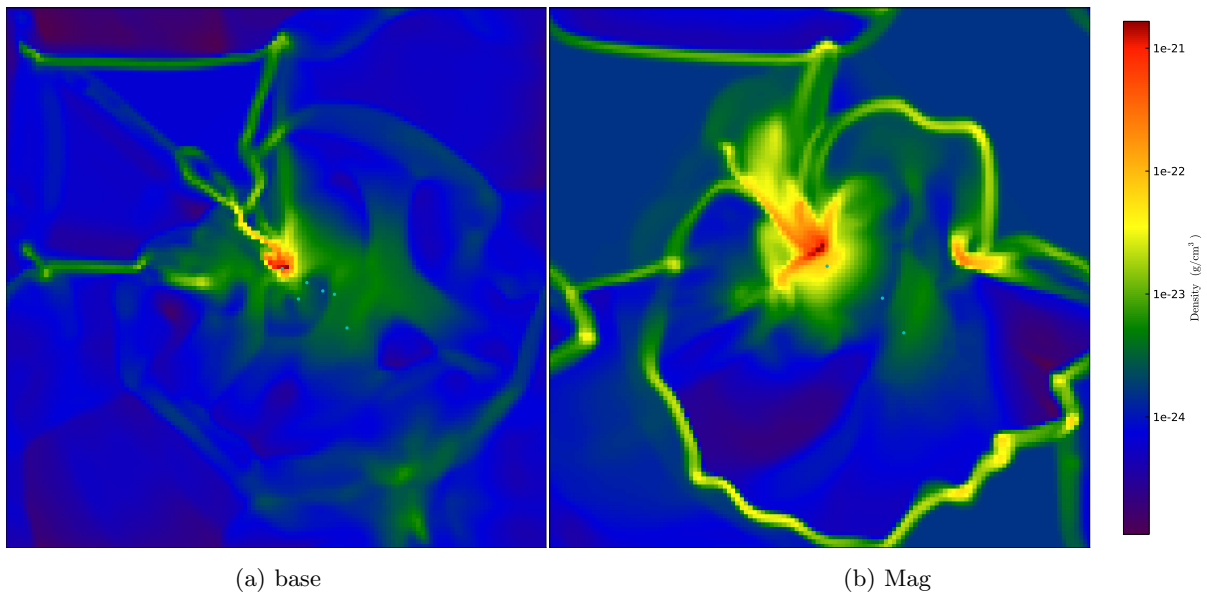
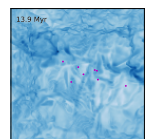


Figure 4.53: Density slices through the centre of the simulation box for *left*: the base simulation and *right*: the simulation with magnetic fields at 9 Myrs. The density scales are identical for both slices. A clear difference in mass in a shell is visible. Higher external density and lower internal density can also be discerned for the simulation with magnetic fields.



4.5 Cloud Mass

All of the previous results are for a relatively small GMC, $0.2 \times 10^6 M_\odot$. To see if the results are valid for more massive clouds I reproduced the simulations for a cloud twice the physical size and the same surface density. Again, I started with a single base simulation set up to be equivalent to the base simulation for the smaller cloud.

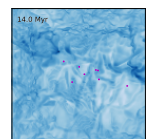
4.5.1 More Massive Cloud Base Simulation

Physical Quantity	Value
Box Size	358.4 pc
Grid Structure	256^3 (no AMR)
Cloud Radius	89.6 pc
Cloud Mass	881,000 M_\odot
Total Mass	1,441,739 M_\odot
Cloud Dynamical Time	9.5 Myrs
Cloud Half Mass Dynamical Time	6.8 Myrs
Turbulence Mach Number	20

Table 4.6: Physical Details for the initial setup of the massive cloud base simulation.

For the more massive cloud base simulation, the simulation box is a cube, 358.4 pc on each side with a 256^3 grid (1.4 pc resolution still). At the centre of the simulation cube is a spherical cloud of radius 89.6 pc. This cloud has a mass of 881,000 M_\odot , four times that of the base simulation. The cloud has a dynamical time, $t_{dyn} = \sqrt{R^3/2GM} = 9.5$ Myrs. The half mass radius of the cloud is $0.633 r_{cl}$ and has $t_{dyn} = 6.8$ Myrs.

Exterior to the cloud the material is homogeneous with a density of $\rho = 1.76 \times 10^{-24}$ g cm $^{-3}$ ($n = 1.05$ cm $^{-3}$). This gives a total mass in the simulation box of 1,441,739 M_\odot , again, four times that of the base simulation. The cloud is approximately virial in turbulence and gravity and starts with Mach 19 turbulence with the same initial structure as the base simulation. Figure 4.54 *left* shows the projected density and temperature at the start. The central density is lower than the base simulation since it is the surface density that has been kept constant, not the volume density. Figure 4.55 *left* shows projected velocity arrows on the projected density for the initial turbulence. The turbulence was initialized to be identical in structure just scaled up to maintain the gravity-turbulence balance in the cloud.



After 7.2 Myrs the same turbulent structure can be seen as in the base simulation at 5.4 Myrs, Figs. 4.54 *right* and 4.55 *right*. The time scales are longer for the more massive base simulation given its longer dynamical time.

The star cluster formation parameters for the more massive cloud simulations are:

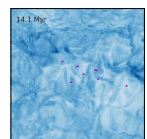
PopIIIOverDensityThreshold = 2×10^4 - two times higher than for the lower mass cloud base but the mean density for the simulation box is half for the more massive cloud base so both simulations have the same critical volume density.

StarClusterMinDynamicalTime = 2×10^6 years - same as for the lower mass cloud base.

StarClusterFormEfficiency = 0.5 - same as for the lower mass cloud base.

StarClusterMinimumMass = $1000 M_{\odot}$ - same as for the lower mass cloud base.

Figure 4.56 shows the column density through the cloud at the simulation set up and just before star cluster formation.



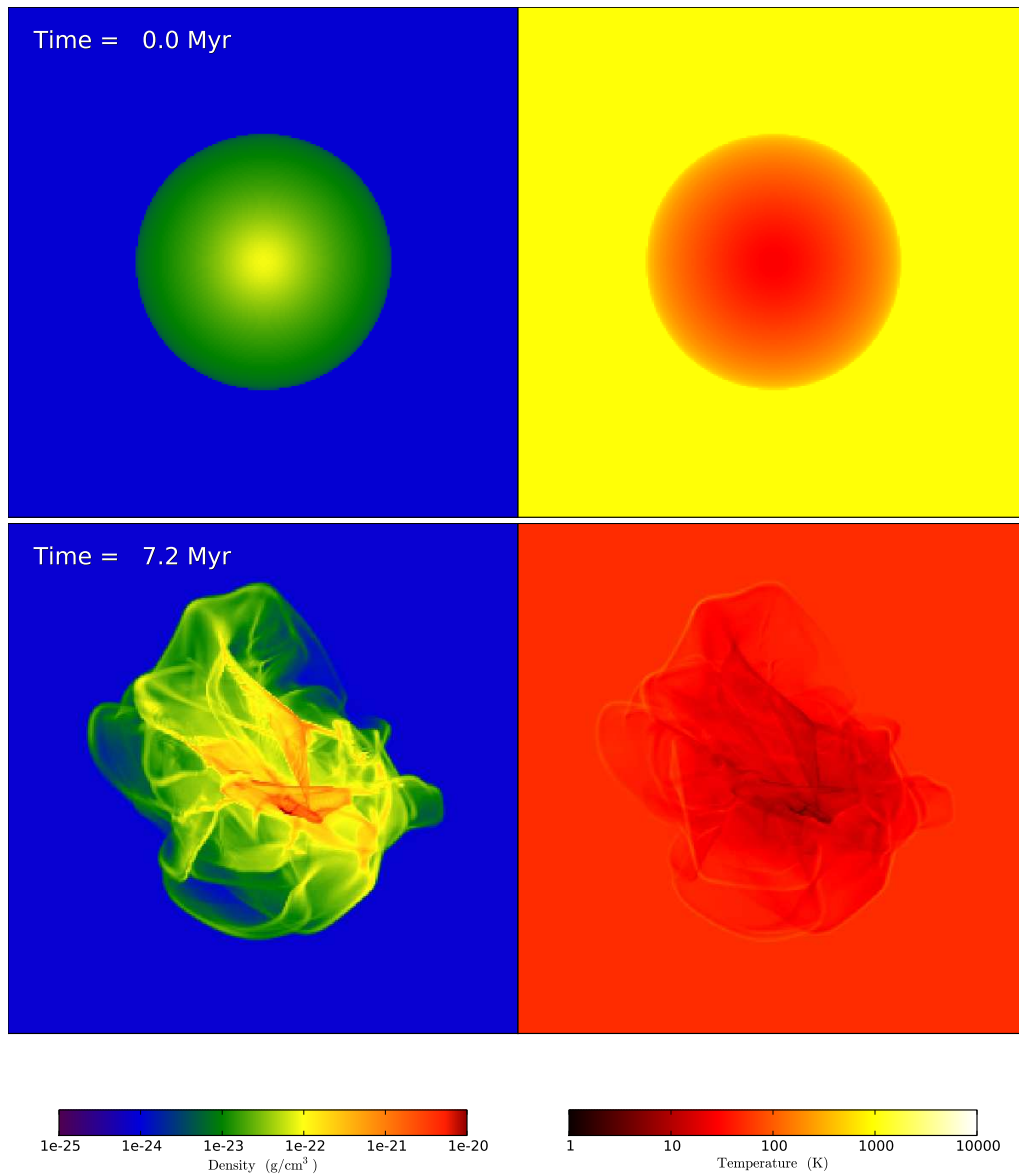
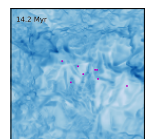


Figure 4.54: *Top:* The cored isothermal sphere embedded in a homogeneous medium for the more massive cloud base simulation at the simulation start. *Bottom:* Within one dynamical time after the more massive base simulation starts a complex turbulent structure can be seen with many filaments and non-spherical features. The structure seen is extremely similar to that for the base simulation, Fig. 4.1. The filaments look thinner as the box is twice as large in this simulation. *Left:* The projected density (density weighted mean density) along the x axis. *Right:* The temperature projected along the x axis. Note the external gas has cooled significantly over the 7 Myrs between images as there is no source of heating yet.



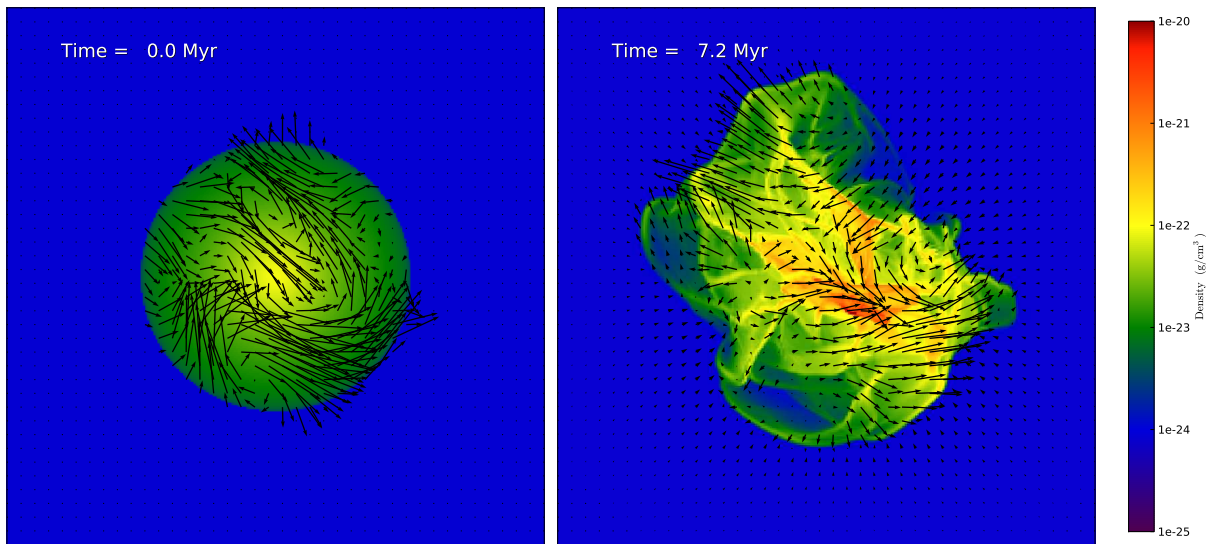


Figure 4.55: *Left*: Projected velocity vectors over-plotted on a density projection for the more massive cloud base simulation to show the initial turbulence at the simulation start. Arrow magnitude shows velocity magnitude. Note the same velocity structure as the base simulation, Fig. 4.2. *Right*: Velocity vectors on a density projection within one dynamical time of the more massive cloud base simulation showing the continued turbulence prior to star cluster formation. Arrow length is proportional to velocity magnitude.

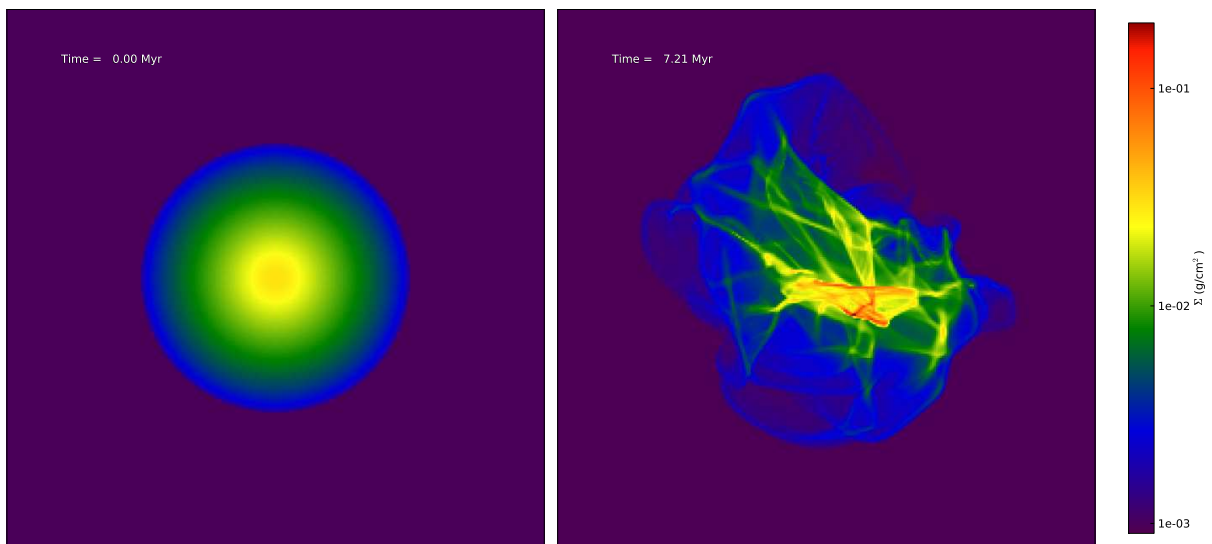
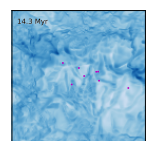


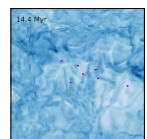
Figure 4.56: The column density through the x axis of the more massive cloud base simulation *left*: at simulation set up and *right*: just before star cluster formation begins.



4.5.2 More Massive Cloud Base Results

Figure 4.57 shows the mass in star clusters against time for the more massive cloud. The simulation forms 11.1% of the original gas into star clusters, comparable to the lower mass cloud base simulation. Similarly to the base simulation, the first cluster forms within one dynamical time and it takes just less than another dynamical time for the star formation to be significantly quenched. Projections of density, temperature, radiation force absorbed, and ionization fraction for the more massive simulation are shown in Figs. 4.58-4.61. At 9.5 Myrs (Fig. 4.58) one of the HII regions is starting to break out and leak into the surroundings. The clusters are forming in the same regions as in the lower mass cloud, as would be expected given the same initial velocity structure. By 11.5 Myrs (Fig. 4.59) the HII regions have combined into one bubble with a distinct bubble shell as seen in the radiation force absorption. The ionization is still mostly contained within the cloud and the leaked gas has not filled the whole volume yet. The more massive cloud and box size is apparent at 13.5 Myrs (Fig. 4.60) as even at 5 Myrs after the first star cluster formed there is gas within the simulation box that is still cool and unionized. By 13.5 Myrs the bubble has blown out with no discernible shell remaining above and below the first star clusters. The final figure in this series, Fig. 4.61, shows the significant effect of the ionizing luminosity reducing as the clusters age. The external gas is recombining and cooling.

Figure 4.62 shows the mass structure for the more massive mass base simulation. The mass within the original cloud location is being reduced as outputs push material away. Both the innermost region (cyan) and the original cloud location (red) only start rapid mass reduction after 12 Myrs. The more massive cloud's dynamical time is 1.4 times longer than the base simulation so relative to dynamical time the clouds are being disrupted at a similar rate. The base simulation has cleared $0.5 R_{cl}$ in 12 Myrs ($1.8 \tau_{dyn}$) and R_{cl} in 16 Myrs ($2.4 \tau_{dyn}$). The more massive cloud has almost cleared $0.5 R_{cl}$ by 17 Myrs ($1.7 \tau_{dyn}$) in agreement with the base simulation.



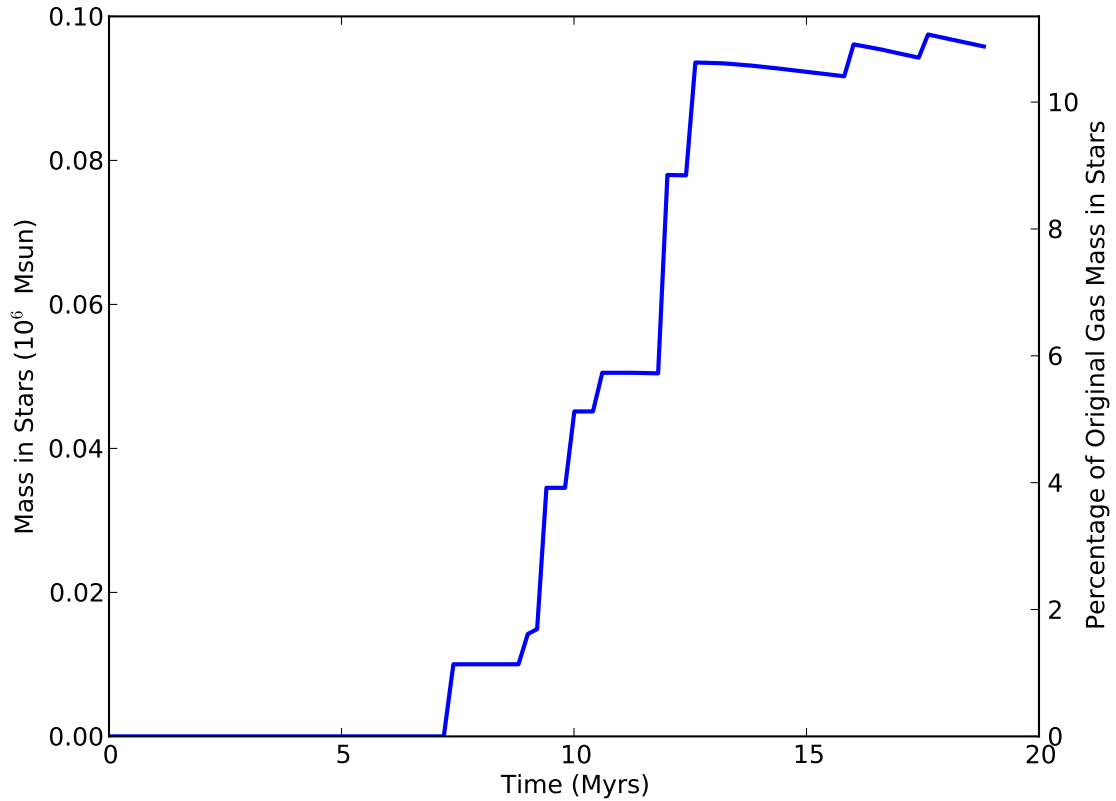
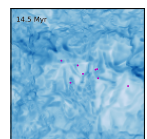


Figure 4.57: The total mass in star cluster particles for the base simulation. The original cloud gas mass in the simulation was $881,000 M_{\odot}$. Similarly to the lower mass cloud base simulation the first cluster forms within one dynamical time and the star formation rate is greatly reduced by another dynamical time giving a burst of star formation.



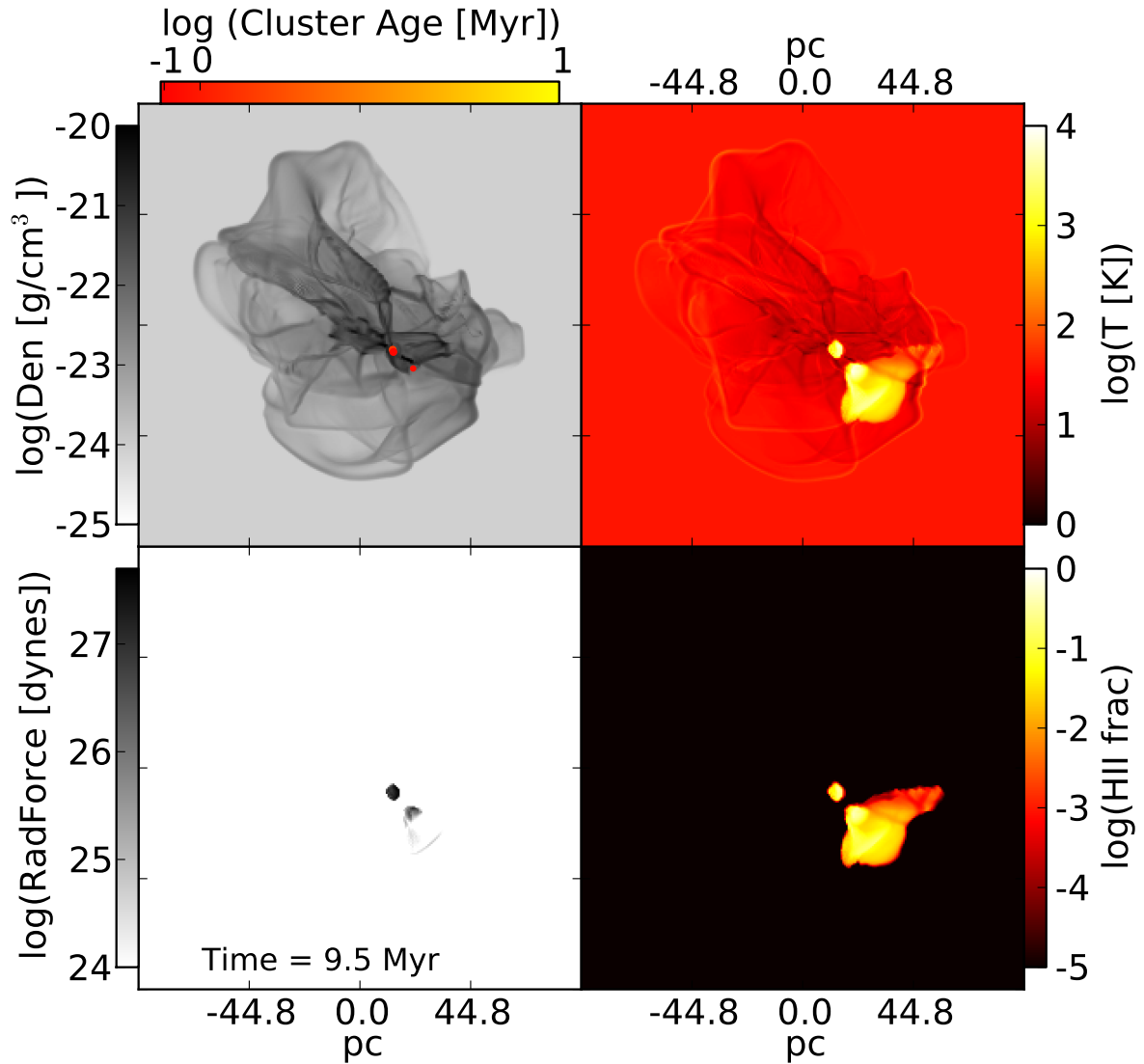
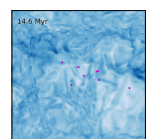


Figure 4.58: Density, temperature, radiation force (momentum deposited), and HII fraction for the more massive cloud base simulation at 9.5 Myrs (1.1 Myrs after first cluster formed). Star cluster particles are shown as filled circles on the density projection. Star cluster circle size is relative to mass and colour indicates the age of the cluster at this time. One HII region is starting to break out along low density direction.



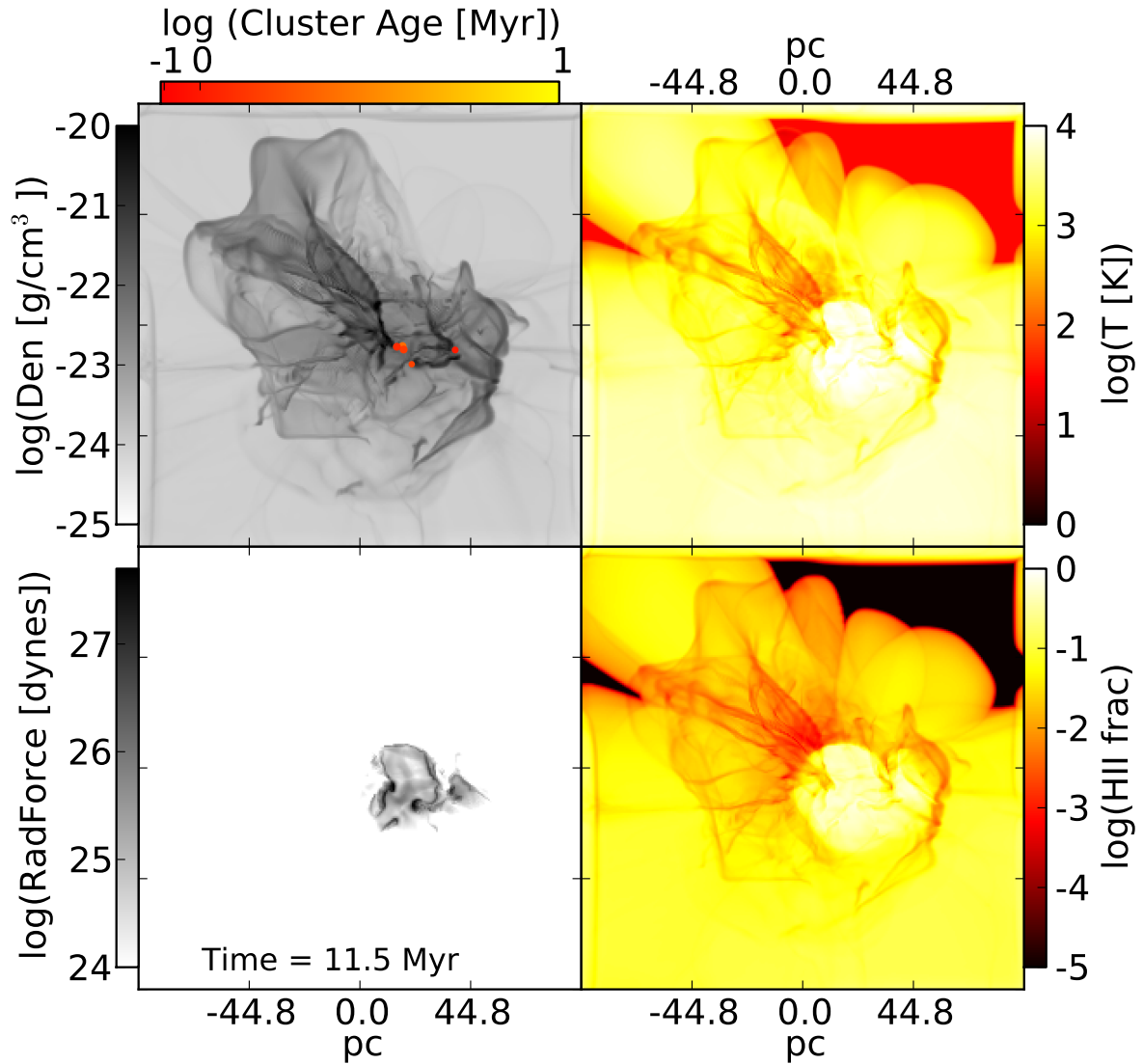
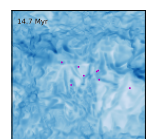


Figure 4.59: Density, temperature, radiation force (momentum deposited), and HII fraction for the more massive cloud base simulation at 11.5 Myrs (3.1 Myrs after first cluster formed). Star cluster particles are shown as filled circles on the density projection. Star cluster circle size is relative to mass and colour indicates the age of the cluster at this time. There is a clear bubble shell formed around the clusters and the hot gas is leaking into the surrounding material.



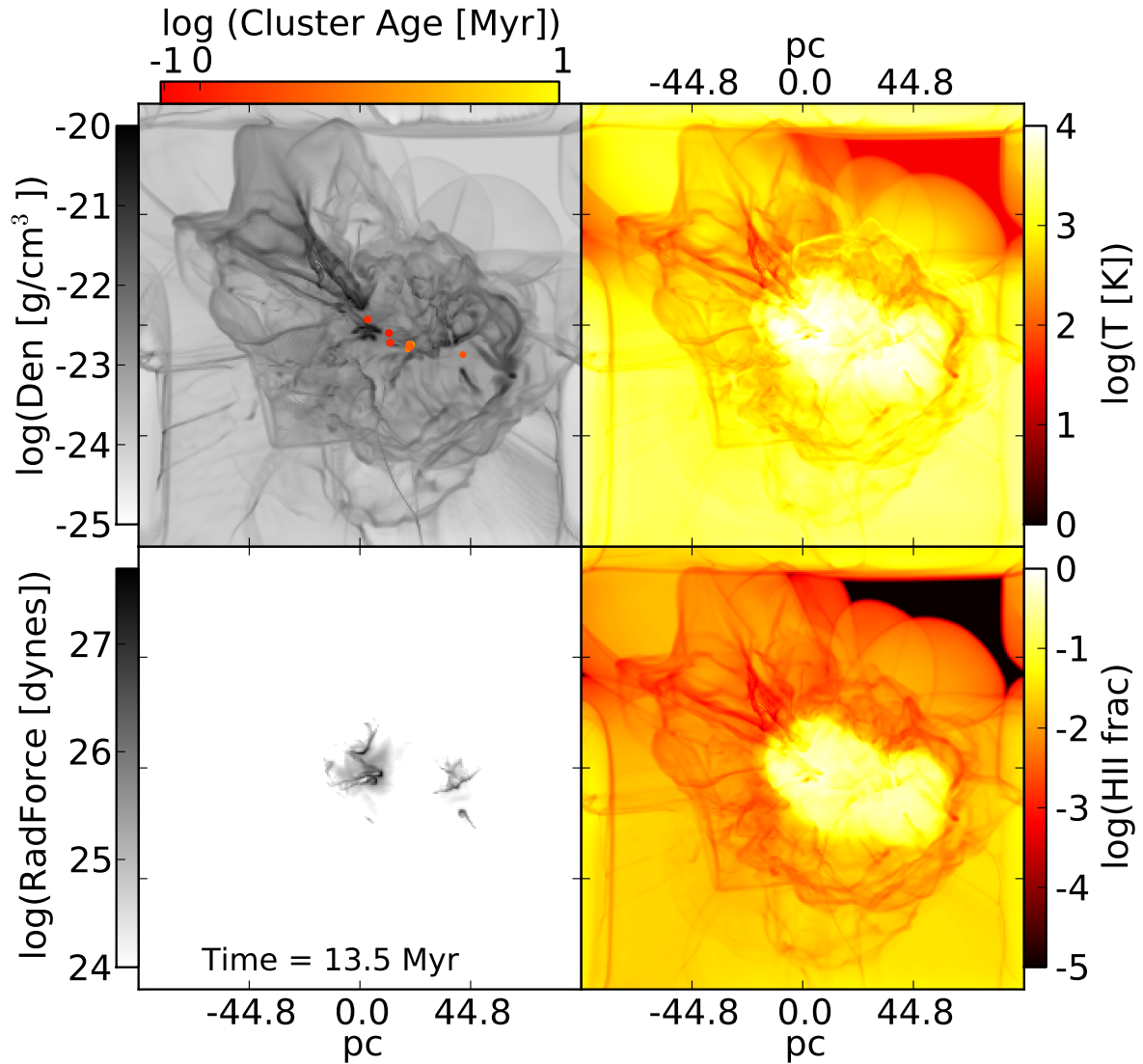
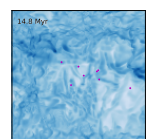


Figure 4.60: Density, temperature, radiation force (momentum deposited), and HII fraction for the more massive cloud base simulation at 13.5 Myrs (5.1 Myrs after first cluster formed). Star cluster particles are shown as filled circles on the density projection. Star cluster circle size is relative to mass and colour indicates the age of the cluster at this time. The bubble has blown apart and the density is significantly disrupted.



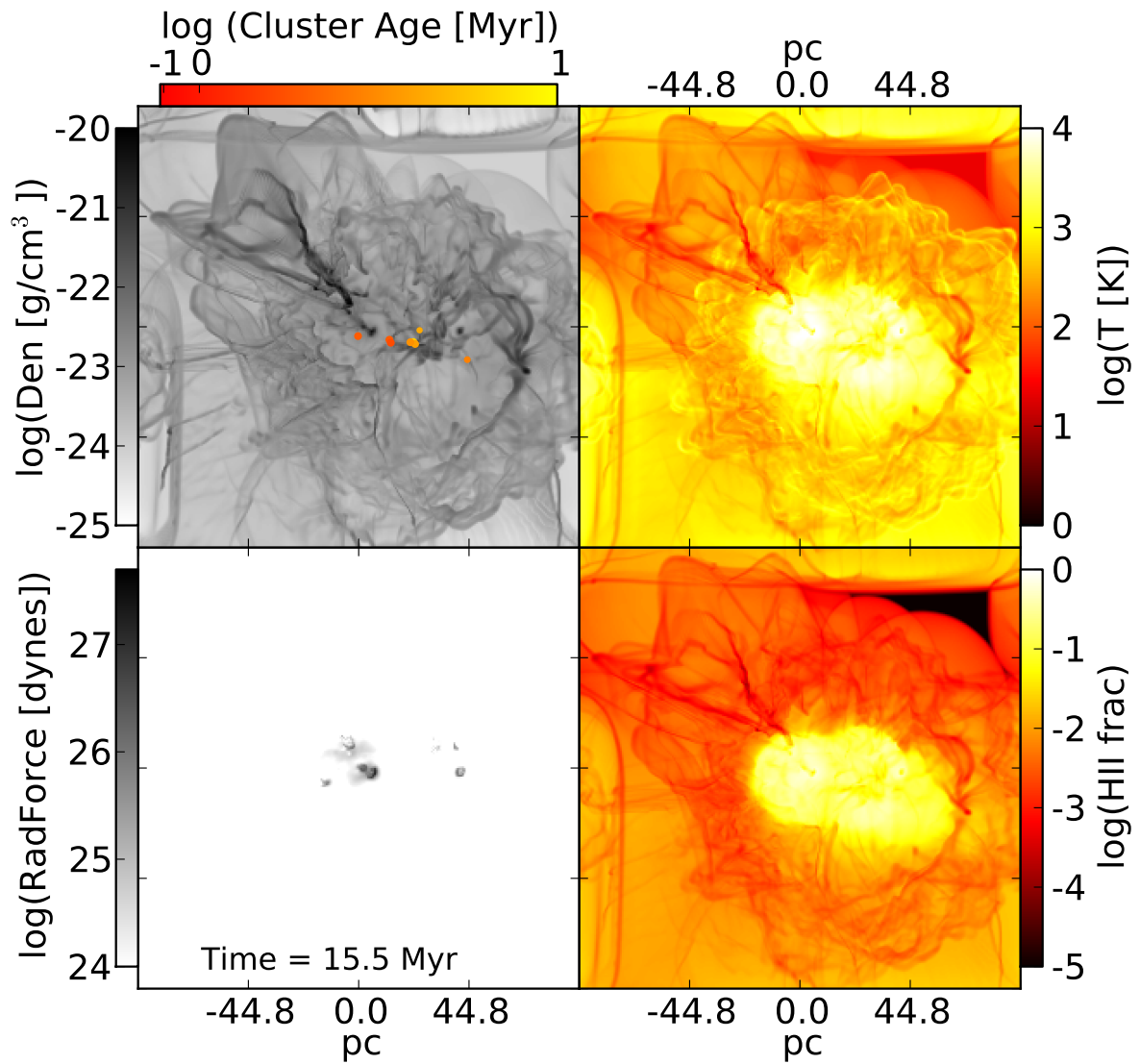
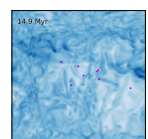


Figure 4.61: Density, temperature, radiation force (momentum deposited), and HII fraction for the more massive cloud base simulation at 15.5 Myrs (7.1 Myrs after first cluster formed). Star cluster particles are shown as filled circles on the density projection. Star cluster circle size is relative to mass and colour indicates the age of the cluster at this time. The oldest star clusters are no longer emitting ionizing radiation and the external material is recombining and cooling. This leads to an underestimation of the momentum deposited by non-ionizing photons.



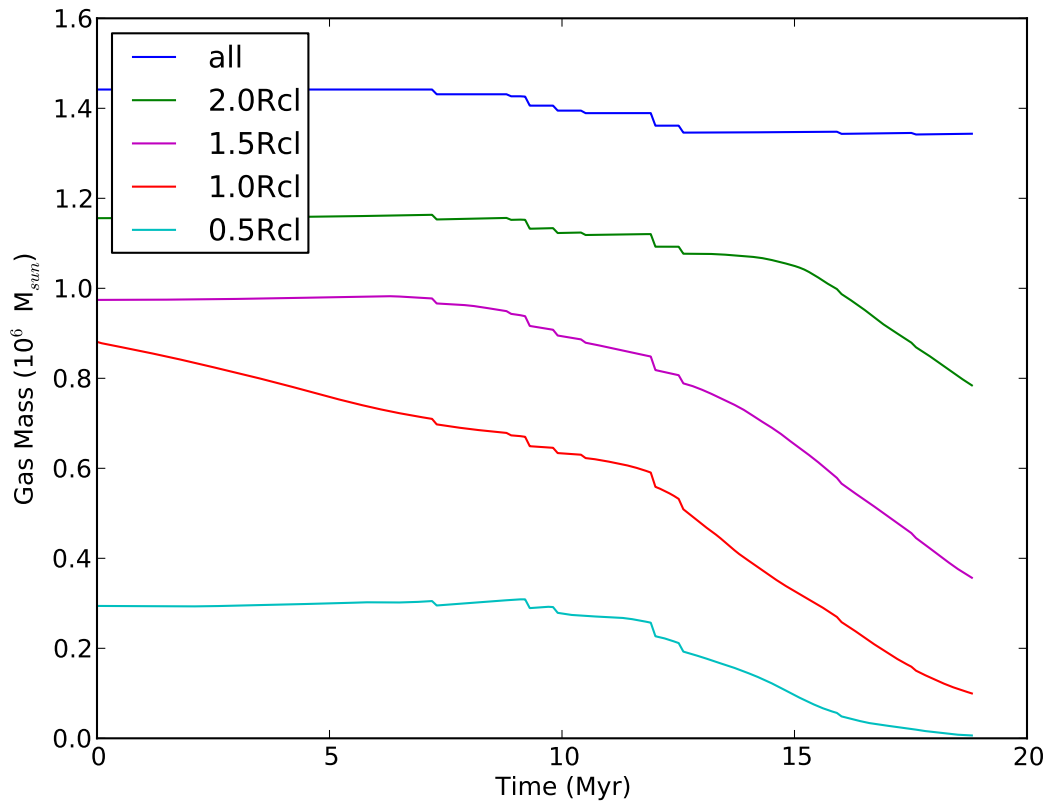
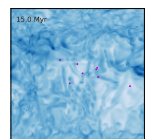


Figure 4.62: The mass structure for the more massive cloud base simulation. The lines show the cumulative mass for 0.5, 1.0, 1.5, and 2.0 times the original cloud radius (89.6 pc) and for the whole simulation box. The drops in total mass (blue line) show conversion of gas mass into star cluster particles. Prior to the first star cluster forming the mass within $1 R_{cl}$ decreases showing the turbulence stirring up the gas. After star cluster formation the bubble can be seen to be forming with the decrease in mass within $0.5 R_{cl}$, and within $1 R_{cl}$ and toward the end within $2 R_{cl}$ as well.

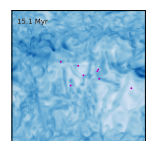


4.5.3 More Massive Cloud Investigations

To confirm results above, the more massive cloud simulation was run with different stellar outputs discussed below and at different resolutions in §5.2.4.

Outputs

The output study run previously, §4.2, showed radiation pressure and HII were the most important outputs for subsequent star formation. To see how the two radiative outputs compete in the more massive simulations I ran the more massive base simulation with no radiation pressure and with no radiative outputs at all. The star formation histories for the three simulations are shown in Fig. 4.63. The presence of ionization alters the star formation from shortly after 8 Myrs onwards as the ionization heats the local gas and prevents star formation. The quenching of star formation by radiation pressure starts to be noticeable around 11 Myrs though the masses do not seem to alter much between with and without RP. Figure 4.64 shows the mass structure for the more massive cloud simulations. Although the mass in clusters is very similar for simulations with and without radiation pressure the inclusion of radiation pressure significantly changes the dynamics of the gas in the centre, evacuating the central regions earlier and more rapidly. Figure 4.65 shows density projections for the inner 150pc (box is 358.4pc wide) at 11Myrs for the three different outputs. The structure in the gas around the clusters is significantly different for the inclusion of radiation pressure.



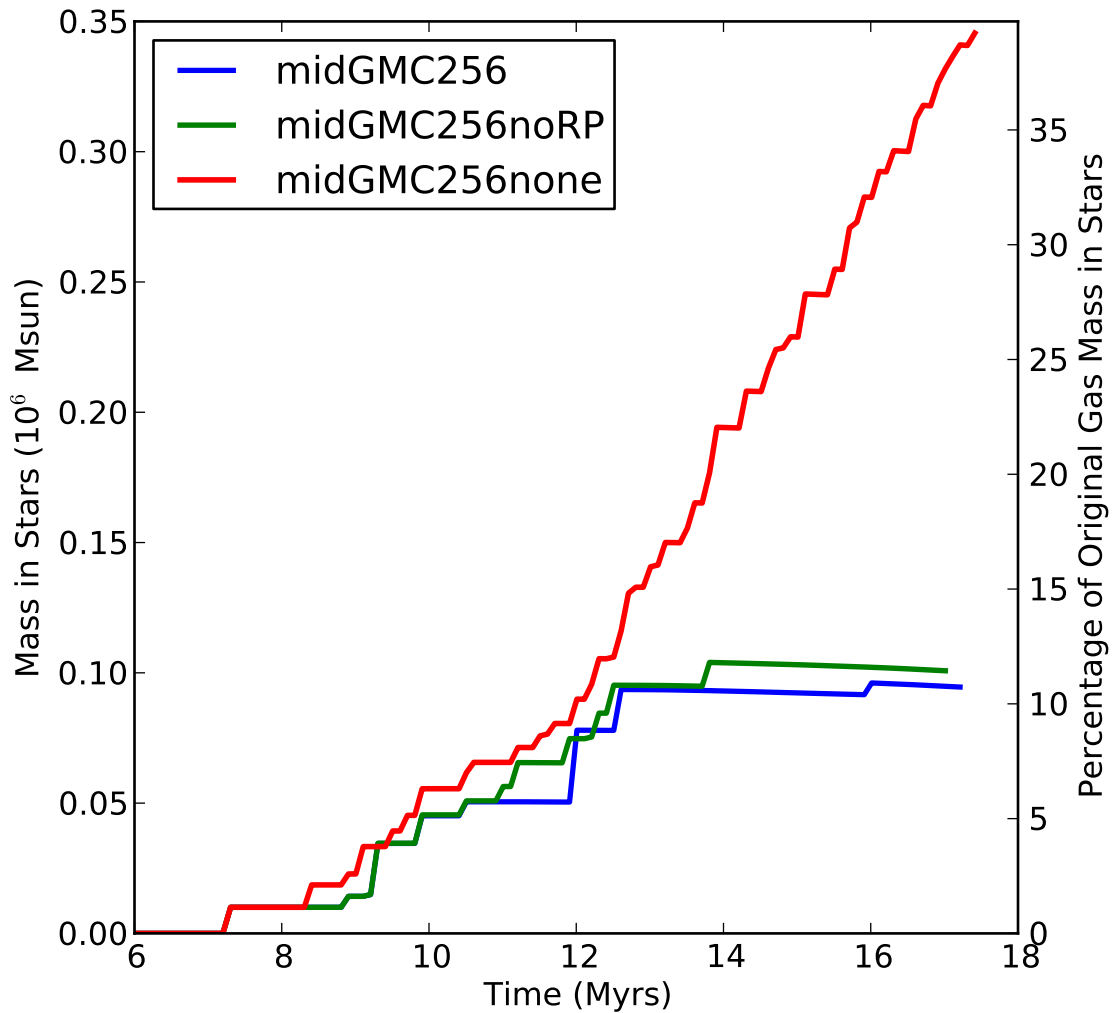
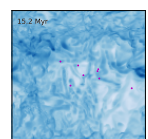


Figure 4.63: Star formation histories for the more massive cloud simulation with no outputs (midGMC256none), just ionization (midGMC256noRP) and both ionization and radiation pressure (midGMC256). Without outputs 35% of the original cloud gas mass is converted into stars within one dynamical time after first cluster formation. Outputs from the stars alter star formation from 8 Myrs on and significantly quench it after 13 Myrs.



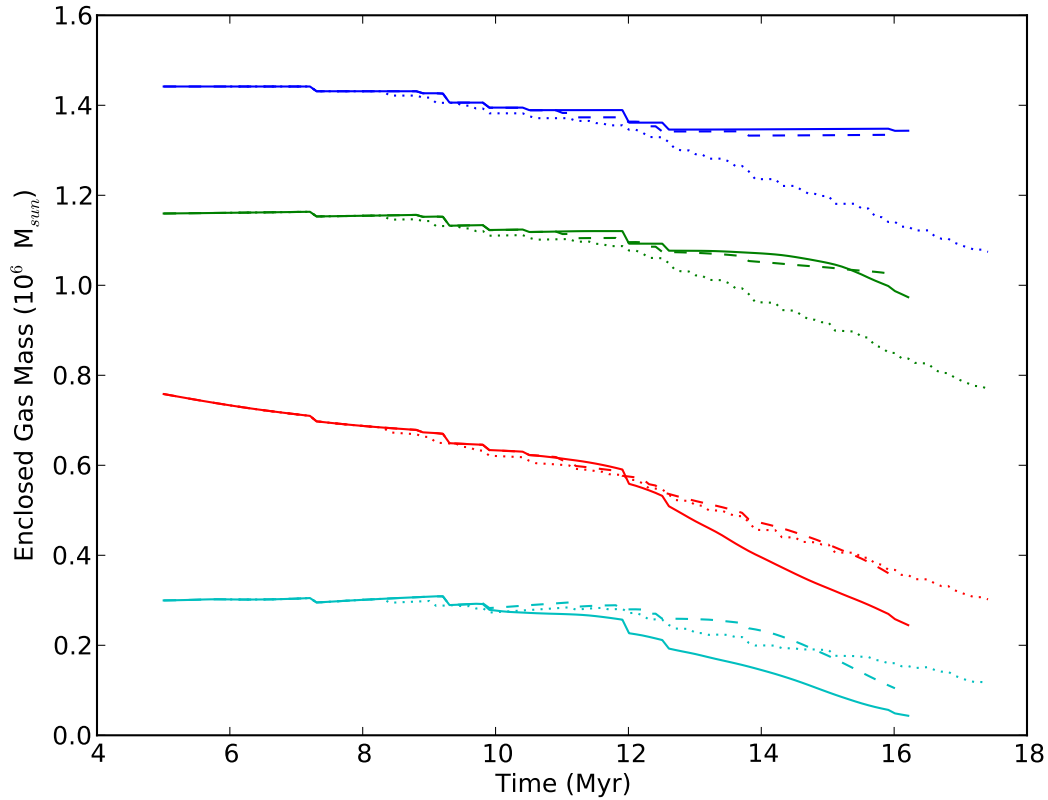
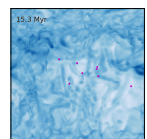
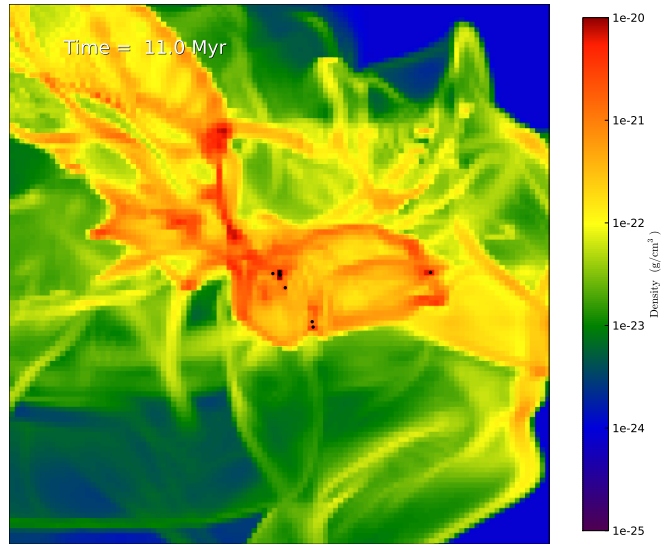
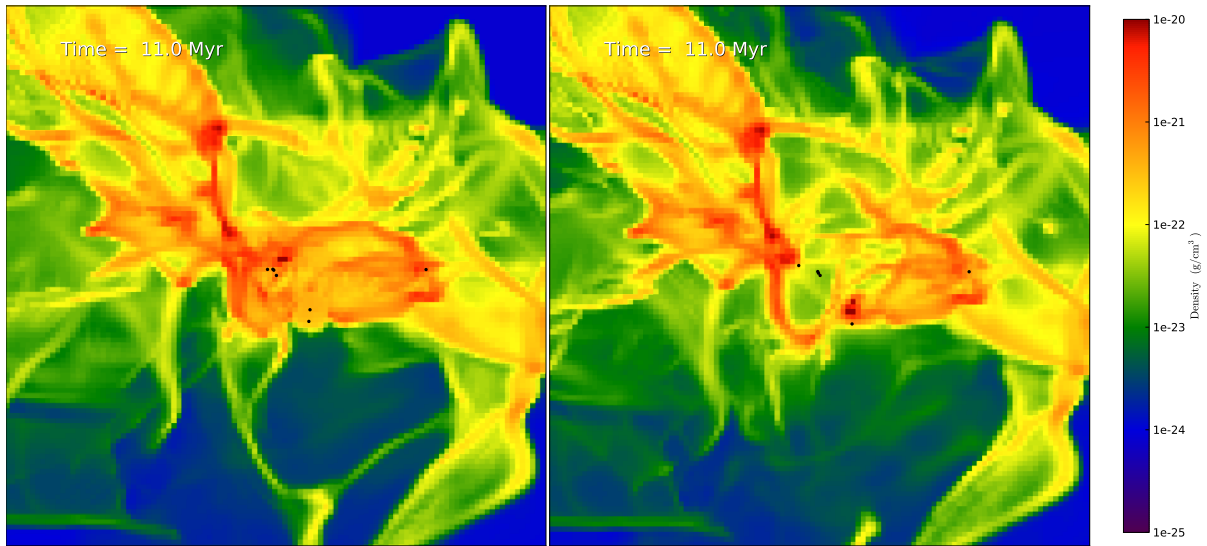


Figure 4.64: The Mass structure for the more massive cloud base simulation (solid lines), more massive cloud with only HII (dashed lines), and the more massive cloud with no outputs from the stars (dotted lines). The colour shows which region of the box is being considered: Blue = all, Green = within $2 R_{cl}$ of the centre, Red = within R_{cl} of the centre, and Cyan = within $0.5 R_{cl}$ of the centre. With no outputs, many more star clusters form, reducing the gas mass in the whole box. Despite the stars forming close to the centre, the mass within $0.5 R_{cl}$ decreases less than the whole box as gravity is pulling mass in. With outputs the centre is disrupted significantly and substantially more rapidly for the inclusion of radiation pressure.





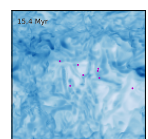
(a) no outputs



(b) only ionization

(c) ionization and radiation pressure

Figure 4.65: Inner 150 pc x-axis projected densities for the more massive clouds simulation with different outputs at 11 Myrs. The original cloud radius was 89.6pc. The significance of the radiation pressure is clear with the more distinct bubble shell and lower density bubble interior around the oldest clusters.



Chapter 5

Testing Numerical Algorithms

This chapter details tests run on the numerics of the 3D simulations. A parameter study in star formation parameters in §5.1 and resolution tests are described in §5.2. A study of different turbulent seeds is in §5.3 and for a different hydrodynamic solver in §5.4.

5.1 Star Formation Parameter Study

Star cluster formation occurs within a cell using a sphere of gas around that cell according to four parameters:

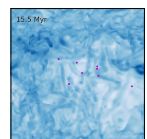
PopIIIOverDensityThreshold - minimum density of the cell relative to average density of the simulation box,

StarClusterMinDynamicalTime - of a sphere of gas around the cell where mass for the star cluster will be taken,

StarClusterFormEfficiency - the fraction of mass from that sphere that will be taken into the cluster particle at formation, and

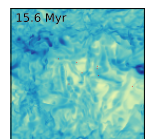
StarClusterMinimumMass - minimum mass of cluster particle to form with the efficiency from the sphere of gas.

PopIIIOverDensityThreshold is a legacy name as the cluster formation routine was built upon the PopIII star formation routines. StarClusterMinDynamicalTime demands a minimum dynamical time for the sphere so that it sets a maximum average density. One reason for this is so the sphere encloses the entire core the cluster is forming within. The assumption is that



Name(s)	PODensityThreshold	SCMDynamicalTime	SCMMass	SCFEfficiency
D40 T63 M30 Ef5 base	10^4	2×10^6	10^3	0.5
D25	3.16×10^2	2×10^6	10^3	0.5
D30	10^3	2×10^6	10^3	0.5
D35	3.16×10^3	2×10^6	10^3	0.5
D45	3.16×10^4	2×10^6	10^3	0.5
D50	10^5	2×10^6	10^3	0.5
D55	3.16×10^5	2×10^6	10^3	0.5
T48	10^4	6.32×10^4	10^3	0.5
T53	10^4	2×10^5	10^3	0.5
T58	10^4	6.32×10^5	10^3	0.5
T68	10^4	6.32×10^6	10^3	0.5
T73	10^4	2×10^7	10^3	0.5
T78	10^4	6.32×10^7	10^3	0.5
M15	10^4	2×10^6	3.16×10^1	0.5
M20	10^4	2×10^6	10^2	0.5
M25	10^4	2×10^6	3.16×10^2	0.5
M35	10^4	2×10^6	3.16×10^3	0.5
M40	10^4	2×10^6	10^4	0.5
M45	10^4	2×10^6	3.16×10^4	0.5
Ef2	10^4	2×10^6	10^3	0.2
Ef3	10^4	2×10^6	10^3	0.3
Ef4	10^4	2×10^6	10^3	0.4
Ef6	10^4	2×10^6	10^3	0.6
Ef7	10^4	2×10^6	10^3	0.7

Table 5.1: The four different star cluster particle formation parameters for the simulations run in the parameter study. Three of the parameters are varied three times in steps of half an order of magnitude both up and down from the base value. The efficiency is varied in steps of 0.1.



that sphere would relatively rapidly form thousands of individual stars which I represent with a single particle at the cluster centre.

To investigate the effects of these parameters on the results I ran a parameter study varying `PopIIIOverDensityThreshold`, `StarClusterMinDynamicalTime`, and `StarClusterMinimumMass` in half an order of magnitude steps. `StarClusterFormEfficiency` was varied in steps of 0.1. Table 5.1 shows the values for the cluster formation parameters for the simulations in this parameter study.

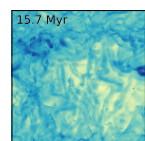
5.1.1 Star Formation Parameter Study Results

There are two separate algorithms for star cluster formation. If a sphere of gas surrounding the cell at critical density with a radius of the cell width has a dynamical time less than the minimum dynamical time set and a mass less than the minimum mass divided by efficiency then the routine as described in §3.7.2 is used. However, if the parameters are set so these conditions are not met then when a cell reaches the critical density a cluster is formed with half the mass of the cell independent of the surrounding conditions. Given that I am trying to form representations of whole clusters, it is important to keep the parameters within the space that the full cluster formation routines are used.

Here follows a discussion of each of the four cluster formation parameters separately. In this section, graphs of mass in clusters against time have the base simulation shown as a cyan dashed line.

`PopIIIOverDensityThreshold`

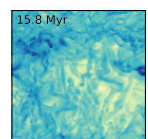
Figure 5.1 shows the graphs of total mass in star clusters and number of star cluster particles for the base simulation and the six simulations with different critical densities for cluster formation. With lower critical density star cluster particles form earlier in the simulation, as soon as the turbulence and self gravity give regions with densities above that critical value. Lower critical density creates lower mass star clusters. However, the rate of mass conversion into stars is approximately the same for all critical densities, as seen by the similar gradients in Fig. 5.1. Taking the simulations that use the resolved cluster formation routine, $10^{3.5} \leq \text{PopIIIOverDensityThreshold} \leq 10^{5.5}$, just over one original cloud dynamical time - 7 Myrs - after the first star cluster formed a mass of $31,072 \pm 7,400 M_{\odot}$ or $14.1 \pm 3.4 \%$ of the original cloud gas mass is in star clusters. Figure 5.1 shows the scatter in cluster mass is not in order of critical density with the lowest mass being from the central density in this range (`PopIIIOverDensityThreshold` = $10^{4.5}$). Thus, the mass in clusters after one dynamical time is a robust result, even with two



orders of magnitude change in critical density.

Figure 5.2 shows the density, temperature, radiation force and HII fraction for the low critical density 3.1 Myrs after the first star cluster particle forms. The star clusters are shown in the density projection. Compared to Fig. 4.8 the star clusters are in the same regions though smaller and more numerous. There is still a small region of shielded gas but otherwise the HII region is comparable. Figure 5.5 shows how the mass structure varies with time. Compared to Fig. 4.12 the central region and original cloud location are cleared in the same length of time after first star cluster forms (1.6 Myrs earlier for low density than base).

For the higher values of density it takes longer and longer for the HII region to break out, in the $\text{PopIIIOverDensityThreshold} = 10^{5.5}$ simulation the HII region never breaks out, as seen in Fig. 5.3 and Fig. 5.4. Figure 5.6 shows the mass structure for the $\text{PopIIIOverDensityThreshold} = 10^{5.5}$ simulation. The central enclosed mass ($0.5 R_{cl}$) decreases after 15 Myrs but this is because the collapsing region is off centre, as seen by the continued increase to mass within the original cloud location ($1 R_{cl}$). Thus, this shows not a bubble expanding but a decentralized collapse. The $\text{PopIIIOverDensityThreshold} = 10^{4.5}$ run took 4.0 Myrs to break out and $\text{PopIIIOverDensityThreshold} = 10^{5.0}$ took 5.5 Myrs. The longer time scales are caused by the higher density in surrounding material as most of the cloud collapses down to a small region before the critical densities are reached. The lack of spherical resolution within a cell of a star cluster means radiation force is significantly under absorbed. If HII pressure is not enough to blow out the radiation to a few cells radiation force is not correctly calculated so the region will remain unrealistically compact.



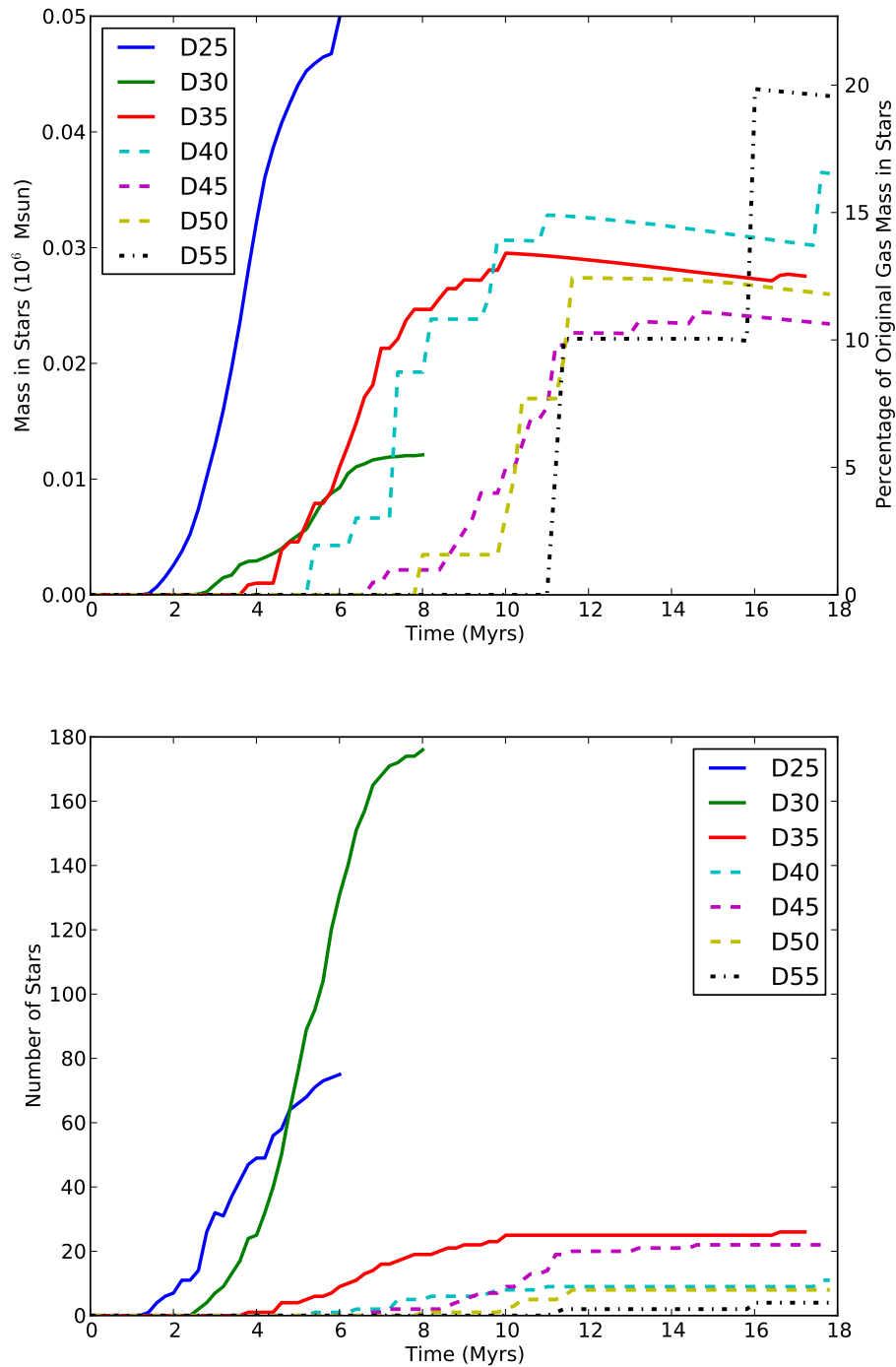
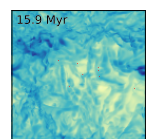


Figure 5.1: Time evolution of *top*: total mass in and *bottom*: number of star cluster particles in the simulations for varying critical density. For lower critical density clusters form earlier and more numerous. For all critical densities mass is converted into stars at approximately the same rate for the first few Myrs after star formation begins. D25, D30, and D55 use the unresolved star cluster formation routine.



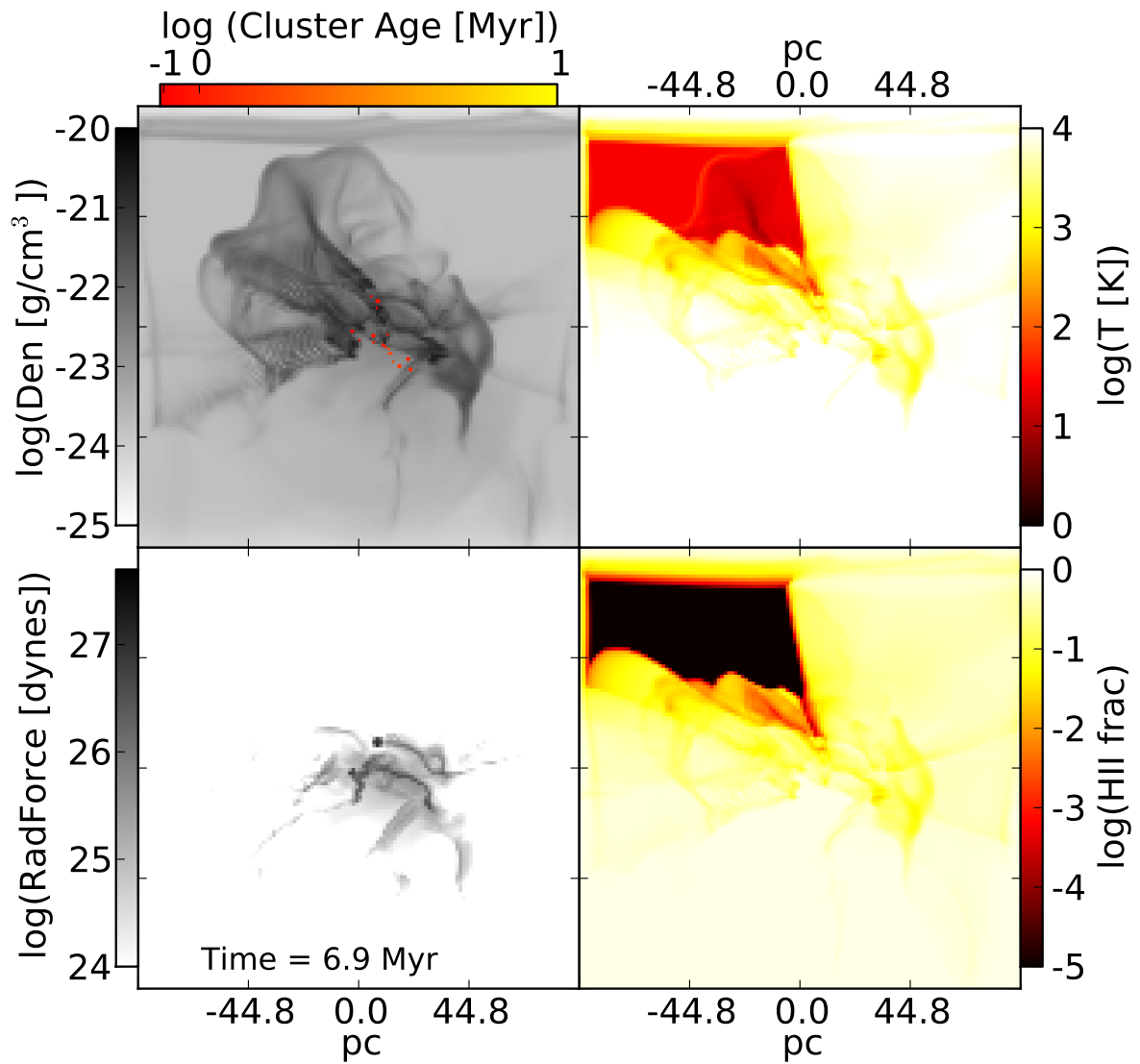


Figure 5.2: Density, temperature, radiation force (momentum deposited), and HII fraction for the simulation with low density threshold ($\text{PopIIIOverDensityThreshold} = 10^{3.5}$) at 6.9 Myrs (3.1 Myrs after first cluster formed). Compared to Fig. 4.8 the star clusters are in the same regions though smaller and more numerous. There is still a small region of shielded gas but otherwise the HII region is comparable. The sum of the radiation force absorbed by the gas in this frame is 1.03×10^{30} dynes, very similar to the base run at the equivalent time.

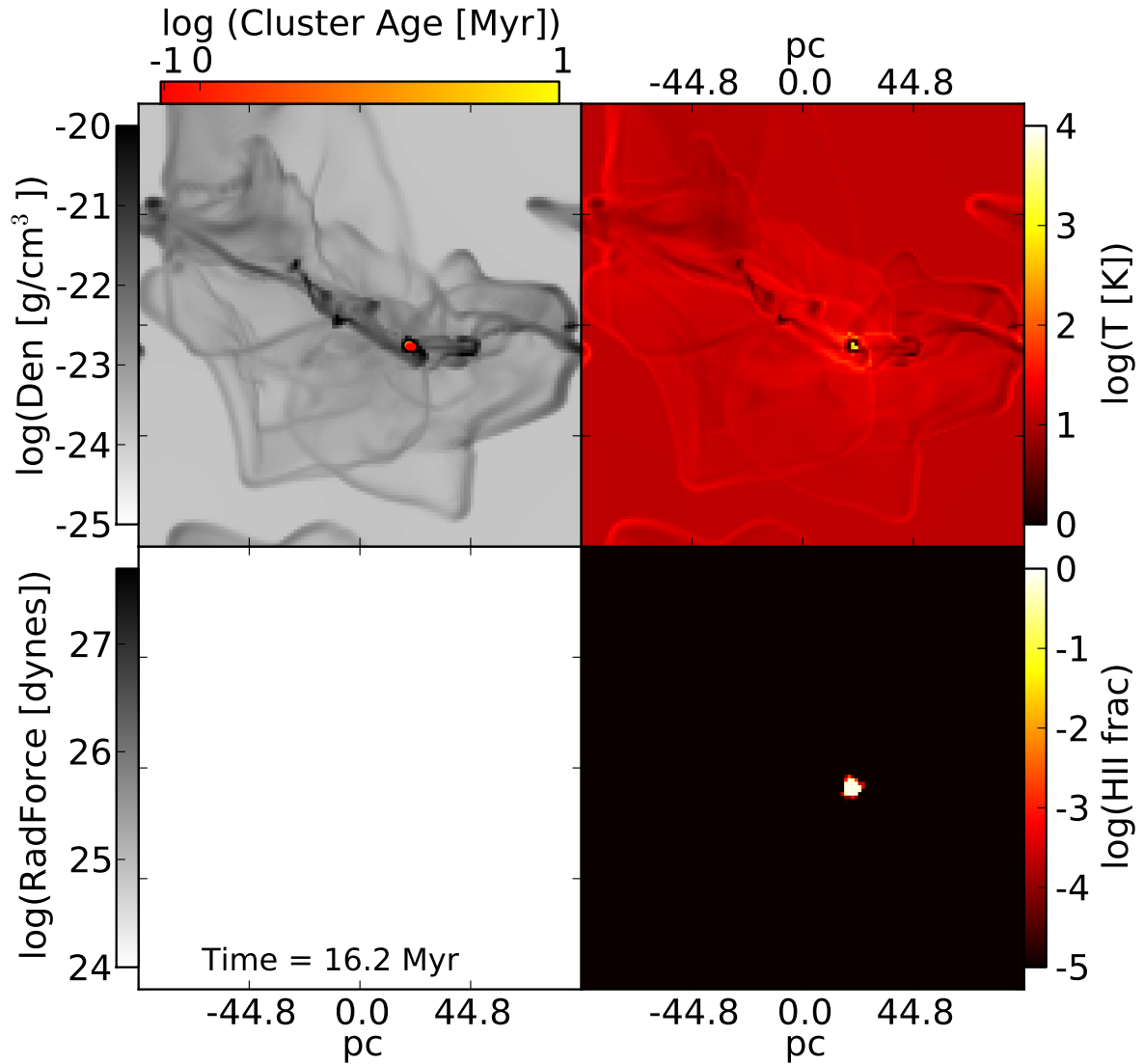


Figure 5.3: Density, temperature, radiation force (momentum deposited), and HII fraction for the simulation with highest density threshold ($\text{PopIIIOverDensityThreshold} = 10^{5.5}$) at 16.2 Myrs (5 Myrs after first cluster formed, 0.1 Myrs after the fourth and final star cluster particle formed). There is zero radiation force absorbed by the gas in this frame as all of the radiation is absorbed within the host cells of the star clusters so the code cannot resolve radiation force.

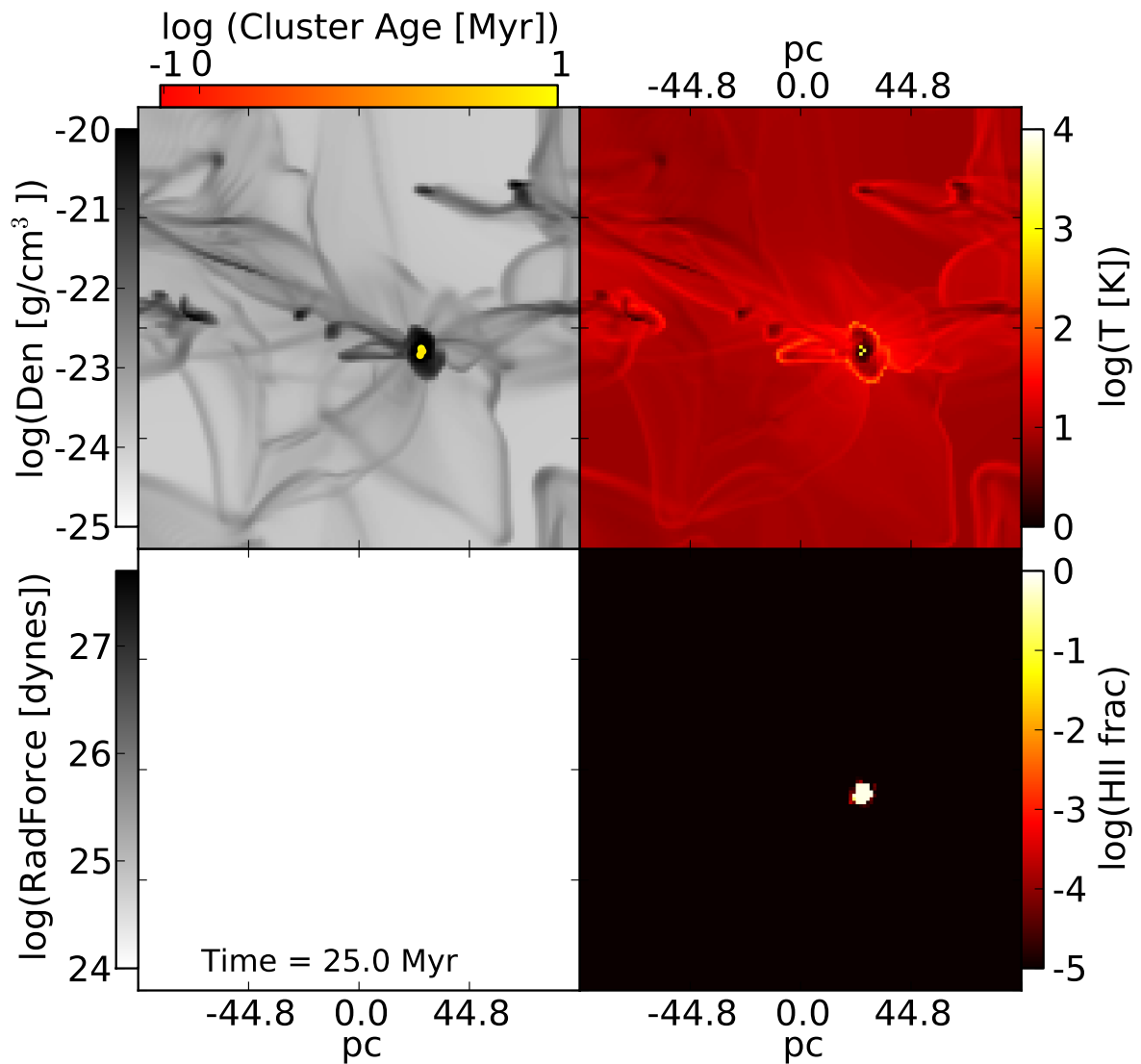


Figure 5.4: Density, temperature, radiation force (momentum deposited), and HII fraction for the simulation with highest density threshold ($\text{PopIIIOverDensityThreshold} = 10^{5.5}$) at 25.0 Myrs (13.2 Myrs after first cluster formed). There is zero radiation force absorbed by the gas in this frame as all of the radiation is absorbed within the cell containing the star clusters as can be seen in the temperature frame. Almost all of the mass has collapsed into one region. The ionization pressure is not enough to disrupt the dense region so it will continue making clusters.

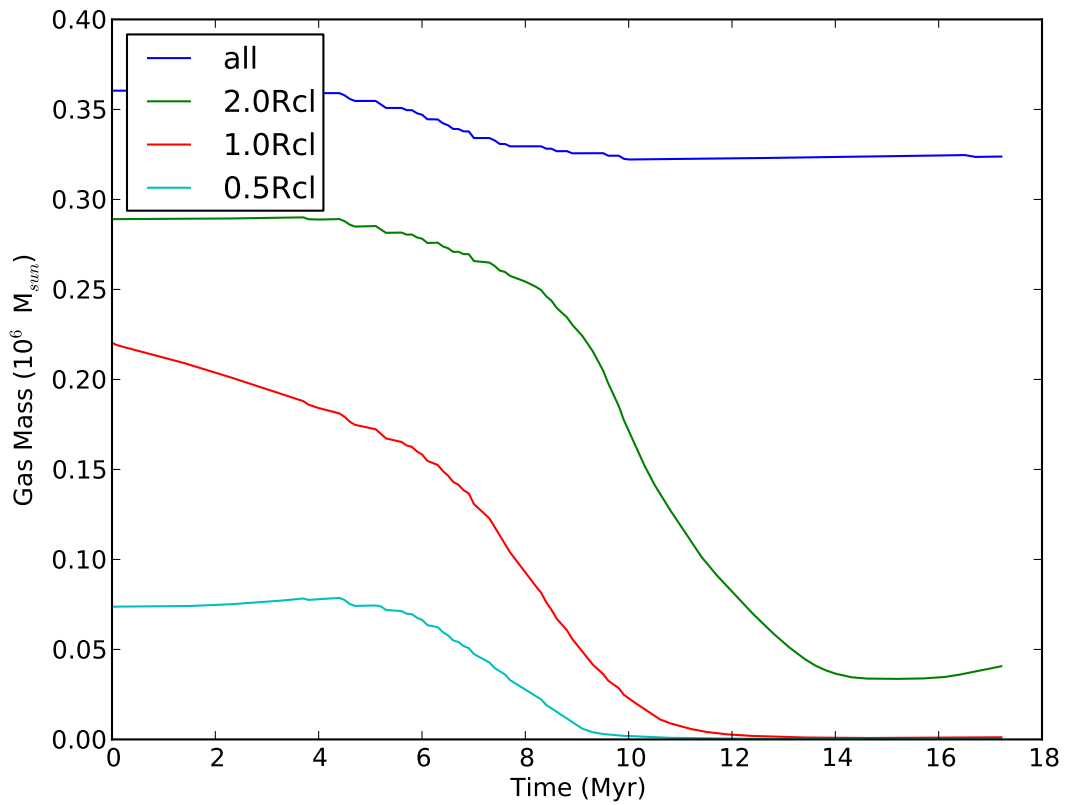


Figure 5.5: The mass structure for the simulation with low critical density, $\text{PopIIIOverDensityThreshold} = 10^{3.5}$. The first cluster forms at 3.8 Myrs and takes just under a dynamical time to completely disrupt the cloud.

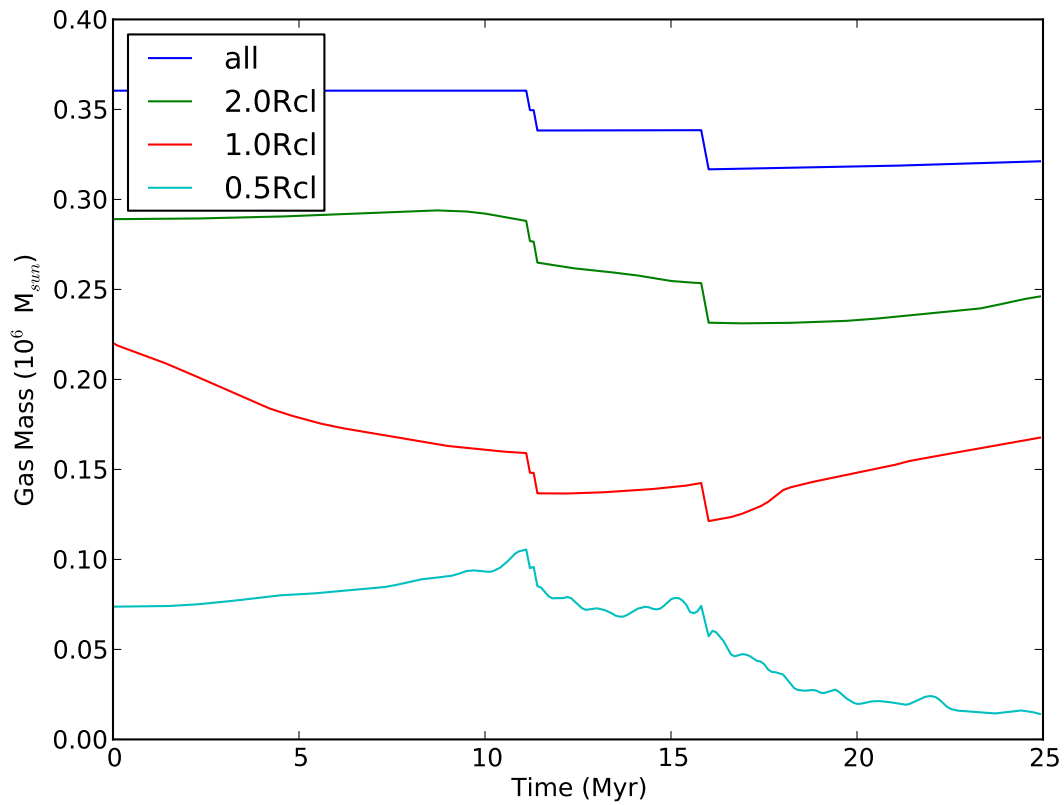


Figure 5.6: The mass structure for the simulation with highest critical density. In this simulation most of the gas collapses into a single core before a star cluster is made. This single core is off centre as can be seen by the decreasing central mass but increasing mass within R_{cl} .

StarClusterMinDynamicalTime

Increasing the dynamical time (StarClusterMinDynamicalTime) increases the size of the sphere used for star formation since it sets a maximum average density for the sphere, $t_{dyn} \sim \sqrt{1/\rho_{mean}}$. Figure 5.7 shows graphs of total mass in star clusters and number of star clusters for the base simulation and the three simulations with shorter and three simulations with longer StarClusterMinDynamicalTime. Increasing the dynamical time did not affect the time of the first star cluster particle forming but does change the mass of that first particle. For larger dynamical times the sphere taken for the star formation is larger. Thus, above a certain value the sphere is significantly bigger than the filament the cell is in and included mass in other filaments making the star cluster particle that forms less realistic. Figure 5.8 shows the sphere taken for the first star cluster forming with StarClusterMinDynamicalTime = 2×10^7 . For the longest dynamical time, StarClusterMinDynamicalTime = 6.32×10^7 , the box is not big enough for the sphere the parameters require. Thus, the code allows smaller star cluster particles to form from a smaller sphere. Interestingly, the total mass in stars then most closely resembles the base simulation supporting the base parameters as the most physically accurate choice.

Given the physical considerations it is unreasonable to have a dynamical time of more than a few million years and given the resolution it is not possible to have a dynamical time of less than a million years. Thus, I looked closer at the dynamical times around a million years, in steps of $10^{0.1}$, as listed in Table 5.2. Figure 5.9 shows the mass in clusters and number of clusters for the finer dynamical time parameter study. The base simulation is shown in cyan (T63). Zoomed in density slices just before the first cluster forms and immediately after for the 8 simulations with the order of a million year dynamical time are shown in Fig.5.10. The size of the sphere increases significantly for longer dynamical times. A dynamical time longer than the lifetimes of the O stars is unrealistic, as is taking mass from neighbouring filaments. Observed massive star clusters are only a few parsecs wide. Given this, and the constraints of resolution, a dynamical time between $10^{6.1}$ and $10^{6.5}$ forms realistic clusters. At 14.3 Myrs there is no further cluster formation within the GMC for any of the runs. Taking the simulations with dynamical time between $10^{6.1}$ and $10^{6.5}$ years at 14.3 Myrs (1.3 dynamical times after first cluster formation) a mass of $28,458 \pm 2,593 M_{\odot}$ or $12.9 \pm 1.1 \%$ of the original cloud gas mass is in star clusters.

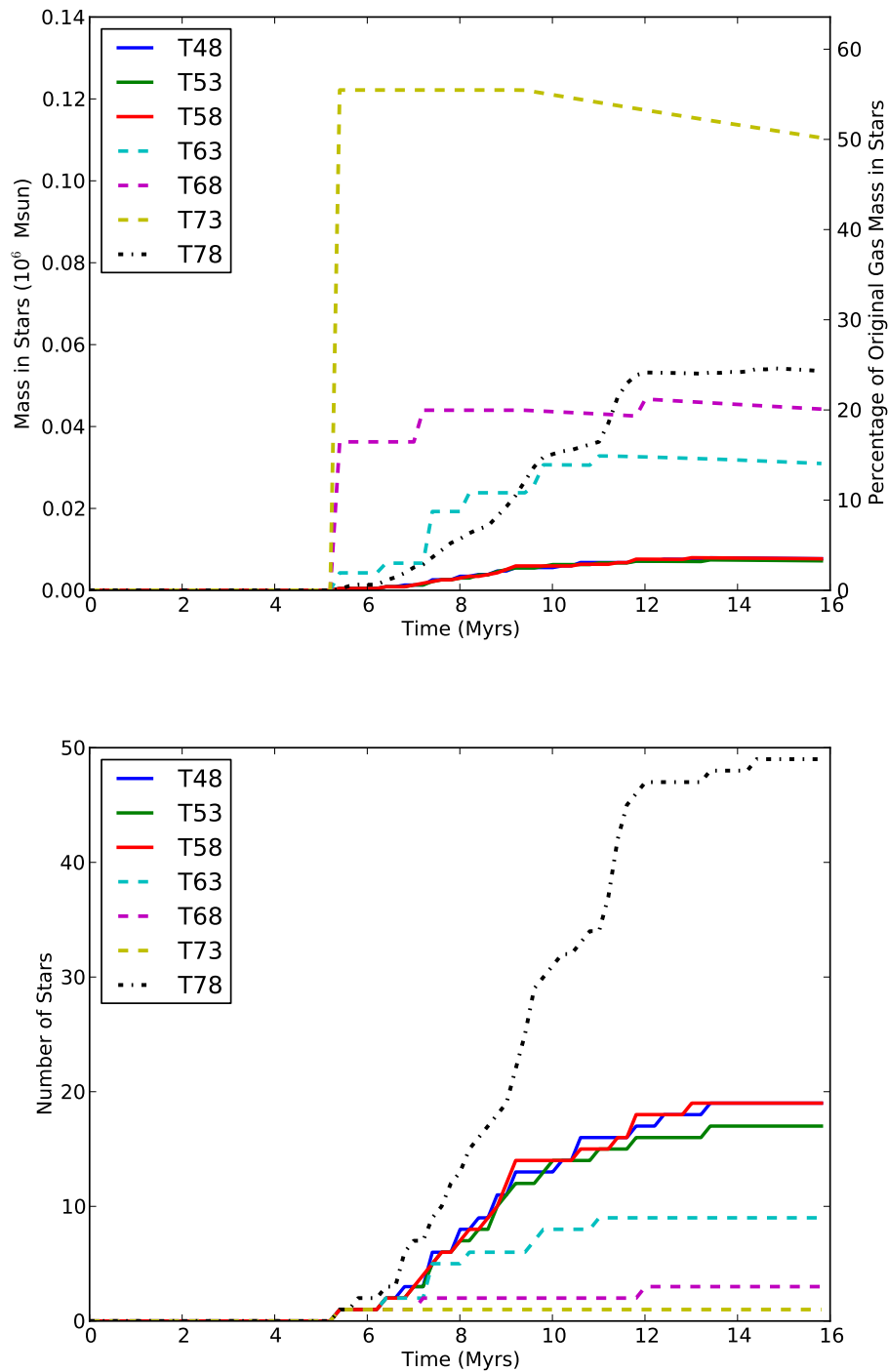


Figure 5.7: Time evolution of *top*: total mass in and *bottom*: number of star cluster particles in the simulations for varying dynamical time. Note the striking difference in the T78 line from the trend of the other lines. This is due to the dynamical time requested being longer than the simulation box dynamical time and therefore being ignored so that stars form according to only the other two parameters only. Note how similar the total mass in the T78 run is to the base (T63) strongly suggesting that the base simulation parameters are a good choice.

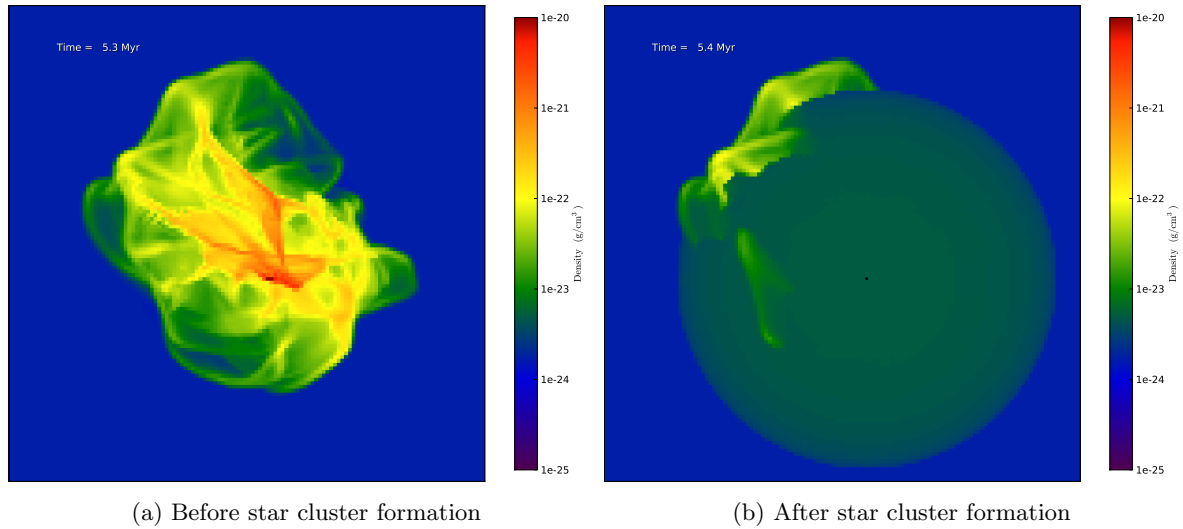


Figure 5.8: Density projection before (a) and after (b) the first star particle forms when $\text{StarClusterMinDynamicalTime} = 2 \times 10^7$. For a 20 Million year dynamical time it takes the whole cloud!

Name	PODensityThreshold	SCMDynamicalTime	SCMMass	SCFEfficiency
T63, base	10^4	2.00×10^6	10^3	0.5
T60	10^4	1.00×10^6	10^3	0.5
T61	10^4	1.26×10^6	10^3	0.5
T62	10^4	1.58×10^6	10^3	0.5
T64	10^4	2.51×10^6	10^3	0.5
T65	10^4	3.16×10^6	10^3	0.5
T66	10^4	3.98×10^6	10^3	0.5
T67	10^4	5.01×10^6	10^3	0.5

Table 5.2: The star cluster particle formation parameters for the simulations run in the finer dynamical time step parameter study.

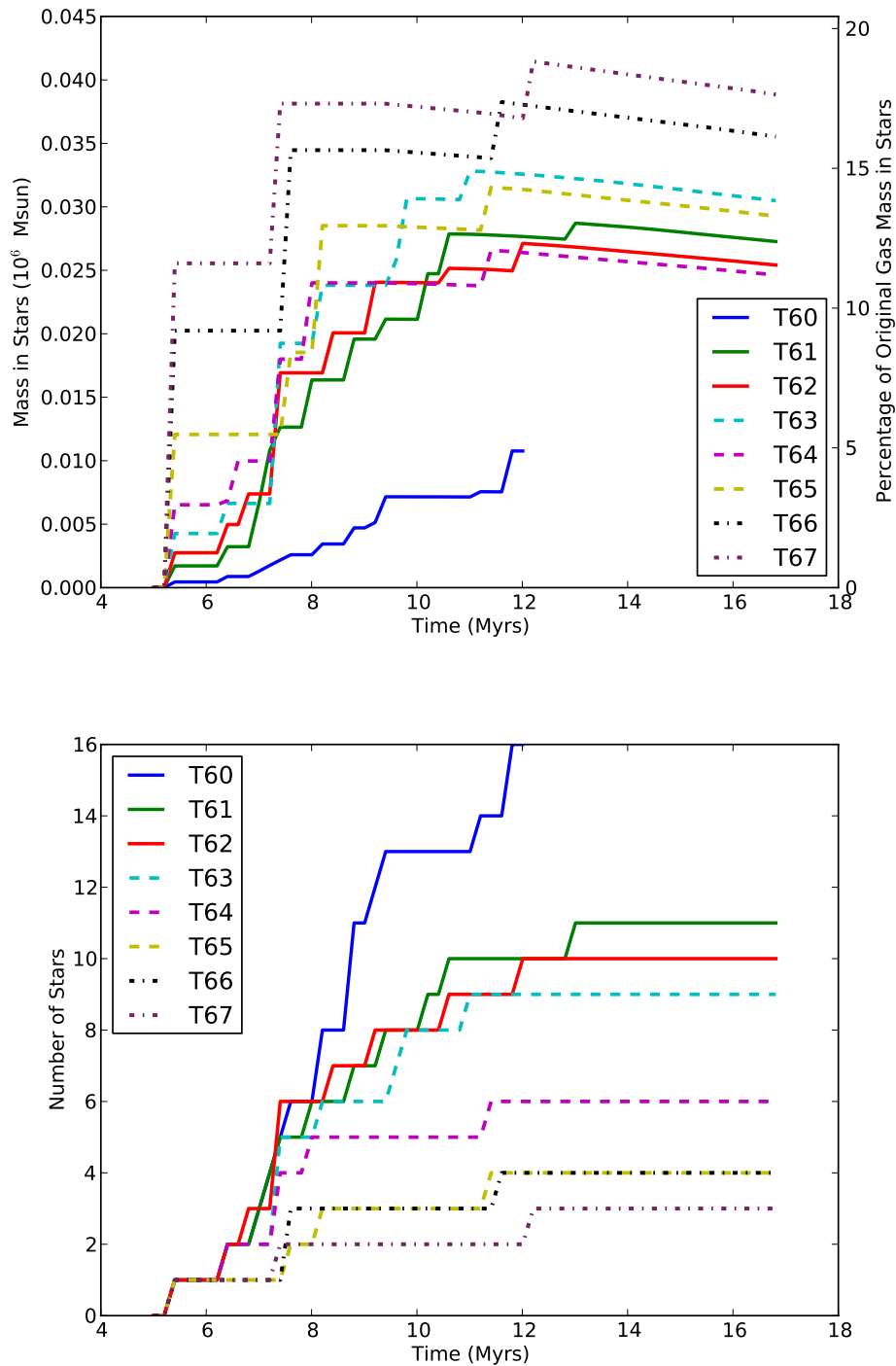


Figure 5.9: Time evolution of *top*: total mass in and *bottom*: number of star cluster particles in the simulations for varying dynamical times around a million years. For dynamical times between $10^{6.1}$ and $10^{6.5}$ years the final mass in star clusters is tightly scattered around 13% of the original cloud gas mass.

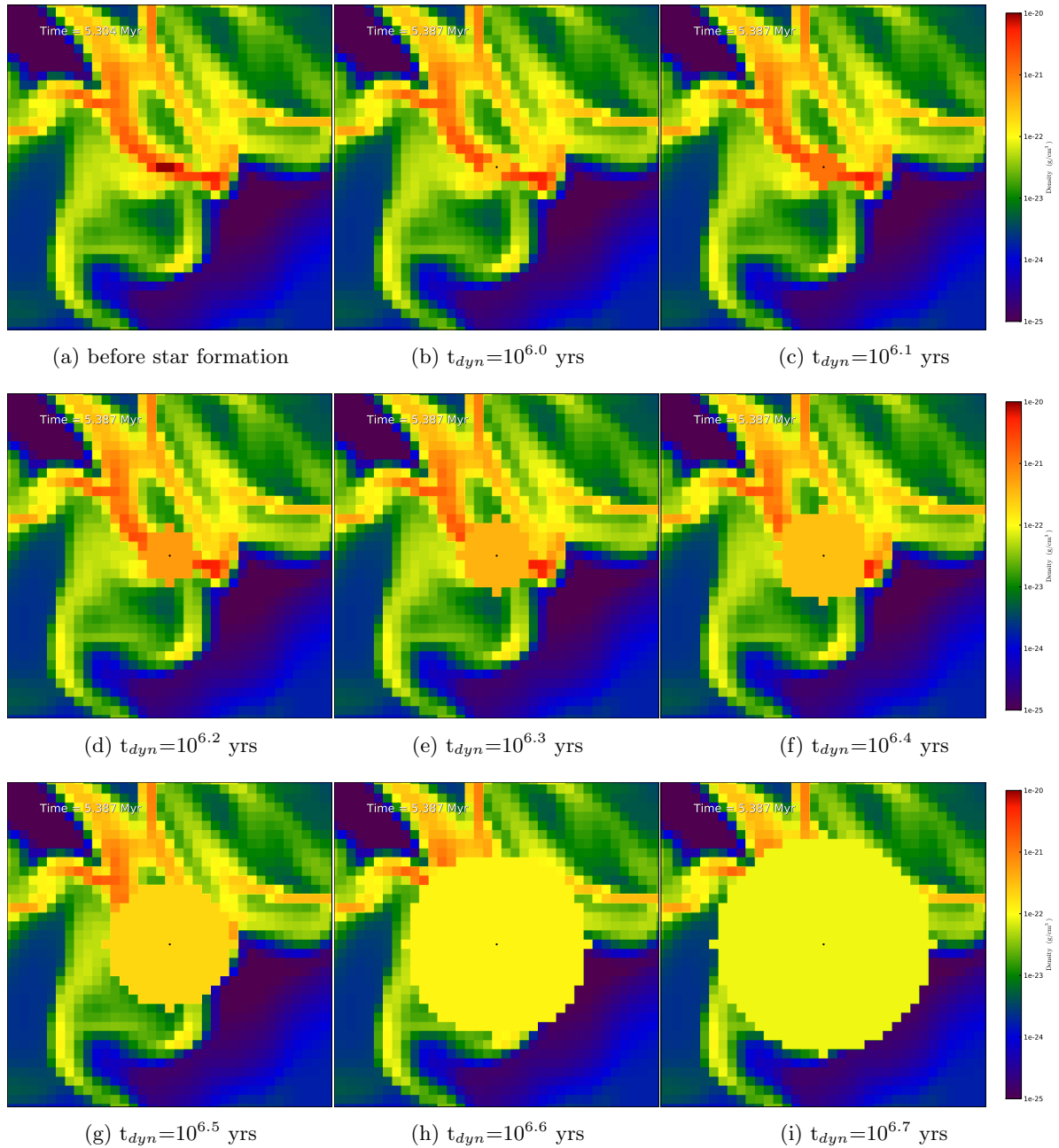


Figure 5.10: Slices of density for the 50 pc centred around the first star cluster just before a cluster forms and just after for 8 different values of StarClusterMinDynamicalTime. The size of sphere used for the cluster formation increases with increasing dynamical time and the density of remaining gas decreases. Observed star clusters are only a few parsecs wide.

StarClusterMinimumMass

Figure 5.11 shows the total mass and number of star cluster particles for the varying minimum mass parameter. The graphs show a distinctly bimodal distribution due to the different star formation algorithms. For a critical density of 10^4 times the average density a cell at that density contains $1709 M_{\odot}$ in gas. Thus for a minimum mass greater than the efficiency times the cell mass the code looks to surrounding cells and creates the sphere to form a star. In these simulations the efficiency is 0.5 so minimum mass must be greater than $855 M_{\odot}$ for resolved star cluster formation with critical density of 10^4 . For the four runs with resolved star formation the mass in clusters at 14 Myrs (1.3 dynamical times after first cluster formation) is $30,524 \pm 1203 M_{\odot}$ or $13.9 \pm 0.5 \%$ of the original cloud gas mass. For the three runs with unresolved star formation the mass in clusters at 14 Myrs is $10,438 \pm 1388 M_{\odot}$ or $4.7 \pm 0.6 \%$ of the original cloud gas mass.

Figure 5.12 shows the density projection for the simulations with parameters closest to the bimodal split shortly before and shortly after the large increase in star clusters. For the lower minimum mass, many more star clusters are formed in the same regions as for the higher minimum mass. However, each star cluster in the lower minimum mass has a smaller region from which gas is taken than the higher minimum mass simulation. This results in a lower overall volume of gas being converted into star clusters. Looking at the distribution of the new star clusters for the lower minimum mass they are very closely grouped together and look like many star clusters particles are forming from a single core region.

Taking a closer look at the simulations with unresolved cluster formation I plotted the mass structure with time, Fig. 5.13. Even though the mass in clusters is almost three times less than for the resolved star cluster formation the outputs are still strong enough to disrupt the cloud in less than two dynamical times. Figures 5.14 and 5.15 show the density, temperature, absorbed radiation force, and ionized fraction at 6.5 and 14.0 Myrs respectively for `StarClusterMinimumMass = 316 M_{\odot}` . Comparing Fig. 5.14 to Fig. 4.6, the base simulation at the same time, the clusters are in the same locations but the lower mass means less radiation. Therefore, all of the radiation is absorbed in the host cell and radiation pressure is not resolved. However, with increasing mass in star clusters over time the radiation breaks out and does disrupt the cloud by 14 Myrs, Fig. 5.15.

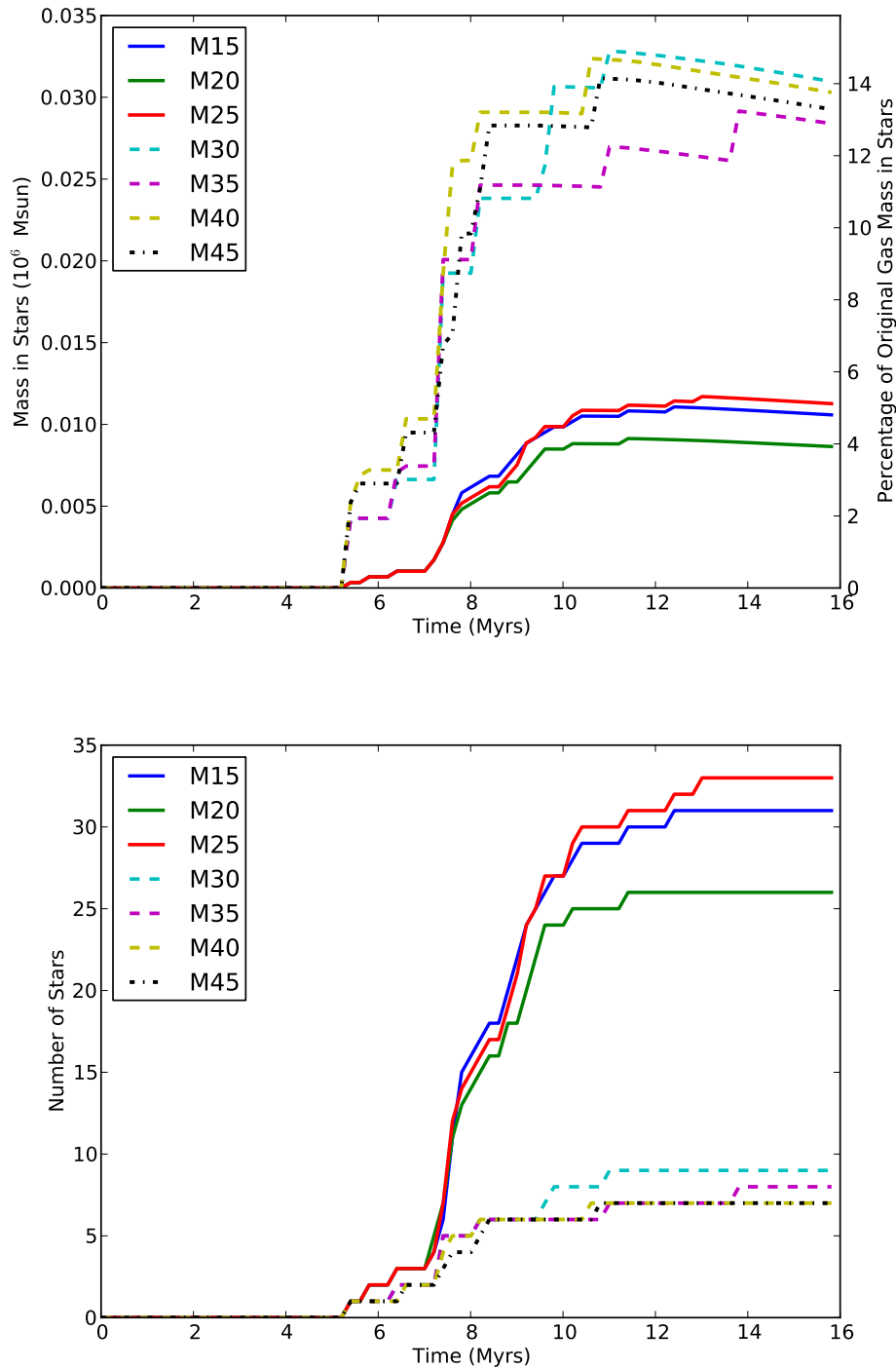


Figure 5.11: Time evolution of *top*: total mass in and *bottom*: number of star cluster particles in the simulations for varying minimum mass. Note the bimodal distribution in mass and number of star particles after 7 Myrs due to the two star cluster formation routines.

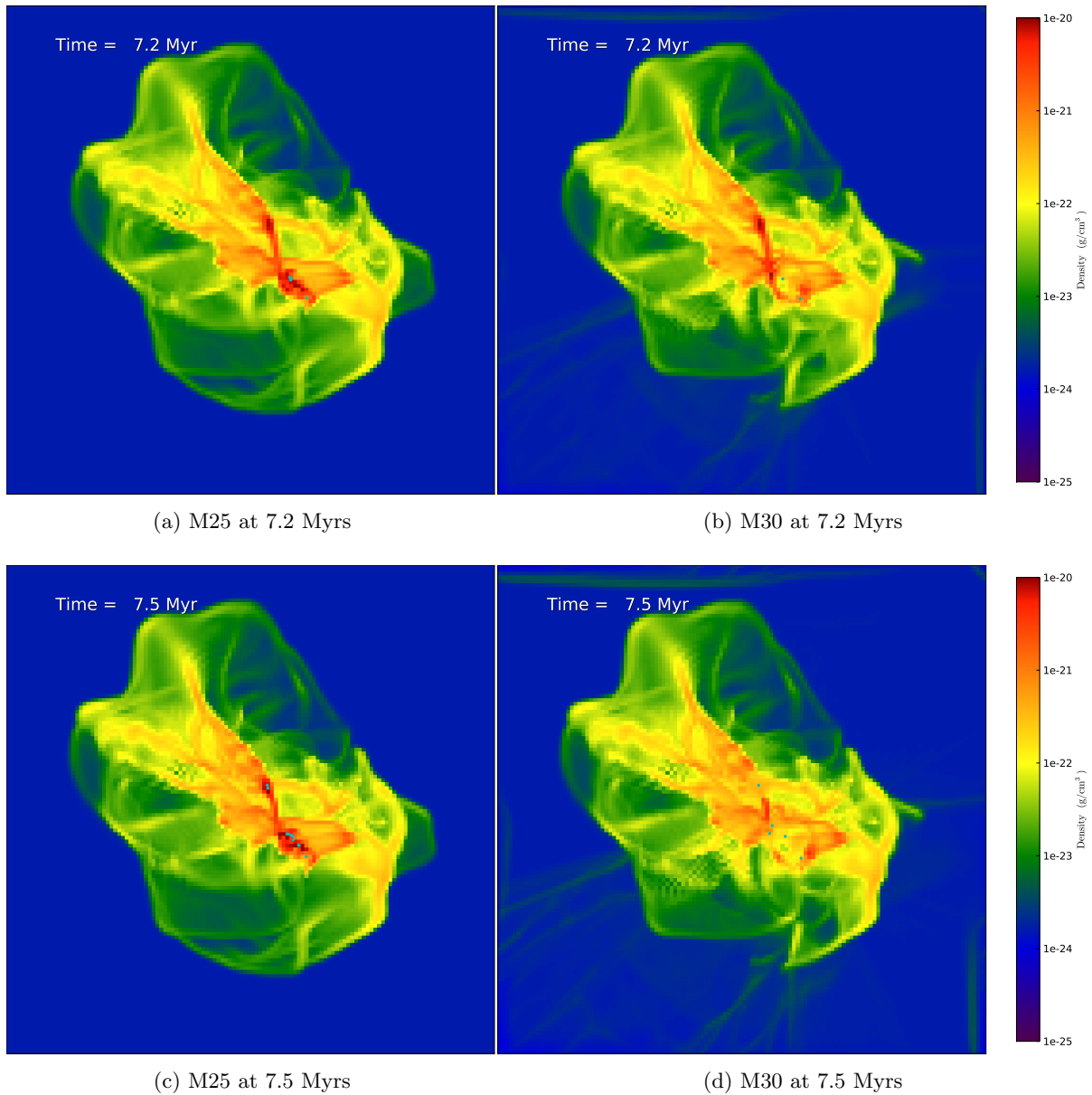


Figure 5.12: Projections of density for the two simulations with minimum mass closest to the bimodal split before (7.2 Myrs) and after (7.5 Myrs) the period of rapid star formation. Stars are shown in cyan. For minimum mass = $316 M_{\odot}$ many more stars form but from less total volume and mass than for minimum mass = $1000 M_{\odot}$. However, for both simulations the new stars are forming in the same regions.

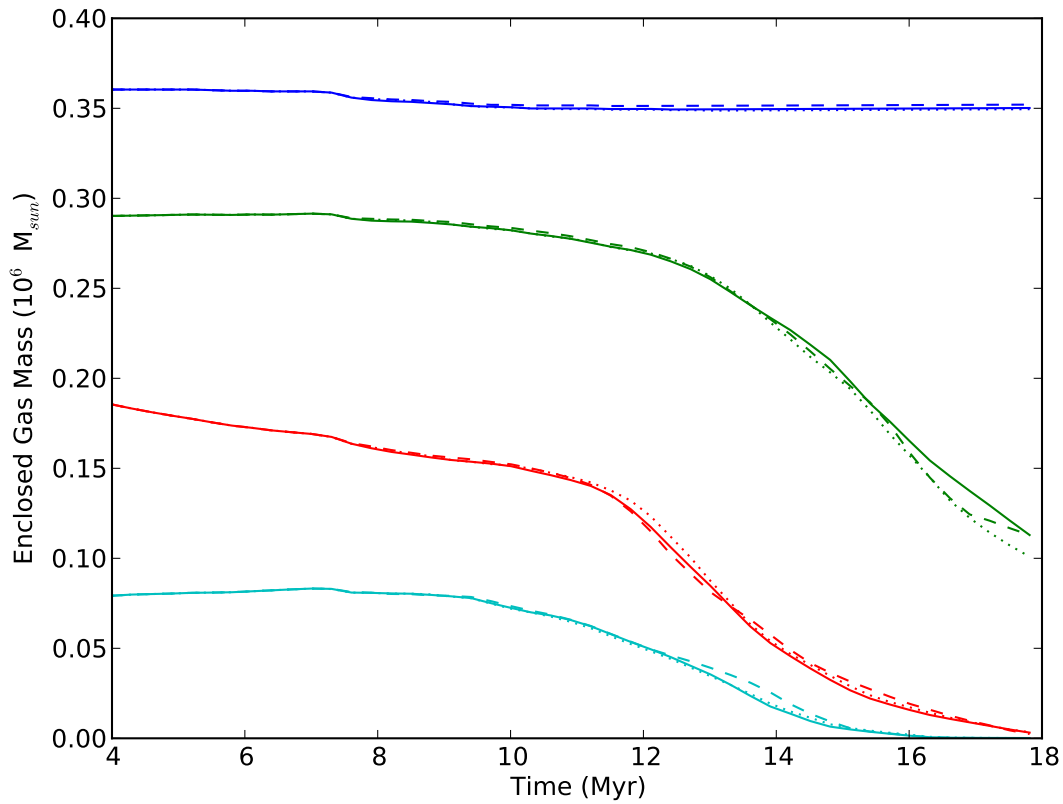


Figure 5.13: The mass structure for the three simulations with lowest minimum mass, *solid*: Minimum mass = $32 M_{\odot}$, *dashed*: Minimum mass = $100 M_{\odot}$, and *dotted*: Minimum mass = $316 M_{\odot}$. In these simulations the minimum mass is less than the mass in a cell at the critical density so clusters form with half of the mass in a cell at critical density rather than with the full cluster formation algorithm. Despite the smaller clusters and different algorithm all three simulations disrupt their host GMC by 18 Myrs. with the lower radiation rates it takes longer for the radiation pressure to disrupt the cloud.

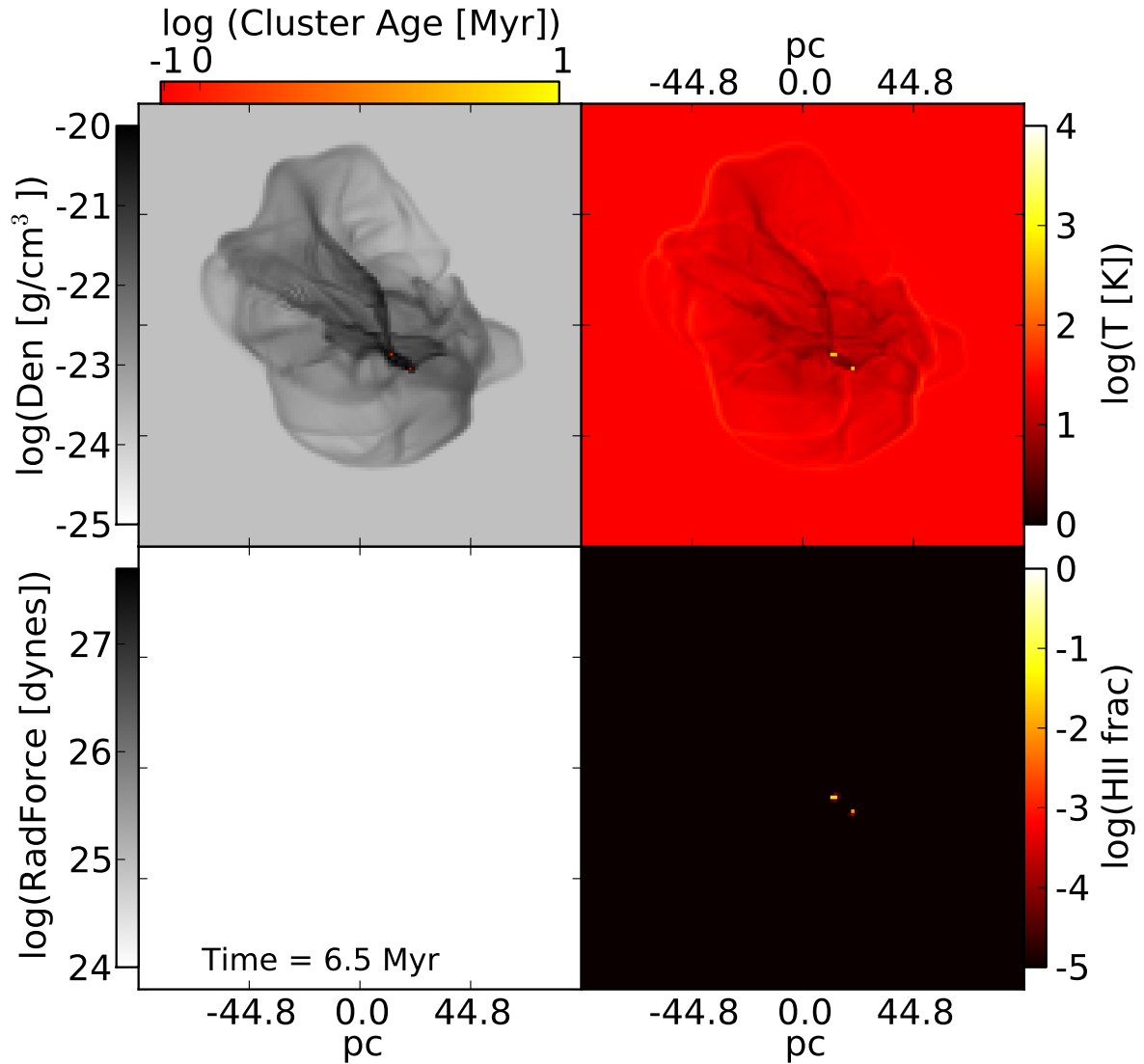


Figure 5.14: Density, temperature, radiation force (momentum deposited), and HII fraction for the simulation with minimum mass = $316 M_{\odot}$ at 6.5 Myrs (1.1 Myrs after first cluster formed). Compare to Fig. 4.6 - the base simulation at the same time. The lower mass clusters have less radiation and thus the HII region has not broken out yet. Please note the imaged cluster size is set to a different scale than all other images as the clusters are of a much lower mass.

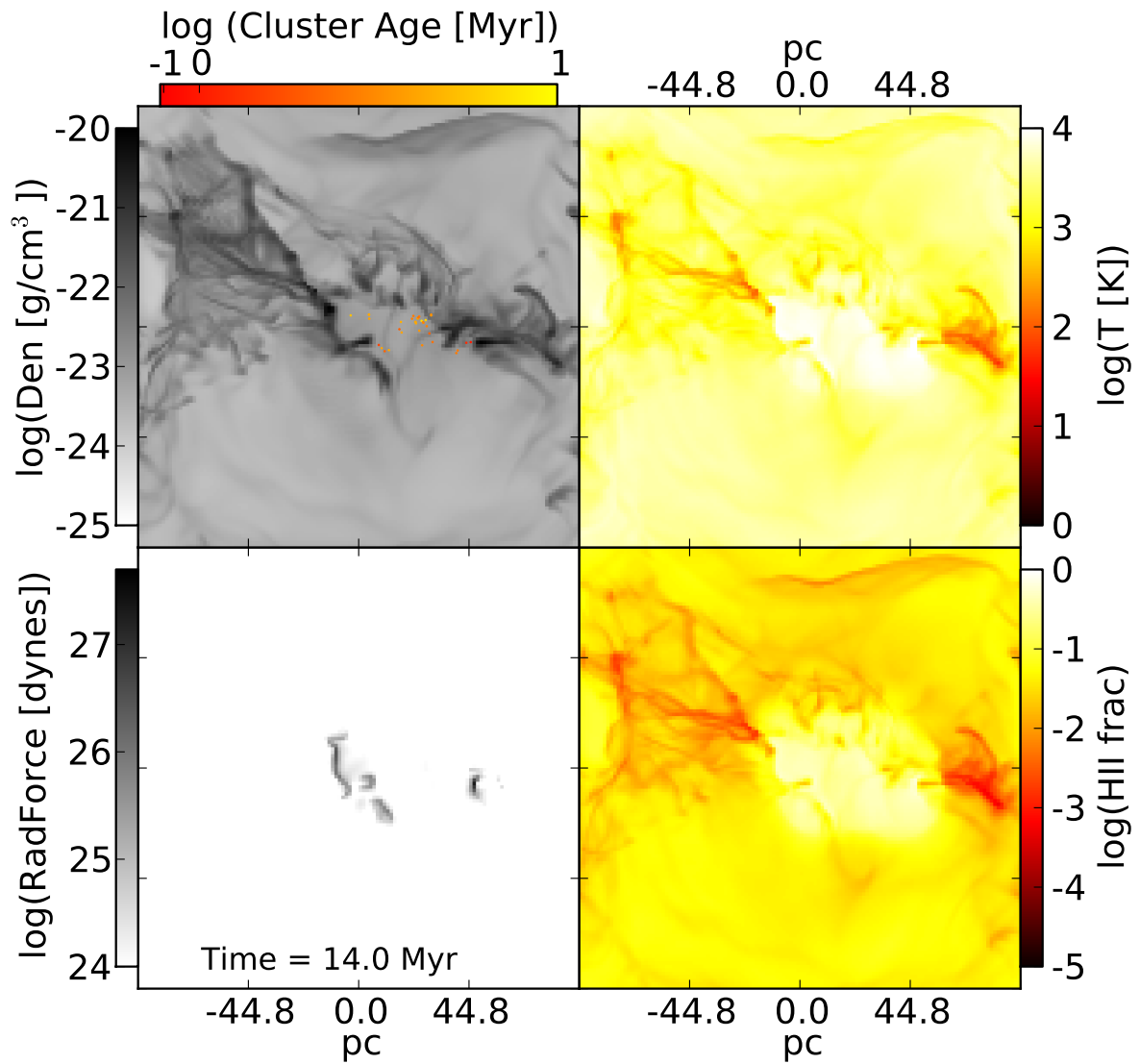


Figure 5.15: Density, temperature, radiation force (momentum deposited), and HII fraction for the simulation with minimum mass = $316 M_{\odot}$ at 14 Myrs (8.6 Myrs after first cluster formed). For this minimum mass the mass in a cell at the critical density is larger than twice the minimum mass so clusters are formed with half the mass of the cell independent of surrounding conditions. Note the cluster particle size is set to a different scale than all other images as the clusters are of a much lower mass. The bubble has blown out and the cloud is significantly disrupted.

StarClusterFormEfficiency

Figure 5.16 shows the total mass and number of star cluster particles for varying efficiency parameter. The base simulation is shown in cyan dashed line (Ef5). Lower efficiency means the clusters form with less mass, especially noticeable for the first star cluster formed. The lowest efficiency runs from a few more star clusters but at a slightly lower star formation rate and quenches later. Thus, although the efficiency varies by almost a factor of four the final masses are much closer. Averaging all six runs the mass at 14 Myrs is: $28,731 \pm 4,881 M_{\odot}$ or 13.0 ± 2.2 % of the original cloud mass.

Figure 5.17 shows the mass structure with time for three runs: StarClusterFormEfficiency equal to 0.3, 0.5, and 0.7. The higher efficiencies lead to higher masses in stars earlier and thus a faster disruption of the cloud. The lower efficiency takes longer to disrupt but still does by 16 Myrs and does so with a lower final mass in clusters. Density projections for all six runs at 8.5 Myrs are shown in Fig. 5.18. The more rapid disruption of the cloud is more evident for the higher efficiency runs and the larger number of star clusters can already be seen in the lower efficiency runs.

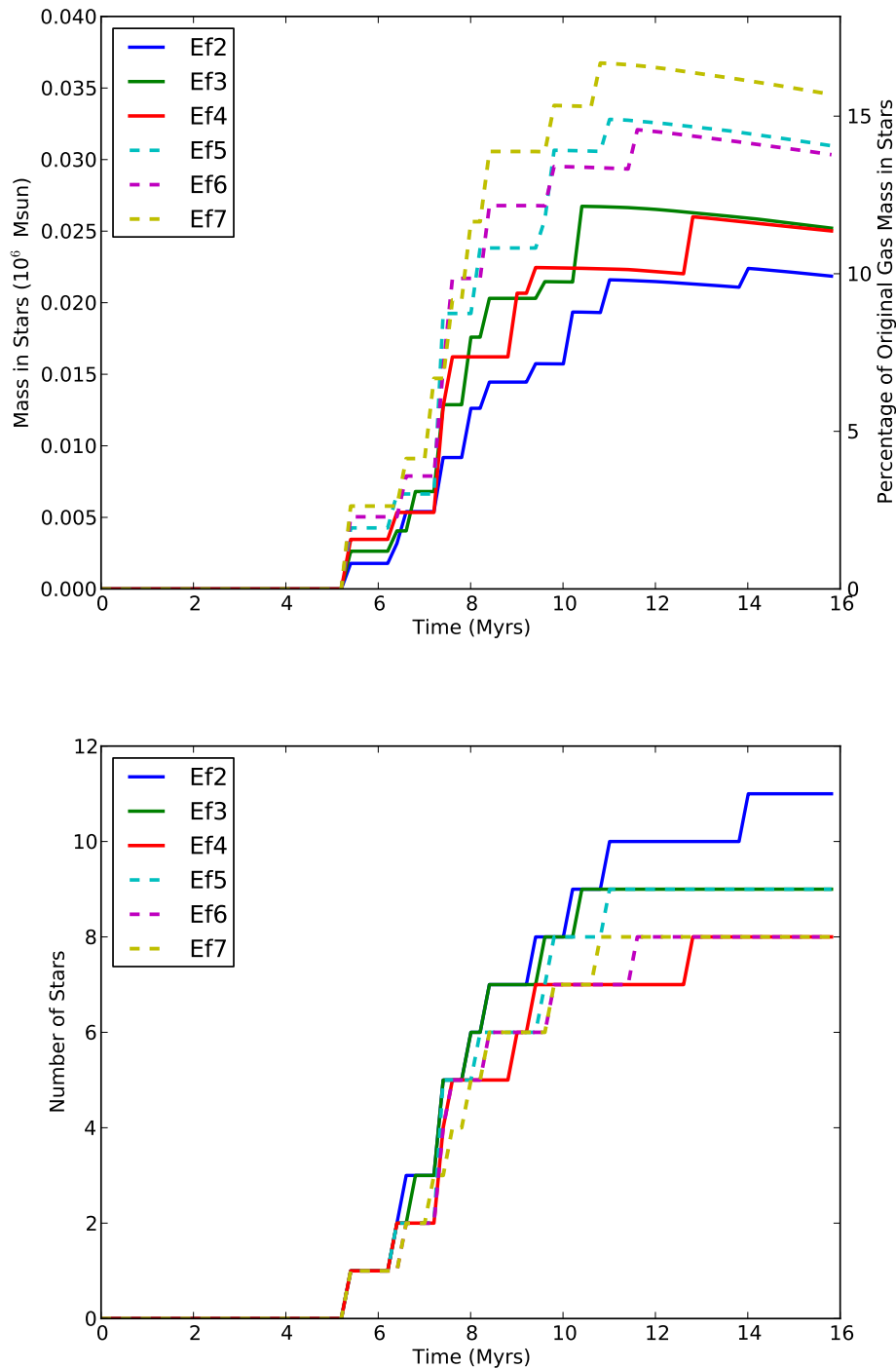


Figure 5.16: Time evolution of *top*: total mass in and *bottom*: number of star cluster particles in the simulations for varying efficiency. Lower efficiency creates lower mass star clusters initially but the higher number formed and therefore the initially weaker outputs results in a similar final mass in clusters.

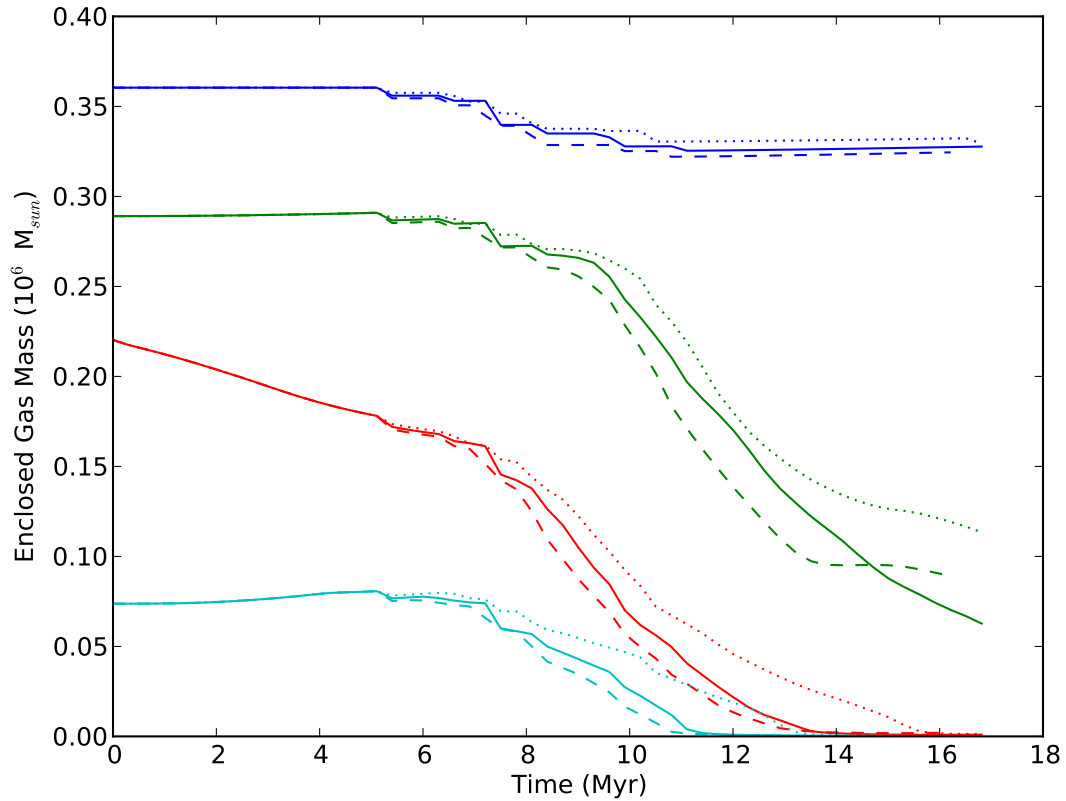


Figure 5.17: The mass structure for the three simulations with different efficiencies, *solid*: `StarClusterFormEfficiency` = 0.5 (base simulation) *dashed*: `StarClusterFormEfficiency` = 0.7, and *dotted*: `StarClusterFormEfficiency` = 0.3. Higher efficiencies lead to higher mass clusters with more radiation and thus faster disruption of the cloud.

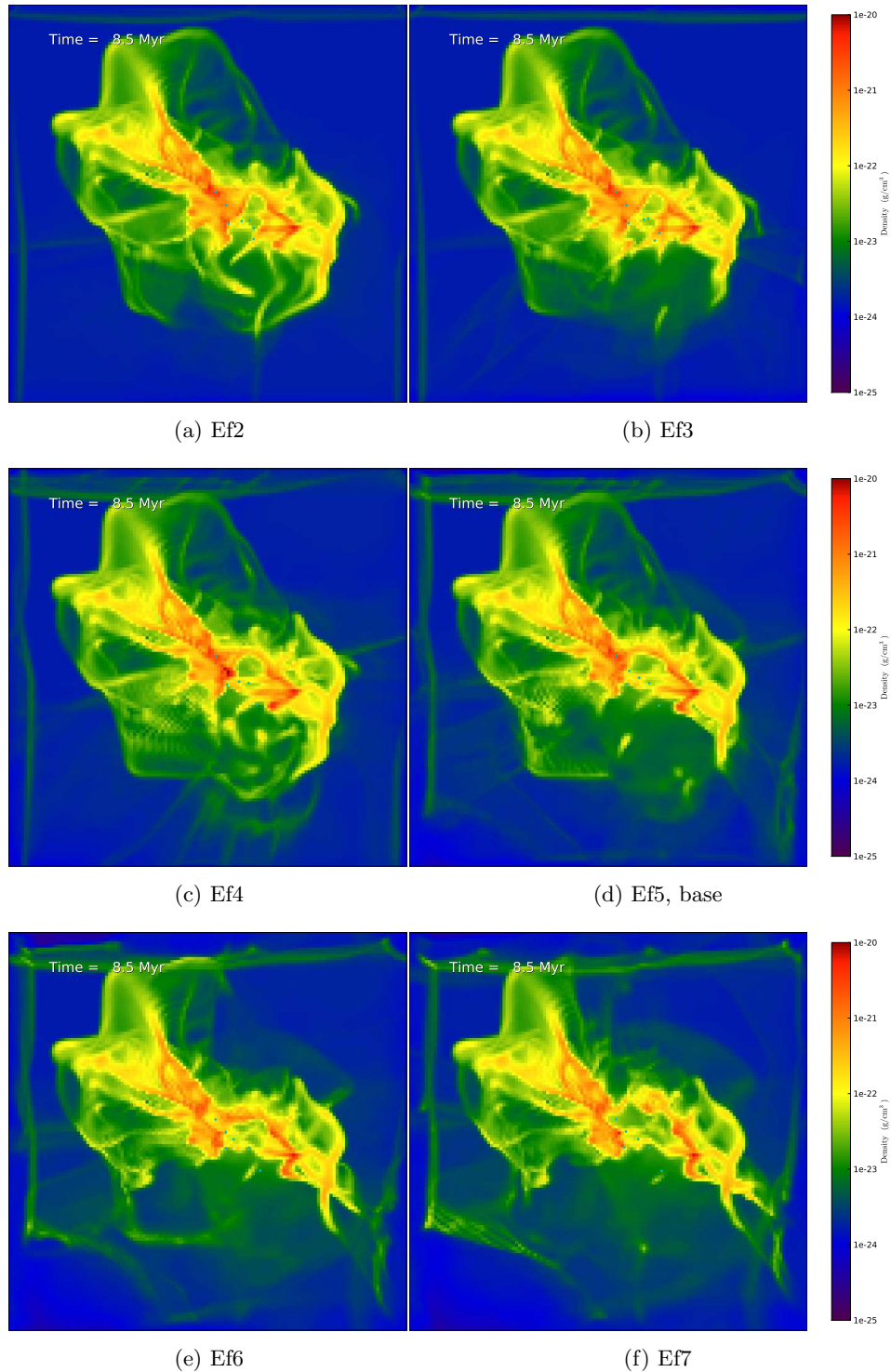


Figure 5.18: Full box projections of density for six simulations with different star cluster formation efficiencies at 8.5 Myrs (3.2 Myrs after first cluster formation). Star clusters are shown as cyan dots. For lower efficiencies there are more star clusters but less disruption as the total mass in clusters is lower. The extent of the break out from the bubble can be seen by the edge effects which are much more significant for the higher efficiencies at this time.

Parameter Study with No Outputs

All of the star formation parameter studies so far were run with ionization and radiation pressure outputs from the star clusters. To check how robust the star formation rates are, I reran the parameter study with no outputs from the stars. I only reran those parameters with resolved star formation, as listed in Table 5.3. The mass in star clusters against time for all of the parameters are shown in Figs. 5.19, 5.21, 5.22, and 5.24. For those figures the simulation with the base parameter combination and no outputs is shown as a solid blue line (nD40, nT63, nM30, nEf5).

As seen in the previous star formation parameter study varying the critical density does not affect the rate of star formation as seen by the very similar gradients for all but the highest critical density run. The mass converted into star clusters per dynamical time once star formation begins for critical densities between $10^{3.5}$ and 10^5 is $66,535 \pm 6,624 M_{\odot}$ or $30.2 \pm 3.0 \%$ of the original gas mass. For a critical density of $10^{5.5}$ the rate of cluster formation seems to be shallower. To compare to the parameter study with outputs I have plotted both D55 runs in Fig. 5.20. The run with outputs is shown in blue, and that without in green. Both of the highest density runs have been run much longer than the other parameter studies as the cloud is not disrupted. At 22 Myrs both simulations have 4 star clusters with masses totalling $4.1 \times 10^4 M_{\odot}$. However, for the run without feedback the fourth star cluster forms later than for the simulation with outputs. For the simulations with highest critical density the lower rate of mass conversion is a resolution effect as the unresolved star cluster formation algorithm is used.

Figure 5.21 shows the parameter study for resolved star formation with varying dynamical times from 1.3 - 3.2 Myrs. The extreme similarity in gradients is easily seen with the only scatter caused by the small changes in mass of the star clusters formed. The mass converted into star clusters per dynamical time once star formation begins for all of the runs is $73,939 \pm 4,614 M_{\odot}$ or $33.6 \pm 2.1 \%$ of the original gas mass.

Figure 5.22 shows the parameter study for resolved star formation with minimum mass for the clusters between 1000 and $31,623 M_{\odot}$. The rates of mass conversion for varying minimum mass are the most similar across the runs. The mass converted into star clusters per dynamical time once star formation begins is $70,627 \pm 3,875 M_{\odot}$ or $32.1 \pm 1.8 \%$ of the original gas mass. Density projections for the whole simulation box for two different critical densities are shown in Fig. 5.23.

Figure 5.24 shows how varying the efficiency parameter for star formation changes the mass in star clusters with time. The rate of star formation is very similar for all of the runs after 9

Myrs. The runs with lower efficiency have star formation rates that ramp up over the first few million years giving lower rates at first but the same rates after that. The mass converted into star clusters in the first dynamical time after star formation begins is $72,870 \pm 6,882 M_{\odot}$ or $33.1 \pm 3.1 \%$ of the original gas mass. The lowest efficiency run has the lowest mass in stars at 12.2 Myrs (one dynamical time after first cluster formed) and the highest efficiency has the highest mass but the efficiencies around the base value are all very close and switch which is higher at any one time.

Name	PODensityThreshold	SCMDynamicalTime	SCMMass	SCFEfficiency
nD40 nT63 nM30 nEf5 none	10^4	2×10^6	10^3	0.5
nD35	3.16×10^3	2×10^6	10^3	0.5
nD45	3.16×10^4	2×10^6	10^3	0.5
nD50	10^5	2×10^6	10^3	0.5
nD55	3.16×10^5	2×10^6	10^3	0.5
nT61	10^4	1.26×10^6	10^3	0.5
nT62	10^4	1.58×10^6	10^3	0.5
nT64	10^4	2.51×10^6	10^3	0.5
nT65	10^4	3.16×10^6	10^3	0.5
nM35	10^4	2×10^6	3.16×10^3	0.5
nM40	10^4	2×10^6	10^4	0.5
nM45	10^4	2×10^6	3.16×10^4	0.5
nEf2	10^4	2×10^6	10^3	0.2
nEf3	10^4	2×10^6	10^3	0.3
nEf4	10^4	2×10^6	10^3	0.4
nEf6	10^4	2×10^6	10^3	0.6
nEf7	10^4	2×10^6	10^3	0.7

Table 5.3: The star cluster particle formation parameters for the simulations run with no stellar outputs.

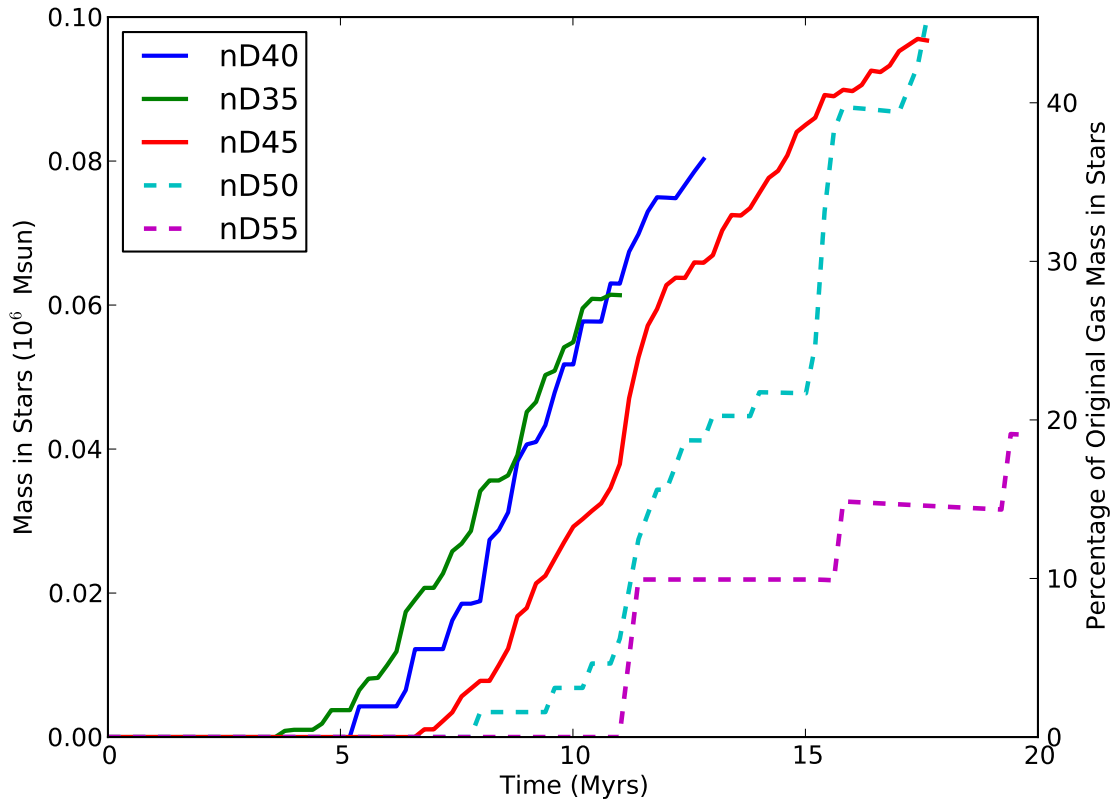


Figure 5.19: Time evolution of total mass in star cluster particles in the simulations with no stellar outputs and varying critical densities for cluster formation. The rate of mass conversion into star clusters is consistent for all but the highest critical density with only the start time varying.

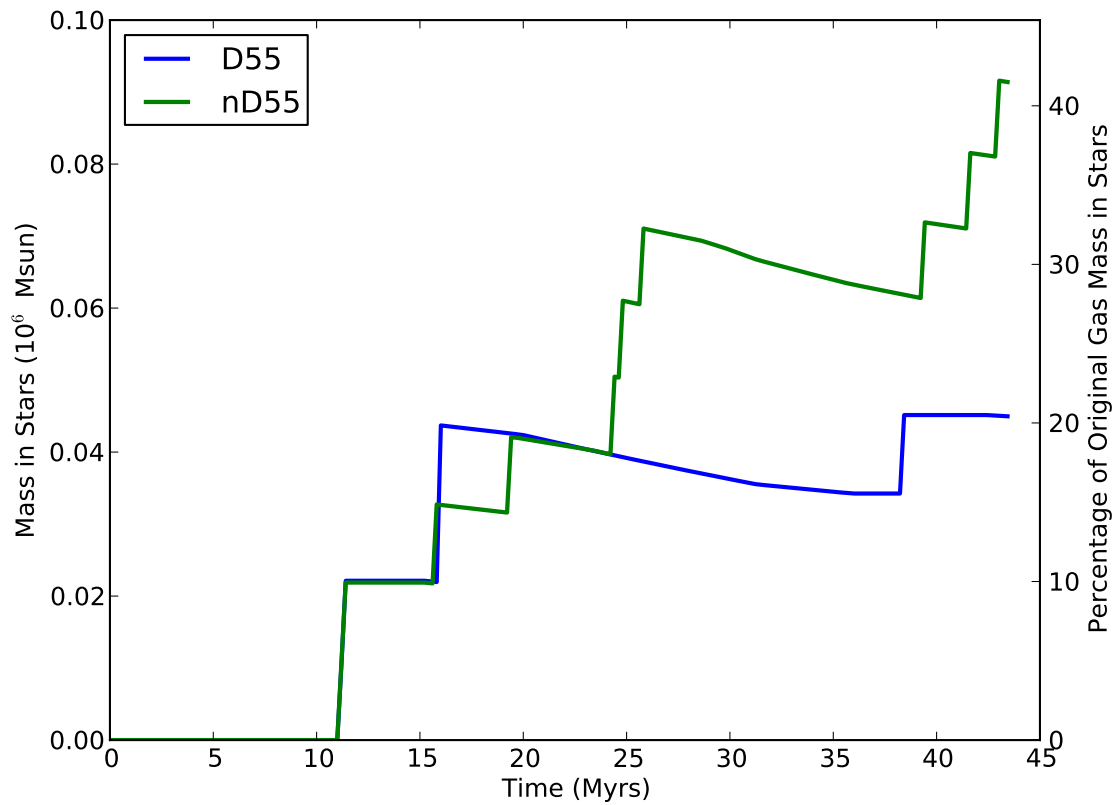


Figure 5.20: Time evolution of total mass in star cluster particles in the simulations with highest critical densities for both no outputs (green) and with ionization and radiation pressure (blue). Even at these extreme densities the outputs do affect star formation.

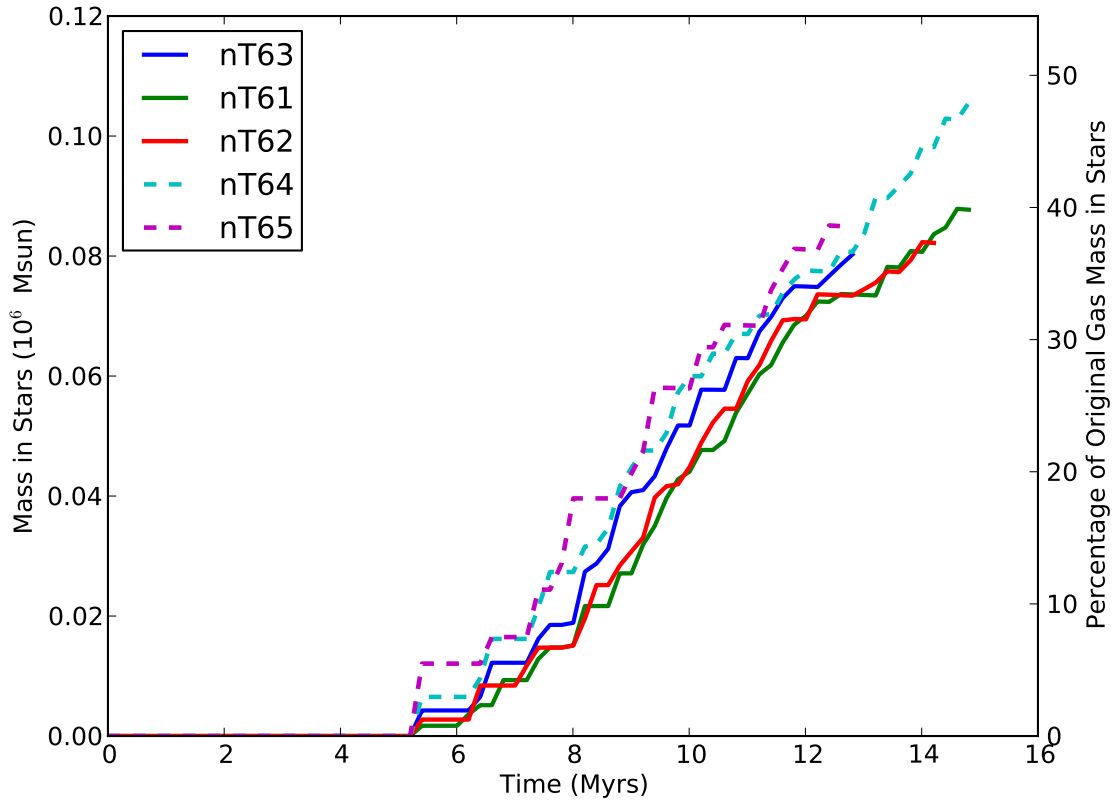


Figure 5.21: Time evolution of total mass in star cluster particles in the simulations with no stellar outputs and varying minimum dynamical time for the sphere involved in cluster formation. After the first couple of star clusters form the rate of star formation for all runs are extremely similar as shown by the gradient of the lines. Larger dynamical times form fewer star clusters with greater mass but the same total mass overall.

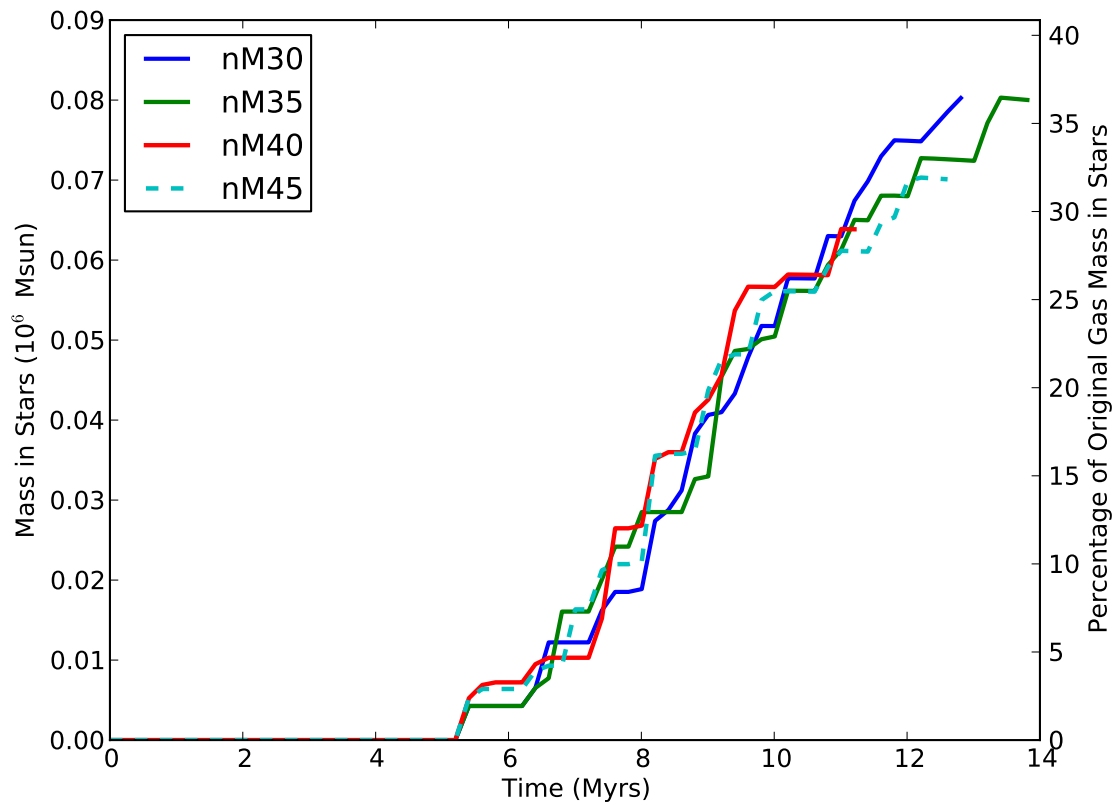


Figure 5.22: Time evolution of total mass in star cluster particles in the simulations with no stellar outputs and varying minimum mass for star clusters. All runs have the same rate of star formation and the same total mass in stars.

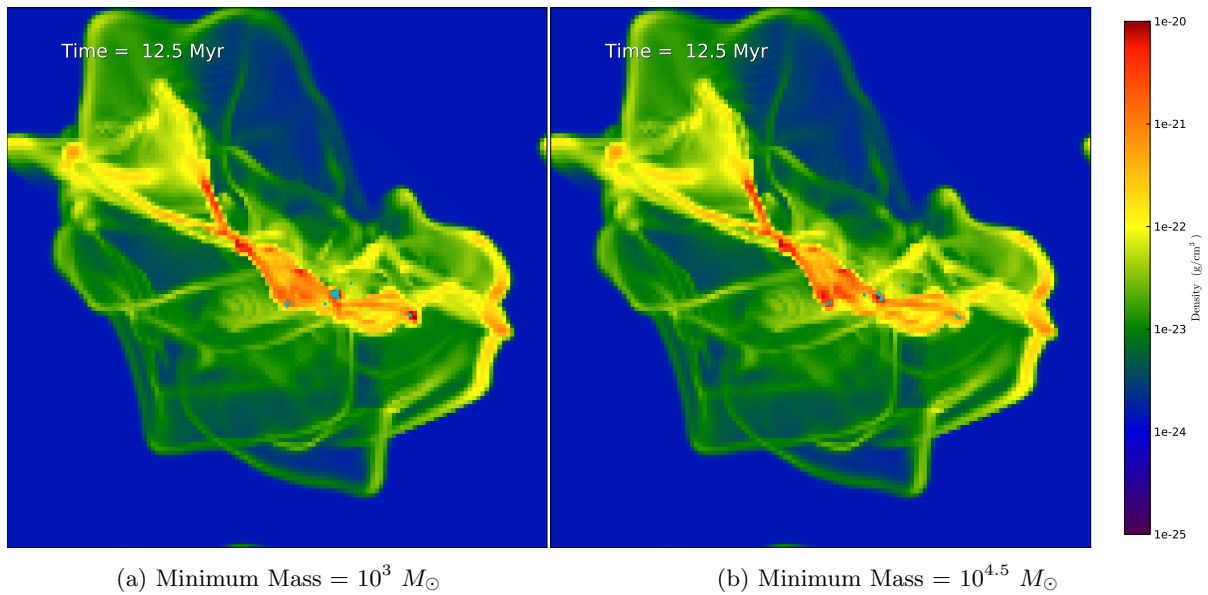


Figure 5.23: Projections of density for the whole simulation box for the simulations with no outputs and *left*: minimum mass for star clusters = $10^3 M_{\odot}$ and *right*: minimum mass for star clusters = $10^{4.5} M_{\odot}$. The clusters are in the same locations the only difference being a higher number but of lower mass clusters for the lower minimum mass.

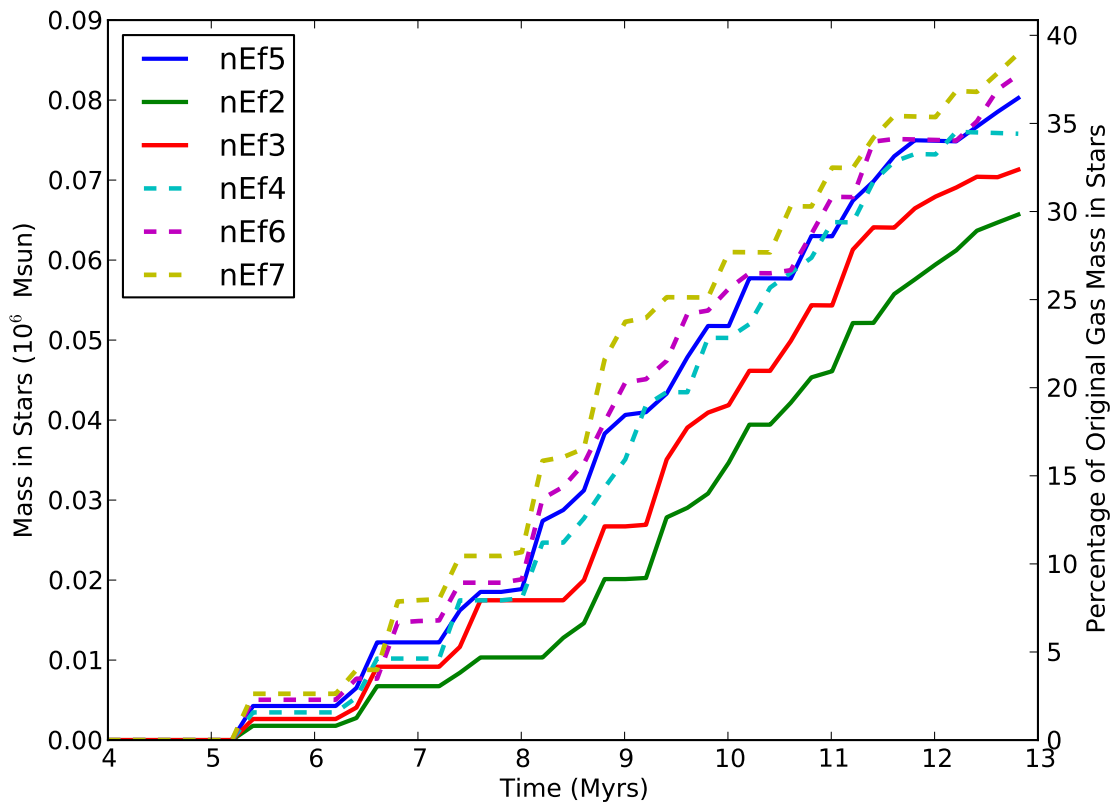


Figure 5.24: Time evolution of total mass in star cluster particles in the simulations with no stellar outputs and varying efficiency for star cluster formation. All lines have very similar gradients after 9 Myrs though the initial star formation rates are lower for the lower efficiencies.

Parameter Study Summary

Varying the star formation parameters within physically and numerically justified limits, even drastically, does not change the final fate of the GMC significantly. The number of star cluster particles formed and the time at which they form changes but ultimately, with approximately the same total mass in star clusters, the GMC is disrupted. The exception to this is when the critical density is set so high a large fraction of the cloud has collapsed into a small region before a star cluster has formed and the ionization gas pressure cannot disrupt it. Even then, the outputs slow the rate of star formation.

For simulations with no outputs from the stars, conversion of mass from gas into stars is 30% per free fall time for a significant range of star cluster formation parameters. For the simulations with stellar outputs, the initial star formation rate is similar to the simulations without outputs but the rate decreases and is almost zero within a dynamical time. Thus the simulations with outputs robustly form clusters with approximately 12 % of the original cloud gas mass by one dynamical time after cluster formation began.

5.2 Resolution Tests

As with all simulations, one serious consideration is resolution. As mentioned in the parameter study, §5.1, the resolution limits the range of star formation parameters that can be used for resolved cluster formation. For these simulations I have tested both unigrid and AMR resolution changes and consider both physical and numerical effects of the changing resolution.

The velocity structure for the turbulence in the cloud is created at initialization on the top grid. To keep the same velocity structure for both 128 and 256 top grids the spectrum is generated to the same maximum wavenumber.

5.2.1 Star formations parameters for changing resolution

According to Colín et al. (2010) when resolution changes the subgrid star formation parameters should be adjusted to maintain the same star formation rates. They found that the critical density for star formation should scale so that the surface density of the cells forming stars remains constant. To keep surface density constant, for every factor of two increase in resolution the density threshold should increase by a factor of two. Although Colín et al. (2010) were simulating on a different scale I noticed that with resolution change the star formation occurred differently so investigated.

5.2.2 Unigrid Results

I ran unigrid simulation a factor of two higher in resolution to investigate how resolution affects the formation and feedback from star clusters. Table 5.4 describes the simulations run in this study. All of the simulations are unigrid (no AMR) and for the 256^3 grid I ran simulations with three different density thresholds.

Name	Top grid resolution	Number of child levels	Density threshold $\times \bar{\rho}$
128r0d1, base	128	0	1×10^4
256r0d1	256	0	1×10^4
256r0d2	256	0	2×10^4
256r0d4	256	0	4×10^4

Table 5.4: Simulation details for unigrid resolution tests.

Graphs showing the mass and number of star clusters for the unigrid simulations are shown in Fig. 5.25. Increased resolution results in star formation starting earlier, especially for the same density threshold, as shown by the cyan lines (128r0d1 and 256r0d1). The higher resolution resolves shocks better and thus creates thinner, higher density filaments. Figure 5.26 shows density projections at 4.5 Myrs for the simulations with different unigrid resolution. The filaments are finer at the higher resolution but the overall structure is very similar.

Changing the density threshold to maintain surface density of cells gives approximately the same time for the first star cluster formation (128r0d1 and 256r0d2). However, increasing the density threshold further for the 256^3 to 4×10^4 times the average density causes the first star to form even closer in time to the base run. Both of the 256^3 with higher density thresholds form the same mass in stars but the 4×10^4 times the average density run does so with fewer stars and more closely resembles the base simulation. This suggest for my simulations the line density rather than surface density should be kept constant to get the most similar cluster formation.

Figure 5.27 shows three unigrid simulations all at 7.6 Myrs. The simulations shown are the base simulation and two of the higher resolution unigrid simulations with different higher critical densities. The number of, and placement of, the star clusters within the existing bubble is more similar to the base simulation for 256r0d4 than 256r0d2. For all three simulations the size of the bubble around the first star cluster is very similar as is the overall structure. For 256r0d2 the different locations and greater spread of star clusters changes the bubble shape a small amount but not significantly.

As the star clusters age and emit radiation into the surrounding medium, differences between 128^3 and 256^3 top grids become more apparent. Figure 5.28 shows the density, temperature, radiation force absorbed, and HII fraction for the 256r0d4 simulation 2.1 Myrs after the first star cluster formed (total time = 7.3 Myrs). Compared to Fig. 4.7, the base simulation the same time since first star formation, the bubble is more contained with little radiation or gas leaking out. The clusters are still only in one region of the cloud. The bubble seems to be a little larger given the structure seen in the radiation force panel and slightly better defined in the density panel. Figure 5.29 shows the density, temperature, radiation force absorbed, and HII fraction for the 256r0d4 simulation 4.1 Myrs after the first star cluster formed (total time = 9.3 Myrs). Compared to Fig. 4.9 the cloud looks equally disrupted. The higher resolution shows more structure in the gas but the bubbles look similar in size.

The mass structure within the simulation boxes for the base simulation (128r0d1) and the higher resolution 256r0d4 are shown in Fig. 5.30. The mass converted into clusters is very similar, as shown by the similar decreases in total mass (blue lines). The masses within $2 R_{cl}$

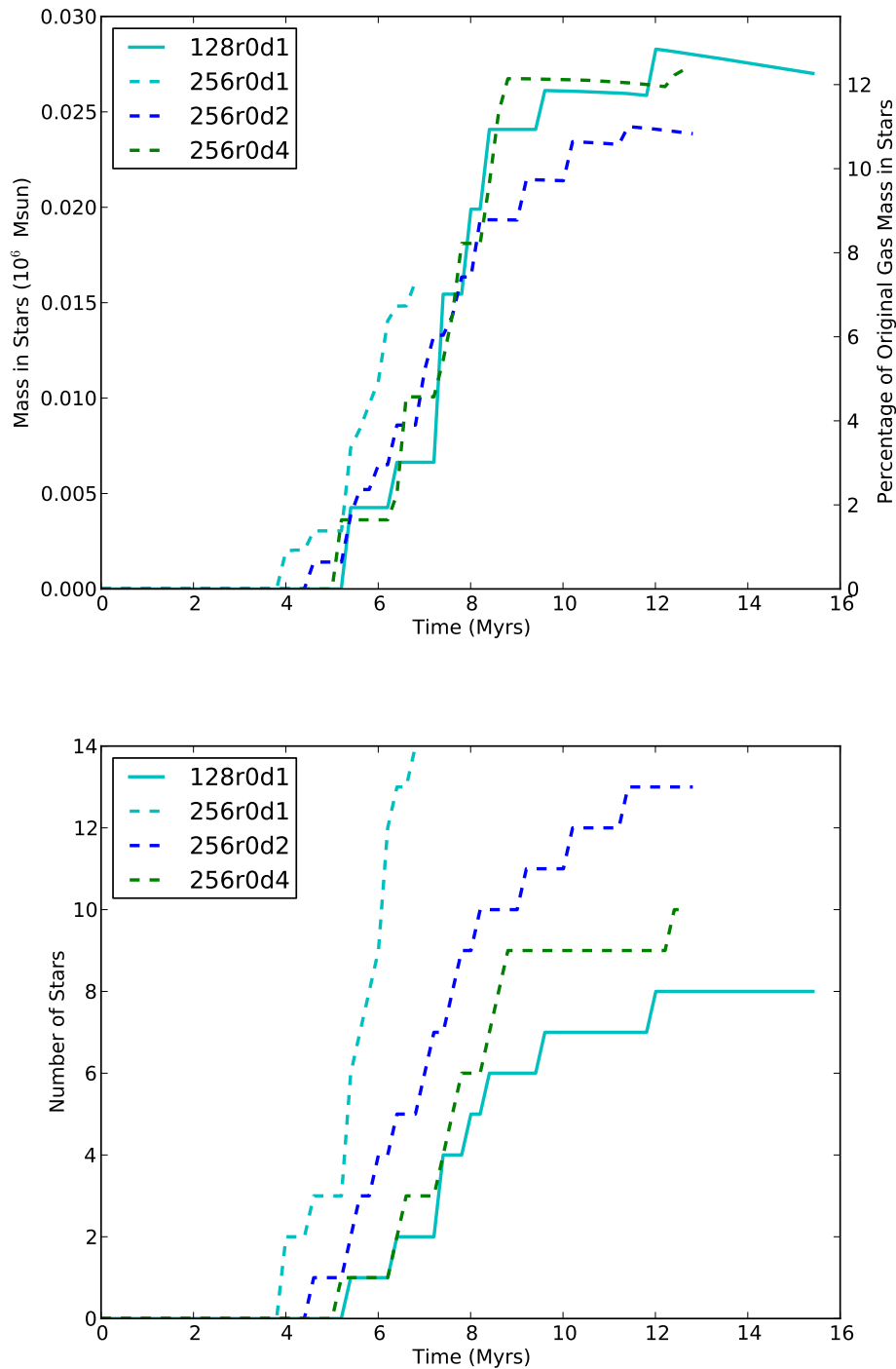


Figure 5.25: Time evolution of *top*: total mass in and *bottom*: number of star cluster particles for unigrid simulations. For the same density threshold clusters form earlier and more numerous for the higher resolution. For the higher density threshold increasing the density by a factor of four most closely resembles the mass and number of stars of the lower resolution.

and R_{cl} seem to evolve in a very similar way in both simulations though the higher containment shows itself in the more rapid decrease in mass within $0.5 R_{cl}$. The 256^3 top grid is much more computationally expensive to run.

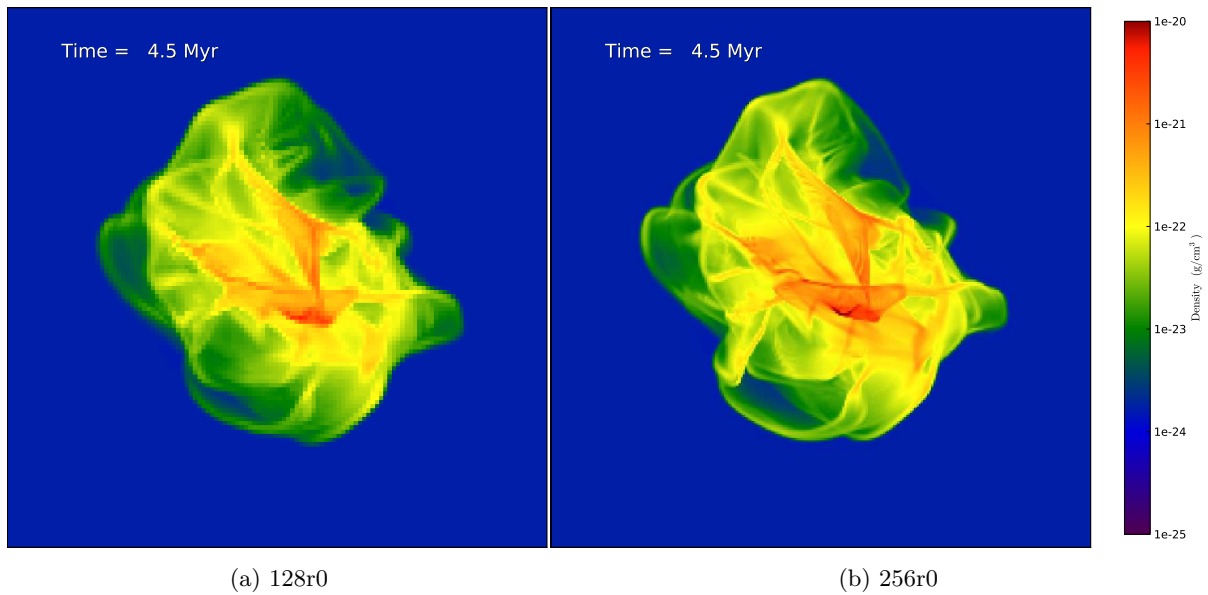


Figure 5.26: Projections of density for unigrid simulations with different resolutions at 4.5 Myrs (before any star formation).

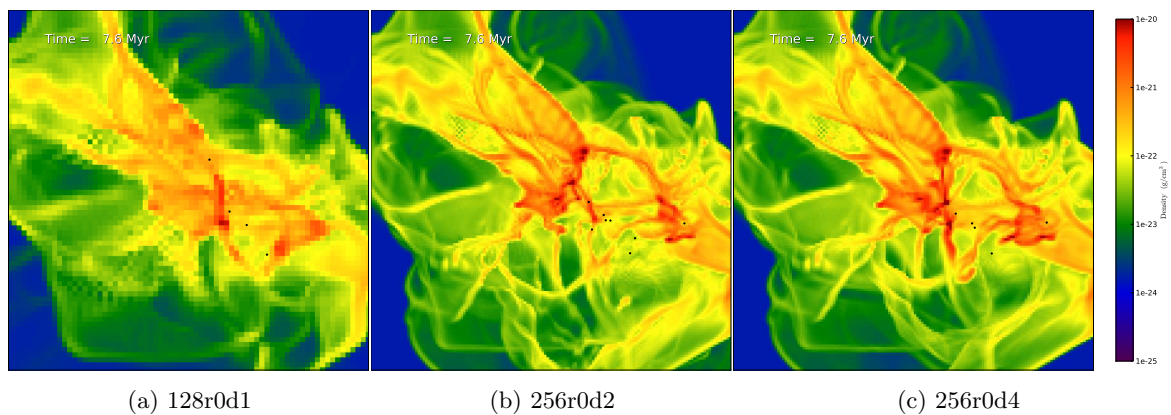


Figure 5.27: Inner 100 pc projections of density for unigrid simulations with different resolutions and critical densities at 7.6 Myrs. At 7.6 Myrs all three simulations have approximately the same mass in stars though the first star clusters formed at different times. All of the bubbles are the same size and have a very similar structure.

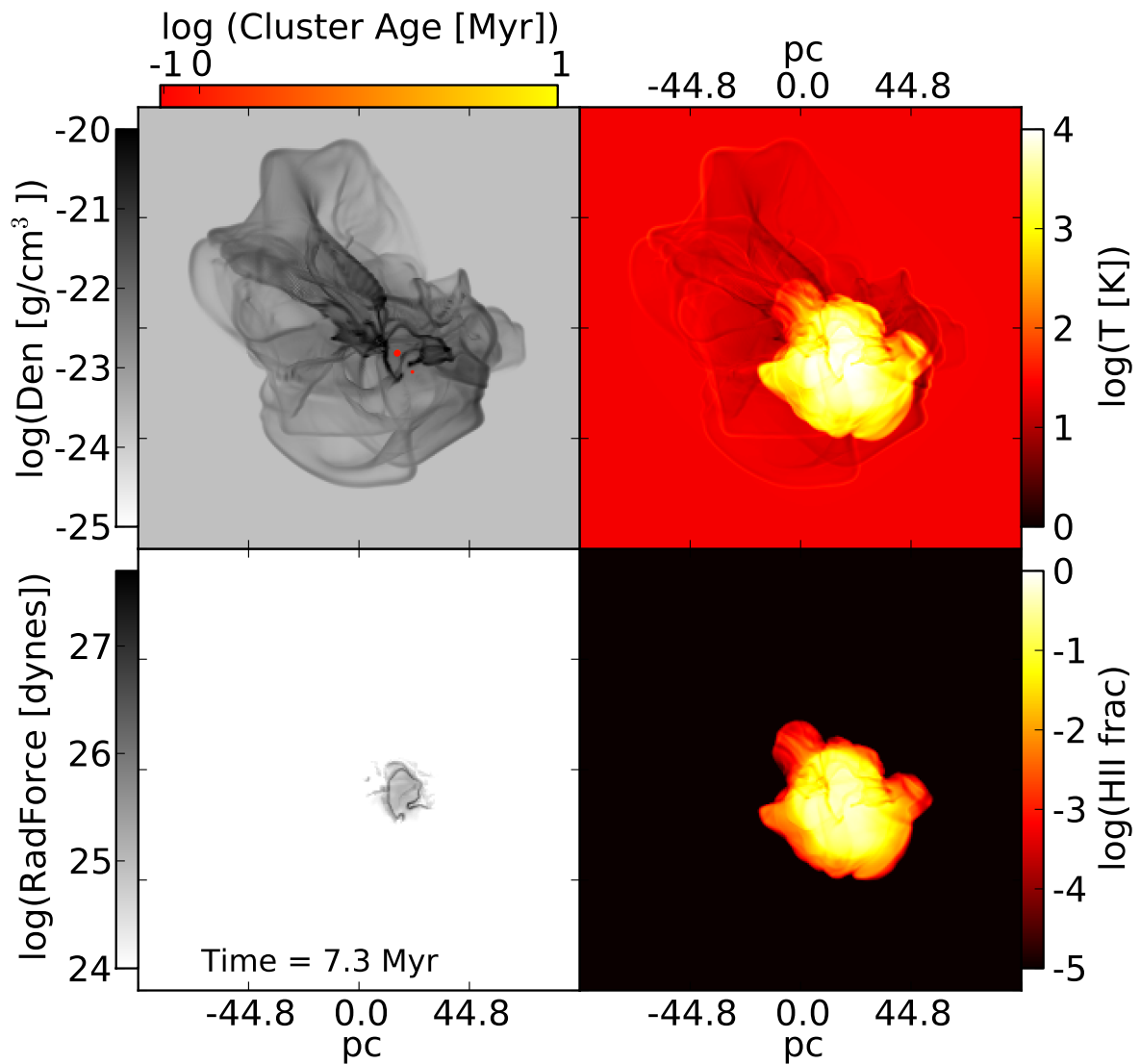


Figure 5.28: Density, temperature, radiation force (momentum deposited), and HII fraction for the 256^3 simulation with 4×10^4 critical density at 7.3 Myrs (2.1 Myrs after first cluster formed). Star cluster particles are shown as filled circles on the density projection. Star cluster circle size is relative to mass and colour indicates the age of the cluster at this time. The sum of the radiation force absorbed by the gas in this frame is 5.42×10^{29} dynes. Compared to Fig. 4.7, the base simulations at the same time after first star cluster formation, the HII region is more confined but the overall structure is still very similar.

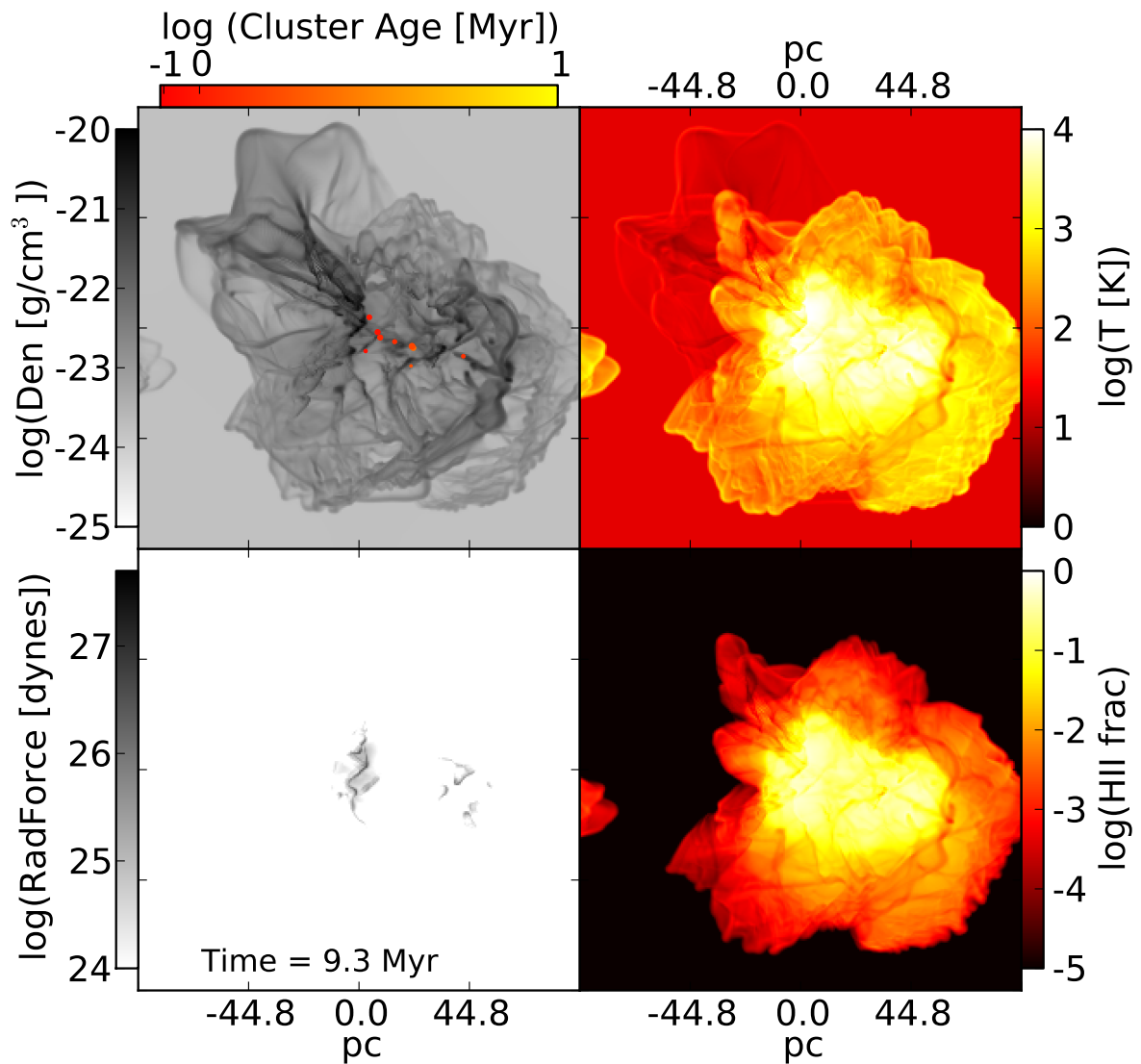


Figure 5.29: Density, temperature, radiation force (momentum deposited), and HII fraction for the 256^3 simulation with 4×10^4 critical density at 9.3 Myrs (4.1 Myrs after first cluster formed). Star cluster particles are shown as filled circles on the density projection. Star cluster circle size is relative to mass and colour indicates the age of the cluster at this time. Compared to Fig. 4.10, the base simulations at the same time after first star cluster formation, there is more structure in the gas but the bubble is the same size. The ionized region is more confined rather than filling the whole box.

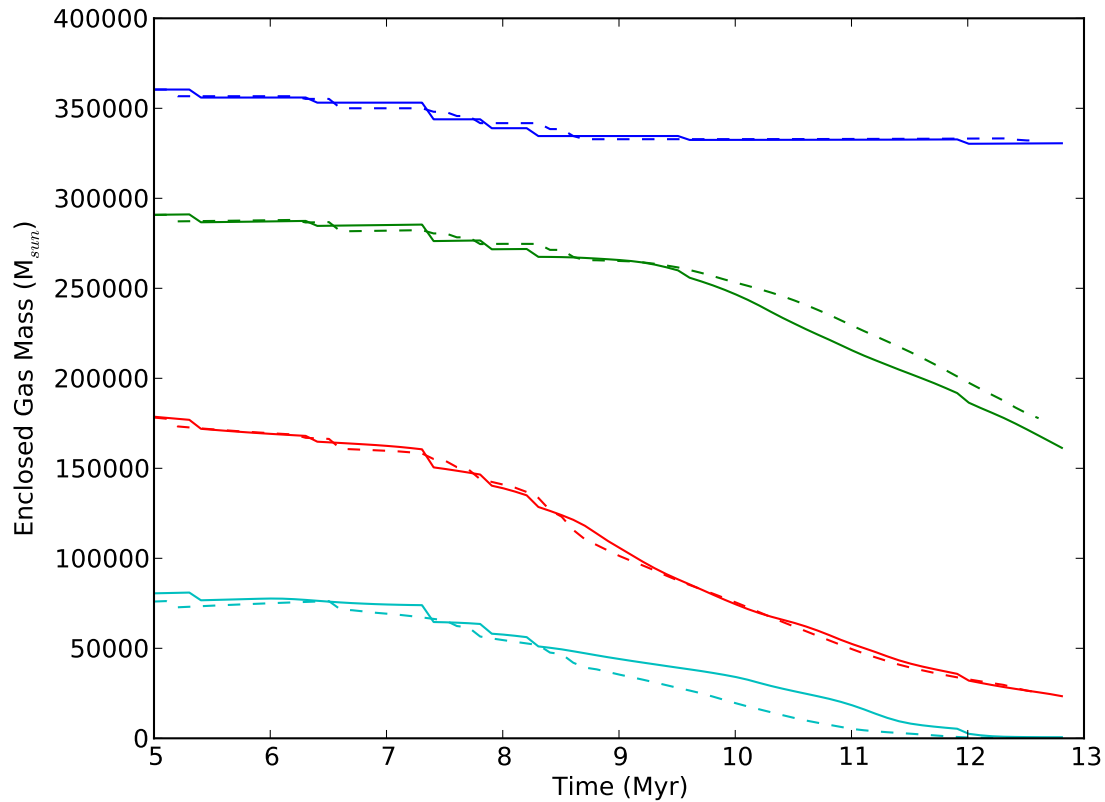


Figure 5.30: Mass structure of simulations. The *solid lines* are for the base simulation and the *dashed lines* for a simulation with twice the resolution and four times the critical density for star formation (256r0d4). The distribution of mass within spheres centred around the simulation box centre, where $R_{cl} = 0.25$ code units = 44.8 pc. Blue = all, Green = within $2 R_{cl}$ of the centre, Red = within R_{cl} of the centre, and Cyan = within $0.5 R_{cl}$ of the centre. The higher resolution run keeps the ionized region more confined and as such the inner most region is disrupted faster. For both simulations the initial cloud region is disrupted at the same rate.

5.2.3 AMR Results

For the AMR investigation I ran simulations with 128^3 and 256^3 top grids and up to two levels of refinement. For several runs I ran with the same grid structure but different `PopIIIOverDensityThreshold` values to investigate how star formation varies with different resolution. Table 5.5 lists the name, top grids, child levels, and critical densities for the simulations considered in this section. The refinement is controlled by Jeans length so that regions where star clusters will form are resolved but lower density and hotter regions are not.

Name	Top grid resolution	Number of child levels	Density threshold
128r0d1, base	128	0	1×10^4
128r1d2	128	1	2×10^4
128r1d4	128	1	4×10^4
128r2d4	128	2	4×10^4
128r2d8	128	2	4×10^4
256r0d2	256	0	2×10^4
256r0d4	256	0	4×10^4

Table 5.5: Table of the simulations considered in the AMR resolution study listing their top grid resolution, number of child levels (each level refines by 2), and the density threshold for star formation (factor of simulation box average density).

Effective 256^3

The first set of AMR simulations to compare are those with effective 256^3 resolution - 256^3 unigrid and 128^3 top grid and one level of refinement. Figure 5.31 shows density projections and cluster locations for the two simulations with effective 256^3 resolution and 4×10^4 critical density at 7.3 Myrs, ~ 2 Myrs after the first cluster forms. The clusters are forming in the same location and the cloud structure is similar. The material immediately around the clusters is a little different due to the slightly different formation time for the clusters.

Figure 5.32 shows the mass in star clusters and number of clusters against time for effective 256^3 resolution simulations. The line colour represents the critical density and the line style the grid structure. The unigrid simulations appear to have a steadier star formation rate whereas the AMR simulations have a period of rapid conversion of mass into clusters at around 7 Myrs. All of the simulations show quenched star formation with their star formation rates flattening out by 11 Myrs, as was found in the lower resolution unigrid simulations. The unigrid simulations formed less mass into clusters than the AMR runs with the same critical density. Figure 5.33 shows the unigrid run clears out the central region slightly earlier than the AMR simulations which is likely the cause of the earlier quenching of star formation. For 128r1d4 between 3% and 10 % of the volume is refined throughout the simulation. Just before star formation begins the refine fraction is highest at around 0.09. As star clusters form and disrupt the cloud, the refine fraction decreases down to between 0.02 and 0.03 from 9 Myrs onwards.

The AMR simulations run much faster and there is no evidence to suggest the star cluster formation is significantly different for the same effective resolution.

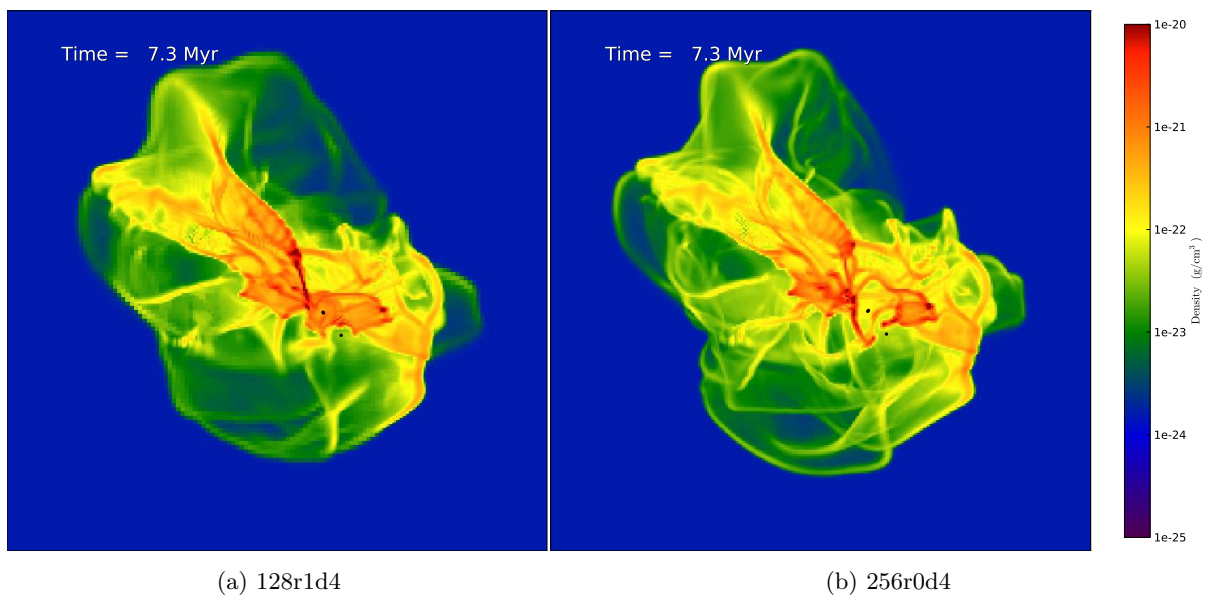


Figure 5.31: Projections of density for simulations with different top grids but the same effective resolution at 7.3 Myrs. The clusters are in the same locations and the overall cloud is very similar.

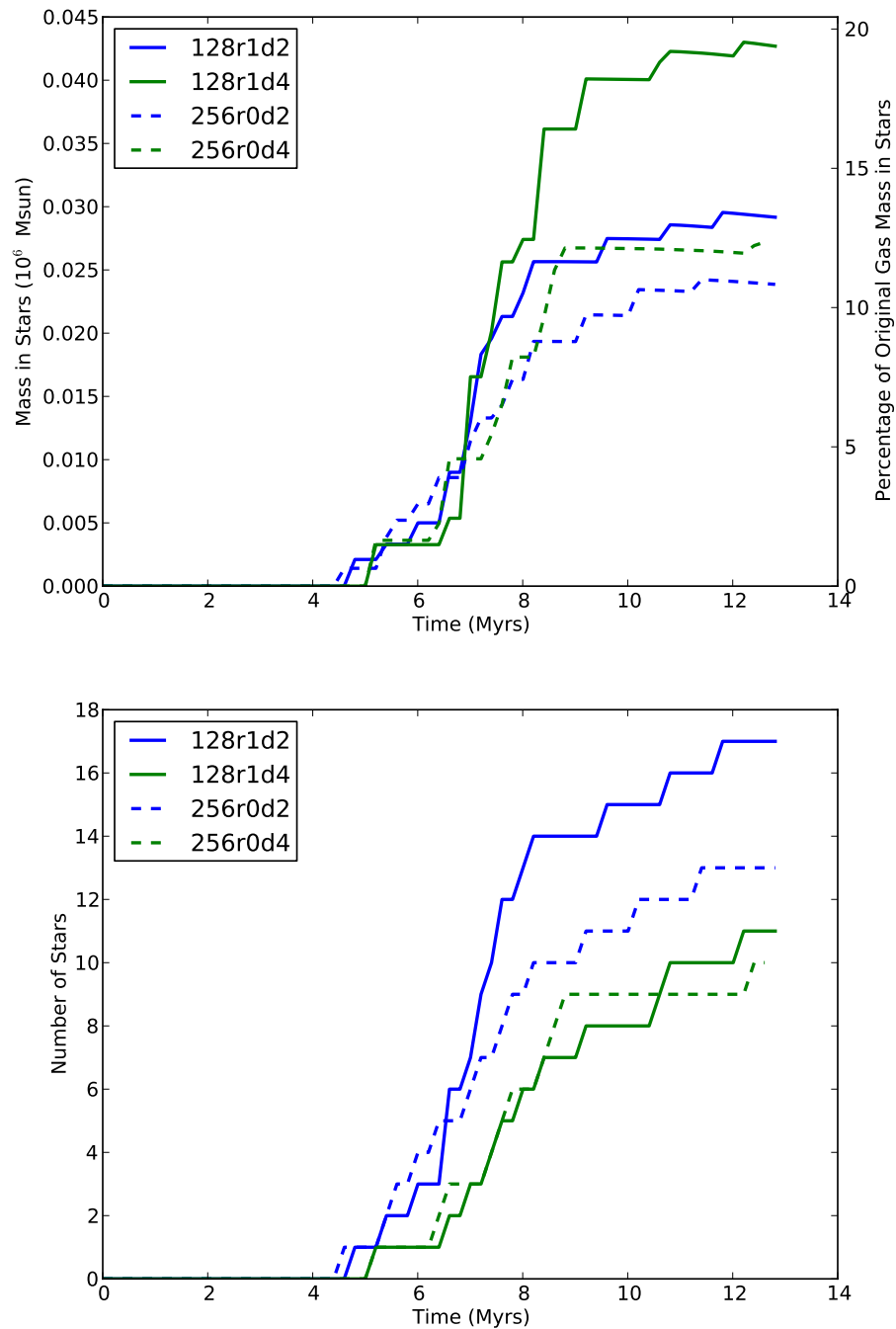


Figure 5.32: Time evolution of *top*: total mass in and *bottom*: number of star cluster particles for simulations with effective 256^3 resolution. For the runs with the same critical densities (same colour) the star formation starts at approximately the same time. However the 256 unigrid simulations form stars at a steadier rate than the AMR runs. The steadier rate quenches star formation earlier.

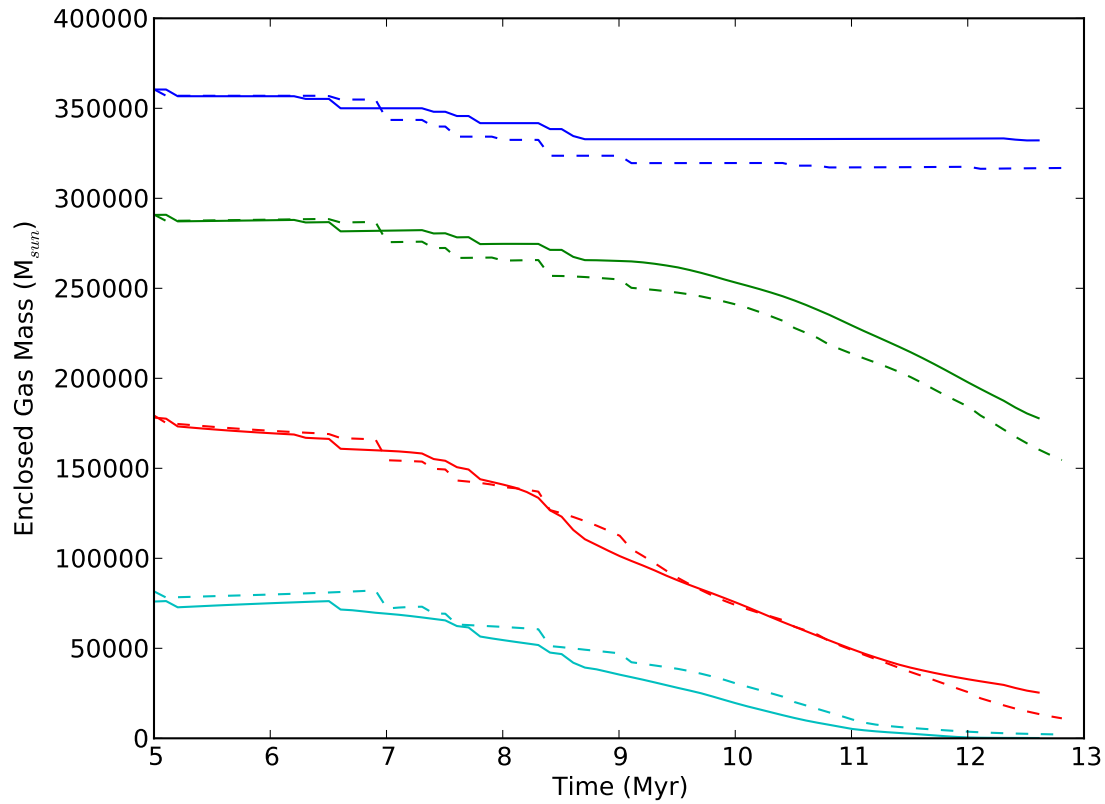


Figure 5.33: Mass structure of simulations. The *solid lines* are for the unigrid run 256r0d4 and the *dashed lines* for AMR run 128r1d4, the same effective resolution and critical density but different top grids. The distribution of mass within spheres centred around the simulation box centre, where $R_{cl} = 0.25$ code units = 44.8 pc. Blue = all, Green = within $2 R_{cl}$ of the centre, Red = within R_{cl} of the centre, and Cyan = within $0.5 R_{cl}$ of the centre. The unigrid run disrupts the inner region faster than the AMR run though both disrupt mass from the original cloud location simultaneously.

128³ Top Grid

Since AMR runs are much faster than unigrid for the same effective resolution I can investigate to higher resolution using AMR. Here I compare all of the simulations with 128³ top grids.

The total cluster mass and number of clusters is shown in Fig. 5.34. The colour represents critical density and line style the number of child levels. The solid cyan line is the base simulation. The two simulations that most closely resemble the base simulation for star formation rate and final mass are 128r1d2 and 128r2d8. 128r1d2 has the same surface density in the critical cells as the base run but 128r2d8 then has the same line density as 128r1d2. The simulations with the critical density equal to 4×10^4 have a final mass that is the most different from the base simulation. This suggests the scatter in final masses for different critical densities is significant and that for a deeper understanding of how parameters need to be changed for different resolution requires a more extensive investigation than presented here. The similarities in cluster number as well as mass for 128r1d2 and 128r2d8 support the earlier suggestion of line density conservation being the critical factor.

Figure 5.35 shows the cluster positions and cloud structure at 10.5 Myrs for the three simulations with most similar final masses. There are many more clusters in 128r1d2 and 128r2d8 than 128r0d1 and they are already spread out further along the filament. All three images show clear signs of advanced disruption with the bubbles blowing out to the same extent and similar bubble shell remnants on the right side. Figure 5.36 supports the similarities between 128r1d2 and 128r2d8 by showing the mass structure for the three runs with most similar final mass. 128r1d2 and 128r2d8 disrupt their host cloud at a very similar rate whereas 128r0d1 takes longer to reduce the mass within 0.5 and 1.0 R_{cl} due to the higher mass in clusters at early times (between 6.5 and 8 Myrs), as shown in Fig. 5.34.

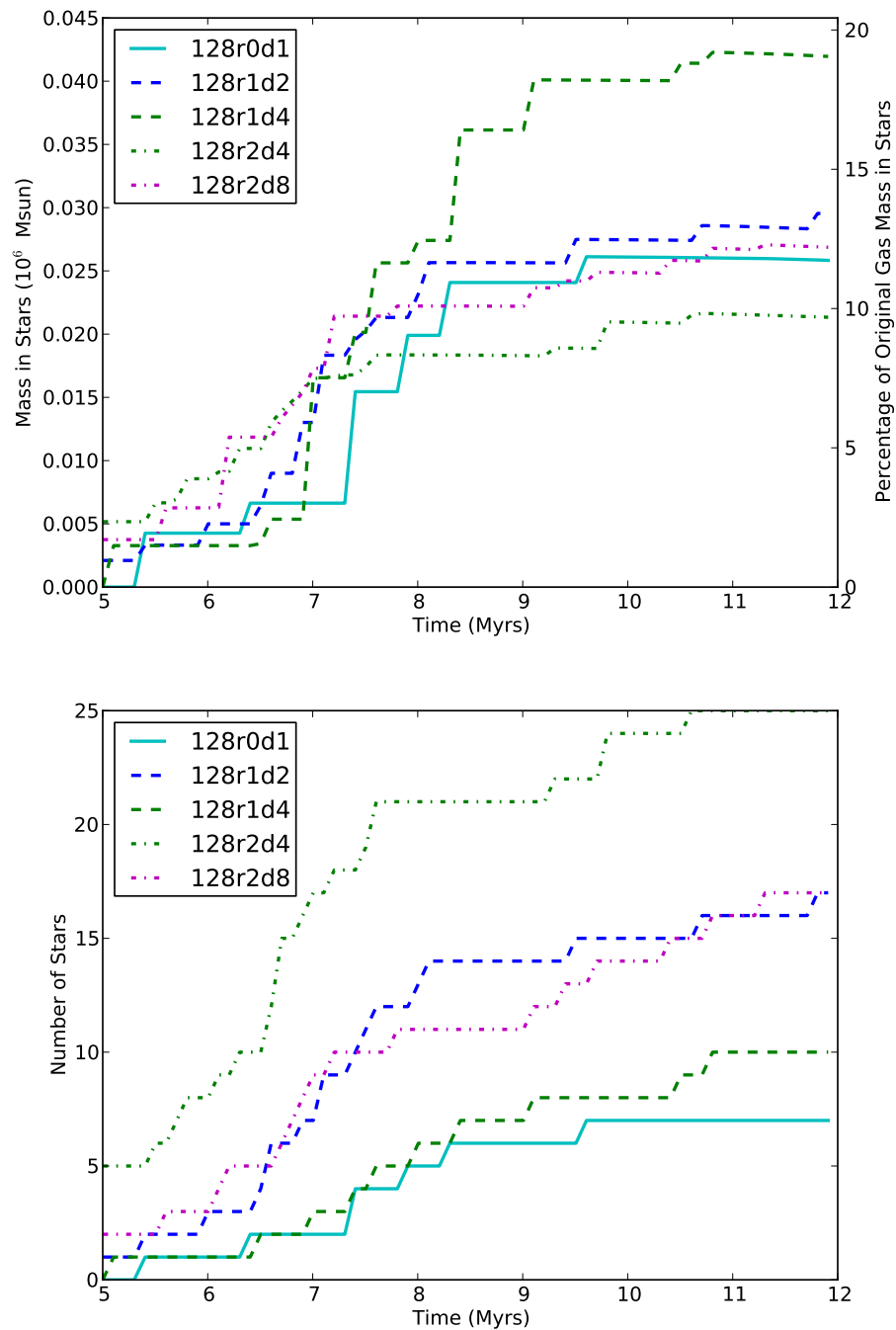
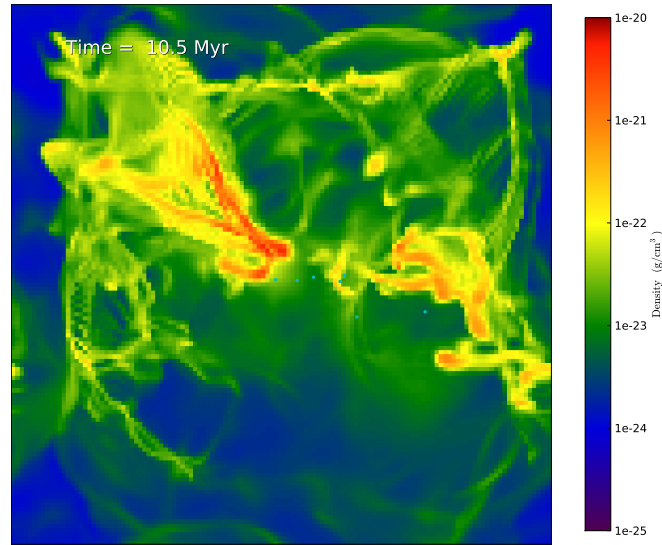
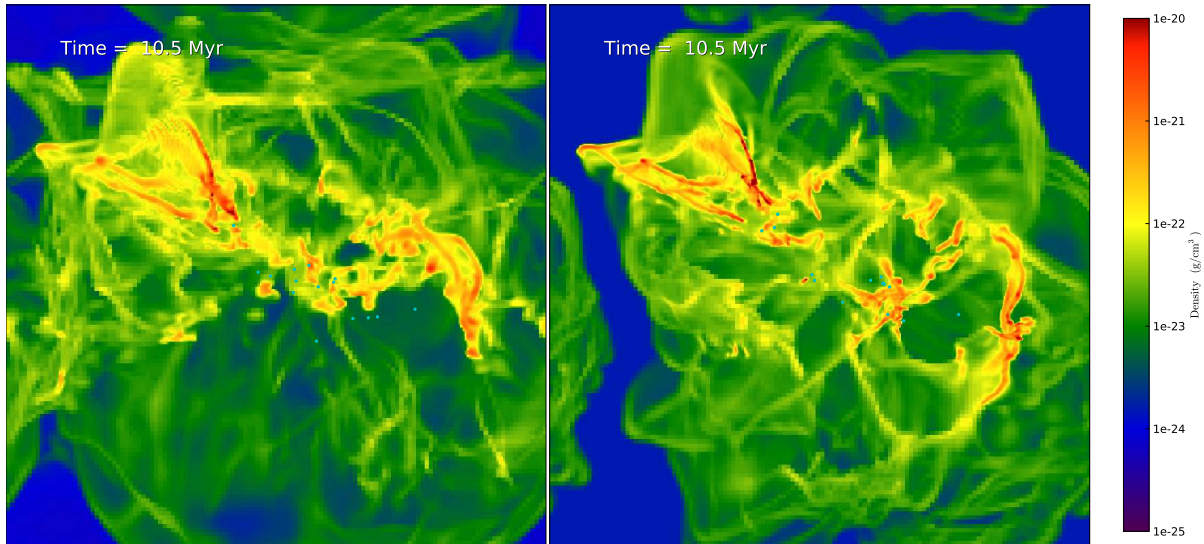


Figure 5.34: Time evolution of *top*: total mass in and *bottom*: number of star cluster particles for simulations with 128^3 Top Grid. Colour indicates critical density and line style indicates number of child levels. The base simulation is the solid cyan line. All of the simulations end with between 9 and 19 % of the original gas mass in clusters with 128r1d2 and 128r2d8 closest in mass to the base simulation. For higher resolution and the same critical density, more smaller mass clusters are formed.



(a) 128r0d1



(b) 128r1d2

(c) 128r2d8

Figure 5.35: Density projections at 10.5 Myrs for the three AMR simulations with most similar final masses. Although the resolution change is significant the positions of the clusters is similar as is the bubble structure.

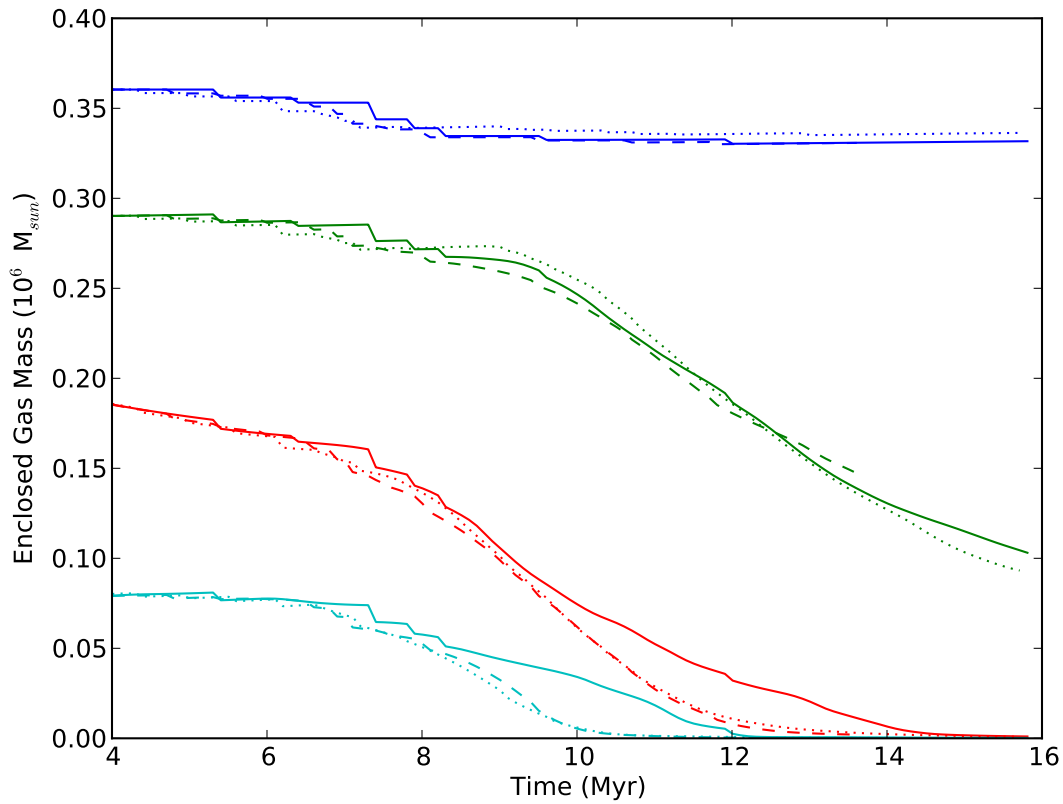


Figure 5.36: The distribution of mass within spheres centred around the simulation box centre where $R_{cl} = 0.25$ code units = 44.8 pc. The *solid lines* are for the base simulation, the *dashed lines* for 128r1d2, and the *dotted lines* for 128r2d8. Blue = all, Green = within $2 R_{cl}$ of the centre, Red = within R_{cl} of the centre, and Cyan = within $0.5 R_{cl}$ of the centre. The base simulation takes longer to disrupt gas out of both $0.5 R_{cl}$ and R_{cl} than the other two simulations despite them all having the same final mass in clusters. The larger mass in clusters at earlier times (between 6.5 and 8 Myrs) for the AMR simulations is the cause.

5.2.4 More Massive Cloud Resolution Tests

I ran simulations of the more massive cloud with 128^3 top grids (2.8 pc resolution). One I ran with one level of refinement to get the same effective resolution and kept the star formation parameters the same (128r1). One was unigrid and the same critical density (128) and the other was unigrid and critical density four times lower to keep the line density constant for the critical density cells (128d). Both 128^3 unigrid runs had minimum mass boosted by a factor of three to ensure resolved star cluster formation. The change in minimum mass should have negligible affect on the star formation rate as seen in §5.1.1. Figure 5.37 shows the mass in star clusters against time for the different resolution runs. The simulations with the same effective resolutions are in strong agreement on final mass though, again, the AMR run forms most of its mass in stars in a brief period compared to the steadier star formation rate of the high resolution unigrid run. The unigrid run with lowered critical density strongly agrees with more massive base simulation and the unigrid run with the same critical density forms stars later and to a lower mass at 18 Myrs. Figure 5.38 shows the mass structure for the three simulations of different resolution and again the AMR and higher resolution run are in strong agreement, both disrupting their host cloud at about the same rate. The lower resolution run with a lower mass in stars has only slightly reduce the mass in the inner most region and only after 15 Myrs. Figure 5.39 is density projections for the two simulations with the same effective resolution (1.4 pc) at 14.5 Myrs. The unigrid simulation has finer structure in the lower density regions but the star clusters are in similar places and the cloud is disrupted in a very similar way.

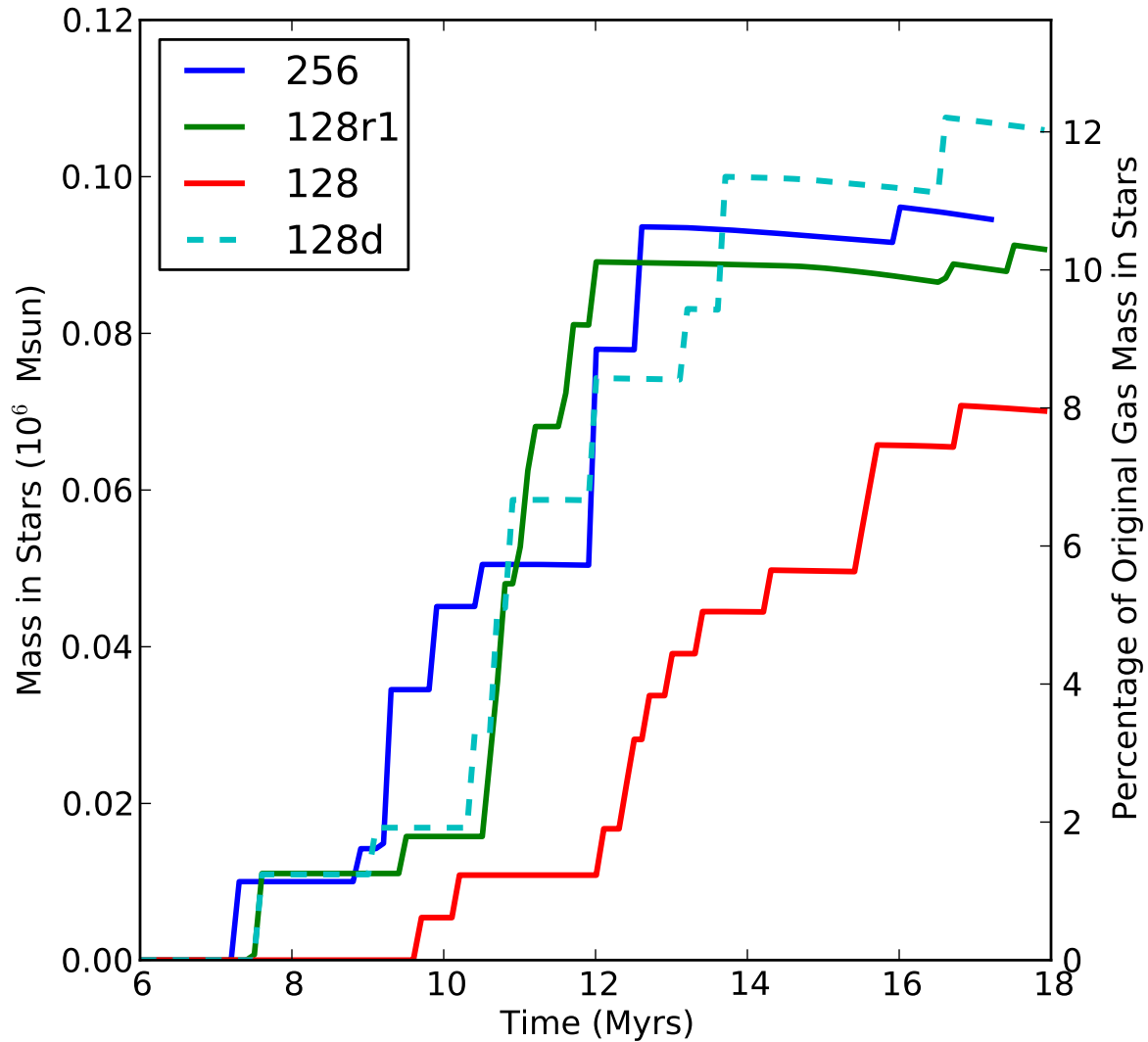


Figure 5.37: The total mass in star cluster particles for the more massive cloud simulation at different resolution. The simulations acted as expected from the lower mass cloud simulations. The AMR simulation is in strong agreement with the high resolution unigrid more massive cloud base simulation. The lower resolution unigrid with critical line density kept constant gave the same final mass in stars as the more massive cloud base simulation.

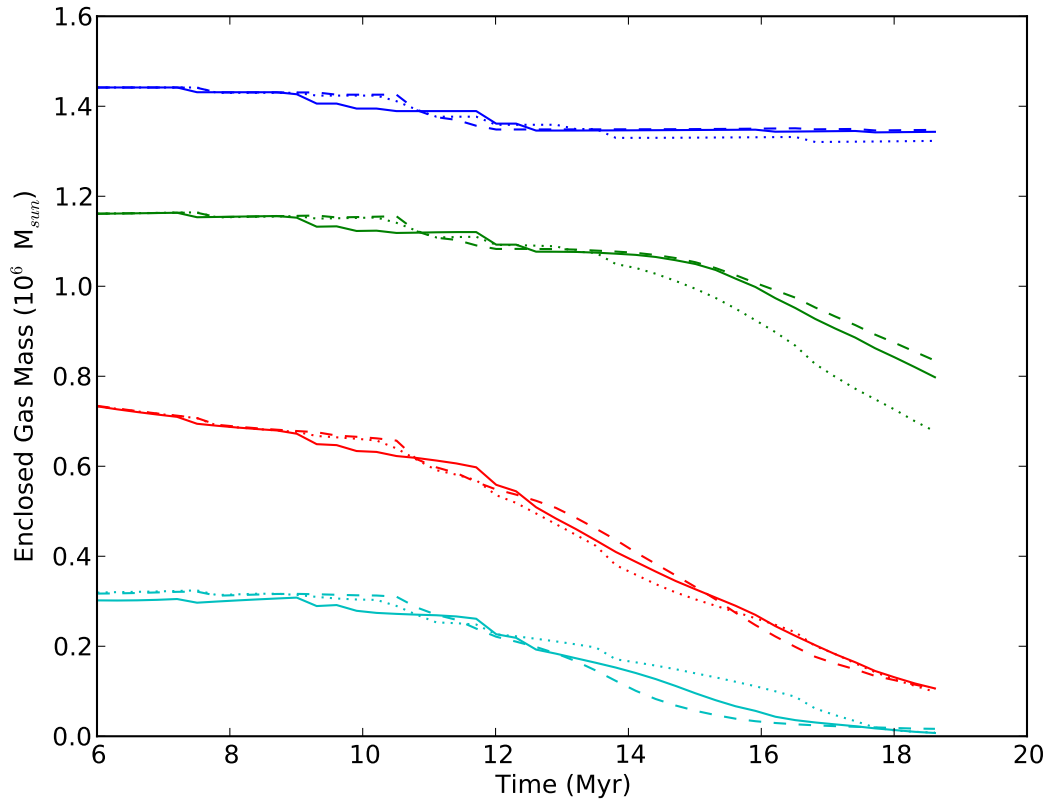


Figure 5.38: The mass structure for the more massive cloud base simulation - 256^3 top grid - (solid lines), more massive cloud with 128^3 top grid and one level of refine by two (dashed lines), and the more massive cloud with only 128^3 top grid but decreased critical density by a factor of four (dotted lines). The colour shows which region of the box is being considered: Blue = all, Green = within $2 R_{cl}$ of the centre, Red = within R_{cl} of the centre, and Cyan = within $0.5 R_{cl}$ of the centre. All three simulation disrupt their host GMC at approximately the same rate. The low resolution unigrd simulation (128^3) does have a slightly different structure especially with a faster reduction in mass inside $2 R_{cl}$ though this is not significant and may be due to edge effects.

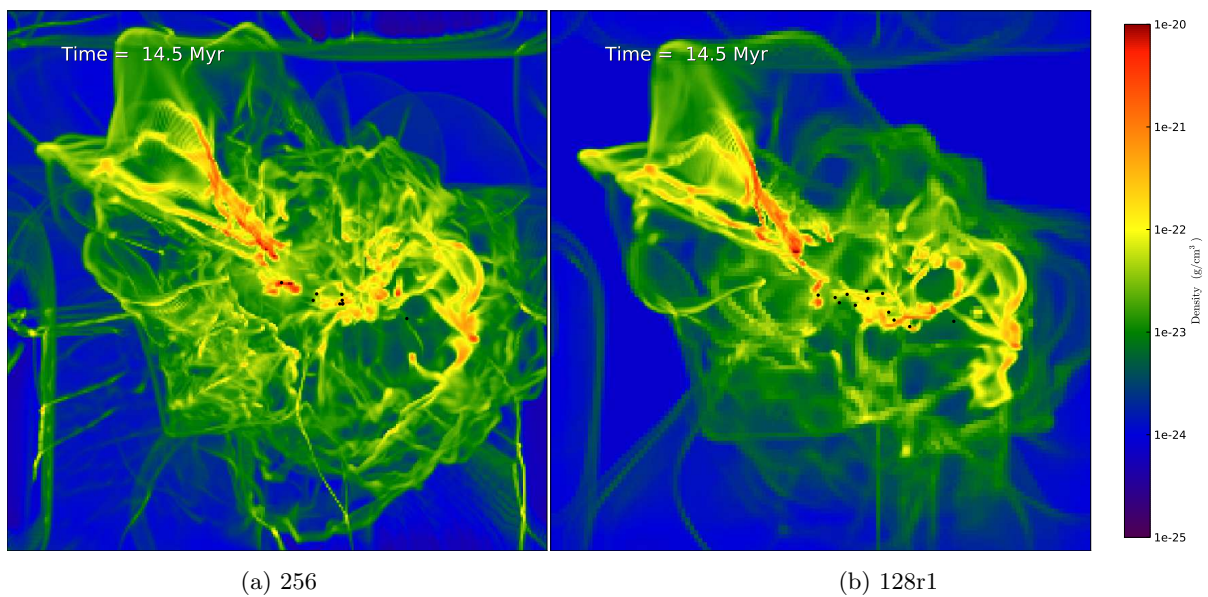


Figure 5.39: X-axis projected densities for the more massive clouds simulation with different resolutions at 14.5 Myrs. There is more detailed structure in the unigrid simulation but the bubble shape and size is the same for both simulations.

5.3 Turbulent Seeds

To investigate how the star formation and subsequent cloud evolution is affected by the turbulence I ran nine simulations with different turbulent seeds. The turbulent seed sets the random directions of the velocities so gives a different initial velocity structure. Table 5.6 shows the seeds used and time of first star cluster formation from the simulations.

Name	Random Seed	First Star /Myrs
Seed1, base	873275	5.4
Seed2	275873	4.8
Seed3	842091	4.7
Seed4	374689	6.9
Seed5	54682	5.1
Seed6	697134	4.2
Seed7	738946	6.0
Seed8	73211	5.6
Seed9	999999	4.8

Table 5.6: Table of the turbulent seeds and first cluster formation for the turbulence investigation. All simulations have the same mass, density structure, size, and initial Mach number.

5.3.1 Turbulent Seeds Results

For all of the seeds, the first star cluster forms in approximately one dynamical time (whole cloud: $t_{dyn} = 6.7$ Myrs and half mass: $t_{dyn} = 4.8$ Myrs) between 4.2 and 6.9 Myrs, as seen in Figure 5.40. The blue solid line is the base run (Seed1). This suggests that gravity is the principle factor determining star cluster formation but that turbulence does affect the time and location of cluster formation. Within the first dynamical time after first cluster formation the different seeded simulations form stars totalling between 4.8% and 21.2% of the original cloud gas mass. All seeds start with a reasonably high rate of star formation and flatten out, quenched, at different times. The time at which the rate drops significantly suggests the initial turbulence determines how many regions of star cluster formation there are and thus how quickly the outputs from clusters feedback and quench subsequent star formation. Despite

the variety in final mass of clusters formed, all of the GMCs were fully disrupted. Figure 5.41 shows the mass contained within sphere centred at the simulation box centre with radii 22.4 pc ($0.5 R_{cl}$), 44.8 pc ($1 R_{cl}$), 89.6 pc ($2 R_{cl}$), and the whole simulation box for Seed2 and Seed9. Both clouds are disrupted as seen by the decreasing mass in the inner regions. Seed9, with its higher mass in stars and thus stronger outputs, is disrupted more rapidly. The mass converted into star clusters at 12 Myrs averaged over all nine runs is $26,042 \pm 13,120 M_{\odot}$ or 11.8 ± 6.0 % of the original gas mass.

Seed2 has the lowest mass fraction in stars because the turbulence focuses the mass mostly into one main filament (Fig. 5.42). When the three clusters form they disrupt the higher density regions rapidly, quenching further star formation. In contrast, Seed9 has more than one high density region so star formation proceeds in each location initially undisturbed by the other star clusters. Figures 5.42 and 5.43 show density projections for Seed2 and Seed9 respectively just before, just after, 2 Myrs after, and 4 Myrs after their first star cluster forms. For both Seed2 and Seed9 the disruption does not appear to be very significant at 2 Myrs but by 4 Myrs the disruption is substantial. This can also be clearly seen in 5.41 comparing the mass structure at 6.8 Myrs (2 Myrs after first star cluster formation) with the structure at 8.8 Myrs (4 Myrs after first star cluster formation). For both runs, there is still substantial mass in the inner regions at 6.8 Myrs but by 8.8 Myrs Seed9 has almost no mass within the centre and for Seed2 the mass is steadily decreasing in the inner regions.

5.3.2 Turbulent Seeds Summary

For all turbulent seeds simulated, the first star cluster forms within one dynamical time and the cloud is disrupted by the stellar outputs within another dynamical time. The final mass in clusters varies from 5% to 21% of the initial cloud mass and although rate of disruption is faster for higher mass the clouds are all fully disrupted eventually.

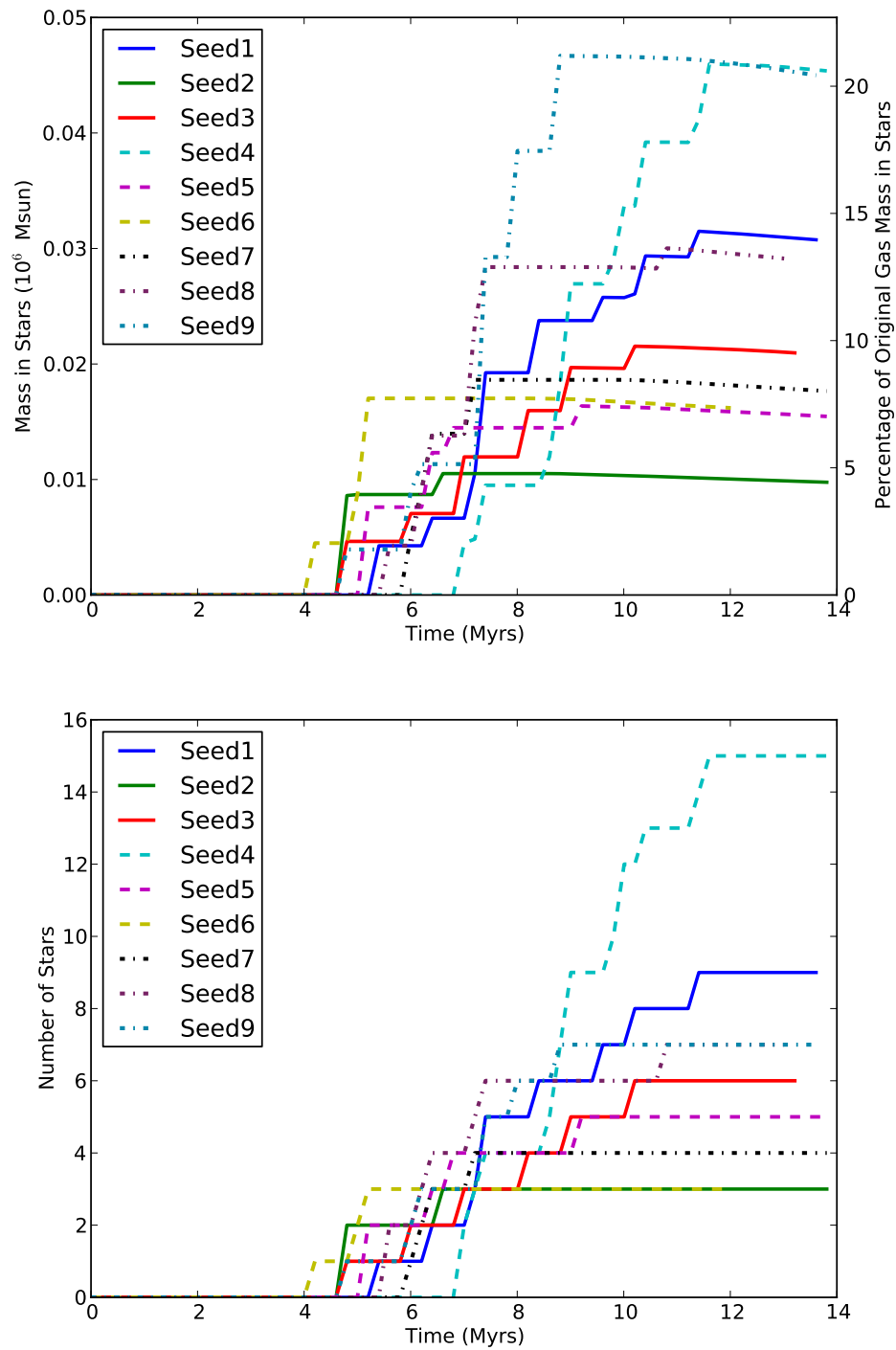


Figure 5.40: Time evolution of *top*: total mass in and *bottom*: number of star cluster particles for simulations with nine different turbulence seeds. For all of the simulations, star clusters form at approximately one dynamical time and form between 5% and 21% of the original cloud gas mass within another dynamical time. In all simulations the star clusters disrupt the surrounding GMC and quench further star formation.

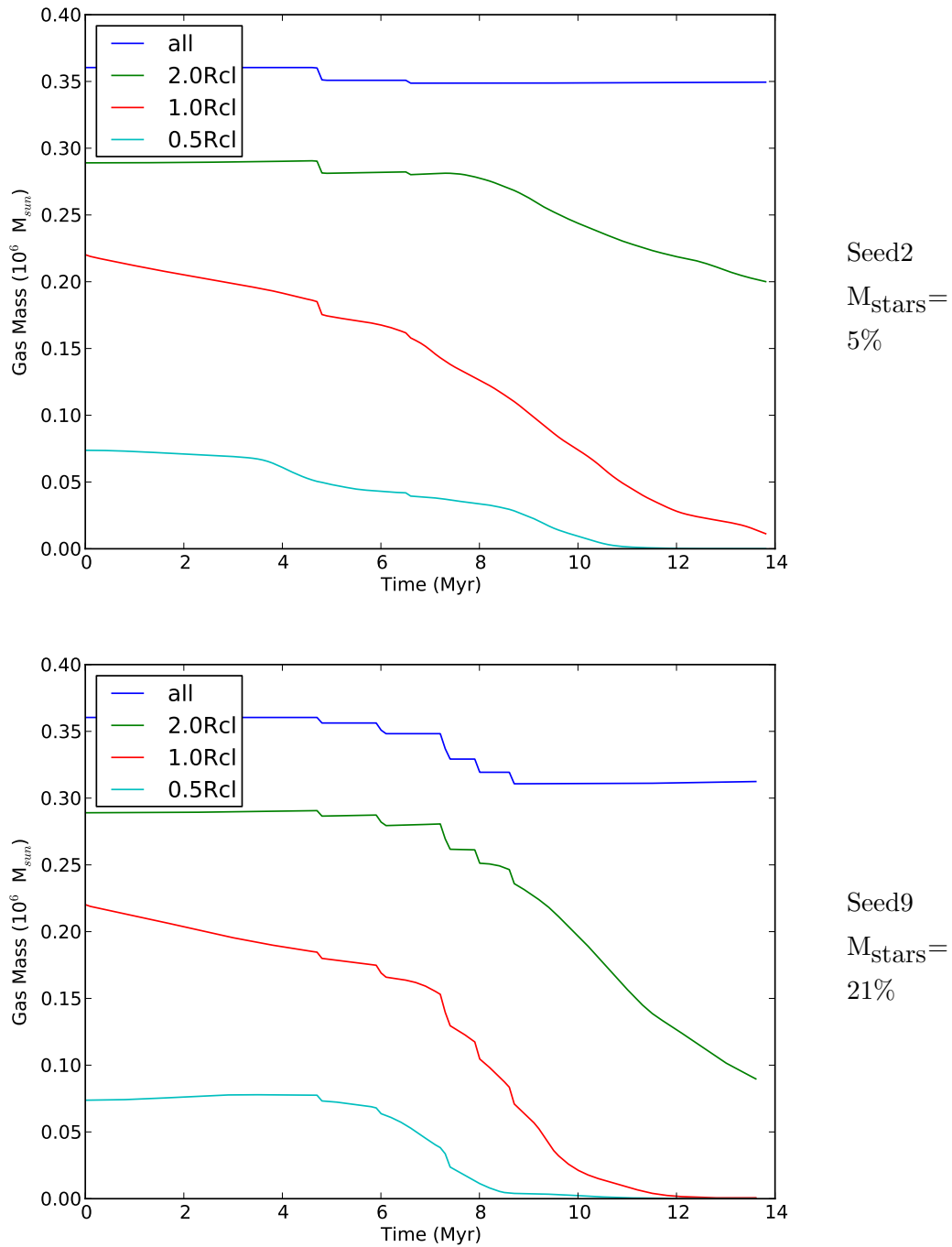


Figure 5.41: Graphs showing the mass structure for *top*: Seed2 and *bottom*: Seed9, the simulations with lowest and highest mass in star clusters respectively. With the higher mass in stars Seed9 disrupts its cloud faster as seen by the steeper gradient in mass enclosed especially for 0.5 and 1.0 R_{cl} . However, even Seed2's cloud is fully disrupted by 14 Myrs.

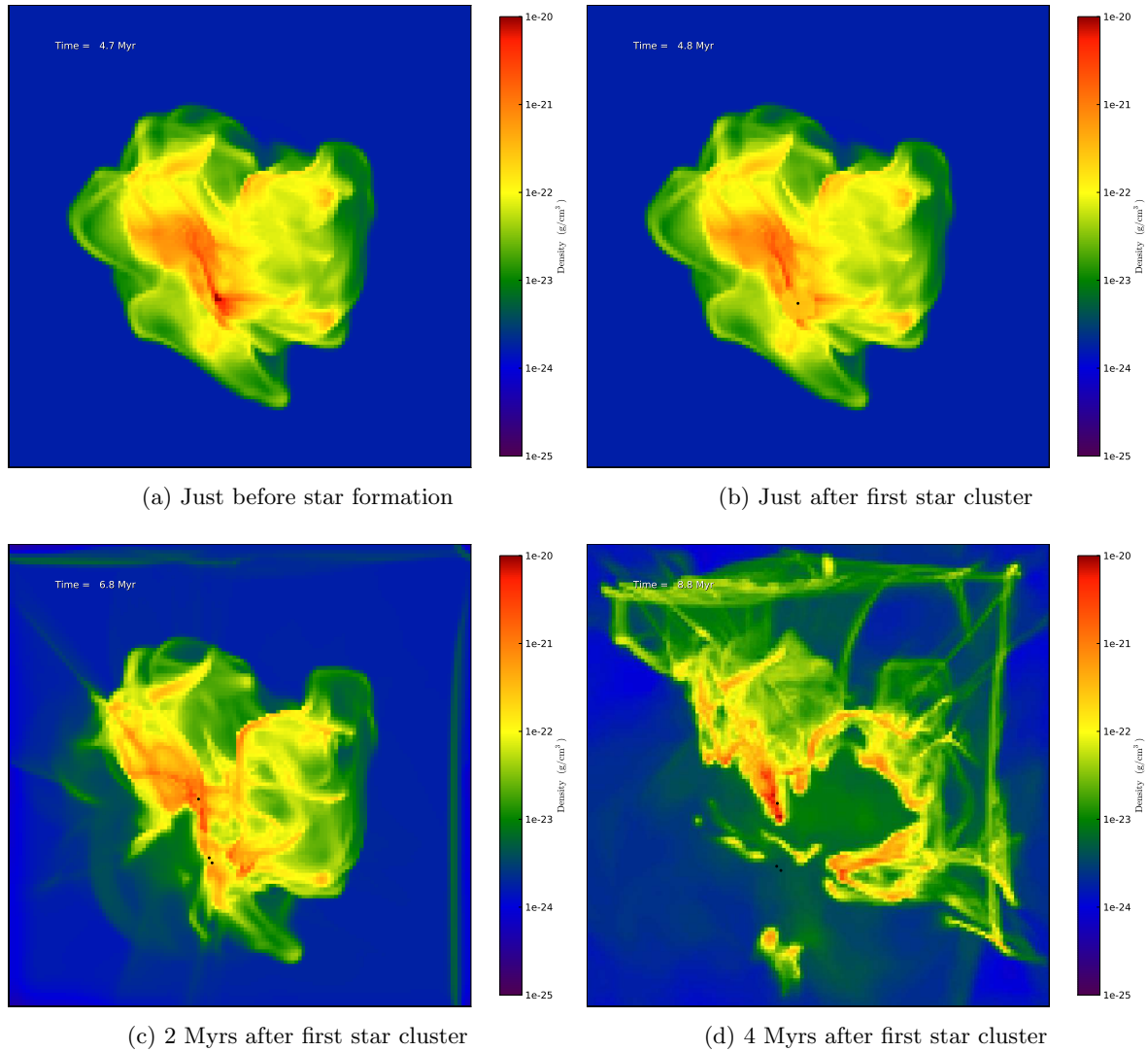


Figure 5.42: Seed2 x-axis density projections at four different times. (a) shows the density immediately before the first star cluster forms. (b) shows after the first star cluster has formed. (c) shows the density projection 2 Myrs after the first star cluster formed (0.2 Myrs after the third and final star cluster forms). (d) shows the disruption of the cloud at 4 Myrs after the first star cluster formed. Even with only 5% of initial cloud mass in stars with this turbulence structure the stellar outputs are enough to disrupt the cloud.

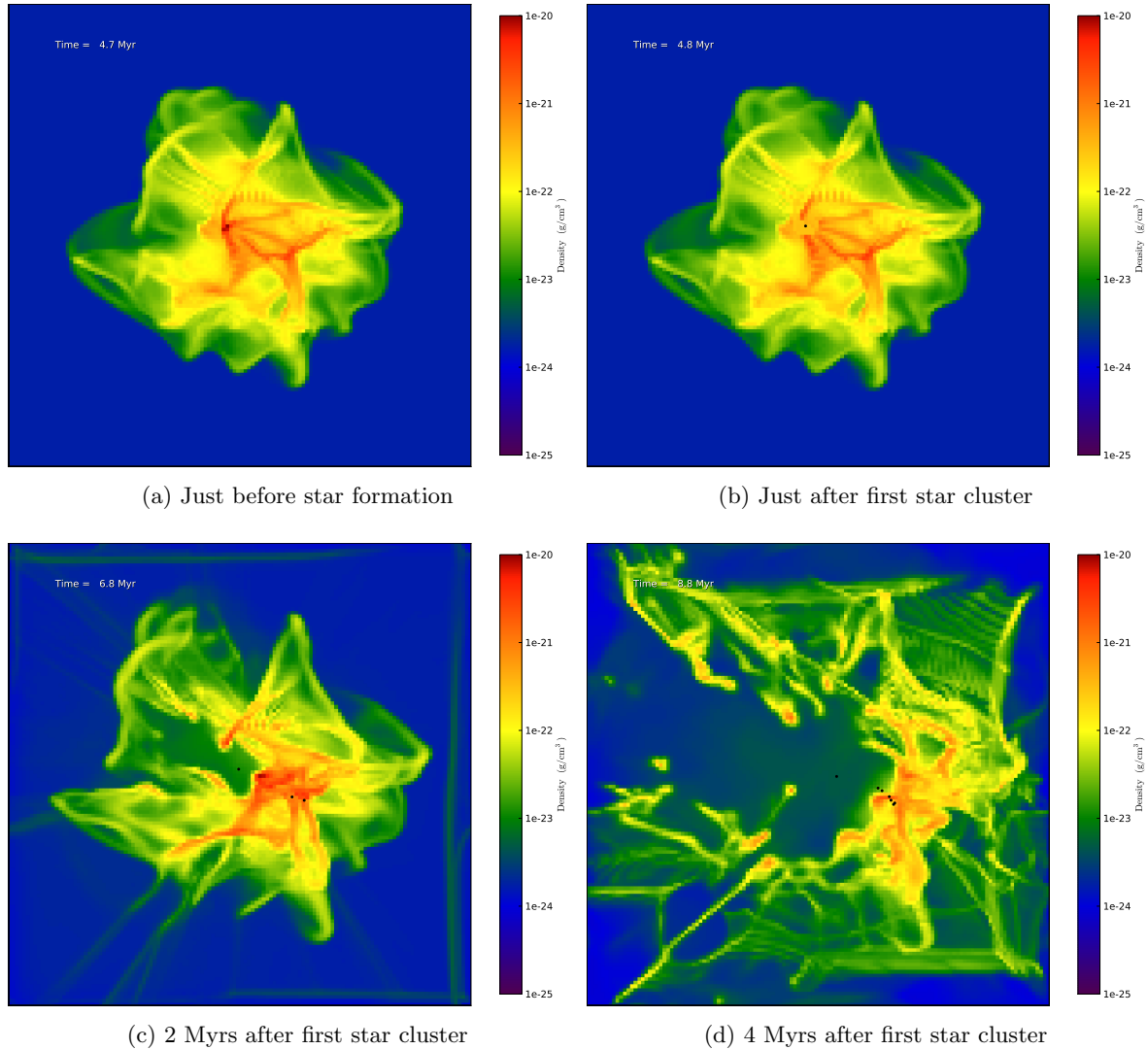


Figure 5.43: Seed9 x-axis density projections at four different times. (a) shows the density immediately before the first star cluster forms. (b) shows after the first star cluster has formed. (c) shows the density projection 2 Myrs after the first star cluster formed. (d) shows the disruption of the cloud at 4 Myrs after the first star cluster formed. With 21% of the initial cloud gas mass converted into stars the disruption is more significant at 4 Myrs than for Seed2.

5.4 Hydrodynamic Solver

When I started my investigations the PPM solver was not robust enough to cope with the highly turbulent clouds I was simulating. John Wise's improvements to the PPM solver at the end of my studies corrected for most of this so I could run my simulations with two different solvers, as discussed in §3.2. I re-ran the base simulation and the turbulent seed study as discussed in §5.3 with the new PPM solver.

5.4.1 Hydrodynamic Solver Base Results

The base simulation was run with the alternative PPM hydro solver from identical initialization.

Figure 5.44 shows the star formation history for the two different hydro solvers. The total mass in stars is mostly the same between the two hydro solvers only diverging slightly after 7 Myrs. The masses in star clusters at 10 Myrs are 26,093 M_{\odot} for the hydro_rk solver and 24,182 M_{\odot} for the PPM (11.8% and 11.0% of the original cloud mass respectively).

Figures 5.45-5.50 show the projected density, temperature, HII ionization fraction, and radiation force absorbed by the gas at 1 Myr intervals through the PPM simulation after star formation. These figures are for the same time since star formation as Figs. 4.5-4.10. The main difference between the two solvers is most noticeable at later times. The PPM solver leads to a more fragmented density structure, whereas the hydro_rk solver had smoother filaments and structures. The fragmented density leads to more numerous yet smaller star clusters forming and to a higher radiation absorption. Overall the evolution of the bubble and HII region are very similar between the two solvers. The ionization initially breaks out on the same side and to a very similar extent in both simulations. The bubble shell expands and sweeps up mass in a very similar fashion between the two solvers.

Figure 5.51 shows the mass structure with time for the base run with the two different solvers. Despite the structural differences seen in the density projections in Figs. 5.45-5.50 the spherically averaged mass structure is the same. The outputs disrupt the cloud at the same rate for both solvers.

Figure 5.52 shows the radiation force emitted and absorbed. Compared to Fig. 4.13, with the PPM solver the radiation force is absorbed to a higher efficiency for longer due to the higher density clumps remaining in the later stages of the simulation. However, this difference is not significant as the outputs disrupt the cloud in the same time. Within one dynamical time after first cluster formation the momentum deposited by the clusters into the bubble shell is comparable for both solvers.

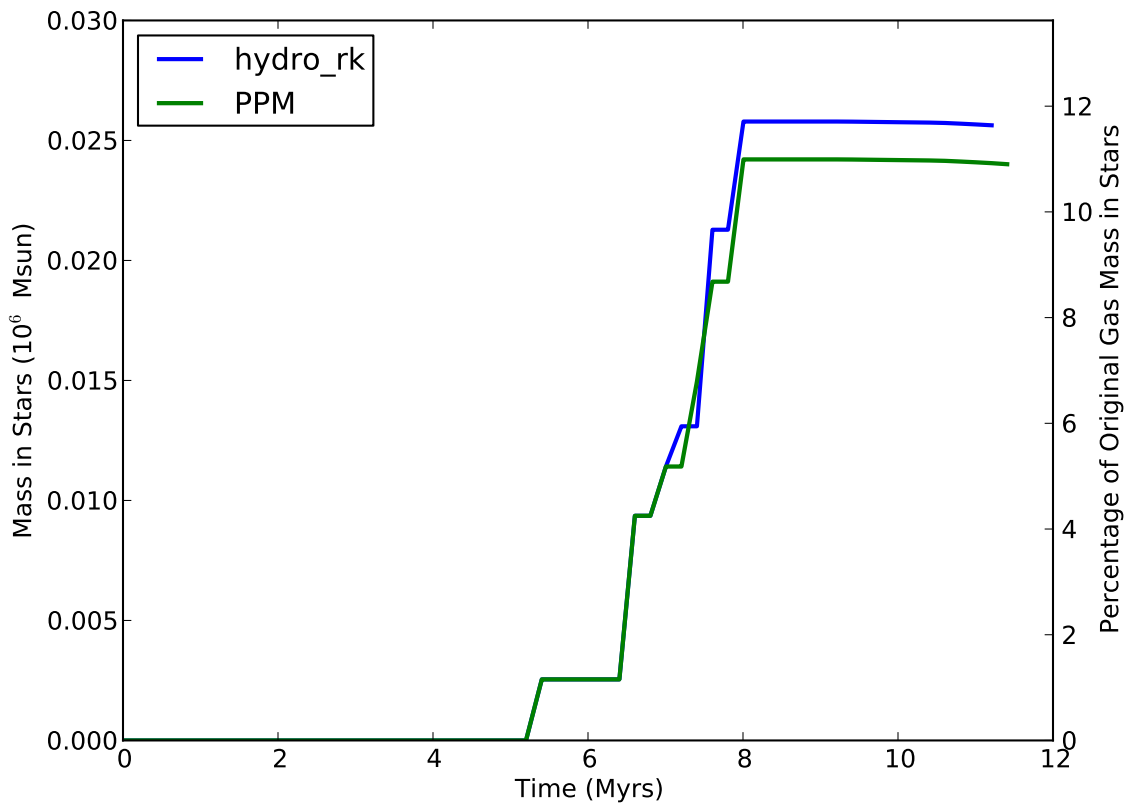


Figure 5.44: The total mass in star cluster particles for the base simulation (blue) and the base simulation run with PPM (green). The original cloud gas mass was $220,237 M_{\odot}$.

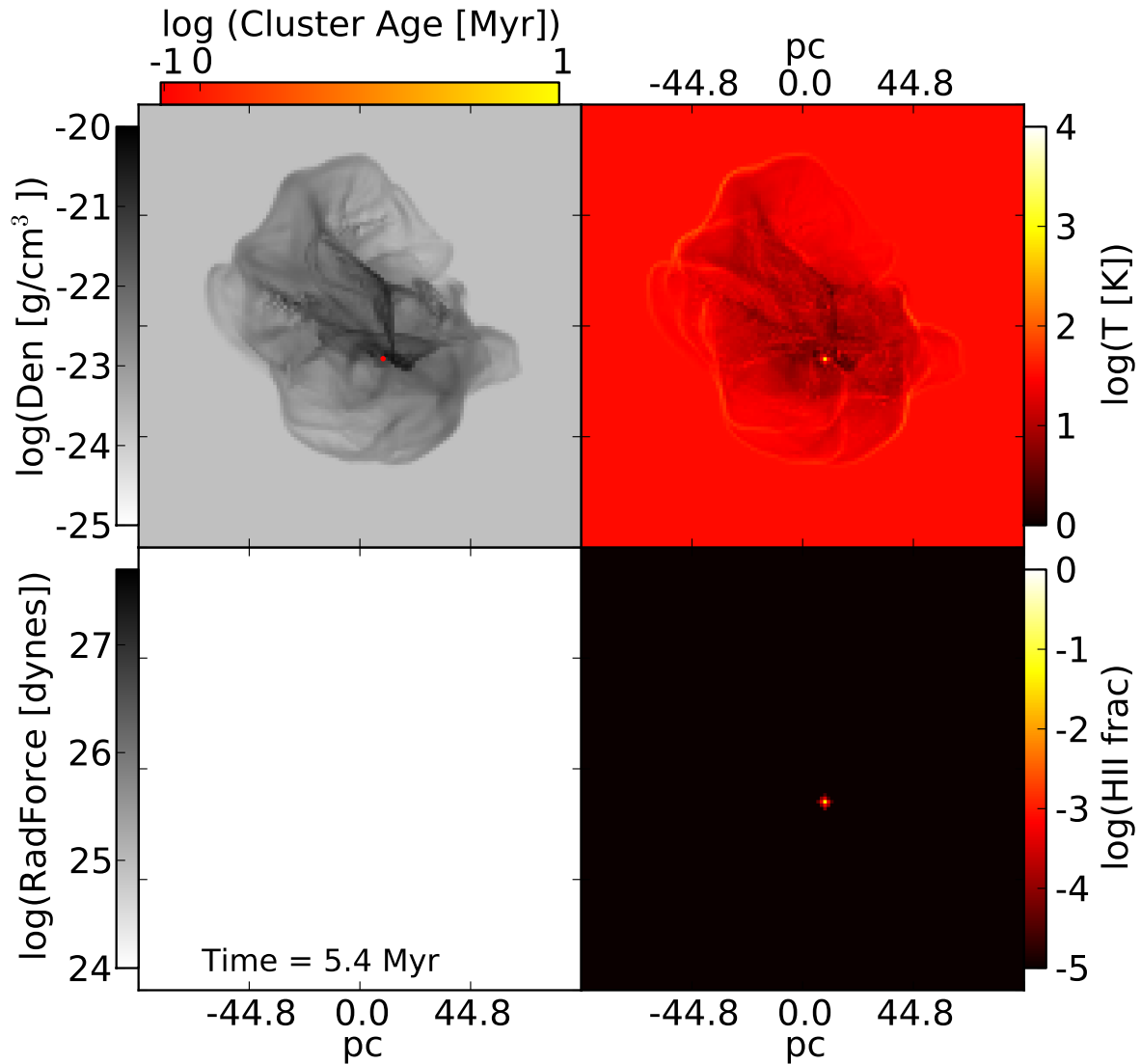


Figure 5.45: Density, temperature, radiation force (momentum deposited), and HII fraction for the base simulation with PPM at 5.4 Myrs (0.1 Myrs after first cluster formed). Star cluster particles are shown as filled circles on the density projection. Star cluster circle size is relative to mass and colour indicates the age of the cluster at this time. Only the material immediately around the star cluster is ionized, heated, and has radiation momentum absorbed. The sum of radiation force absorbed by the gas in this frame is 0.0 dynes as all of the radiation is absorbed by the host cell. Compared to Fig. 4.5 the simulations look very similar despite the hydro solver change.

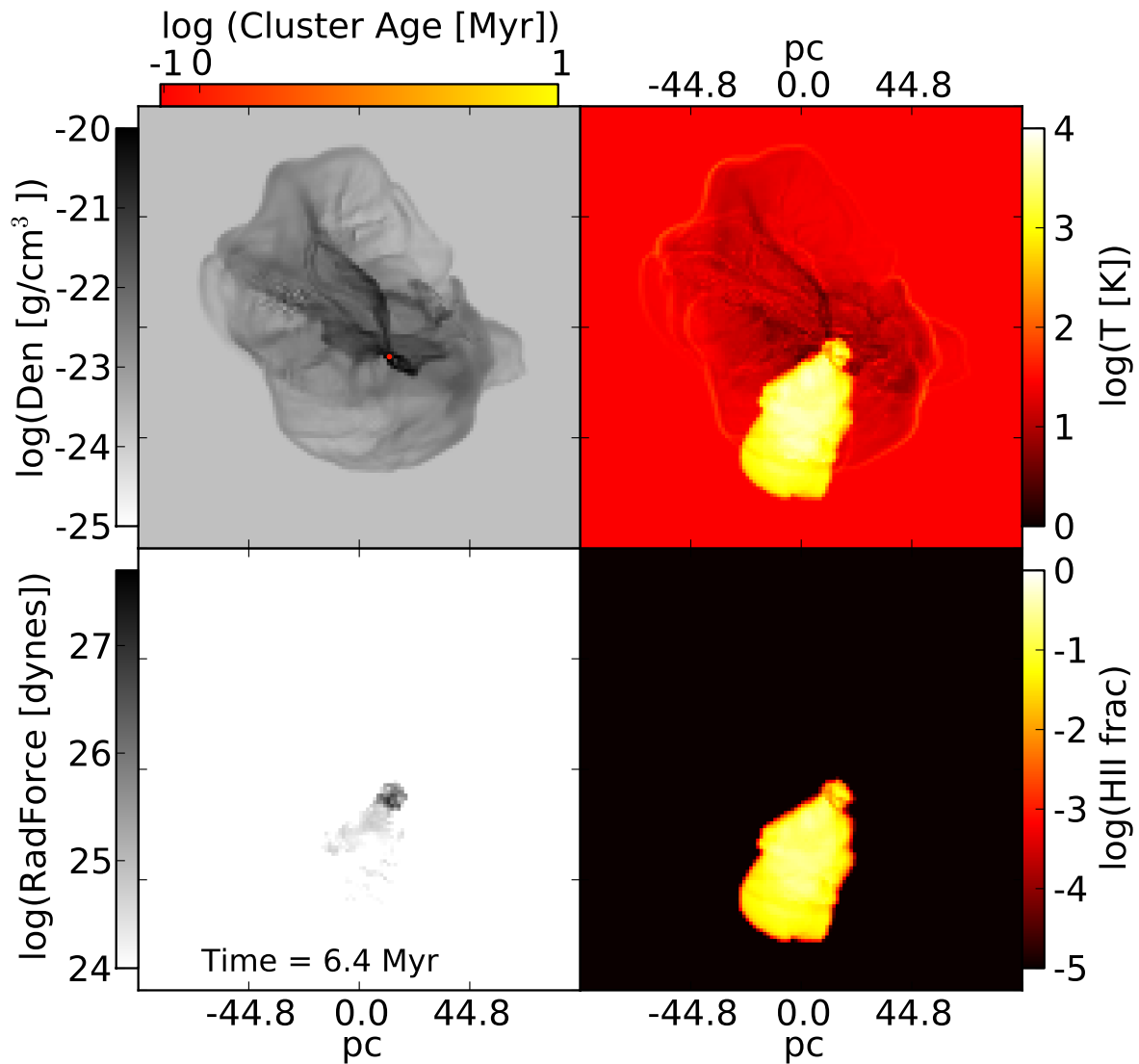


Figure 5.46: Density, temperature, radiation force (momentum deposited), and HII fraction for the base simulation with PPM at 6.4 Myrs (1.1 Myrs after first cluster formed). Star cluster particles are shown as filled circles on the density projection. Star cluster circle size is relative to mass and colour indicates the age of the cluster at this time. After 1 Myrs of radiating clusters the radiation pressure and ionized gas pressure have expanded the HII region and it is starting to leak out of the side with the least resistance. The sum of radiation force absorbed by the gas in this frame is 2.29×10^{29} dynes. Compared to Fig. 4.6, small differences can start to be seen. In the base simulation the HII region had blown out over a larger area and slightly further. However, for the base simulation there are two star clusters at this time explaining the difference.

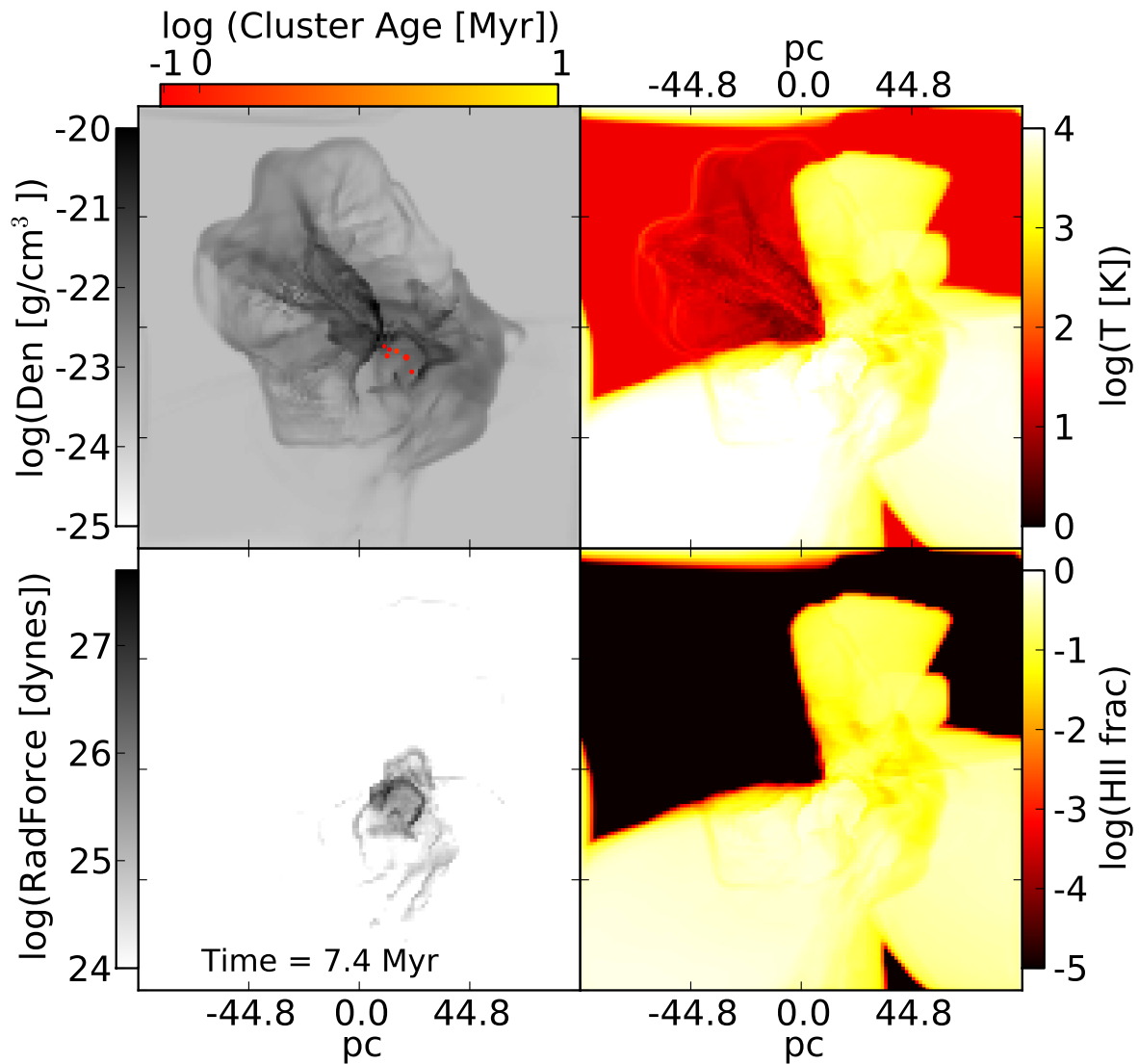


Figure 5.47: Density, temperature, radiation force (momentum deposited), and HII fraction for the base simulation with PPM at 7.4 Myrs (2.1 Myrs after first cluster formed). Star cluster particles are shown as filled circles on the density projection. Star cluster circle size is relative to mass and colour indicates the age of the cluster at this time. Note the bubble shell seen in density and radiation force projections. The HII region has now blown out on many sides. The sum of radiation force absorbed by the gas in this frame is 8.85×10^{29} dynes. Compared to Fig. 4.7, the most significant difference is the location and masses of the forming star clusters. With the PPM solver the gas is fragmenting more and thus forming more, smaller mass star clusters. However, the total mass in stars is comparable. The bubble forming around the first star cluster is of comparable size for both simulations, as seen in the radiation force panels.

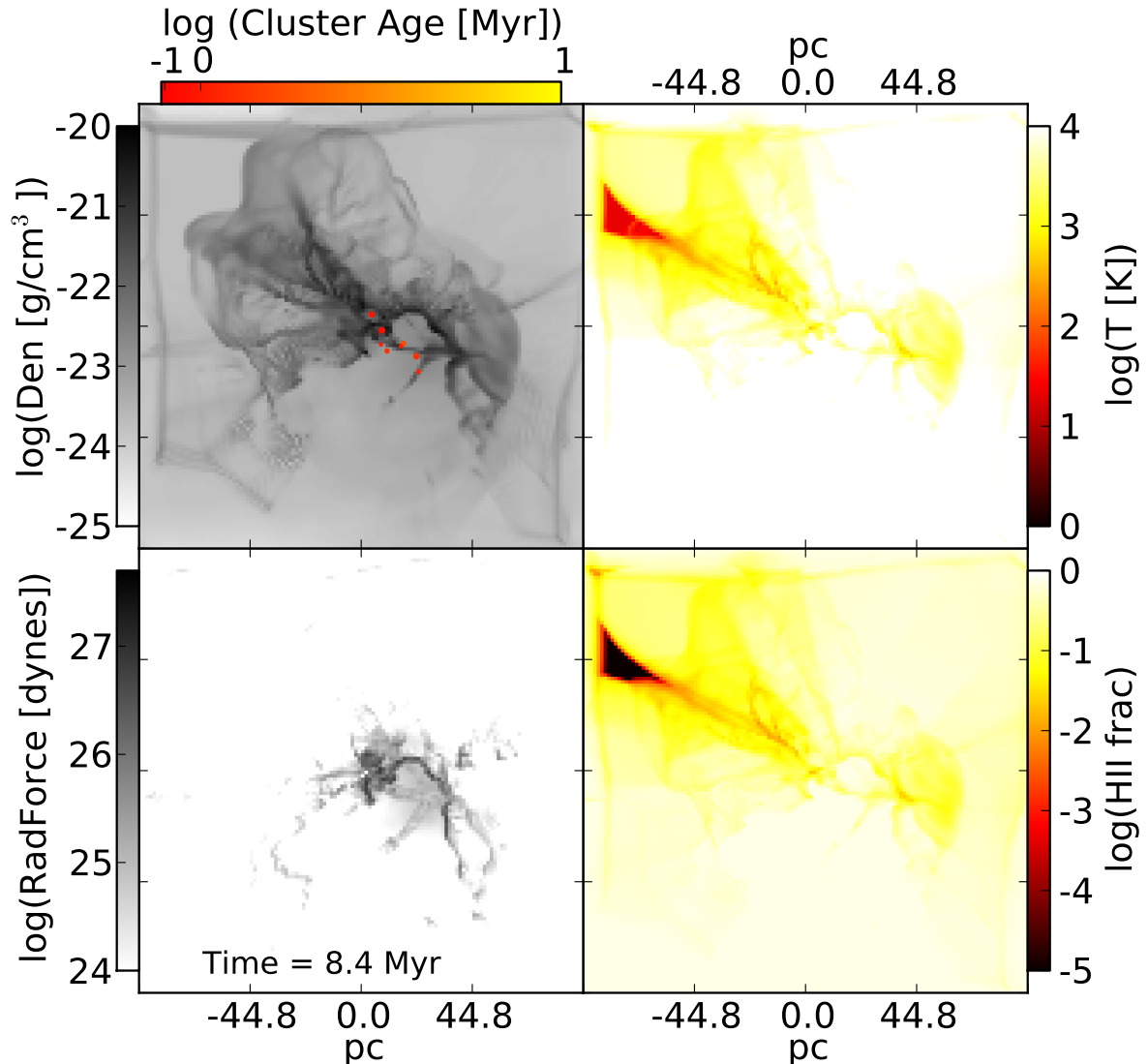


Figure 5.48: Density, temperature, radiation force (momentum deposited), and HII fraction for the base simulation with PPM at 8.4 Myrs (3.1 Myrs after first cluster formed). Star cluster particles are shown as filled circles on the density projection. Star cluster circle size is relative to mass and colour indicates the age of the cluster at this time. The remaining bubble shell is clearly seen in radiation force and density. Almost the entire simulation box is ionized and heated by the radiation from the stars. The sum of radiation force absorbed by the gas in this frame is 1.40×10^{30} dynes. Compared to Fig. 4.8 the shielding of the upper left corner is slightly stronger with the PPM solver, probably due to the later formation time of the upper right star cluster. The central bubble still has a very similar shape as seen by the radiation force panel.

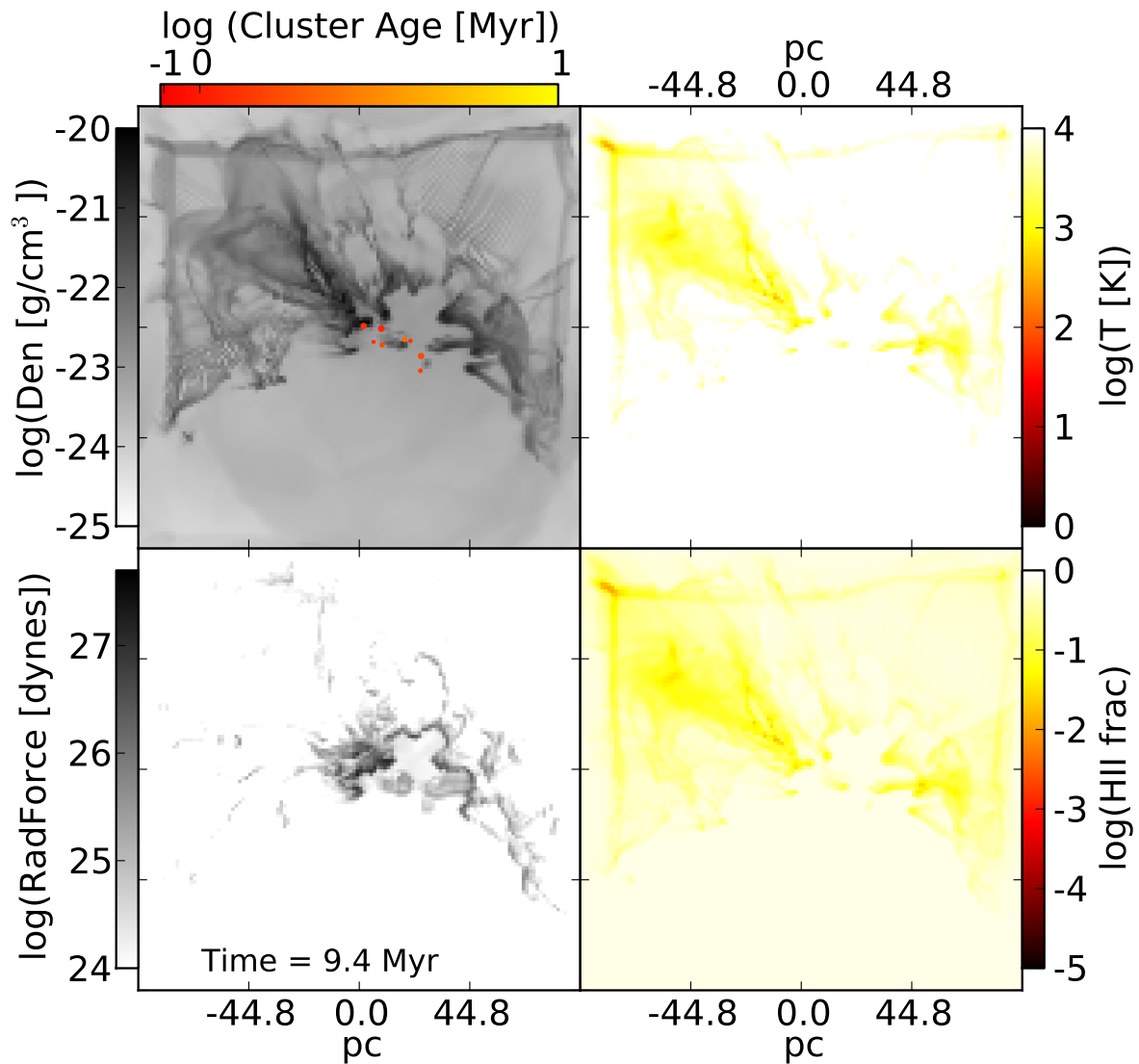


Figure 5.49: Density, temperature, radiation force (momentum deposited), and HII fraction for the base simulation with PPM at 9.4 Myrs (4.1 Myrs after first cluster formed). Star cluster particles are shown as filled circles on the density projection. Star cluster circle size is relative to mass and colour indicates the age of the cluster at this time. The remaining shell is still absorbing significant radiation force and is being pushed away from the stars. The sum of radiation force absorbed by the gas in this frame is 1.47×10^{30} dynes. Compared to Fig. 4.9, the more fragmented nature of the gas with the PPM solver is starting to make more of a difference. In this image there are more pillar structures and more high density regions surrounding the bubble leading to a higher radiation force absorption. For both hydro solvers the full simulation box is heated and ionized by the stars.

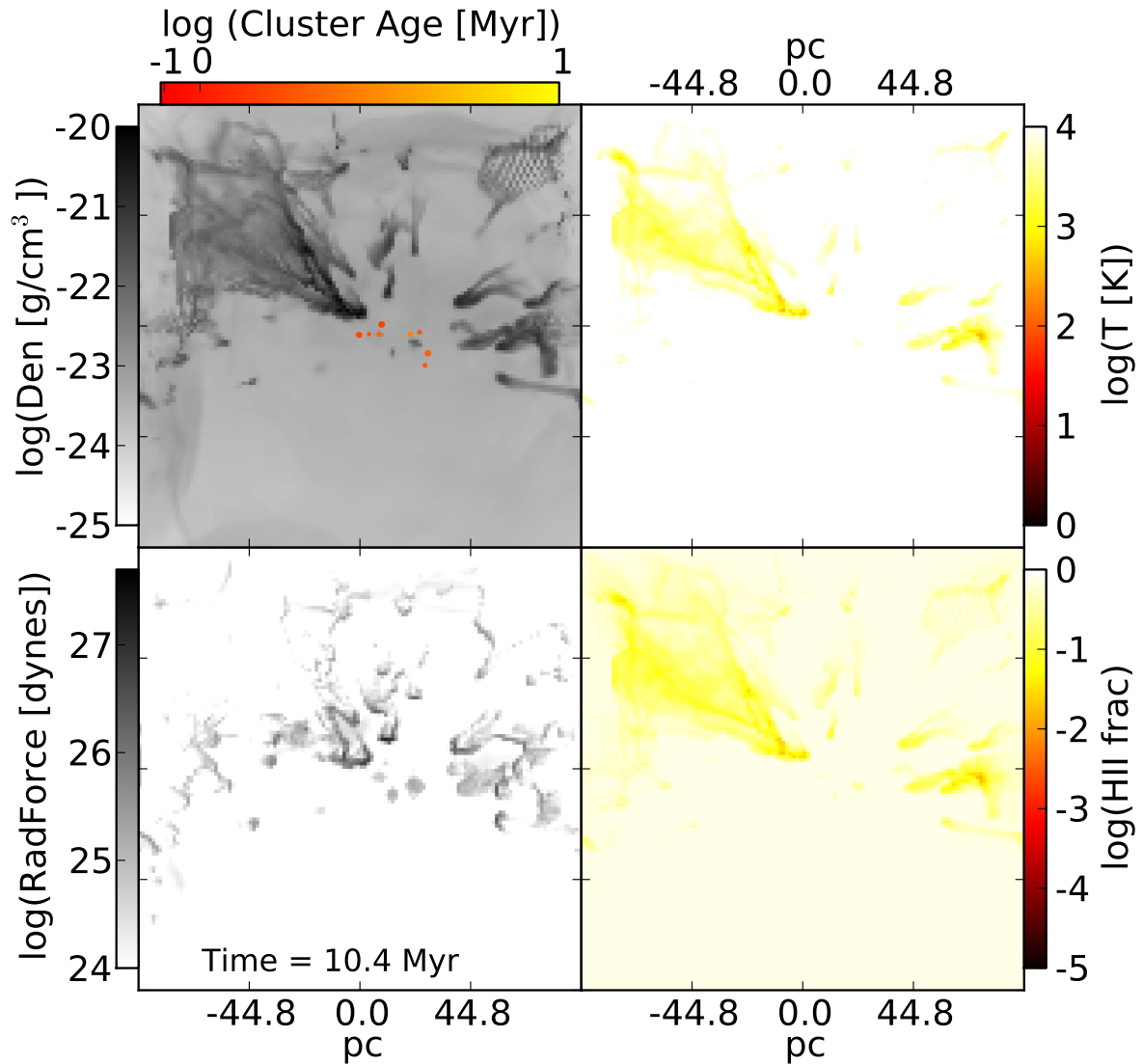


Figure 5.50: Density, temperature, radiation force (momentum deposited), and HII fraction for the base simulation at 10.4 Myrs (5.1 Myrs after first cluster formed). Star cluster particles are shown as filled circles on the density projection. Star cluster circle size is relative to mass and colour indicates the age of the cluster at this time. The sum of radiation force absorbed by the gas in this frame is 9.63×10^{29} dynes. Compared to Fig. 4.10, the more complex structure with PPM is the most noticeable now. The density and radiation force panels show this most clearly. Also, the whole region is still ionized and heated unlike with `hydro_rk` where the outer regions were starting to recombine and cool by this time.

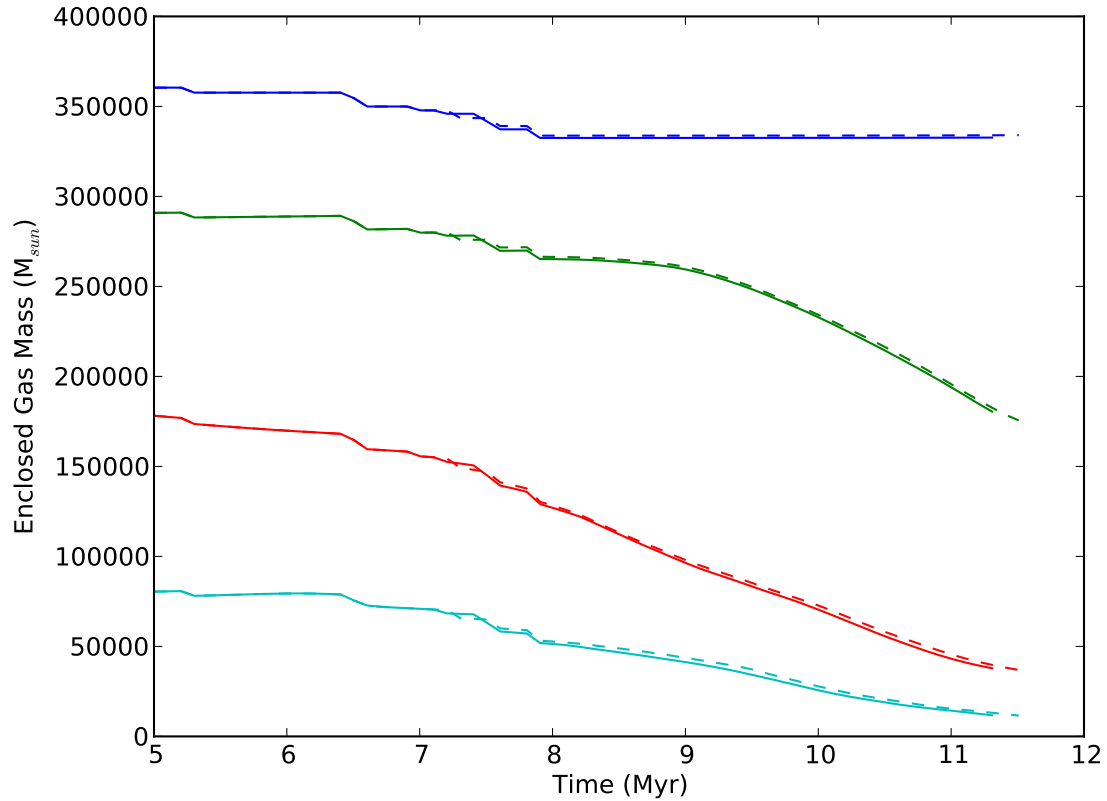


Figure 5.51: The mass structure for *solid lines*: the base simulation and *dashed lines*: the base simulation with the PPM solver. The lines show the cumulative mass for 0.5 (cyan), 1 (red), and 2 (green) times the original cloud radius (44.8pc) and for the whole simulation box (blue). Note the extreme similarity between the two different solvers.

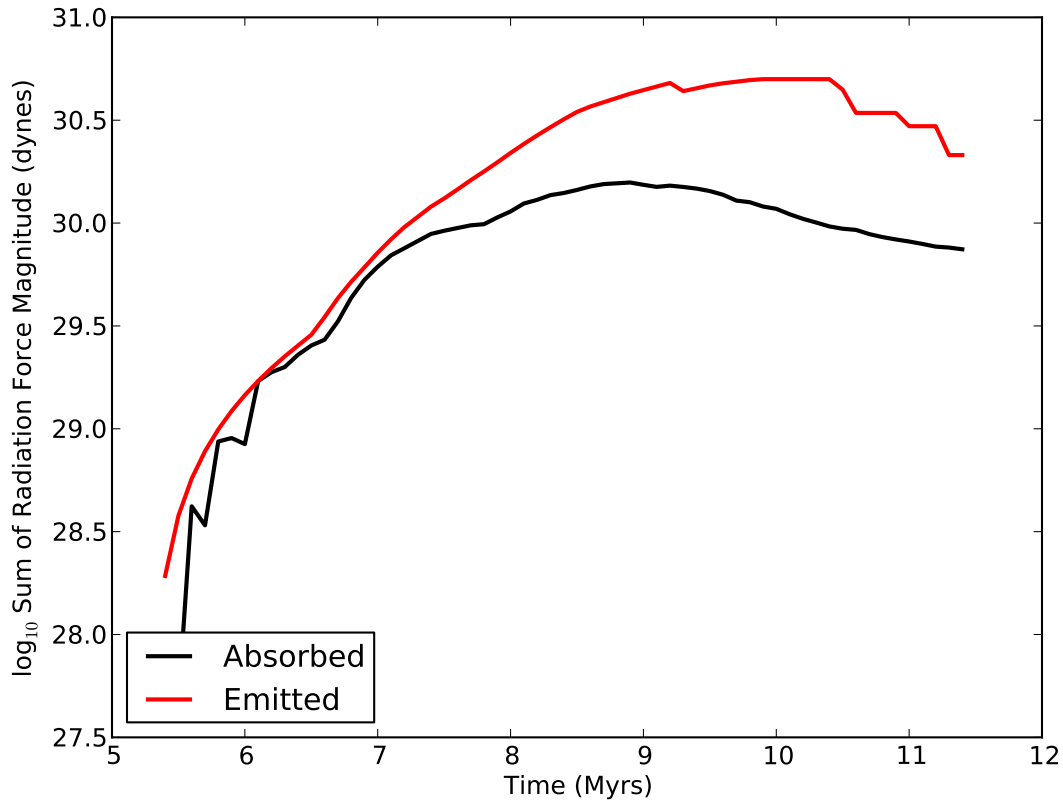


Figure 5.52: Graph showing the rate of momentum emitted by the stars in radiation and the rate of momentum absorbed by the gas in the simulation cube from the stellar radiation. The initial increase in absorbed momentum rate is a numerical effect due to unresolved spherical effects. In contrast to Fig. 4.13 less radiation leaks out after 9 Myrs with the PPM solver due to the dense clumps present. However, this simulation was not run as long as the base simulation.

5.4.2 Hydrodynamic Solver Seeds Results

I reran the turbulent seed investigation with the PPM hydro solver. Table 5.7 shows that for each of the nine seeds the first star is formed at approximately the same time with both hydrodynamic solvers. Seed7 has the most significant change from 6.0 to 5.3 Myrs. Seed3, Seed5, and Seed7 form their first stars in a significantly different position for the different hydro solvers. All other seeds form the first star cluster in approximately the same location.

Name	Random Seed	First Star /Myrs	<i>1st star with hydro_rk /Myrs</i>	Δ position of 1st star cluster / pc
Seed1, base	873275	5.3	<i>5.4</i>	1.4
Seed2	275873	4.8	<i>4.8</i>	0.2
Seed3	842091	4.6	<i>4.7</i>	17.8
Seed4	374689	6.7	<i>6.9</i>	3.2
Seed5	54682	4.9	<i>5.1</i>	20.9
Seed6	697134	3.8	<i>4.2</i>	1.4
Seed7	738946	5.3	<i>6.0</i>	27.2
Seed8	73211	5.2	<i>5.6</i>	6.0
Seed9	999999	4.8	<i>4.8</i>	0.1

Table 5.7: Table of the turbulent seeds and results for the Hydrodynamic investigation.

Figure 5.53 shows the mass in stars for the nine turbulent seeds for the two different hydro solvers. The final star mass range is much smaller for the PPM solver than for hydro_rk, ranging from 7.7% to 13.7% of the original cloud gas mass. Unfortunately there were still some simulation crashing errors with the PPM solver so not all of the simulations ran until no more star formation was possible. Thus, it is possible Seed4 and Seed9 would continue making stars as they do with the hydro_rk solver, though Seed9 is past the time the final star cluster was made with hydro_rk. For all seeds, the times of subsequent star formation and the masses in star clusters is quite significant though the final mass is similar. Taking the five seeds that show the clearest signs of flattened star formation rate: Seed1, Seed2, Seed6, Seed7, and Seed8, the final mass in star clusters is: $19,703 \pm 3,119 M_{\odot}$ or $8.9 \pm 1.4 \%$ of the original gas mass. Taking the same seeds at the same times for the hydro_rk solver I get: $21,124 \pm 8,700 M_{\odot}$ or $9.6 \pm 4.0 \%$ of the original gas mass - a wider range but final masses that statistically agree. In addition, taking the final masses for the PPM solver for those 5 seeds and the masses for the

hydro_rk solver at the same times the masses have a linear regression correlation value of 0.93 supporting strong correlation between the two solvers.

Figure 5.54 shows the masses in stars against time for simulations with the same seeds but for two different hydro solvers. The seeds chosen are the base simulation (Seed1) and the seeds with earliest and latest first cluster formation time. The star formation histories are slightly different but overall very similar between the solvers. Figure 5.55 shows the direct comparison between hydro solvers for the three simulations with the largest distance between first cluster formation. All three of these simulations have multiple sites of star formation and form approximately the same final mass for both hydro solvers despite the different order of formation.

Figure 5.56 shows the central 100 pc of the Seed7 simulation for both hydro solvers. Despite the differences in the solvers the overall structure, filament shape, size and placement is very similar. The filaments are slightly smoother for the hydro_rk solver as is the densities in between filaments. The star clusters form at slightly different times and in a different order but still within the same two distinct locations within the cloud.

The mass structure within the simulation box for Seed2 and Seed9 are shown in Fig. 5.57 . The structures and evolution of structure between the two solvers for both seeds is extremely similar. Seed2 is clearing slightly faster with PPM than it did with hydro_rk but it has slightly more mass in stars with PPM so this is not surprising. Seed9's rapid dissipation of gas is the same for both hydro solvers. Figures 5.58 and 5.59 take a closer look at the densities at different times for Seed2 and Seed9 respectively. By comparing to Figs. 5.42 and 5.43 it can be seen that the location of star formation and bubble creation and evolution is very similar for both solvers. The less smooth nature of the filaments with PPM leads to more cells of higher density and thus more stars forming in Seed2 where the bubble shell meets the remaining parts of the dense filaments. These later star clusters have less of a dynamical effect than the first clusters as they are mostly of lower mass and the cloud is significantly disrupted by the time they form.

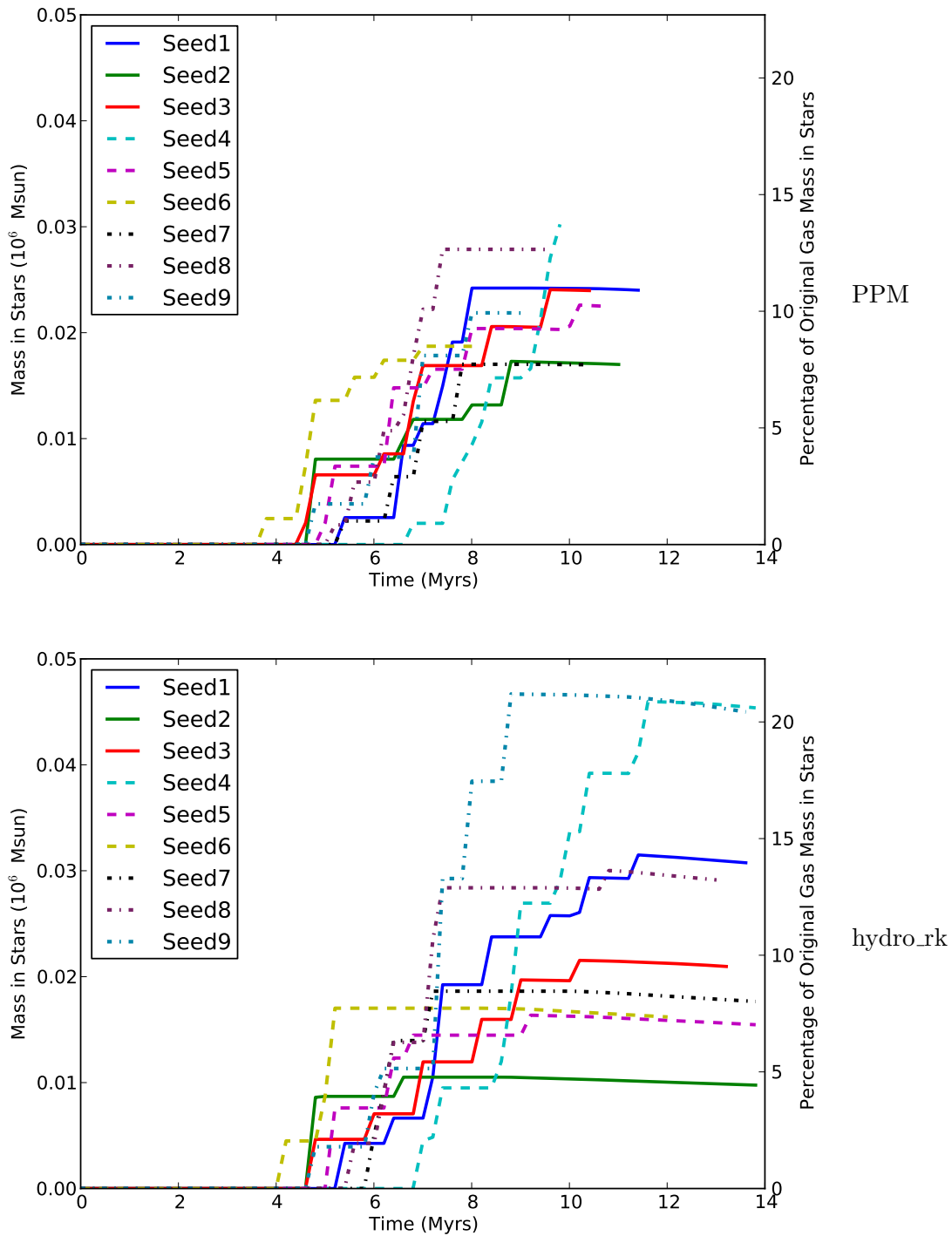


Figure 5.53: Mass in stars for the nine different seeds for *top*: PPM and *bottom*: hydro_rk. For the PPM solver there is a much smaller spread in final mass for the simulations though a similar spread in first star cluster formation start time.

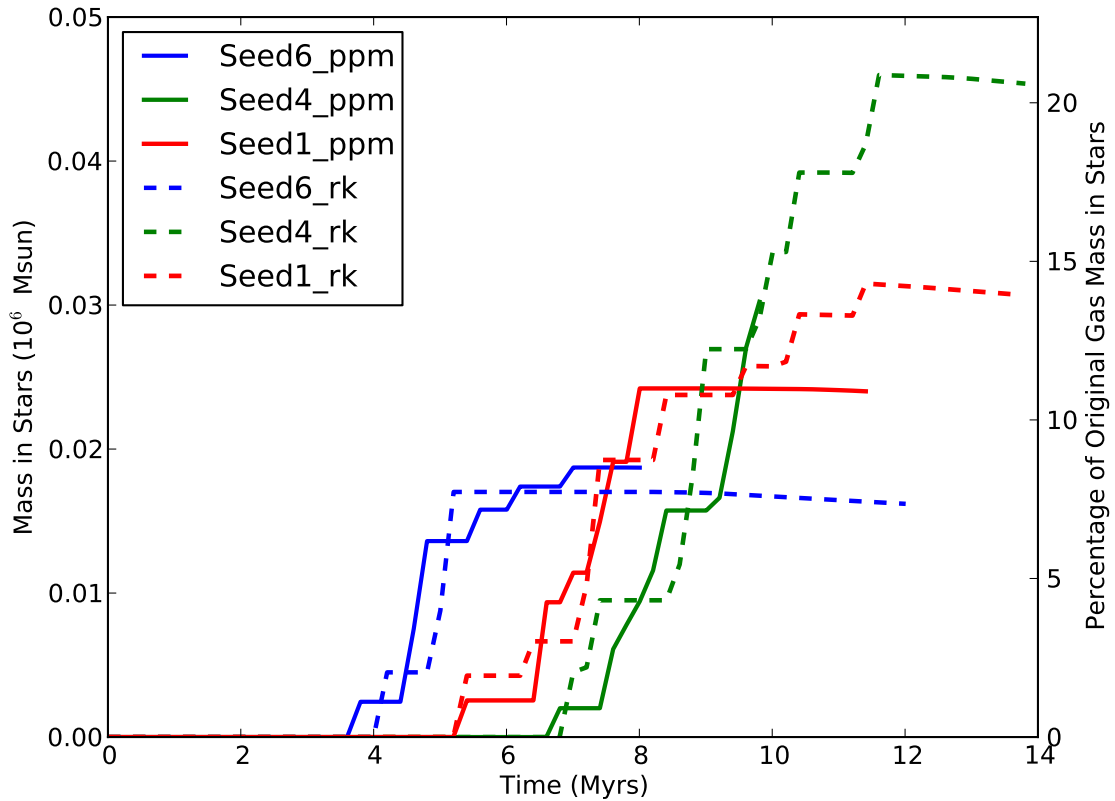


Figure 5.54: Direct comparisons between mass in star clusters for three of the different seeds for the different hydro solvers: the base simulation and simulations with the earliest and latest first star cluster formation time. Overall star formation history for the seeds is similar between the two hydro solvers.

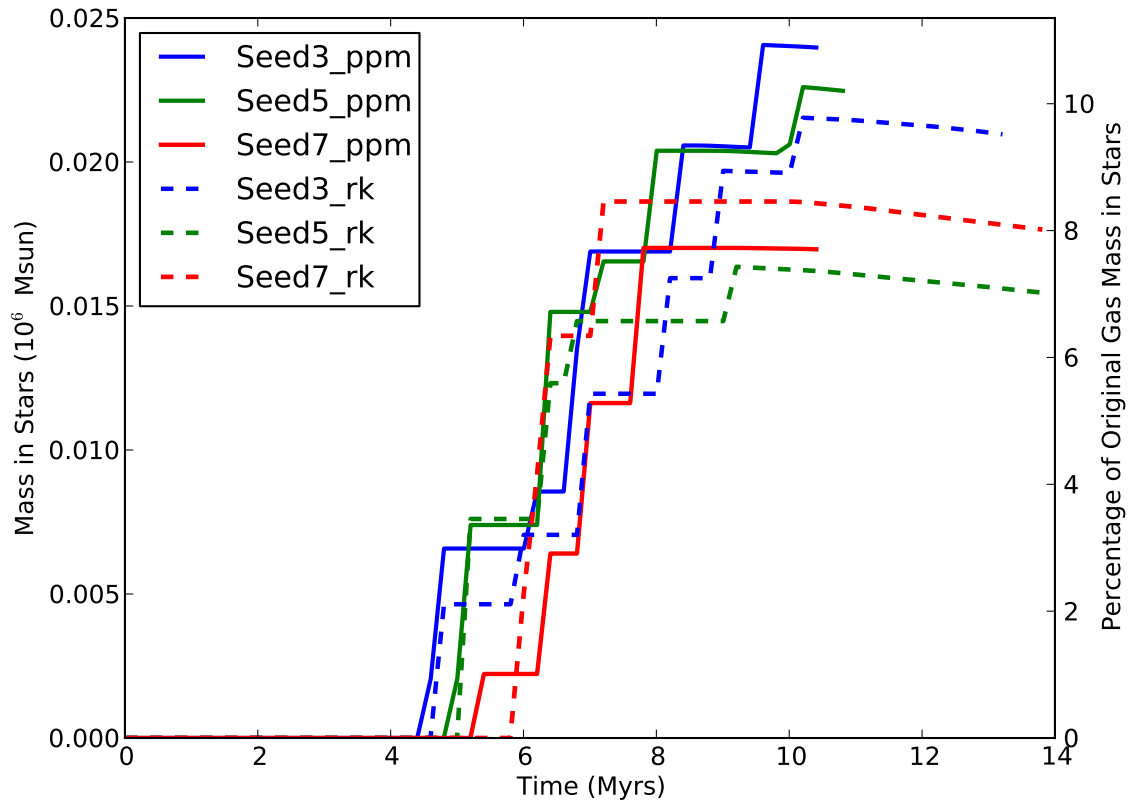


Figure 5.55: Direct comparisons between mass in star clusters for three of the different seeds for the different hydro solvers: the three simulations where the first star cluster formed was furthest apart for the different hydro solvers. Despite the first stars forming in different areas of the simulation box the overall star formation rate is very similar between the two solvers suggesting that for all three seeds there are multiple regions of star formation that may start at different times between the different solvers but do form ultimately either way.

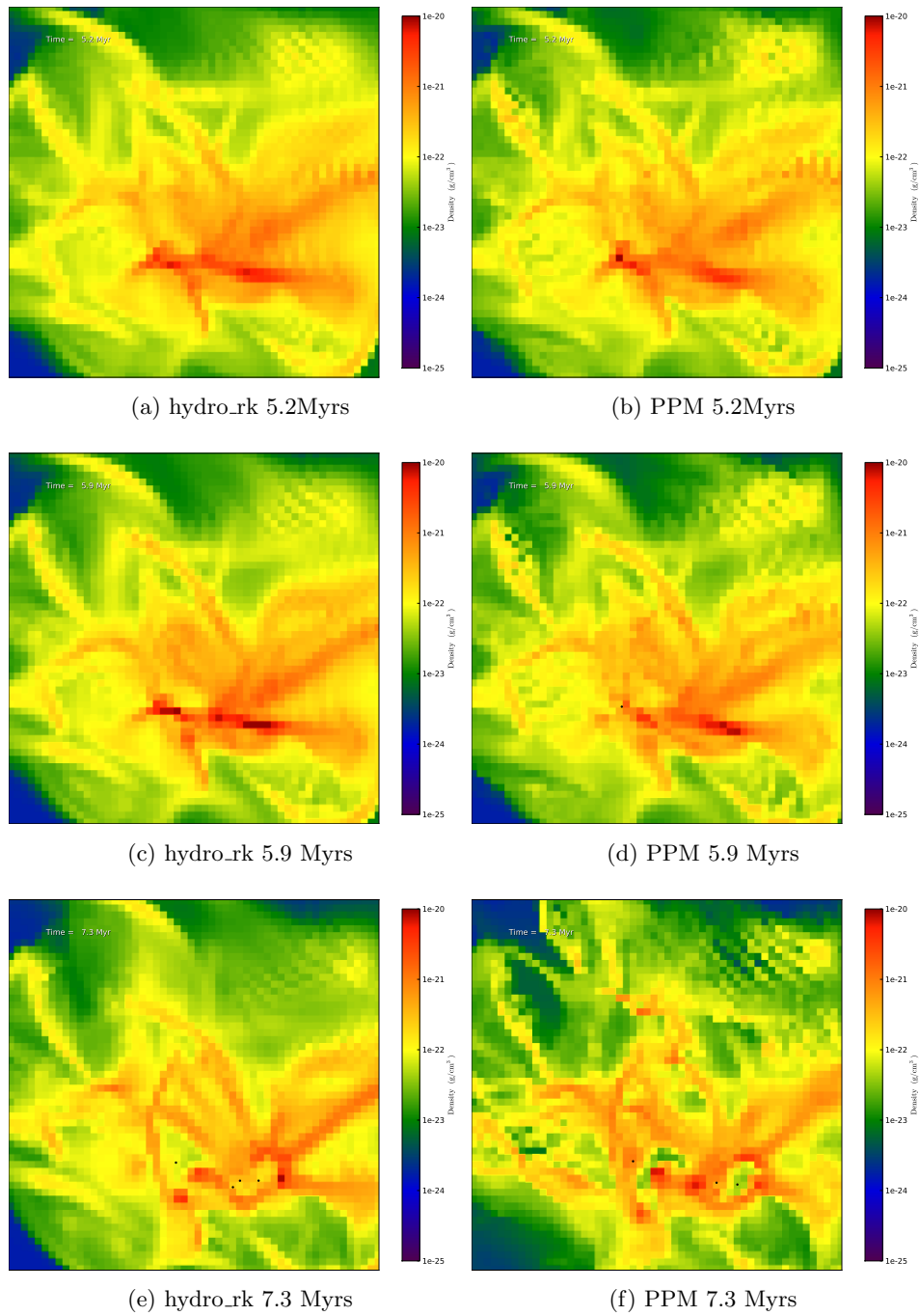


Figure 5.56: Seed7 simulations at three different times for two different hydro solvers. Images are density projections of the central 100 pc. For the hydro_rk solver the filaments look smoother at all times. However, the position, shape and approximate density for all filaments are the same for both solvers. Star clusters are formed at slightly different times but in the same locations.

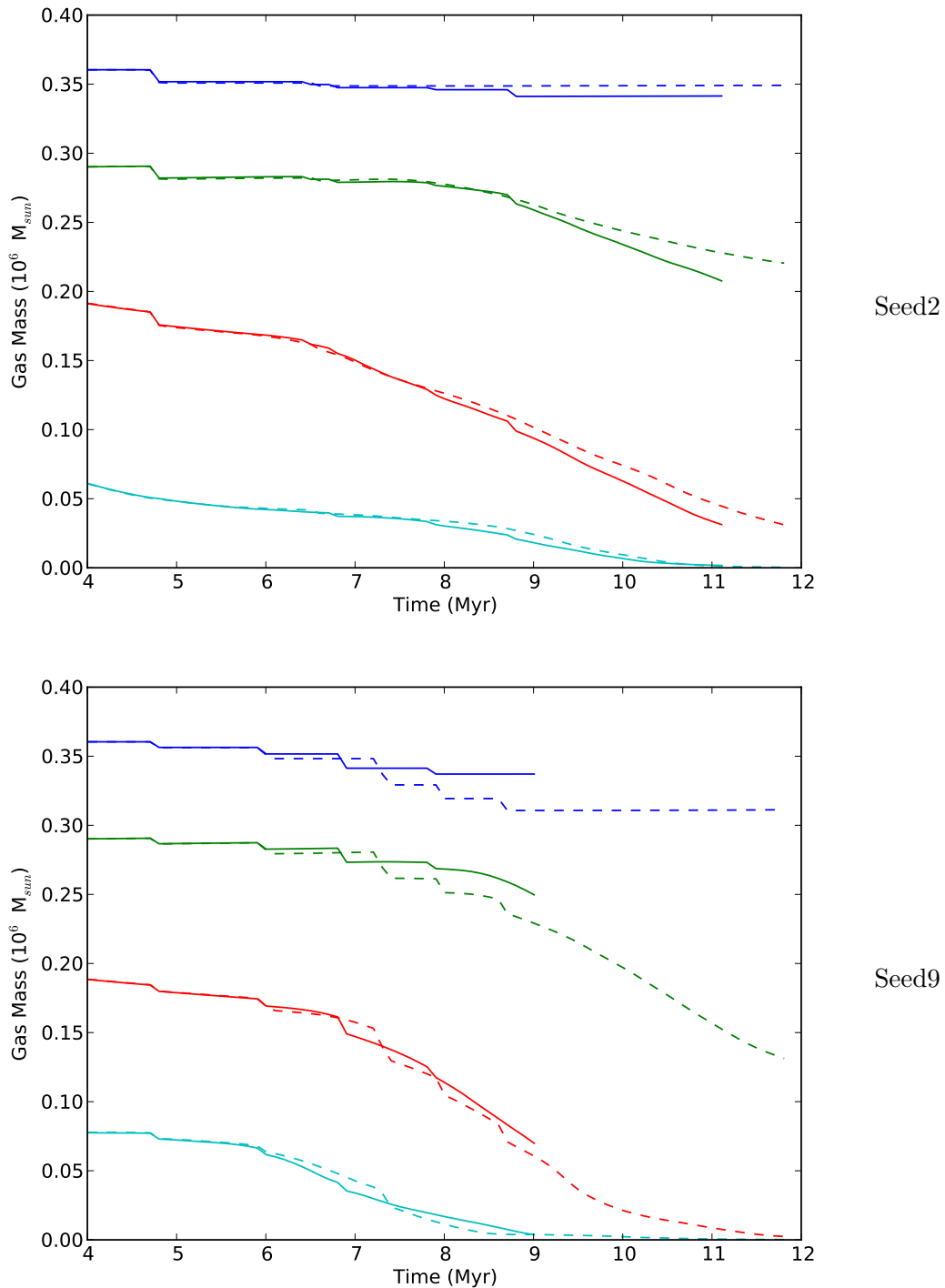


Figure 5.57: Graphs showing the mass structure for *top*: Seed2 and *bottom*: Seed9. *Solid lines* are for the PPM solver and *dashed lines* are for the hydro_rk solver. The mass structure is very similar for the different solvers. Seed2 is clearing slightly faster with PPM than it did with hydro_rk but it has slightly more mass in clusters with PPM. Seed9's rapid dissipation of gas is the same for both hydro solvers.

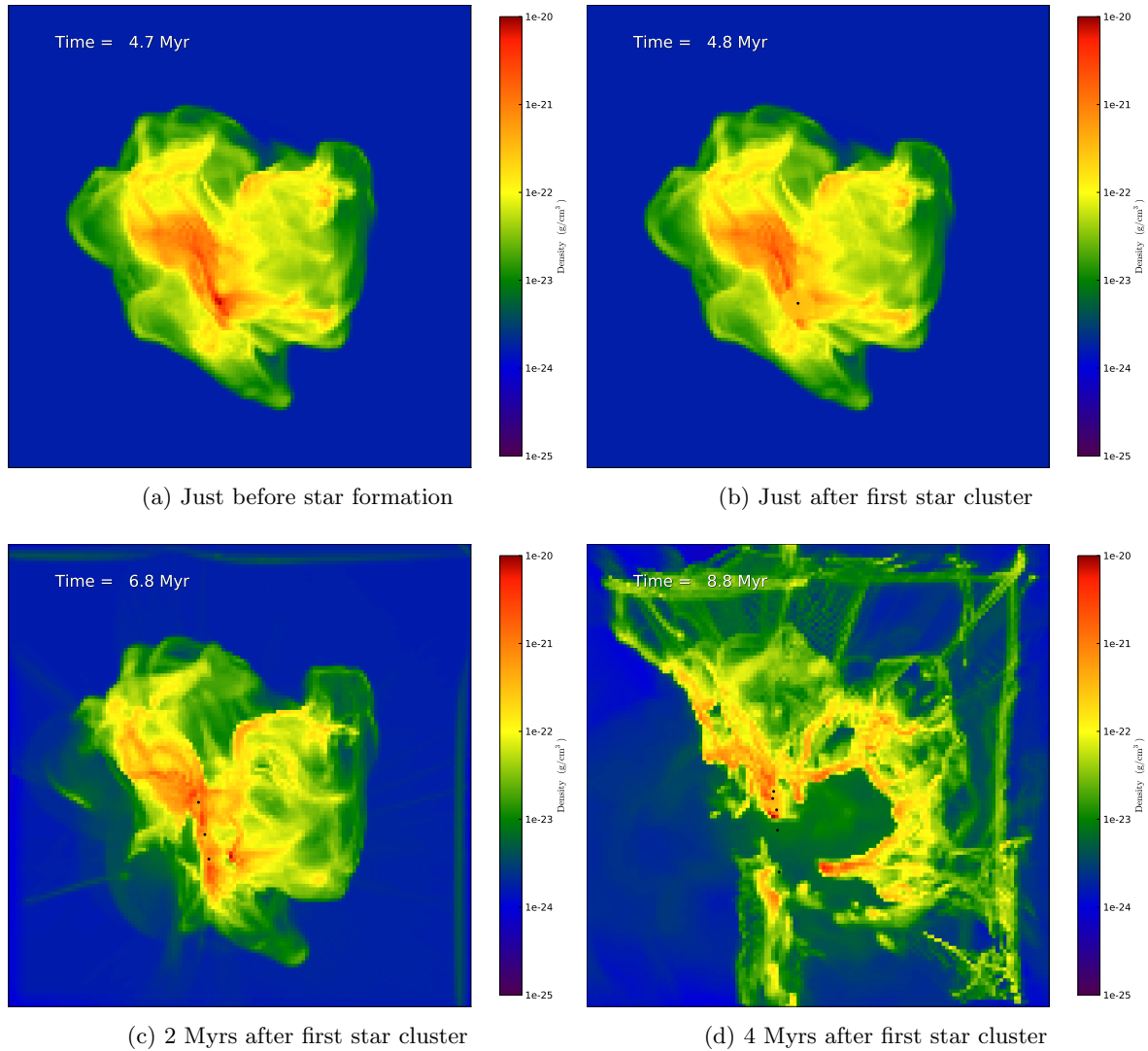


Figure 5.58: Seed2 x-axis density projections at four different times for the PPM solver. (a) shows the density immediately before the first star cluster forms. (b) shows after the first star cluster has formed. (c) shows the density projection 2 Myrs after the first star cluster formed (0.2 Myrs after the third and final star cluster forms). (d) shows the disruption of the cloud at 4 Myrs after the first star cluster formed. The disruption of the cloud is very similar to with the hydro_rk solver, Fig. 5.42.

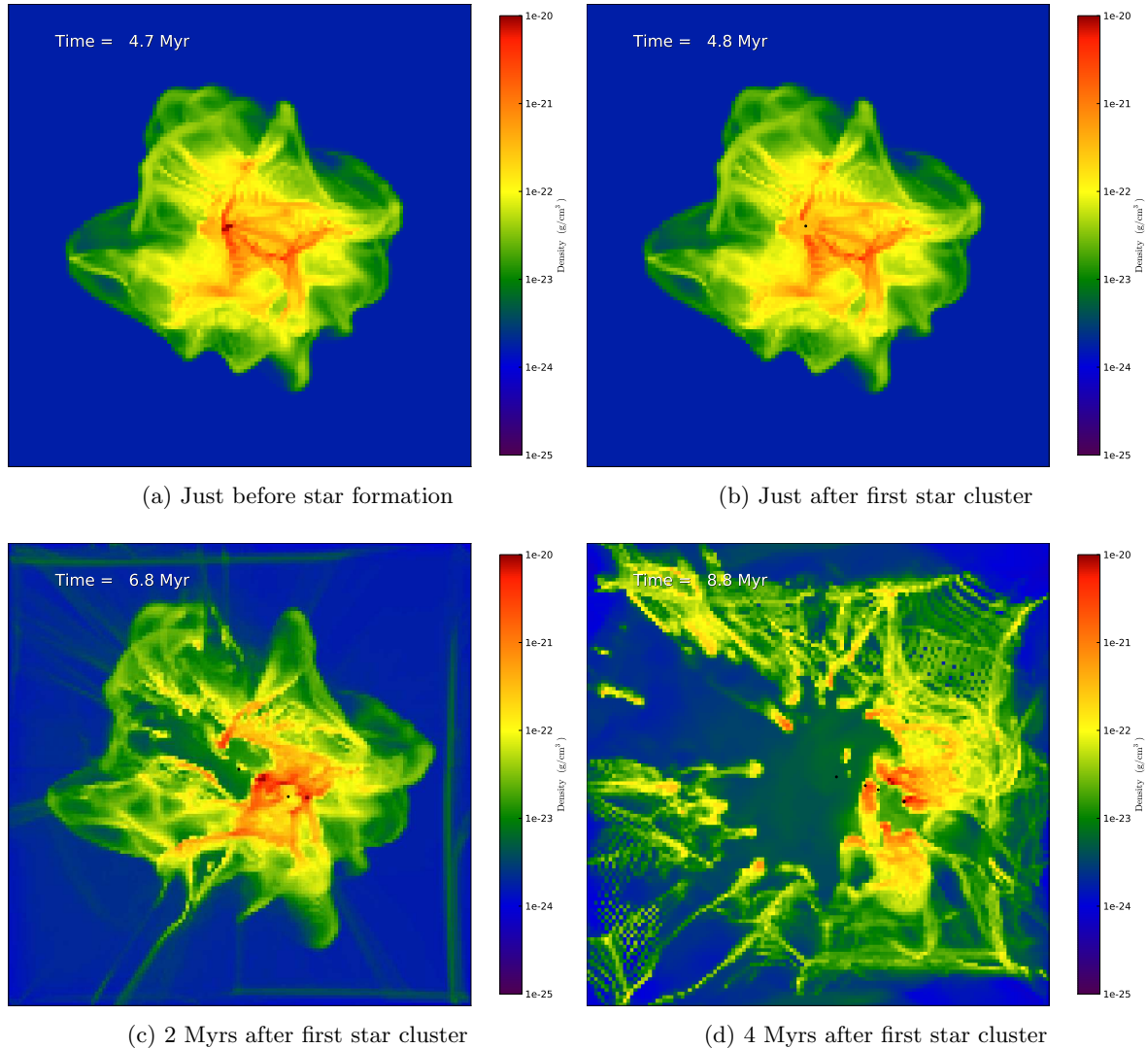


Figure 5.59: Seed9 x-axis density projections at four different times for the PPM solver. (a) shows the density immediately before the first star cluster forms. (b) shows after the first star cluster has formed. (c) shows the density projection 2 Myrs after the first star cluster formed. (d) shows the disruption of the cloud at 4 Myrs after the first star cluster formed. The disruption of the cloud is very similar to with the hydro_rk solver, Fig. 5.43.

Chapter 6

Interesting Asides

This chapter presents some interesting results seen in our simulations that are not central to the main argument of the thesis. Here I simulated the stars individually rather than as a combined cluster.

A version of this chapter has been published in the Conference Proceedings for the International Astronomical Union Symposium 270: Computational Star Formation (referred), (Harper-Clark & Murray, 2011). Reprinted with permission.

6.1 Abstract

Using the AMR code Enzo we are simulating the formation of massive star clusters within turbulent Giant Molecular Clouds (GMCs). Here we discuss the simulations from the first stages of building realistic turbulent GMCs, to accurate star formation, and ultimately comprehensive feedback. These simulations aim to build a better understanding of how stars affect GMCs, helping to answer the questions of how long GMCs live and why only a small fraction of the GMC gas becomes stars.

6.2 Introduction

Within the Milky Way there are ~ 300 Giant Molecular Clouds (GMCs) with masses of the order a million solar masses. For these GMCs, the average star formation rate per free-fall time (SFR_{ff}) is 2% (Kennicutt, 1998). However, the majority of the star formation is contained within fewer than 50 of these GMCs (Murray & Rahman (2010) and Murray (2011)). The small fraction of GMCs with high SFR_{ff} suggests that the SFR_{ff} of a GMC changes over its

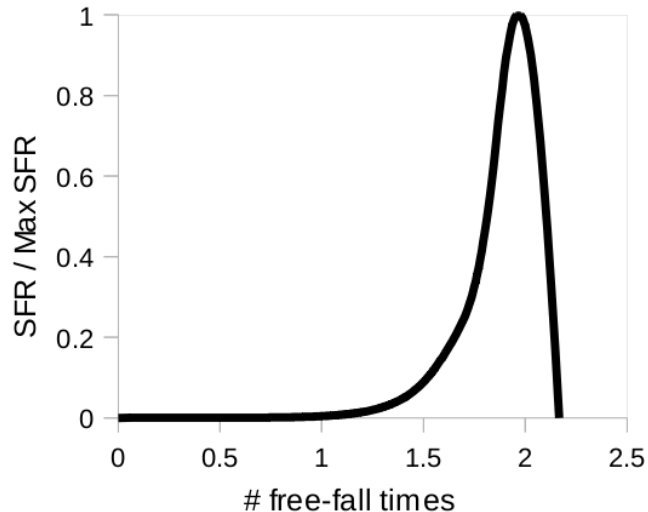


Figure 6.1: A cartoon of our propose star formation rate per free-fall time over an individual clouds lifetime ending with its destruction at ~ 2 free fall times.

lifetime. We propose that the star formation rate increases over a cloud’s lifetime, as shown in cartoon form in Fig. 6.1. The GMCs with highest SFR_{ff} are seen to be in the process of disruption, Fig. 6.2. Once a large star cluster forms it will blow apart its parent GMC (Harper-Clark & Murray (2009) and Fig. 6.2), thus the last period of star formation is likely the GMCs most rapid.

6.3 Code

The high-resolution Eulerian AMR code Enzo (Bryan & Norman (1997) and O’Shea et al. (2004) etc.) contains all necessary physics for accurate testing of turbulent GMC gravitational collapse. We are using the developer’s version which includes MHD, protostellar jets, radiative transfer, and an alternative hydro solver using a total variation diminishing second order Runge-Kutta scheme for time-integration (see Wang & Abel (2009) and Wise & Abel (2008) for details).

6.4 Simulation Set-up

To model an entire GMC we set up a cubic simulation box 128pc wide. The top grid has dimensions 256^3 (0.5pc) and is refined by 2 for up to 8 levels (effective resolution of 65 536, 0.002pc, 400AU). Refinement is based upon Jeans’ length or the presence of stars. Subgrids are

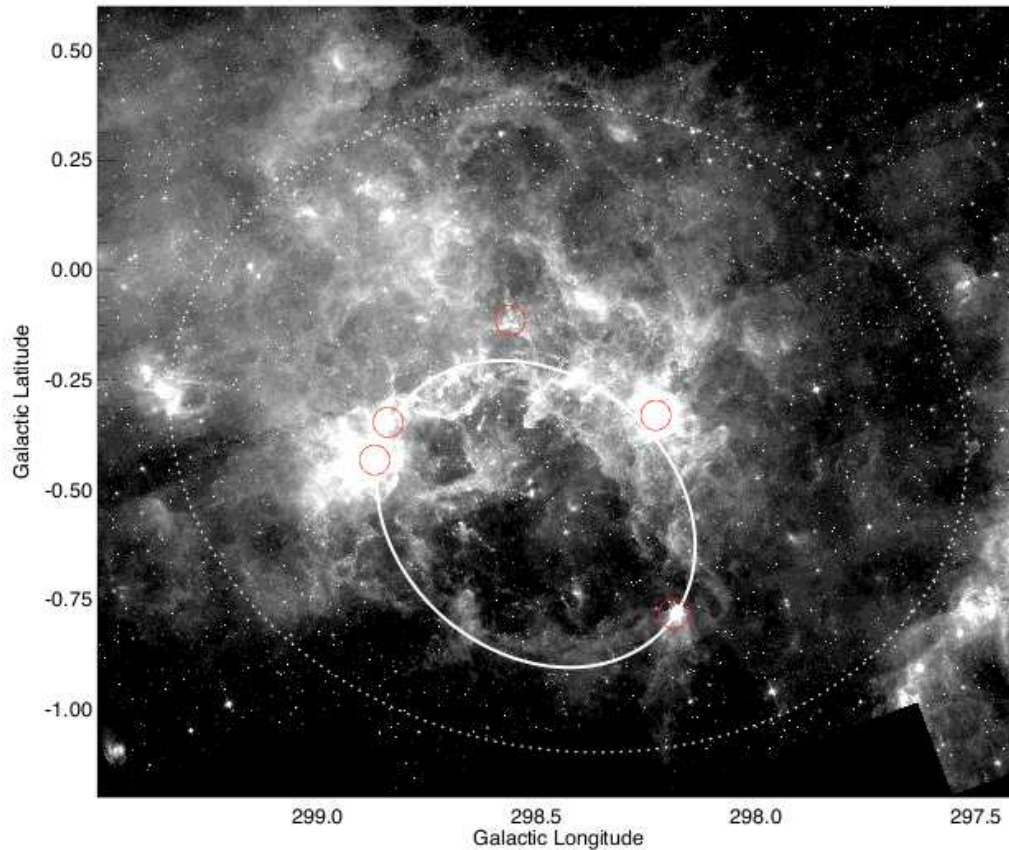


Figure 6.2: A Spitzer Glimpse image of G298-0.34, a GMC in the process of being blown apart by an invisible central massive star cluster (Murray & Rahman (2010)). The small red dashed ellipses show compact HII regions from triggered star formation. The solid oval is the bubble wall and the large dotted oval is the extent of the WMAP source, suggesting the hot gas is leaking from the bubble (Harper-Clark & Murray (2009)).

set up so that each star is always surrounded by at least 0.03pc of maximally refined region in all directions.

The initial velocities of the gas are set by a seeded random distribution fitting a Larson turbulent spectrum with $2 \leq k \leq 32$ (e.g., Mac Low et al. (1998)) at Mach 9 and decay appropriately.

The initial density distribution is a cored isothermal sphere with radius of 44.8pc. The size of the core can be varied to get different distributions whilst maintaining a mass of a million solar masses of gas within the cloud. Although a smooth spherically symmetric density distribution is not realistic for a GMC the random velocities cause filamentary structures to form rapidly and before any stars form the densities look much more realistic (Fig. 6.3).

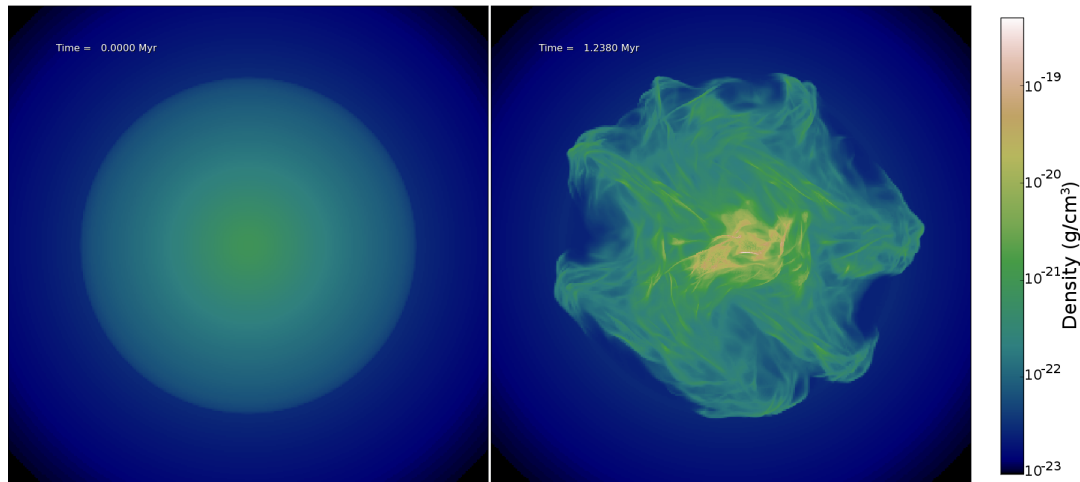


Figure 6.3: Initial density distributions. Left: time = 0 the cloud is a spherically symmetric cored isothermal sphere. Right: after 1.238 million years the turbulence has formed a filamentary structure and the first stars are about to form.

Stars are formed according to the Truelove criterion (Truelove et al. (1997)). Once the Jeans' length (l_J) is less than 4 maximum refinement level cell widths only the mass needed to bring the Jeans length back to 4 cell widths is taken out of the cell and forms a sink particle conserving momentum and mass.

6.5 Preliminary Results

While the simulations have only run as far as forming the first star cluster to date, there are some interesting results from our simulations worth discussing.

6.5.1 Local conditions for star formation

By construction, the stars in our simulation form where the Jeans length becomes less than 0.008pc. Upon close inspection this typically occurs where three or more filaments of inflow meet or when two filaments collide, as shown in Fig. 6.4.

6.5.2 Location of first stars within the GMC

Precisely where within a GMC the first stars form depends strongly upon the central concentration of the density. For example Fig. 6.5 shows two different GMCs with identical initial

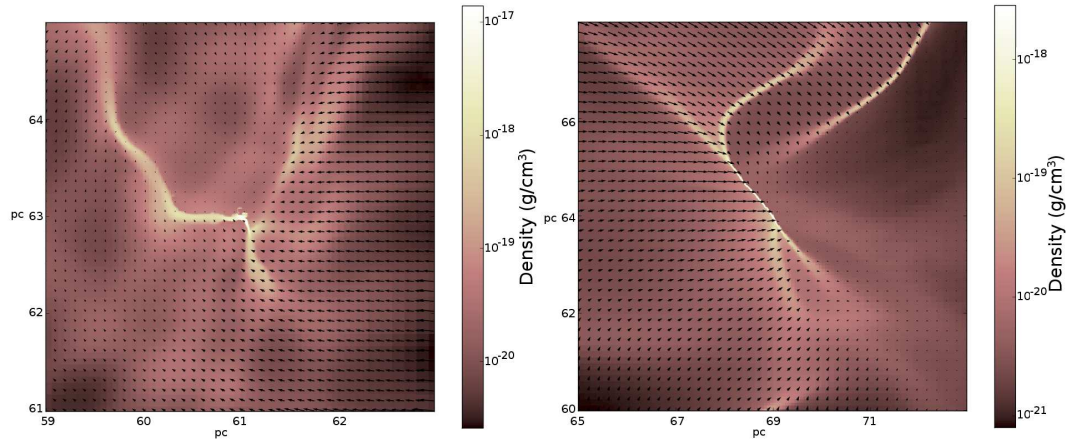


Figure 6.4: Density slices of a core about to form a star from hydrodynamic simulations showing the velocities of the surrounding gas (black arrows). Left: three or more filaments of inflow meeting. Right: just after two filaments have collided

velocity distribution, the same mass but different radial density profiles. Both clouds are cored isothermal spheres, one with density varying as: $\rho(r) = 4.25\rho_c/(1 + (9r/r_{cl})^2)$ so half mass radius = 0.57 (left in Fig. 6.5) and the other: $\rho(r) = 1.05\rho_c/(1 + (4r/r_{cl})^2)$ so half mass radius = 0.63 (right in Fig. 6.5) where ρ_c is a set density and r_{cl} is the radius of the cloud.

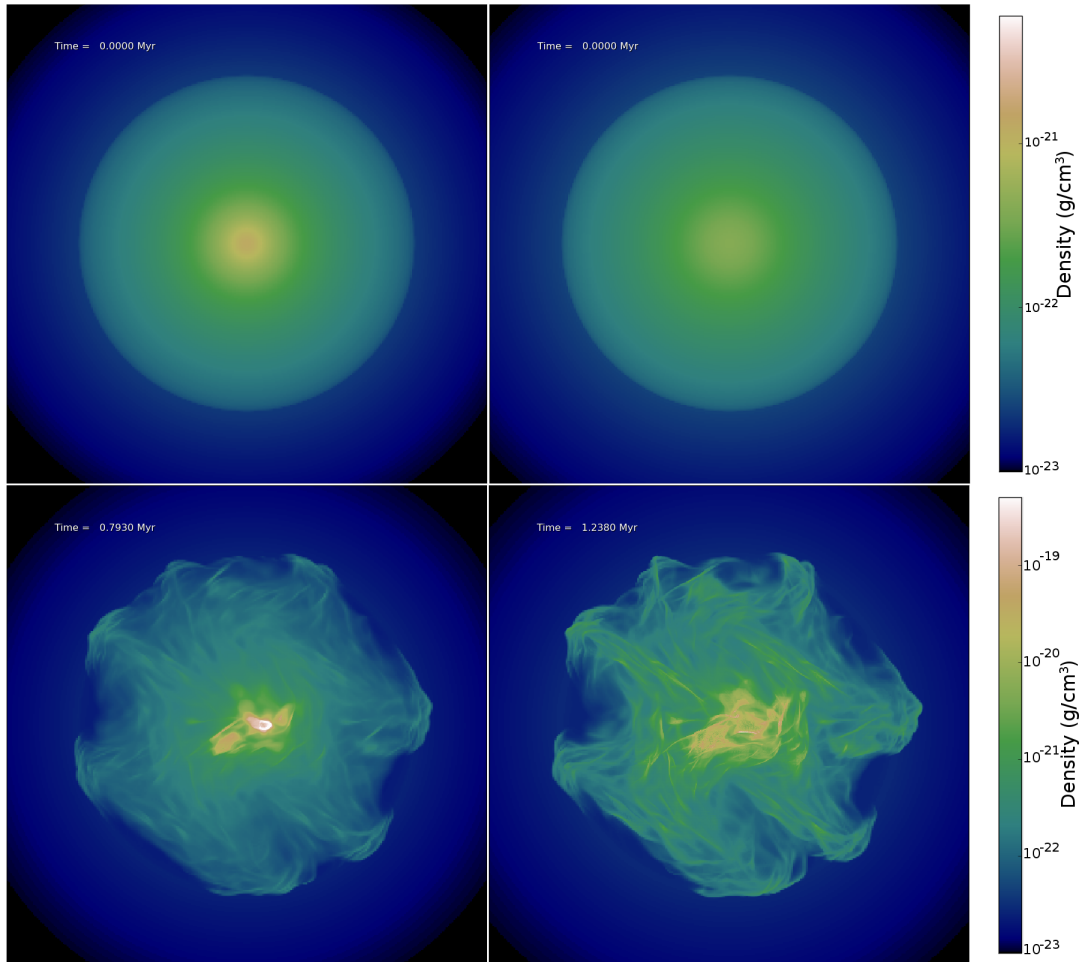


Figure 6.5: Two clouds with different central concentrations but identical initial velocity distribution and total mass. The top two images show the initial density when spherically symmetric and the bottom images are the corresponding clouds just before the first stars form in each. Please note the different colourbars between the top and bottom images (colourbars on right).

Chapter 7

Conclusions

7.1 Summary

It is important to understand what part stellar outputs play in feedback and quenching of subsequent star formation not only for in the Milky Way but for simulations of our universe on many scales. The more accurate galaxy scale and cosmological simulations get, the more researchers are realizing how important it is to include feedback from stars.

Most stars form in massive clusters within Giant Molecular Clouds (GMCs). In clusters of several thousand solar masses there will be around one hundred O-type stars. O-type stars emit strong stellar winds of up to a few millionths of a solar mass per year at thousands of kilometres per second. These winds shock with gas surrounding the star heating the gas to 10^7 K. One-dimensional models (Chapter 2) showed that for observed bubbles there is substantial leaking which causes the stellar winds to have negligible dynamical effect on the GMC removing it as a contender for feedback. Recent observations of 30 Dor support this, showing that it is ionization and radiation pressure that dominate the feedback during stellar lives (Lopez et al., 2011).

I ran simulations of cluster formation and stellar outputs using the three dimensional radiative hydro code Enzo. All simulations were variations of a single base simulation, 179.2 pc wide box containing a 44.8 pc radius, quarter of a million solar mass cloud: §4.1. The cloud started with Mach 13 turbulence and evolved for close to one dynamical time before star cluster formation began. Clusters formed in cell above a minimum density, taking material from a small sphere around the cell to form the cluster. Once the clusters formed, they shone with ionizing radiation. As the ionization is absorbed the momentum from the light is deposited into the gas. With no other outputs from the stars the cloud was completely disrupted within

another dynamical time and formed star clusters from only 13% of the original cloud gas mass.

I investigated the relative importance of ionization, radiation pressure, and supernovae in an output study: §4.2. I found that supernovae had little dynamical effect and only very minor effects on subsequent star formation. Ionization heats the surrounding gas stalling star formation but only slowly disrupts the cloud implying further star formation could occur after the O-type stars have died and the gas has cooled again. Radiation pressure had the most significant dynamical effect on the gas, steadily pushing the gas away from the star clusters and out of the original cloud location definitively quenching further star formation in the cloud.

I ran a parameter study around four of the parameters used in star cluster formation: §5.1. I found that within reasonable limits the star cluster formation routine is very robust forming the same mass into star clusters for drastically varying parameters. The parameter study was run with ionization and radiation pressure and also with no outputs. The differences between parameters was even less for no outputs as small changes in total star cluster mass early in the simulation did not affect the subsequent star formation. For no outputs, a star formation rate of 30% per free fall time was found. For the simulations with outputs the cumulative stellar mass was quenched at approximately 12% of the GMC mass.

Resolution tests of the code showed that AMR is an efficient and effective way to track star cluster formation at higher resolutions, only slightly altering the star formation history of the cloud: §5.2. To maintain the same *number* of star clusters our simulations suggest that line density for the critical cells should be kept constant, but this study is not conclusive. However, the cumulative mass does not change significantly with changing resolution.

I ran 8 additional simulations with different turbulent seeds to give different initial velocity structures: §5.3. This changed the precise time of first cluster formation and the final mass. All simulations formed between 5% and 21% of the original cloud mass into stars. Despite this wide range of final stellar mass, all of the simulations fully disrupted the cloud, moving almost all of the remaining gas out of the original cloud location within a dynamical time of the first cluster forming. The mass converted into star clusters at 12 Myrs averaged over all nine runs is $26,042 \pm 13,120 M_{\odot}$ or $11.8 \pm 6.0 \%$ of the original gas mass. Thus, averaged over the lifetime of the cloud the star formation rate is 6% per free-fall time. Assuming it takes at least a couple of free fall times for the gas that is disrupted to collect back together into a GMC then the galactic average star formation rate would be at most 3%.

Towards the end of my studies the PPM hydro solver was altered to be more robust and I reran the base simulation and turbulent seed study with the different solver: §5.4. The different solvers formed subtly different structures within the cloud - the PPM simulations were more clumpy. However, for all of the runs the star cluster formation and disruption of the cloud was

in strong agreement. Unfortunately, there are still some numerical problems with the PPM solver for my simulations but the agreement between the runs as far as they could run strongly validates the use of the more robust hydro_rk solver.

I ran a simulation with the cloud embedded in a denser surrounding medium to slow the expansion of the HII region outside of the cloud and test if the box edges affect the subsequent star formation: §4.3. The star cluster formation rate and disruption of the inner cloud were in good agreement suggesting the box edges do not affect the cloud interior.

Enzo has the capacity to include magnetic fields. I ran a simulation with initially uniform 10^{-6} Gauss magnetic field in the z direction which was rapidly increased to an average of a few microGauss within the cloud by the turbulent motion: §4.4. The magnetic field did not significantly alter the star formation rate. However, it did cause the bubble shell to be less leaky and as such resulted in the inner regions clearing out faster as a larger angular fraction of the shell remained and absorbed the radiation pressure.

I ran several simulations of a larger cloud with four times the mass and all results agreed with the lower mass simulations: §4.5. The more massive cloud did highlight one of the limitations of my radiation pressure approximation. Once the dynamical time became significantly longer than the ionizing radiation lifetimes of the star clusters the under sampling of radiation pressure without ionizing radiation became important.

Looking at individual star formation, Chapter 6, we found that stars often form where multiple filaments collide or regions of multiple inflows coincide. This is where density can get high enough for star formation to occur. We also found that the central concentration of the original cloud is the main factor determining where the stars form within the cloud. The simulations with clusters rather than individual stars also agree with this.

7.2 Conclusions

Giant Molecular Clouds can be completely disrupted by the radiation outputs during massive star clusters lifetimes within a dynamical time even with as little as 5% of the mass converted into stars.

Our simulations give robust answers within reasonable range of parameters for our sub-grid star formation routine, for two different hydro solvers, and for varying resolution. This agrees with larger scale simulations (Hopkins et al., 2011) which found that reducing the star formation efficiency per free fall time led to denser regions and thus the same actual star formation rate that was only limited by stellar feedback.

With no stellar outputs we find a star formation rate of 30% per free fall time once star formation begins. This suggests that turbulence is not significantly limiting star formation.

Our simulations show supernovae are not dynamically important to the local surroundings and do not affect the subsequent star formation, especially when exploding within an already significantly vacated bubble from ionization and radiation pressure. When supernovae are included with no other outputs they explode in a dense region and rapidly cool, reducing any dynamical effects they can have. When supernovae explode with other outputs they are exploding into an already vacated and leaky bubble causing the hot gas to escape, resulting in a limited effect on the surrounding medium.

The inclusion of radiative outputs (ionization and radiation pressure) quenches star formation and disrupts the GMC forming around 12% of the original gas into stars, almost three times less than the rate with no outputs. This amount agrees with observations (Murray, 2011) though further testing of the subgrid models will be conducted. Ionization pressure alone can disrupt the cloud and quench star formation but disruption and quenching occur earlier when radiation pressure is included. Radiation pressure will disrupt clouds and quench further star formation alone though its effect is limited by numerical issues within these simulations.

Different turbulent structures cause different numbers of star forming regions within a GMC. If there are multiple regions it takes time for the outputs from the first region to reach others causing higher overall rates of star formation. This is the only significant affect turbulence has on star formation in our simulations.

Magnetic fields of the order a few microGauss across the cloud do not affect star formation rate and actually make the outputs more efficient by reducing leaking from, and disruption of, the bubble shell.

Simulations of a more massive cloud agree with the above conclusions.

7.3 Further Work

There are many interesting investigations continuing on from this work.

The magnetic field simulation is interesting and warrants further investigation at higher magnetic field strength and for different turbulent seeds. Do the magnetic fields always make the bubbles less leaky? Does this cause faster dispersion or can it halt the expansion and cease disruption leading to a large mass in star clusters? Do stronger magnetic fields delay star cluster formation by reducing the effects of turbulent collapse or accelerate formation by reducing turbulent motions and allowing gravitational collapse?

With improvements to the parallelisation of the code under the conditions I use it I would like to run a few simulations at much higher resolution. If the simulation can be set up so the cells in which cluster formation occurs have dynamical times of tens of thousands of years rather than millions of years we can test how valid the star formation routines used in these simulations are. Also, further investigations of critical densities and how the turbulent structure changes with increasing resolution would test the sub grid approximations used in larger simulations.

A stellar winds code can be included based upon the supernovae code used in these simulations. Careful consideration of resolution, mixing, and cooling of the gases will be required to ensure the code is accurate. With stellar winds included the pressure balance between HII and stellar wind shocked hot gas observed can be tested and the leaking predicted and observed investigated.

It would be useful to bridge the gap between GMCs and galaxies by simulating a GMC embedded within a region of a galaxy. It would be interesting to see what happens to the leaked gas and how more realistic cloud exteriors affect the disruption of the GMCs.

It would be fascinating to extend simulations like those presented in this thesis to more extreme situations. The higher densities and stronger turbulence observed in ULIRGs (e.g. Arp 220) should result in the radiation pressure becoming more dominant in stellar feedback than the equal share between radiation pressure and HII gas pressure in our own galaxy. ULIRG GMCs will be significantly more computationally expensive to run so the extensive investigation of numerics explored in this thesis will be important for their accurate simulation.

Bibliography

- Allen, D. A. & Hillier, D. J. 1993, Proceedings of the Astronomical Society of Australia, 10, 338
- Arthur, S. J., Henney, W. J., Mellema, G., de Colle, F., & Vázquez-Semadeni, E. 2011, MNRAS, 541
- Battaglia, N., Bond, J. R., Pfrommer, C., Sievers, J. L., & Sijacki, D. 2010, ApJ, 725, 91
- Berger, M. J. & Colella, P. 1989, JoCP, 82, 64
- Bertschinger, E. & Gelb, J. M. 1991, Computers in Physics, 5, 164
- Bigiel, F., Leroy, A., Walter, F., Brinks, E., de Blok, W. J. G., Madore, B., & Thornley, M. D. 2008, AJ, 136, 2846
- Bondi, H. 1952, MNRAS, 112, 195
- Bouret, J.-C., Lanz, T., & Hillier, D. J. 2005, A&A, 438, 301
- Bournaud, F., Chapon, D., Teyssier, R., Powell, L. C., Elmegreen, B. G., Elmegreen, D. M., Duc, P., Contini, T., Epinat, B., & Shapiro, K. L. 2011, ApJ, 730, 4
- Bressan, A., Fagotto, F., Bertelli, G., & Chiosi, C. 1993, A&AS, 100, 647
- Bryan, G. L. & Norman, M. L. 1997, arXiv:astro-ph/9710187
- Cantó, J., Raga, A. C., & Rodríguez, L. F. 2000, ApJ, 536, 896
- Castor, J., McCray, R., & Weaver, R. 1975, ApJ, 200, L107
- Ceverino, D., Dekel, A., & Bournaud, F. 2010, MNRAS, 404, 2151
- Chakraborty, A. & Anandarao, B. G. 1997, AJ, 114, 1576
- . 1999, A&A, 346, 947

- Chevalier, R. A. & Clegg, A. W. 1985, *Nature*, 317, 44
- Chu, Y.-H., Chang, H.-W., Su, Y.-L., & Low, M.-M. M. 1995, *ApJ*, 450, 157
- Chu, Y.-H. & Low, M.-M. M. 1990, *ApJ*, 365, 510
- Colella, P. & Woodward, P. R. 1984, *JoCP*, 54, 174
- Colín, P., Avila-Reese, V., Vázquez-Semadeni, E., Valenzuela, O., & Ceverino, D. 2010, *ApJ*, 713, 535
- Cowie, L. L. & McKee, C. F. 1977, *ApJ*, 211, 135
- Crutcher, R. M., Wandelt, B., Heiles, C., Falgarone, E., & Troland, T. H. 2010, *ApJ*, 725, 466
- Cunningham, A. J., Klein, R. I., Krumholz, M. R., & McKee, C. F. 2011, *arXiv:astro-ph/1104.1218*
- de Pree, C. G., Mehringer, D. M., & Goss, W. M. 1997, *ApJ*, 482, 307
- De Pree, C. G., Wilner, D. J., Deblasio, J., Mercer, A. J., & Davis, L. E. 2005, *ApJ*, 624, L101
- Dedner, A., Kemm, F., Kröner, D., Munz, C., Schnitzer, T., & Wesenberg, M. 2002, *JoCP*, 175, 645
- Dopita, M. A., Groves, B. A., Fischera, J., Sutherland, R. S., Tuffs, R. J., Popescu, C. C., Kewley, L. J., Reuland, M., & Leitherer, C. 2005, *ApJ*, 619, 755
- Dorland, H. & Montmerle, T. 1987, *A&A*, 177, 243
- Dorland, H., Montmerle, T., & Doom, C. 1986, *A&A*, 160, 1
- Dunne, B. C., Chu, Y.-H., Chen, C.-H. R., Lowry, J. D., Townsley, L., Gruendl, R. A., Guerrero, M. A., & Rosado, M. 2003, *ApJ*, 590, 306
- Elmegreen, B. G. 2000, *ApJ*, 530, 277
- . 2007, *ApJ*, 668, 1064
- Evans, C. J., Crowther, P. A., Fullerton, A. W., & Hillier, D. J. 2004, *ApJ*, 610, 1021
- Everett, J. E. & Churchwell, E. 2010, *ApJ*, 713, 592
- Fall, S. M., Krumholz, M. R., & Matzner, C. D. 2010, *ApJ*, 710, L142
- Ferland, G. J., Korista, K. T., Verner, D. A., Ferguson, J. W., Kingdon, J. B., & Verner, E. M. 1998, *PASP*, 110, 761

- Flaccomio, E. 2005, *Massive star birth: A crossroads of Astrophysics*, 227, 247
- Fukui, Y. & Kawamura, A. 2010, *ARA&A*, 48, 547
- Fullerton, A. W., Massa, D. L., & Prinja, R. K. 2006, *ApJ*, 637, 1025
- Gilman, R. C. 1974, *ApJS*, 28, 397
- Goldbaum, N. J., Krumholz, M. R., Matzner, C. D., & McKee, C. F. 2011, *arXiv:astro-ph/1105.6097*
- Goodman, A. A., Pineda, J. E., & Schnee, S. L. 2009, *ApJ*, 692, 91
- Górski, K. M., Hivon, E., Banday, A. J., Wandelt, B. D., Hansen, F. K., Reinecke, M., & Bartelmann, M. 2005, *ApJ*, 622, 759
- Governato, F., Willman, B., Mayer, L., Brooks, A., Stinson, G., Valenzuela, O., Wadsley, J., & Quinn, T. 2007, *MNRAS*, 374, 1479
- Grabelsky, D. A., Cohen, R. S., Bronfman, L., & Thaddeus, P. 1988, *ApJ*, 331, 181
- Hamaguchi, K., Petre, R., Matsumoto, H., Tsujimoto, M., Holt, S. S., Ezoe, Y., Ozawa, H., Tsuboi, Y., Soong, Y., Kitamoto, S., Sekiguchi, A., & Kokubun, M. 2007a, *PASJ*, 59, 151
- Hamaguchi, K., Team, S. . C., & Team, C. D.-. 2007b, *Progress of Theoretical Physics Supplement*, 169, 174
- Harper-Clark, E. & Murray, N. 2009, *ApJ*, 693, 1696
- Harper-Clark, E. & Murray, N. 2011, in *IAU Symposium*, Vol. 270, *IAU Symposium*, ed. J. Alves, B. G. Elmegreen, J. M. Girart, & V. Trimble, 235–238
- Hennebelle, P., Commerçon, B., Joos, M., Klessen, R. S., Krumholz, M., Tan, J. C., & Teyssier, R. 2011, *A&A*, 528, A72+
- Hopkins, A. M. & Beacom, J. F. 2006, *ApJ*, 651, 142
- Hopkins, P. F., Quataert, E., & Murray, N. 2011, *arXiv:astro-ph/1101.4940*
- Huchtmeier, W. K. & Day, G. A. 1975, *A&A*, 41, 153
- Karim, A., Schinnerer, E., Martínez-Sansigre, A., Sargent, M. T., van der Wel, A., Rix, H., Ilbert, O., Smolčić, V., Carilli, C., Pannella, M., Koekemoer, A. M., Bell, E. F., & Salvato, M. 2011, *ApJ*, 730, 61

- Kawamura, A., Mizuno, Y., Minamidani, T., Filipović, M. D., Staveley-Smith, L., Kim, S., Mizuno, N., Onishi, T., Mizuno, A., & Fukui, Y. 2009, *ApJS*, 184, 1
- Kennicutt, R. C. 1989, *ApJ*, 344, 685
- . 1998, *ApJ*, 498, 541
- Kereš, D., Katz, N., Davé, R., Fardal, M., & Weinberg, D. H. 2009, *MNRAS*, 396, 2332
- Krumholz, M. R. & Matzner, C. D. 2009, *ApJ*, 703, 1352
- Krumholz, M. R., Matzner, C. D., & McKee, C. F. 2006, *ApJ*, 653, 361
- Krumholz, M. R. & McKee, C. F. 2005, *ApJ*, 630, 250
- Kurganov, A. & Tadmor, E. 2000, *JoCP*, 160, 241
- Laor, A. & Draine, B. T. 1993, *ApJ*, 402, 441
- Larson, R. B. 1981, *MNRAS*, 194, 809
- Leroy, A. K., Walter, F., Brinks, E., Bigiel, F., de Blok, W. J. G., Madore, B., & Thornley, M. D. 2008, *AJ*, 136, 2782
- Li, Z. & Nakamura, F. 2006, *ApJ*, 640, L187
- Lopez, J. A. & Meaburn, J. 1984, *Rev Mex AA*, 9, 119
- Lopez, L. A., Krumholz, M. R., Bolatto, A. D., Prochaska, J. X., & Ramirez-Ruiz, E. 2011, *ApJ*, 731, 91
- Lucke, P. B. & Hodge, P. W. 1970, *AJ*, 75, 171
- Mac Low, M., Klessen, R. S., Burkert, A., & Smith, M. D. 1998, *Physical Review Letters*, 80, 2754
- Mac Low, M.-M., Toraskar, J., Oishi, J. S., & Abel, T. 2007, *ApJ*, 668, 980
- Matzner, C. D. 2002, *ApJ*, 566, 302
- McGee, R. X., Brooks, J. W., & Batchelor, R. A. 1972, *Australian Journal of Physics*, 25, 581
- McKee, C. F., van Buren, D., & Lazareff, B. 1984, *ApJ*, 278, L115
- Mellema, G., Arthur, S. J., Henney, W. J., Iliev, I. T., & Shapiro, P. R. 2006, *ApJ*, 647, 397
- Murray, N. 2011, *ApJ*, 729, 133

- Murray, N., Ménard, B., & Thompson, T. A. 2010a, arXiv:astro-ph/1005.4419
- Murray, N., Quataert, E., & Thompson, T. A. 2010b, *ApJ*, 709, 191
- . 2010c, *ApJ*, 709, 191
- Murray, N. & Rahman, M. 2010, *ApJ*, 709, 424
- Netterfield, C. B., Ade, P. A. R., Bock, J. J., Chapin, E. L., Devlin, M. J., Griffin, M., Gundersen, J. O., Halpern, M., Hargrave, P. C., Hughes, D. H., Klein, J., Marsden, G., Martin, P. G., Mauskopf, P., Olmi, L., Pascale, E., Patanchon, G., Rex, M., Roy, A., Scott, D., Semisch, C., Thomas, N., Truch, M. D. P., Tucker, C., Tucker, G. S., Viero, M. P., & Wiebe, D. V. 2009, *ApJ*, 707, 1824
- Nickerson, S., Stinson, G., Couchman, H. M. P., Bailin, J., & Wadsley, J. 2011, arXiv:astro-ph/1103.3285
- Norman, M. L., Bryan, G. L., Harkness, R., Bordner, J., Reynolds, D., O'Shea, B., & Wagner, R. 2007, arXiv:astro-ph/0705.1556
- Oey, M. S. 1996, *ApJ*, 467, 666
- O'Shea, B. W., Bryan, G., Bordner, J., Norman, M. L., Abel, T., Harkness, R., & Kritsuk, A. 2004, arXiv:astro-ph/0403044
- Ostriker, E. C. & Shetty, R. 2011, *ApJ*, 731, 41
- Ostriker, E. C., Stone, J. M., & Gammie, C. F. 2001, *ApJ*, 546, 980
- Passot, T. & Vázquez-Semadeni, E. 1998, *Physical Review E (Statistical Physics)*, 58, 4501
- Penston, M. V. & Brown, F. E. 1970, *MNRAS*, 150, 373
- Petkova, M. & Springel, V. 2011, *MNRAS*, 412, 935
- Povich, M. S., Benjamin, R. A., Whitney, B. A., Babler, B. L., Indebetouw, R., Meade, M. R., & Churchwell, E. 2008, *ApJ*, 689, 242
- Povich, M. S., Benjamin, R. A., Whitney, B. A., Babler, B. L., Indebetouw, R., Meade, M. R., & Churchwell, E. 2008, *ApJ*, 689, 242
- Pree, C. G. D., Wilner, D. J., Deblasio, J., Mercer, A. J., & Davis, L. E. 2005, *ApJ*, 624, L101
- Press, W., Teukolsky, S., Vetterling, W., & Flannery, B. 1996, *Numerical Recipes in Fortran 90* (Cambridge University Press)

- Puls, J., Markova, N., Scuderi, S., Stanghellini, C., Taranova, O. G., Burnley, A. W., & Howarth, I. D. 2006, *A&A*, 454, 625
- Rauw, G., Nazé, Y., Gosset, E., Stevens, I. R., Blomme, R., Corcoran, M. F., Pittard, J. M., & Runacres, M. C. 2002, *A&A*, 395, 499
- Repolust, T., Puls, J., & Herrero, A. 2004, *A&A*, 415, 349
- Retallack, D. S. 1983, *MNRAS*, 204, 669
- Reynolds, D. R., Hayes, J. C., Paschos, P., & Norman, M. L. 2009, *JoCP*, 228, 6833
- Robertson, B. E., Ellis, R. S., Dunlop, J. S., McLure, R. J., & Stark, D. P. 2010, *Nature*, 468, 49
- Sanchawala, K., Chen, W.-P., Lee, H.-T., Chu, Y.-H., Nakajima, Y., Tamura, M., Baba, D., & Sato, S. 2007, *ApJ*, 656, 462
- Schruba, A., Leroy, A. K., Walter, F., Sandstrom, K., & Rosolowsky, E. 2010, *ApJ*, 722, 1699
- Scoville, N. Z. & Kwan, J. 1976, *ApJ*, 206, 718
- Scoville, N. Z. & Wilson, C. D. 2004, in *Astronomical Society of the Pacific Conference Series*, Vol. 322, *The Formation and Evolution of Massive Young Star Clusters*, ed. H. J. G. L. M. Lamers, L. J. Smith, & A. Nota, 245–+
- Seward, F. D., Forman, W. R., Giacconi, R., Griffiths, R. E., Harnden, F. R., Jones, C., & Pye, J. P. 1979, *ApJ*, 234, L55
- Shu, C. & Osher, S. 1988, *JoCP*, 77, 439
- Shull, J. M. 1980, *ApJ*, 238, 860
- Smith, B. J., Struck, C., & Nowak, M. A. 2005, *AJ*, 129, 1350
- Smith, N. 2006a, *MNRAS*, 367, 763
- . 2006b, *ApJ*, 644, 1151
- Smith, N. & Brooks. 2008, *Handbook of Star Forming Regions*, ed. B. Reipurth (Astronomical Society of the Pacific)
- Smith, N. & Brooks, K. J. 2007, *MNRAS*, 379, 1279
- Smith, N. & Brooks, K. J. 2007, *MNRAS*, 379, 1279

- Spitzer, L. 1962, *Physics of Fully Ionized Gases*, ed. Spitzer, L. (Interscience)
- Springel, V. & Hernquist, L. 2003, *MNRAS*, 339, 312
- Stark, D. P., Ellis, R. S., Bunker, A., Bundy, K., Targett, T., Benson, A., & Lacy, M. 2009, *ApJ*, 697, 1493
- Stevens, I. R. & Hartwell, J. M. 2003, *MNRAS*, 339, 280
- Stinson, G., Seth, A., Katz, N., Wadsley, J., Governato, F., & Quinn, T. 2006, *MNRAS*, 373, 1074
- Stinson, G. S., Bailin, J., Couchman, H., Wadsley, J., Shen, S., Nickerson, S., Brook, C., & Quinn, T. 2010, *MNRAS*, 408, 812
- Stone, J. M. & Norman, M. L. 1992, *ApJS*, 80, 753
- Sutherland, R. S. & Dopita, M. A. 1993, *ApJS*, 88, 253
- Tenorio-Tagle, G., Bodenheimer, P., & Yorke, H. W. 1985, *A&A*, 145, 70
- Townsley, L. K., Broos, P. S., Feigelson, E. D., Brandl, B. R., Chu, Y.-H., Garmire, G. P., & Pavlov, G. G. 2006, *AJ*, 131, 2140
- Truelove, J. K., Klein, R. I., McKee, C. F., Holliman, II, J. H., Howell, L. H., & Greenough, J. A. 1997, *ApJ*, 489, L179+
- Tsujimoto, M., Hosokawa, T., Feigelson, E. D., Getman, K. V., & Broos, P. S. 2006, *ApJ*, 653, 409
- Turk, M. 2008, in *Proceedings of the 7th Python in Science Conference*, ed. G. Varoquaux, T. Vaught, & J. Millman, Pasadena, CA USA, 46 – 50
- Turner, B. E., Balick, B., Cudaback, D. D., Heiles, C., & Boyle, R. J. 1974, *ApJ*, 194, 279
- van Leer, B. 1979, *JoCP*, 32, 101
- Walborn, N. R. & Hesser, J. E. 1975, *ApJ*, 199, 535
- Walborn, N. R. & Hesser, J. E. 1982, *ApJ*, 252, 156
- Wang, P. & Abel, T. 2009, *ApJ*, 696, 96
- Wang, P., Li, Z., Abel, T., & Nakamura, F. 2010, *ApJ*, 709, 27
- Wang, Q. & Helfand, D. J. 1991, *ApJ*, 373, 497

- Weaver, R., McCray, R., Castor, J., Shapiro, P., & Moore, R. 1977, *ApJ*, 218, 377
- Weinmann, S. M., Neistein, E., & Dekel, A. 2011, [arXiv:astro-ph/1103.3011](https://arxiv.org/abs/1103.3011)
- Whiteoak, J. B. Z. 1994, *ApJ*, 429, 225
- Whitworth, A. 1979, *MNRAS*, 186, 59
- Williams, J. P. & McKee, C. F. 1997, *ApJ*, 476, 166
- Wise, J. H. & Abel, T. 2008, *ApJ*, 685, 40
- . 2010, [arXiv:astro-ph/1012.2865](https://arxiv.org/abs/1012.2865)
- Wong, T., Ladd, E. F., Brisbin, D., Burton, M. G., Bains, I., Cunningham, M. R., Lo, N., Jones, P. A., Thomas, K. L., Longmore, S. N., Vigan, A., Mookerjee, B., Kramer, C., Fukui, Y., & Kawamura, A. 2008, *MNRAS*, 386, 1069
- Woosley, S. E. & Weaver, T. A. 1986, *ARA&A*, 24, 205
- Yonekura, Y., Asayama, S., Kimura, K., Ogawa, H., Kanai, Y., Yamaguchi, N., Barnes, P. J., & Fukui, Y. 2005, *ApJ*, 634, 476